Geochemistry and petrology of lamprophyres from the Hellenides and the European Variscides

Christian Soder

INAUGURAL - DISSERTATION

zur
Erlangung der Doktorwürde
der
Naturwissenschaftlich-Mathematischen
Gesamtfakultät
der
Ruprecht-Karls-Universität
Heidelberg

vorgelegt von
Christian Soder (M.Sc.)
aus Heidelberg

Tag der mündlichen Prüfung: 20.07.2017

Thema

Geochemistry and petrology of lamprophyres from the Hellenides and the European Variscides

Gutachter: Prof. Dr. Rainer Altherr
Prof. Dr. Mario Trieloff

Contents

Abstract

Mantle-derived potassic to ultrapotassic magmatism is a typical feature of collisional orogens and is also occasionally present above oceanic subduction zones. Lamprophyres are part of this magmatism and are of particular interest, as they carry information about the chemical and mineralogical conditions of the uppermost mantle. They offer insights into the process of element cycling during subduction and collision, when a strong physical and chemical interactions between the geochemical reservoirs, specifically between the continental crust, the oceanic crust as well as the upper mantle, take place. This thesis presents examples from active subduction settings (the Greek Hellenides) as well as fossil subduction and collision zones (the European Variscides). Both studies focus on detailed whole-rock geochemical and isotopic data sets. Additional information about the lithospheric evolution are obtained from high-pressure xenoliths hosted in these lavas. Xenoliths from Variscan lamprophyres provide a snapshot of the lower orogenic crust during the Variscan collisional process and record the dynamics of regional extension.

The island of Kos at the eastern end of the South Aegean Volcanic Arc hosts numerous late Neogene amphibole and mica lamprophyres. The Sr and Nd isotope ratios of these mantle-derived rocks correlate negatively in narrow ranges, extending from the undepleted end of the mantle array towards values typical for continental crust. The crust-like signature is linked to the addition of subducted SE Mediterranean sediments, which dominate the Pb isotopic composition of all lamprophyres. The mantle endmember of the Sr–Nd isotope mixing array is strongly enriched in incompatible trace elements and shows anorogenic affinities. Whole-rock geochemistry indicates that the lamprophyres originated from the depleted lithospheric mantle above the Hellenic subduction zone that was modified by (i) K-rich silicic partial melts or supercritical fluids from subducted metasediments and (ii) melts from the asthenosphere below the subducting slab. The first metasomatic component formed phlogopite-orthopyroxene-rich veins, whereas the second led to the formation of amphibole-bearing clinopyroxenites. Subsequent melting preferentially affected these enriched domains. Variable dilution by contributions from ambient peridotite and mixing between both components caused the large chemical variation observed in the lamprophyres. The asthenosphere-derived component represents incipient melt with a carbonatite-like trace element signature (e.g. superchondritic Nb/Ta and Zr/Hf; low Ti/Eu). This metasomatic agent was probably introduced into the mantle wedge along ruptures in the slab of the retreating Hellenic subduction zone. Lamprophyres dominated by the sediment signature have isotopic and chemical similarities to basaltic rocks erupted along the South Aegean Volcanic Arc. The much stronger enrichment in incompatible trace elements of the lamprophyres is related to only minor dilution by melts from the ambient mantle. Partial melting in the lithospheric mantle is attributed to extensional tectonics, probably during a stage of rapid slab rollback, with a limited availability of fluid as a fluxing agent. Lamprophyre emplacement occurred along sinistral 'en-échelon' structures in a crustal-scale shear zone, which separates Anatolia from the faster extending Aegean back-arc basin.

In the Variscides, K-rich magmatic rocks form intrusions throughout the internal zones of the orogen (durbachites, melanocratic quartz-monzonites/-syenites, lamprophyres, lamproites, tra-

chybasalts, basaltic trachyandesites, shoshonites). Based on a detailed whole-rock geochemical dataset of post-collisional dykes from SW Germany and E France, a generic petrogenetic model for this chemically and isotopically heterogeneous mantle-derived magmatism is presented. The lamprophyres have crust-like trace element patterns and elevated initial $^{87}Sr/^{86}Sr$ and $^{207}Pb/^{204}Pb$ as well as low $^{143}Nd/^{144}Nd$ ratios. High mantle-compatible element concentrations reflect significant contributions from mantle peridotite to the melts. This hybrid nature requires at least two source components: continental material and mantle peridotite. Continental subduction during Variscan collisional processes resulted in the physical and chemical interaction between the crust and the upper mantle. Systematic sampling of dyke rocks across tectonic zones of contrasting development reveals two groups of mantle-derived potassic to ultrapotassic rocks with distinct trace element patterns and isotopic compositions. Deeply subducted crustal lithologies were affected by high-degree partial melting at mantle depth due to the breakdown of hydrous phases like phengite. Whether the trace element signature is transferred unmodified into these melts or not, largely depends on the behaviour of accessory phases (e.g. zircon, allanite or monazite) that sequester significant amounts of incompatible trace elements. For instance, high Th/La–Sm/La and low Th/U ratios of some lamprophyres are related to residual allanite during generation of the metasomatic crustal melts. The melts migrate from the slab into the overlying lithospheric mantle, react with peridotite and solidify to phlogopite–pyroxenites. Reaction between siliceous melt and peridotitic wallrock leads to the crystallisation of orthopyroxene $\pm$ garnet at the expense of olivine, resulting in a depletion in Al_2O_3 and garnet-compatible trace elements in the coexisting melt. Progressive wall-rock interaction causes enrichment in incompatible trace elements and eventually produces peralkaline melt compositions. Post-collisional extension preferentially triggers melting within the metasomatic domains. Mobilisation of the diverse olivine-poor hybridisation products generates geochemically and mineralogically heterogeneous melt-compositions, ranging from medium-K basalts to peralkaline lamproites.

Crustal xenoliths entrained in post-collisional Variscan lamprophyres from the crystalline Odenwald (Mid-German Crystalline Zone, MGCZ) include felsic granulites and retrogressed eclogites. Classical thermobarometry, Zr-in-rutile thermometry and equilibrium phase diagrams (pseudosections) reveal temperatures of 700–800°C and pressures of 1.7–1.8 GPa. Both lithologies record isothermal decompression and provide evidence for the presence of partial melt. The felsic granulite is partially molten at peak conditions. Instead, the solidus of the eclogite is crossed during isothermal decompression, causing fracturing of mineral grains and crystallisation of a plagioclase-bearing assemblage along grain boundaries and cracks crossing garnet, indicating pressures of 1.2$\pm$0.2 GPa. Both lithologies got entrained into the mantle-derived magma, causing a high-temperature overprint at temperatures in excess of 1100°C that resulted in the development of diverse fine-grained microstructures. As no deformation or cooling related to a tectonic exhumation process occurred, rare mineralogical and textural features are preserved. Compositional sector zonation in garnet is caused by rapid crystallisation, related to reaction overstepping. Sudden nucleation and crystallisation possibly takes place due to shearing and fluid-inflow during incipient decompression. During continuing extension, the wet solidus is crossed. Small amounts of partial melt cause a drastic reduction in rock strength due to brittle failure. A consequence of rheological weakening may be a localisation of deformation, resulting in crust-scale shear zones. Such shear zones may accommodate orogenic extension, provide pathways and trigger the ascend of the mantle-derived lamprophyres. For this reason, the lower crustal xenoliths are rare documents of the Variscan collision process, resulting in crustal thickening to at least 60 km, and

the subsequent regional extension. A Lower Carboniferous age of metamorphism is supported by SIMS U-Pb zircon dating, which gave ages of 332±7 (2σ) Ma (felsic granulite) and 335±6 Ma (eclogite). An age of 440±10 Ma obtained for the oldest zircon population in the eclogite is interpreted as the age of the magmatic protolith. Abundant discordant zircons with oscillatory zonation in the felsic ganulite have an upper concordia intercept at 2110±25 Ma, giving the age of crystallisation of the granitic protolith. While Silurian magmatism is well established within the MGCZ, Paleoproterozoic basement was previously unknown and is generally very rare in the European Variscides.

Kurzfassung

Das Auftreten kaliumreicher Mantelmagmen ist ein typisches Phänomen von Kollisionsorogenen. Diese Magmen treten volumenmäßig deutlich hinter die weit verbreiteten granitischen Gesteine zurück, sind jedoch von besonderem Interesse, da sie Informationen über die chemische und mineralogische Zusammensetzung des oberen Erdmantels liefern. Sie geben dadurch Einblicke in Wechselwirkungsprozesse, die während Subduktion und Kollision zwischen ozeanischer bzw. kontinentaler Kruste sowie dem peridotitischen Erdmantel ablaufen. In dieser Studie werden sowohl Beispiele aus dem Bereich einer aktiven Subduktionszone (den griechischen Helleniden) sowie fossilen Subduktions- und Kollisionszonen (den europäischen Variziden) behandelt. Beide Studien basieren im Wesentlichen auf geochemischen und isotopischen Gesamtgesteinsanalysen von potassischen bis ultrapotassischen Magmen (Lamprophyren). Zusätzliche Informationen über die Entwicklung der kontinentalen Lithosphäre können jedoch auch von Xenolithen mit Hochdruckparagenesen gewonnen werden, welche in einigen der untersuchten Ganggesteinen vorkommen. Diese Einschlüsse liefern eine Momentaufnahme der unteren orogenen Kruste im post-kollisionalen Stadium und dokumentieren damit den spätvariszischen Kollisions- sowie Extensionsprozess.

Auf der Insel Kos, am östlichen Ende des quartären Südägäischen Vulkanbogens, treten zahlreiche Amphibol- und Glimmer-Lamprophyre auf. Diese Ganggesteine zeigen eine deutlich ausgeprägte negative Korrelation in ihren Sr- und Nd-Isotopenzusammensetzungen. Die Isotopenverhältnisse variieren zwischen Werten des unverarmten Erdmantels und typischen Signaturen der kontinentalen Kruste. Die kontinentalen Signaturen werden auf subduzierten Sedimenten zurückgeführt. Das Mantel-Endglied der Sr–Nd-Mischungsreihe ist durch sehr starke Anreicherung an inkompatiblen Elementen gekennzeichnet und besitzt eine anorogene Spurenelementsignatur. Basierend auf der Gesamtgesteins-Geochemie der Magmen ist anzunehmen, dass die Lamprophyre aus dem verarmten lithosphärischen Erdmantel stammen, der über der Hellenischen Subduktionszone chemisch und mineralogisch modifiziert wurde. Die Anreicherung erfolgte durch K- und Si-reiche partielle Schmelzen aus subduzierten Metasedimenten und durch Schmelzen aus dem asthenosphärischen Mantel unterhalb der subduzierenden Platte. Die erstgenannte Komponente kristallisierte zu Phlogopit-Orthopyroxen-reichen Adern und Gängen im lithosphärischen Mantel, die zweite zu Amphibol-führenden Klinopyroxeniten. Erneutes partielles Schmelzen des lithosphärischen Mantels führte zur bevorzugten Remobilisierung der angereicherten Bereiche. Unterschiedliche Mischungsverhältnisse zwischen Schmelzen beider Komponenten, sowie unterschiedlich starke Verdünnung durch Zumischung partieller Schmelzen aus dem umgebenden Peridotit, führte zu der ausgeprägten geochemischen und mineralogischen Variabilität der Lamprophyre von Kos. Die aus der Asthensphäre stammende Komponente resultiert aus einer niedriggradigen Schmelze mit Karbonatit-artiger Spurenelement-Signatur (z. B. super-chondritische Verhältnisse von Nb/Ta und Zr/Hf; niedriges Ti/Eu). Diese metasomatische Komponente wurde womöglich über Risse innerhalb der subduzierenden Platte in den Mantelkeil der zurückweichenden Hellenischen Subduktionszone zugeführt. Lamprophyre mit einer deutlich ausgeprägten Sediment-Signatur zeigen isotopische und chemische Ähnlichkeiten mit den basaltischen Gestei-

nen, die entlang des Südägäischen Inselbogens eruptiert sind. Die deutlich stärkere Anreicherung an inkompatiblen Spurenelementen der Lamprophyre ist durch bevorzugtes Schmelzen von pyroxenitischen Bereichen und nur untergeordneten Beimengungen von 'basaltischen' Schmelzen aus peridotitischem Mantel bedingt. Partielle Schmelzbildung im lithosphärischen Mantel geht vermutlich auf extensionale tektonische Prozesse zurück, die mit einer Phase erhöhten Zurückrollens der Subduktionszone in Zusammenhang stehen. Die Platznahme der Lamprophyre erfolgte in sinistrale „en-échelon"-Strukturen einer womöglich die gesamte Kruste ergreifenden Scherzone, die Anatolien von dem sich schneller ausdünnenden Ägäischen Back-arc-Becken trennt.

Die internen Zonen des Variszischen Gebirges sind durch das Auftreten zahlreicher K-reicher Plutonite, Subvulkanite und Vulkanite gekennzeichnet (Durbachite, melanokrate Quarz-Monzonite/-Syenite, Lamprophyre, Lamproite, Trachybasalte, basaltische Trachyandesite, Shoshonite). Basierend auf einem detaillierten Gesamtgesteins-Datensatz post-kollisionaler Ganggesteine aus Ostfrankreich und Südwestdeutschland wird ein neues petrogenetisches Modell für diese chemisch und isotopisch heterogenen Mantelmagmen vorgestellt. Die Lamprophyre besitzen Spurenelement-Muster sowie Sr–Nd–Pb-Isotopenzusammensetzungen, die der kontinentalen Kruste entsprechen. Hohe Konzentrationen Mantel-kompatibler Elemente zeigen deutliche peridotitische Beiträge in diesen Schmelzen an. Diese „hybride" Natur erfordert mindestens zwei Komponenten in der Quelle der Magmen: kontinentales Material und Mantelperidotit. Kontinentale Subduktion während des variszischen Kollisionsprozesses verursachte eine physikalische und chemische Interaktion zwischen Kruste und oberem Erdmantel. Die systematische Beprobung von Ganggesteinen quer zur tektonischen Zonengliederung des Orogens mit unterschiedlicher Vorgeschichte lässt zwei Gruppen von K-reichen Mantelmagmen erkennen, die jeweils charakteristische Spurenelement- und Isotopensignaturen besitzen. In tief subduzierten krustalen Lithologien bildeten sich hochgradige partielle Schmelzen aufgrund des Instabilwerdens von wasserhaltigen Phasen wie Phengit. Ob die Spurenelement-Signatur der kontinentalen Kruste unverändert auf diese Schmelzen übertragen wird, hängt größtenteils vom Verhalten akzessorischer Minerale (wie z.B. Zirkon, Allanit (Orthit) oder Monazit) ab, welche signifikante Anteile an Spurenelementen aufnehmen. Die hohen Th/La–Sm/La- und niedrigen Th/U-Verhältnisse einiger Lamprophyre zeigen beispielsweise residuellen Allanit während der Bildung der metasomatischen, krustalen Schmelzen an. Diese Schmelzen migrieren von der subduzierten Platte in den überlagernden lithosphärischen Mantel und reagieren mit dem Peridotit, wo sie schließlich kristallisieren und Phlogopit-Pyroxenite bilden. Die Reaktion zwischen diesen Silizium-reichen Schmelzen und dem peridotitischen Nebengestein resultiert in der Kristallisation von Orthopyroxen $\pm$ Granat auf Kosten von Olivin, was zu einer Verarmung der koexisterenden Schmelze an Al_2O_3 und Granat-kompatiblen Spurenelementen führt. Fortschreitende Wechselwirkung zwischen Schmelze und Nebengestein verursacht eine passive Anreicherung an inkompatiblen Elementen und kann zu peralkalinen Schmelzzusammensetzungen führen, die schließlich im lithosphärischen Mantel kristallisieren. Während post-kollisionaler und späterer Extension erfahren diese metasomatischen Bereiche bevorzugtes Aufschmelzen. Die Mobilisierung der diversen Olivin-armen Hybridisierungsprodukte resultiert in geochemisch und mineralogisch heterogenen Magmen, die von Amphibol-Lamprophyren bis hin zu peralkalinen Lamproiten variieren.

Einige Lamprophyre des kristallinen Odenwaldes (Mitteldeutsche Kristallinzone, MGCZ) enthalten eine große Anzahl von Mantel- und Krustenxenolithen. Unter diesen befinden sich felsische Granulite sowie retrograde Eklogite. Klassische Thermobarometrie, Zr-in-Rutil-Thermometrie und Gleichgewichts-Phasendiagramme ergeben Temperaturen von 700°C (Eklogit) und 800°C

(felsischer Granulit) bei Drücken von 1.7–1.8 GPa. Beide Lithologien zeigen isotherme Dekompression an und geben Hinweis auf die Anwesenheit von partiellen Schmelzen. Hierbei zeigt der Eklogit bei Drücken von 1.2±0.2 GPa eine Überprägung im Stabilitätsfeld von Plagioklas. Die neue Paragenese kristallisiert entlang von Korngrenzen und Brüchen, die sich in Granat bilden und gibt Hinweis auf Kristallisation aus einer Schmelze. Schließlich erfahren die Lithologien eine Hochtemperatur-Überprägung im aufsteigenden Magma bei Temperaturen über 1100°C, was zur Entwicklung diverser feinkörniger Mikrostrukturen führt. Der Transport zur Oberfläche im Lamprophyr-Magma erfolgte rasch. Die Xenolithe enthalten deshalb mineralogische und strukturelle Merkmale, die bei tektonischen Exhumierungsprozessen durch Deformation und retrograde Abkühlung womöglich einer starken Überprägung unterliegen würden. Der Granat der Eklogite ist sektorzoniert, was rasches Kristallwachstum anzeigt und mit Reaktions-Überschreitung im Zusammenhang steht. Die Erhaltung dieses Zonarbaus bedeutet, dass die während Dekompression und unter Anwesenheit partieller Schmelzen stattfindende Überprägung nur kurzfristig gewirkt haben kann und unmittelbar auf die eklogitfazielle Metamorphose folgte. Die plötzliche Nukleation und Kristallisation ist möglicherweise mit Scherbewegungen und Fluidzutritt bei gleichzeitiger Dekompression verbunden. Bei fortgesetzter Extension wird der nasse Solidus überschritten. Geringgradige Teilschmelzen bewirken eine drastische Verringerung der Gesteinsfestigkeit durch sprödes Versagen. Eine Folge dieser rheologischen Schwächung kann eine Lokalisierung von Deformationsprozessen und schließlich die Ausbildung krusten-skaliger Scherzonen sein. Entlang solcher Scherzonen können post-kollisionale Extensionsprozesse ablaufen sowie Lamprophyr-Magmen aus dem Erdmantel aufsteigen. Die Unterkusten-Xenolithe sind somit seltene Dokumente des variszischen Kollisionsprozesses und zeigen eine Krustenverdickung auf mindestens 60 km an. Darüber hinaus verleihen sie Einblicke in die Dynamik des post-kollisionalen Extensionsprozesses. Ein unterkarbonisches Metamorphosealter von 332±7 Ma (felsischer Granulit) und 335±6 Ma (Eklogit) konnte durch U-Pb-Datierungen an Zirkonen mittels SIMS bestätigt werden. Die älteste Zirkon-Population im Eklogit besitzt ein Alter von 440±10 Ma, was als magmatisches Protolith-Alter interpretiert wird. Zirkone mit oszillierendem Zonarbau im felsischen Granulit sind diskordant und besitzen einen oberen Einstichpunkt auf der Konkordia bei 2110±25 Ma, der das Kristallisationsalter des granitischen Protoliths anzeigt. Während silurischer Magmatismus innerhalb der MGCZ gut dokumentiert ist, war paläoproterozoisches Grundgebirge bisher nicht bekannt, und ist generell in den europäischen Varisziden sehr selten anzutreffen.

1. Introduction

1.1. K-rich mantle-derived magmatism

The dense oceanic crust is recycled back into the mantle within some 200 Ma. In contrast, the average age of continental crust is almost 2 Ga, as its buoyant quartzofeldspathic materials are difficult to subduct. Due to differentiation during the evolution of the Earth, the crust is enriched in incompatible elements and depleted in compatible components compared to the primordial chondritic composition. The mass of the continental crust only accounts for 0.57% of the bulk silicate Earth, and yet it contains 35% of the potassium (Kemp & Hawkesworth, 2003, Rudnick & Gao, 2003). Chemical elements present in amounts of nanogram per gram within the Earth's mantle may be enriched by some two orders of magnitude in the average continental crust and locally form deposits of economic interest. Understanding the origin of the continents is critical for understanding the origin and differentiation of our planet.

Since the first findings of coesite in continental lithologies (Chopin, 1984; Smith, 1984) and the continuing discovery of new ultrahigh-pressure (UHP) metamorphic terrains, it became obvious that continental crust subduction and UHP metamorphism are necessary consequences of collision tectonics. Since then, much attention has been paid to these exhumed UHP crustal sections. In order to understand the origin and evolution of the continents, an understanding of not only the crust is required, but also of the lithospheric mantle. The subcontinental lithospheric mantle formed more or less contemporaneously with the crust. The geochemical memory of this mantle domain is a recorder of past enrichment episodes, as it does not participate in solid-state convection. Fluids or melts may have modified the chemical and mineralogical composition of the lithospheric mantle over time. Hydrous silicate melts or aqueous fluids may be liberated from subducting lithosphere. Additionally, silicate melts or carbonatite liquids originating in the deeper (asthenospheric) mantle may have modified the lithosphere. Many different processes may affect the lithospheric mantle, ultimately resulting in a broad range of compositions in mantle-derived melts (e.g. Tappe *et al.*, 2006; Pilet *et al.*, 2008; Prelević *et al.*, 2015).

Samples of subcontinental mantle lithosphere are collected as xenoliths in mantle-derived lavas. However, orogenic magmas usually bring few mantle xenoliths to the surface. Additionally, slices of upper mantle can be tectonically emplaced into the crust during orogenesis or obducted on continental margins as ultramafic sections in ophiolite complexes. However, these peridotites usually provide an incomplete picture of the nature and composition of the orogenic lithospheric mantle. Mantle-derived magmas represent another possibility to study the subcontinental lithosphere. Enrichment of K_2O in mantle-derived melts is one of the most striking features of most post-collisional volcanic provinces, such as those of the Alpine–Himalayan orogenic belt. Ultrapotassic

post-collisional lavas are present in the Mediterranean region (e.g. Altherr *et al.*, 2004; Conticelli *et al.*, 2009) or the Tibetan plateau (e.g. Turner *et al.*, 1996), for instance. These K-rich melts usually postdate subduction and, therefore, are interpreted to be derived from the lithospheric mantle. In this thesis, K-rich mantle-derived melts from two contrasting geodynamic settings are discussed. The lamprophyres from the Island of Kos (Greece) are outstanding as they are located above an active subduction zone. Back-mixing (recycling) plays a fundamental role in the large scale redistribution of elements between the different reservoirs of the Earth. The geochemistry of the lamprophyres is used to test whether it is possible to trace the nature of subducted material. A second study deals with a systematic whole-rock data set of Variscan lamprophyres that is used to investigate the role of element recycling in continental collision zones. The strong trace element enrichment and crust-like signatures in radiogenic isotopes show that recycled continental crust plays an important role in the continental mantle within palaeo-subduction zones. This lithospheric mantle hosts metasomatic domains formed during an earlier stage of subduction or collision when upper crustal lithologies reached depths within the field of diamond stability.

Lamprophyre magmatism above the Hellenic subduction zone The geological evolution of the Aegean region is governed by the convergent motion between the major African and Eurasian plates. Seismic tomography studies strongly suggest a single north-vergent subduction zone, active throughout the Cenozoic below the Aegean (e.g. Faccenna *et al.*, 2003). The lamprophyres from the Island of Kos are attractive to study, as they are located above this active subduction zone and as they are among the youngest known lamprophyre occurrences on Earth. The trench of the subduction zone is covered by the thick sedimentary pile of the Mediterranean Ridge accretionary complex. An emerging issue is, whether it is possible to trace the subducted crustal material in the geochemistry of the melts. Furthermore, many different petrographic types, comprising amphibole- and mica-rich varieties are present. How are these different types of dykes related to each other?

Despite ongoing convergence, the Aegean and other areas in the Mediterranean are affected by strong extensional tectonics. As the subducting oceanic lithosphere is old and dense, the slabs are sinking steeply into the mantle, causing back arc extension in the hanging plate. Coevally, neighbouring areas already are undergoing collisional tectonics, resulting in arcuate belts with narrow oceanic basins (e.g. Wortel & Spakman, 2000). The Island of Kos is positioned at the transition between both such contrasting crustal domains. It is therefore expected that the geochemistry of these melts is affected by the slab-edge processes active along the margin of the retreating subduction zone.

K-rich mantle-derived magmatism of the Variscan belt Countless lamprophyre dykes were emplaced across the internal parts of the Variscan orogen during post-collisional extension. The orogen includes several different subduction zones. Therefore, a systematic set of samples of these post-collisional dykes along a traverse across the various Variscan

tectonic units in SW Germany and E France was obtained. A striking feature of the Variscides is the wide distribution of felsic high- to ultrahigh-pressure nappes that are commonly associated with garnet peridotites and may locally contain diamond, testifying for deep continental subduction (e.g. Kotková *et al.*, 2011). The juxtaposition of crustal lithologies against hot peridotite causes metasomatic alteration of the mantle lithosphere and eventually results in the K-rich mantle-derived magmatism. The key questions for this comparison are: What is the role and nature of fluid phases and melt-rock interactions during metasomatism of the mantle? Is there a regional distribution of geochemical signatures and does it follow major tectonic zones of the orogen? Does such a regional pattern trace different types of subducted crust and does it therefore identify the nature of different ancient subduction zones?

A petrogenetic model is presented to explain the large chemical heterogeneity observed in local mantle-derived magmatic suites, which range from high-K basalts, shoshonitic lamprophyres to lamproites. The model describes (i) selective mobilisation from the slab, whereby the metasomatic agent and restite may show different incompatible element signatures and contrasting isotopic compositions, (ii) reactive melt transport into the lithospheric mantle with intense interaction with the peridotitic mantle to form mineralogically and chemically zoned veins within the lithospheric mantle, (iii) partial melting of sections of the veined mantle and (iv) modification of these melts during fractional crystallisation.

Historically, early investigations of the rock group of lamprophyres were carried out in the study area and pioneering contributions to the geological literature were made by Harry Rosenbusch in Heidelberg (e.g. Delesse, 1856; Rosenbusch, 1887, 1896). Essential features of Rosenbusch's 1896 classification of lamprophyres are part of the current IUGS classification of magmatic rocks (Le Maitre, 2002). Several 'type localities' are present in the study area (spessartite, vogesite and minette).

Xenoliths in post-collisional lamprophyres Lower crustal and upper mantle xenoliths are rarely described from orogenic mantle-derived lavas. They are mostly absent in Variscan lamprophyres and only few examples of xenolith-rich dykes were encountered during field work in the course of this thesis. A spessartite–kersantite dyke cutting the Weschnitz pluton of the Odenwald crystalline complex is an outstanding example, as it contains fragments of a plethora of different upper mantle and lower crustal lithologies. The location of the lamprophyre is positioned above the inferred Rheic suture zone, the principal oceanic suture of the Variscan orogen. The xenoliths therefore may provide insights into the crustal structure of the suture zone. They comprise dunites, phlogopite-clinopyroxenites, phlogopite-orthopyroxenites, hornblendites, amphibolites, gabbros, felsic granulites and retrogressed eclogites. Some of the upper mantle lithologies, such as depleted peridotites and metasomatic assemblages like phlogopite-orthopyroxenite, may correspond to the source region of the lamprophyres (see Chapter 3). Additionally, the metamorphic evolution of the lower crust is of particular interest. Until now, no late Variscan high-pressure metamorphic event has been described for this part of the orogen (the Mid-German Crystalline Zone). However, abundant post-collisional granitoids

strongly suggest crustal thickening (Altherr *et al.*, 1999a). Indeed, some granitoids from the MGCZ contain adakite-like trace element signatures, indicative of garnet-rich lower crustal lithologies undergoing partial melting. Due to the post-collisional timing of lamprophyre magmatism, extraction of the xenoliths from the lower crust takes place after the peak of the orogeny. These rock fragments may therefore provide a snapshot of the lower orogenic crust during Variscan collision and regional extension. Although severe pyrometamorphic overprinting occurred during transport in the mantle-derived melt, valuable microstructural and mineralogic features are preserved, due to the absence of recrystallisation and overprinting during tectonic exhumation.

1.2. Structure of the thesis

Each of the main chapters of the thesis deals with a different aspect of K-rich mantle-derived magmatism.

Chapter 2 presents a study on lamprophyres from the Island of Kos (Greece). A total of 44 dykes of amphibole- and mica-lamprophyre were sampled, examined in thin sections and analysed for major elements by X-ray fluorescence (XRF). Whole-rock trace element analyses were obtained from all samples by inductively coupled plasma mass spectrometry (ICP-MS). 18 representative samples were analysed for Sr, Nd and Pb isotopes. A modified version of the chapter has already been published in Soder *et al.* (2016) in *Journal of Petrology* and results from a study performed in cooperation with Rainer Altherr (Heidelberg) and Rolf L. Romer (Potsdam).

Chapter 3 is a study of post-collisional lamprophyres from the Variscan orogen. A total of 143 lamprophyre dyke rocks were sampled in SW Germany and E France, examined in thin sections and analysed for whole-rock major and trace elements. A total of 36 representative samples were analysed for Sr, Nd and Pb isotopes. Additionally, the mineral chemistry of major phases in genetically important and representative samples was analyzed. This chapter has been submitted for publication to *Journal of Petrology* and results from a study performed in cooperation with Rolf L. Romer (Potsdam).

Chapter 4 deals with crustal xenoliths entrained in a Variscan lamprophyre dyke from the crystalline Odenwald (Mid-German Crystalline Zone). Metabasic and metagranodioritic lithologies were examined using scanning electron microscopy and electron probe microanalysis. *P–T* information was derived from equilibrium assemblage modelling and classical phase and trace element thermobarometry. Additionally, U-Pb zircon dating was carried out using SIMS. The chapter is currently in preparation for publication.

Chapter 5 provides the final conclusion of the thesis.

The **Appendix** provides a description of the analytical methods used. Furthermore, it contains a list with sample localities. Tables contain major and trace element whole-rock data, representative electron microprobe analyses of mineral phases as well as the results of SIMS U-Pb zircon analysis.

2. Mantle metasomatism at the edge of a retreating subduction zone: Late Neogene lamprophyres from the Island of Kos, Greece

2.1. Introduction

The retreat of subduction zones may cause segmentation of the downgoing slab by lithosphere-scale ruptures and slab windows or gaps (e.g. Wortel & Spakman, 2000; Faccenna *et al.*, 2004; Govers & Wortel, 2005). Along such gaps, the mantle of the upper plate can be influenced by lateral or vertical inflow of material from the asthenosphere below the subducting plate. This process may cause the replacement of orogenic (subduction-related) geochemical signatures by anorogenic (convecting mantle) signatures in associated igneous rock suites (e.g. Ferrari, 2004; Prelević *et al.*, 2015). In the Mediterranean region, subduction-related basaltic rocks erupt along volcanic arcs but can be accompanied by mantle-derived melts with intra-plate signature in close proximity (Gvirtzman & Nur, 1999; Gasperini *et al.*, 2002; Duggen *et al.*, 2005; Rosenbaum *et al.*, 2008).

In the eastern Mediterranean, northward subduction of old oceanic lithosphere and westward extrusion of Asia Minor results in retreat of the subduction zone marked by the Pliocene to Recent South Aegean Volcanic Arc (SAVA) and crustal extension in the Aegean. In the easternmost Aegean, lamprophyre dykes were emplaced above the active subduction zone on the island of Kos in the Late Neogene. Lamprophyres are well known to appear in collisional zones but rarely along volcanic arcs, which is why Kos is an unusual example of lamprophyre magmatism. Numerous dykes are present, showing highly variable petrographic characteristics ranging from amphibole to mica lamprophyres (Wimmenauer, 1977). In contrast, such dykes are absent in the western and central Aegean Sea. The spatial restriction to the eastern margin of the back-arc basin strongly suggests a tectono-magmatic relation to structures that control the eastern termination of the Aegean magmatic arc. It is to be expected that the Kos dykes not only deliver a geochemical record of subduction-zone metasomatism, but also one of the slab-edge process.

2.2. Geological setting

Lithosphere dynamics in the Mediterranean is governed by the convergence between the Eurasian, African and Arabian plates. In the Eastern Mediterranean, the Hellenides of Greece and the Anatolide belt of western Turkey are stacks of nappes that are aligned parallel to the Hellenic subduction zone (Fig. 2.1). Since the Late Cretaceous to Eocene

collision between the internal Hellenides and the Pelagonian realm (i.e. the closure of the Vardar ocean), a single north-vergent subduction system is active (Bijwaard *et al.*, 1998; Wortel & Spakman, 2000; Faccenna *et al.*, 2003). Despite the ongoing convergence of Africa and Eurasia, the Aegean region shows strong post-Oligocene crustal extension, leading to the formation of the Aegean back-arc basin (e.g. Avigad *et al.*, 1997; Dinter, 1998). This is related to the south-directed rollback of old and dense oceanic lithosphere along the Hellenic subduction zone (Le Pichon & Angelier, 1979; Jolivet, 2001; Faccenna *et al.*, 2003). Following the exhumation of 24–20 Ma old HP/LT-metamorphic rocks on Crete and the Peloponnese (Seidel *et al.*, 1982; Bassias & Triboulet, 1994), continued subduction of oceanic lithosphere resulted in the development of the SAVA (Meulenkamp *et al.*, 1988; Brun & Sokoutis, 2010). To the east, in western Anatolia, extension rates are much smaller than in the Aegean, resulting in a significant change in crustal thickness between the two regions (e.g. Makris & Stobbe, 1984; Saunders *et al.*, 1998). The differential motion between the Aegean and the west-Anatolian domain is taken up by a lithosphere-scale shear zone, which separates the two regions and which was active at least since the early Miocene (Ring *et al.*, 1999, Ring *et al.*, 2010). This shear zone is located in the upper plate of the subduction zone and results from variable amounts of slab retreat. In the east, the SAVA terminates at this transition zone.

The island of Kos is located at the eastern end of the SAVA. Seismic tomographic studies reveal the subducting slab beneath Kos, but no slab tear fault, which may be too small to be resolved by seismic tomography. The structure of the upper mantle changes approximately 100 km to the east of Kos, where a slow P-wave velocity anomaly beneath western Anatolia is interpreted as gap in the subducting slab allowing uprise of the asthenosphere (de Boorder *et al.*, 1998; Wortel & Spakman, 2000; Piromallo & Morelli, 2003; Govers & Wortel, 2005; Biryol *et al.*, 2011).

Extensive igneous activity accompanied the Cenozoic subduction-collision history of the Aegean and western Anatolia regions (Fig. 2.1). The oldest magmatic rocks are of Eocene to Oligocene age and are exposed in the Bulgarian Rhodopes. They have a medium- to high-K calc-alkaline to shoshonitic character (Kirchenbaur *et al.*, 2012). Further to the south, widespread plutonism of monzonitic to granitic compositions affected the Aegean region coeval with Miocene extension (Altherr *et al.*, 1982; Altherr & Siebel, 2002; Bolhar *et al.*, 2010). Mafic mantle-derived igneous rocks are especially widespread in western Anatolia and in the eastern Aegean, but seem to be absent in the central and western Aegean (Aldanmaz *et al.*, 2000; Agostini *et al.*, 2007; Dilek & Altunkaynak, 2009; Pe-Piper *et al.*, 2014; Prelević *et al.*, 2012, 2015). Volcanism is mostly potassic with minor ultrapotassic occurrences. Subduction-related volcanic activity occurs along the active SAVA since the Early Pliocene (Fytikas *et al.*, 1984; Matsuda *et al.*, 1999; Francalanci *et al.*, 2005). From north to south, the age of magmatism in western Anatolia decreases systematically (e.g. Prelević *et al.*, 2012). The spatial extent of the slow P-wave velocity anomaly (see bold outline in Fig. 2.1a) corresponds to the distribution of mantle-derived igneous rocks with a distinct geochemical signature that resembles an anorogenic component. Within individual volcanic centers, magmatic rocks derived from melting of the enriched subcontinental lithospheric mantle are followed by melts with

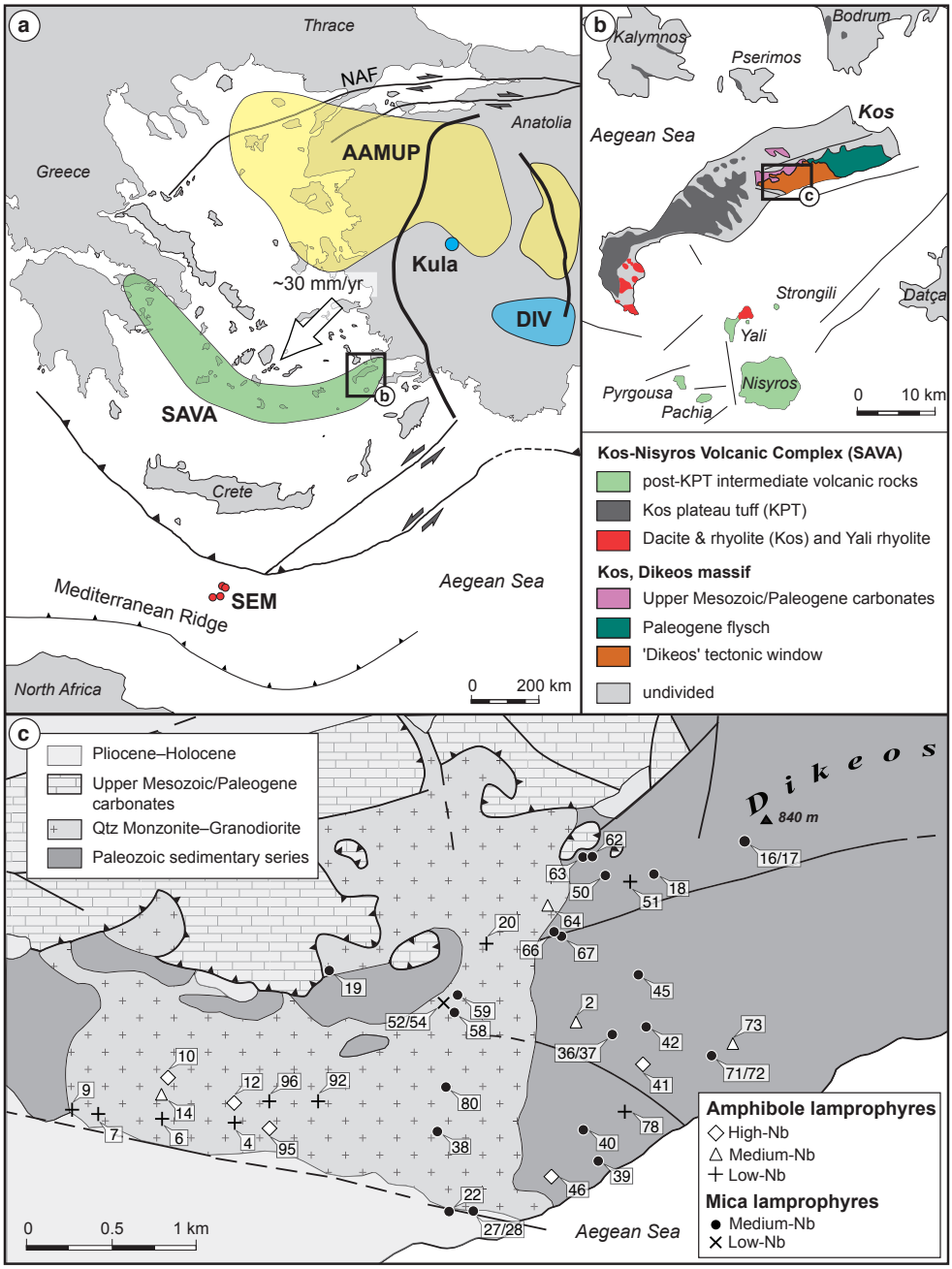

Fig. 2.1. (a) Map of the Aegean and western Anatolia regions. The shaded fields mark volcanic associations referred to in the text [SAVA, South Aegean Volcanic Arc; AAMUP, North Aegean–West Anatolian Miocene (ultra)potassic province; DIV, Denizli-Isparta volcanism comprising localities Denizli, Bucak, Gölcük–Isparta; Kula, Quaternary Kula alkali basaltic field (Prelević *et al.*, 2012; Ersoy & Palmer, 2013; Klaver *et al.*, 2016)]. SEM, SE Mediterranean sediments, indicating locations of Ocean Drilling Program (ODP) Leg 160 sites (970A, 917A, 917B, KL53, 969A). Outline of slab window beneath West Anatolia (bold black lines bracketing Kula and DIV) and major tectonic structures (NAF, North Anatolian fault) are taken from Biryol *et al.* (2011). (b) Geological map of Kos and surrounding areas showing Pliocene–Quaternary volcanic rocks (Pe-Piper & Moulton, 2008) and geological units of eastern Kos. (c) Geological map of the study area showing the sample locations [modified from Triantaphyllis (1998)].

increasing contributions from the rising asthenosphere. In some places, such a sequence ends with a transition to Na-alkaline lavas (Aldanmaz *et al.*, 2000; Dilek & Altunkaynak, 2009; Elitok *et al.*, 2010; Prelević *et al.*, 2012, 2015). At Kula, Na-alkaline volcanism with OIB-like geochemical signature is active since 1.7 Ma (Alıcı *et al.*, 2002).

The eastern part of Kos exposes a tectonic window with a quartz monzonite that intruded into folded Permo-Carboniferous sedimentary to very low-grade metamorphic rocks. The depth of the intrusion was estimated to 5–8 km from calculated and experimentally determined phase equilibria of metapelites in the contact aureole. Maximum temperatures at the contact of the intrusion were near 800°C (Altherr *et al.*, 1976; Kalt *et al.*, 1998). Based on K-Ar ages of amphibole from the monzonite (11.85–10.85 Ma) given by Altherr et al. (1988), the age of the intrusion was estimated to be 12 Ma. K-Ar dates on biotite and Rb-Sr isochron age values on biotite/whole-rock pairs of monzonite samples yield ages in the range from 9.6 to 9.4 Ma. Fission-track age data on titanite range from 8.9 to 8.6 Ma (Altherr *et al.*, 1988). The partial annealing zone of the titanite fission-track system is 265–310°C (Coyle & Wagner, 1998). The major intrusion was followed by aplitic and micromonzonitic dykes and finally by numerous lamprophyric dykes that cut the monzonite and its contact aureole (Wimmenauer, 1977; Altherr *et al.*, 2000). The lamprophyres intruded when the temperature of the monzonite was below the brittle-ductile transition of quartz (ca. 280°C, Stöckhert *et al.*, 1999). Thus, the maximum age of the lamprophyre dykes is c. 8–9 Ma.

The monzonite, its contact aureole and the lamprophyres form the lowest tectonic unit of Kos, which is tectonically overlain by klippen of non-metamorphic Mesozoic to Paleogene carbonates. The contact between both units is a top-to-the-north brittle detachment fault zone of possible Pliocene age (Papanikolaou & Nomikou, 1998; van Hinsbergen & Boekhout, 2009). To the ENE, a Paleogene wildflysch with olistoliths tectonically overlies the contact-metamorphosed Permo-Carboniferous series (Fig. 2.1). To the north, Middle Miocene to Early Pliocene sediments tectonically overlay these units (Böger, 1983).

The thickness of the NNE to NNW (N15°E to N20°W) striking lamprophyre dykes ranges from centimeters to a maximum of 20 m. They are vertical or dip steeply to the east. Mica lamprophyres (medium-Nb group; see below for classification) were observed to cut amphibole lamprophyres (medium-Nb group). Lamprophyres commonly intruded 'en-échelon' in several parallel-arranged fissures. The orientation of these structures indicates magma uprise and dyke emplacement during sinistral shear, which is in accordance with the sinistral shear zone between the Aegean and western Anatolia. Ultrapotassic dykes are described from the nearby Bodrum peninsula with one reported whole-rock K-Ar age of 7.90 ± 0.25 Ma (Robert & Cantagrel, 1977; Robert *et al.*, 1992). A genetic relationship between these rocks and the Kos lamprophyres is likely.

Together with the island of Nisyros, the island of Kos forms the easternmost volcanic complex of the SAVA, active at least since ~ 3 Ma (e.g. Matsuda *et al.*, 1999; Pe-Piper & Moulton, 2008; Bachmann *et al.*, 2012). The volcanic products on Kos are mostly highly differentiated dacites and rhyolites with rare intermediate rocks (e.g. Pe-Piper & Moulton, 2008). The volcanic products on the nearby island of Nisyros range in composition from basaltic andesites to rhyolites (e.g. Buettner *et al.*, 2005; Braschi *et al.*, 2012).

2.3. Petrography and mineral chemistry

The Kos lamprophyres are amphibole- or mica-rich dykes that always show chilled margins and have porphyritic to glomeroporphyritic textures. Mica lamprophyres contain phenocrysts of phlogopite/biotite, clinopyroxene, and olivine (Fig. 2.2a and c). The groundmass consists of plagioclase, K-feldspar, biotite, apatite, titanite, magnetite, epidote-allanite, chlorite, calcite and in some cases interstitial quartz. The majority of the mica lamprophyres are kersantites (groundmass plagioclase > K-feldspar), while the dykes with the highest K-contents are minettes (K-feldspar > plagioclase). None of the minerals shows deficiency in tetrahedral Al, which is in line with the overall metaluminous composition of the Kos lamprophyres. Therefore, no tetraferriphlogopite component, as it is observed for phlogopite from lamproites (Mitchell & Bergman, 1991) or peralkaline minettes (e.g. Wagner & Velde, 1985), is present. Clinopyroxene is Al-rich and does not fall into the compositional field of clinopyroxene typical for lamproites. The TiO_2 content of phlogopite ranges from $2.5-5.2$ wt%. Tiny octahedrons of magmatic Cr-spinel [X_{Cr} = Cr/(Cr+Al+Fe^{3+}) =$0.55-0.71$] are commonly enclosed in pseudomorphs after olivine and more rarely in clinopyroxene. K-feldspar (Or_{95}–Or_{58}) is the dominant feldspar in the groundmass of minettes, while plagioclase (An_{65}–An_{10}) is more common in kersantites.

Phenocrysts in amphibole lamprophyres are amphibole, clinopyroxene, olivine (Fig. 2.2b and d) and in some types (high-Nb group, see below) also apatite. As the amphibole lamprophyres are less K-rich, their dominant matrix feldspar is plagioclase, hence they are classified as spessartites. The groundmass consists of hornblende, plagioclase, K-feldspar, apatite, magnetite, epidote-allanite, actinolite, albite, chlorite, and calcite and in some cases interstitial quartz. Amphibole compositions correspond to magnesiohastingsite with transitions to hastingsite, pargasite and ferropargasite. Since increasing P_{H_2O} depresses the feldspar solidus, the H_2O-rich lamprophyric melts do not carry feldspar phenocrysts. Some more evolved and degassed spessartites are an exception. Matrix K-feldspar ranges from Or_{95} to Or_{88}, plagioclase from An_{66} to An_{14}.

In many dykes, normally and reversely zoned clinopyroxene, amphibole and phlogopite phenocrysts coexist. Alternating zones of primitive and more evolved compositions are present (Fig. 2.2e and f). These disequilibrium textures may be explained by local magma differentiation in small magma chambers or by local sidewall crystallisation, followed by mingling and mixing with more primitive magma batches. Partial resorption of differentiated cores or growth shells and its replacement by more primitive compositions is a common feature in all phenocryst phases (Fig. 2.2e). Some lamprophyres contain diopside phenocrysts that host chemically distinct green cores (Fig. 2.2c), indicating crystallisation at greater depths (Duda & Schmincke, 1985). The green cpx cores generally have lower Mg content and are chemically distinct (lower Al at given Mg) from the rims which have the composition of 'normal' cpx phenocrysts. Feldspathic millimeter-sized spherical and ellipsoidal globular structures occur in numerous dykes. These structures, known as ocelli, are rimmed by tangentially aligned phlogopite or amphibole, although some ocelli merge into the enclosing groundmass. In some cases, the ocelli amalgamate.

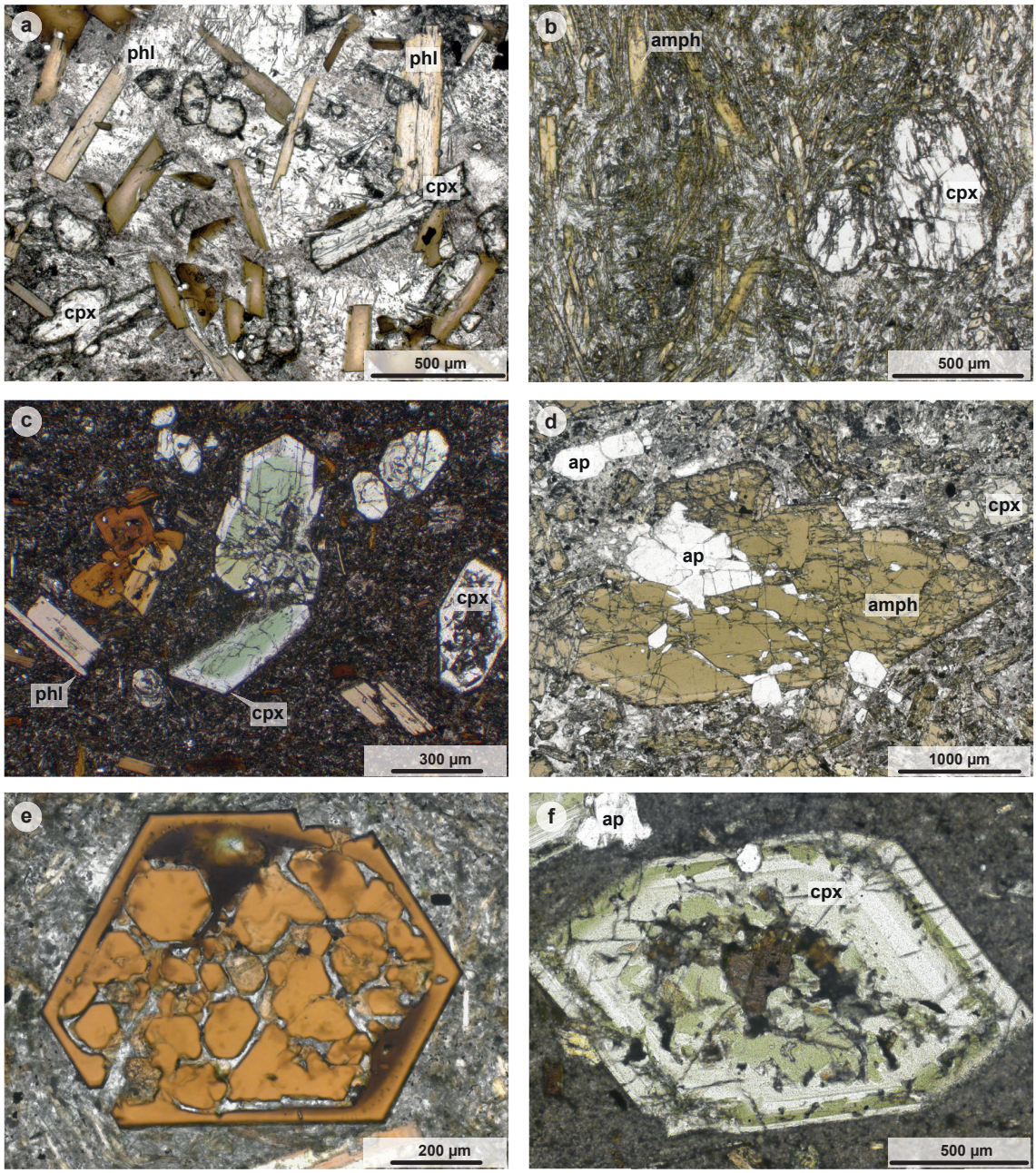

Fig. 2.2. Photomicrographs (plane-polarised light) of the Kos lamprophyres: (a) Mica lamprophyre (kersantite) with porphyritic texture containing phenocrysts of phlogopite/biotite and clinopyroxene (cpx) as well as magnetite and tabular apatite crystals in a coarse feldspathic (dominantly plagioclase) groundmass. (b) Low-Nb group amphibole lamprophyre (spessartite) with colorless clinopyroxene phenocrysts and abundant acicular amphibole crystals, embedded in a feldspathic groundmass. (c) Porphyritic mica lamprophyre with phenocrysts of phlogopite/biotite and 'green core' clinopyroxene. (d) Porphyritic high-Nb group amphibole lamprophyre (spessartite) with phenocrysts of large inversely zoned amphibole, apatite and clinopyroxene. (e) Mica lamprophyre with complexly zoned biotite phenocryst. Low-Mg biotite was partly dissolved and overgrown by phlogopite. Re-equilibration of more differentiated phenocryst zones is a common feature in lamprophyres. (f) Growth and resorption zones in cpx phenocrysts in a mica lamprophyre record the history of magma ascend.

These structures most probably result from buoyant rise of more differentiated volumes of magma (Shand *et al.*, 1994). In a few cases ocelli-rich mica lamprophyres contain syenitic schlieren and veinlets. On rare occasions, embayed xenocrysts of quartz, overgrown by clinopyroxene, indicate interaction between lamprophyric melts and continental crust. The groundmass texture of individual dykes is highly variable, ranging from medium-grained to submicron-size, while glass was present along chilled margins. Due to undercooling of the melts in the upper crust, thinner dykes are characterised by fine-grained textures with radiating feldspar-sheaves and acicular apatite, phlogopite and/or amphibole. On weathered surfaces, thin, fine-grained dykes show globular structures due to spherulitic crystallisation of the groundmass. These spherules grow thicker towards the middle of the dykes and form a polygonal mosaic.

The Kos lamprophyres show the typical hydrothermal alteration features known from lamprophyre dykes (Rock, 1991). Autometasomatic processes caused a complete replacement of olivine and sometimes also affected clinopyroxene and the feldspar groundmass. Secondary minerals represent a greenschist-facies assemblage and comprise chlorite, epidote, actinolite, albite, and more rarely, Fe-rich biotite. Calcite is a common autometasomatic alteration product.

2.4. Whole-rock geochemistry

2.4.1. Major and trace element compositions

Major and trace element data of selected lamprophyres from Kos are presented in Table C.1. Major element compositions of the lamprophyres fall in the range of 42–57 wt% SiO_2, 0.6–1.5 wt% TiO_2, 13.0–17.5 wt% Al_2O_3, 5.7–11.7 wt% CaO, 2.8–9.2 wt% MgO, 1.2–7.2 wt% K_2O, 1.9–3.6 wt% Na_2O and 0.35–1.78 wt% P_2O_5. Based on the K_2O vs SiO_2 diagram (Fig. 2.3a), a rough distinction between amphibole lamprophyres on the low-K side and mica lamprophyres on the high-K side is possible. Some of the mica lamprophyres (minettes) are ultrapotassic according to the criteria of Foley *et al.* (1987).

Despite the small outcrop area, the lamprophyres show considerable chemical variations that are most pronounced for amphibole lamprophyres. For instance, Nb concentrations vary by an order of magnitude ($14 - 144\,\mu g/g$). Therefore, the Nb content was used as an additional grouping criteria, resulting in five groups of lamprophyres: Low-Nb, medium-Nb and high-Nb amphibole lamprophyres and low-Nb and medium-Nb mica lamprophyres (Fig. 2.3b).

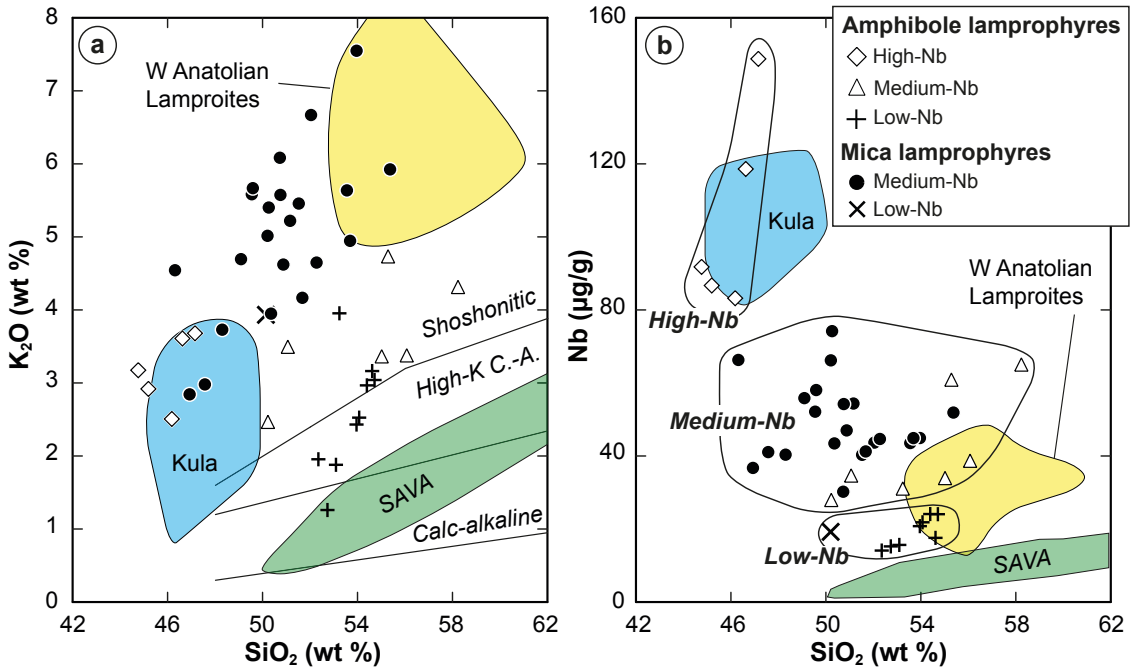

Fig. 2.3. Classification diagrams for lamprophyres from Kos. Chemical analyses are recalculated to 100% anhydrous. (a) SiO_2 vs K_2O classification diagram of Peccerillo & Taylor (1976). (b) SiO_2 vs Nb classification scheme. The subdivision of the investigated lamprophyres based on the Nb content is used throughout the paper. Data for Kula, W Anatolian Lamproites and South Aegean Volcanic Arc (SAVA) see Fig. 2.6

The lamprophyres have extreme light rare earth element (LREE) enriched patterns with La_{cn} (cn = chondrite-normalised) values ranging from 230 to 1,100 and $(La/Yb)_{cn}$ from 18.5 to 82.9 (Fig. 2.4). A subtle negative Eu anomaly is present in some dykes, be-

ing strongest in the low-Nb amphibole lamprophyre group. Primitive mantle-normalised element abundance patterns (Fig. 2.4) are characterised by strong enrichments in large-ion lithophile elements (LILE). All lamprophyre samples, including the high-Nb group, are characterised by negative Nb-Ta anomalies. The high-Nb lamprophyres also show the highest Ti concentrations, but still have strongly negative Ti anomalies. Positive Pb anomalies are present in all groups and are most pronounced in the low-Nb group of lamprophyres, whereas they are only weakly developed in the high-Nb group. All lamprophyres show negative Zr-Hf anomalies (relative to Nd and Sm), while negative P anomalies are present in all medium- and low-Nb lamprophyres (Fig. 2.5).

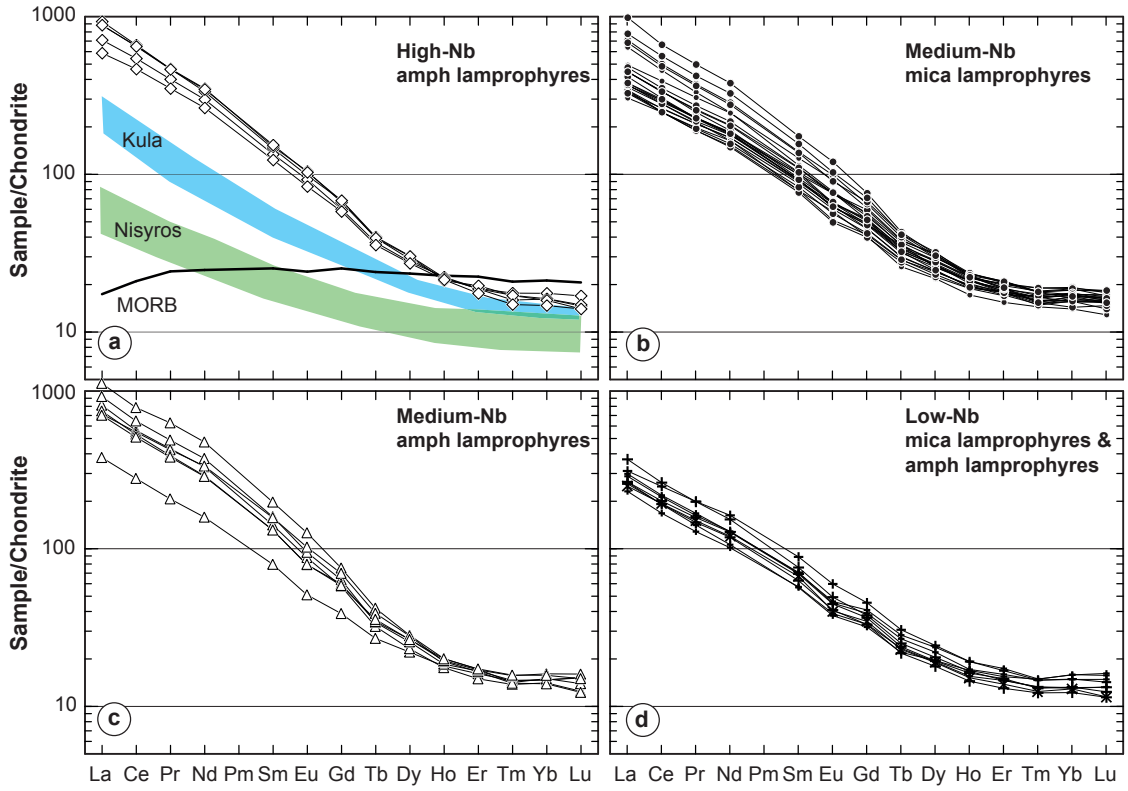

Fig. 2.4. Chondrite-normalised rare earth element patterns for Kos lamprophyres. The data sources for Kula and Nisyros fields in (a) are the same as in Fig. 2.6; MORB from Niu & O'Hara (2003). The patterns exhibit steep slopes from La to Ho and show relatively flat heavy rare earth element (HREE) patterns with $(Ho/Lu)_{cn}$ values between 1.51 and 1.07. A subtle negative Eu anomaly is present in some dykes, being strongest in the low-Nb amphibole lamprophyre group. Chondrite concentration values from McDonough & Sun (1995). Symbols as in Fig. 2.3.

2.4.2. Sr–Nd–Pb isotopic compositions

The overall variation in initial Sr, Nd, and Pb isotopic ratios of the lamprophyres is small (Table 2.1 and Table 2.2). The initial εNd and $^{87}Sr/^{86}Sr_i$ values range from $+1.46$ to -1.86 and 0.70393 to 0.70546, respectively. They are negatively correlated and ex-

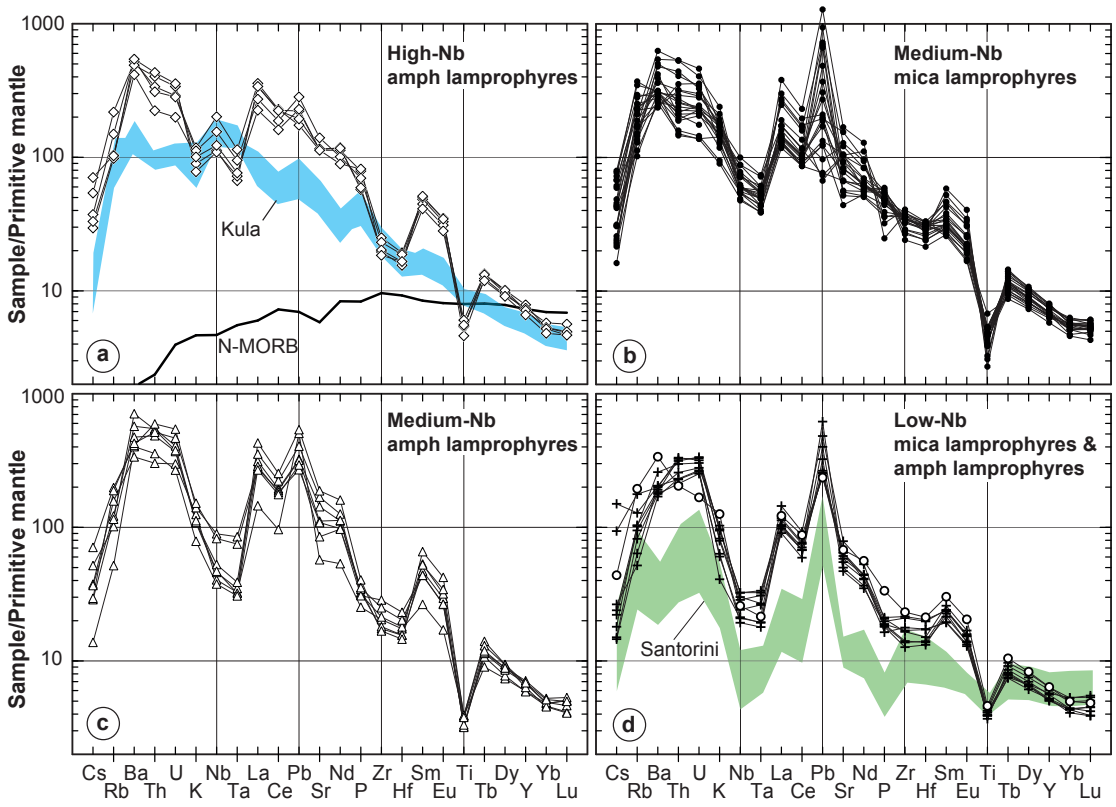

Fig. 2.5. Primitive mantle-normalised element concentration diagrams (normalisation values from Sun & McDonough, 1989) for Kos lamprophyres. Reference fields for N-MORB (Niu & O'Hara, 2003), Kula Na-alkaline basalts (Chakrabarti *et al.*, 2012) and Santorini (Kirchenbaur *et al.*, 2012) are shown for reference. Symbols as in Fig. 2.3.

tend from the undepleted end of the mantle array towards crustal compositions (Fig. 2.6). There are no systematic differences between amphibole and mica lamprophyres. However, on the Sr–Nd array the high-Nb lamprophyres and the low-Nb lamprophyres form the mantle- and the crust-like endmember, respectively. The trend points towards the composition of recent southeastern Mediterranean sediments. The initial lead isotopic compositions fall in the range typically encountered for upper continental crust, as represented by Pb isotope evolution curves, with high $^{207}Pb/^{204}Pb$ = 15.62–15.66 at $^{206}Pb/^{204}Pb$ = 18.60–18.95 and $^{208}Pb/^{204}Pb$ = 38.43–38.86 (Fig. 2.7). The Pb data are similar to the composition of recent sediments to the south of Crete with a predominantly North African provenance (Weldeab *et al.*, 2002) and are indistinguishable from those of primitive volcanic rocks of the SAVA. Shoshonitic rocks from the N Aegean area and lamproites from western Anatolia have higher $^{207}Pb/^{204}Pb$ values for a given $^{206}Pb/^{204}Pb$, indicating a different crustal source.

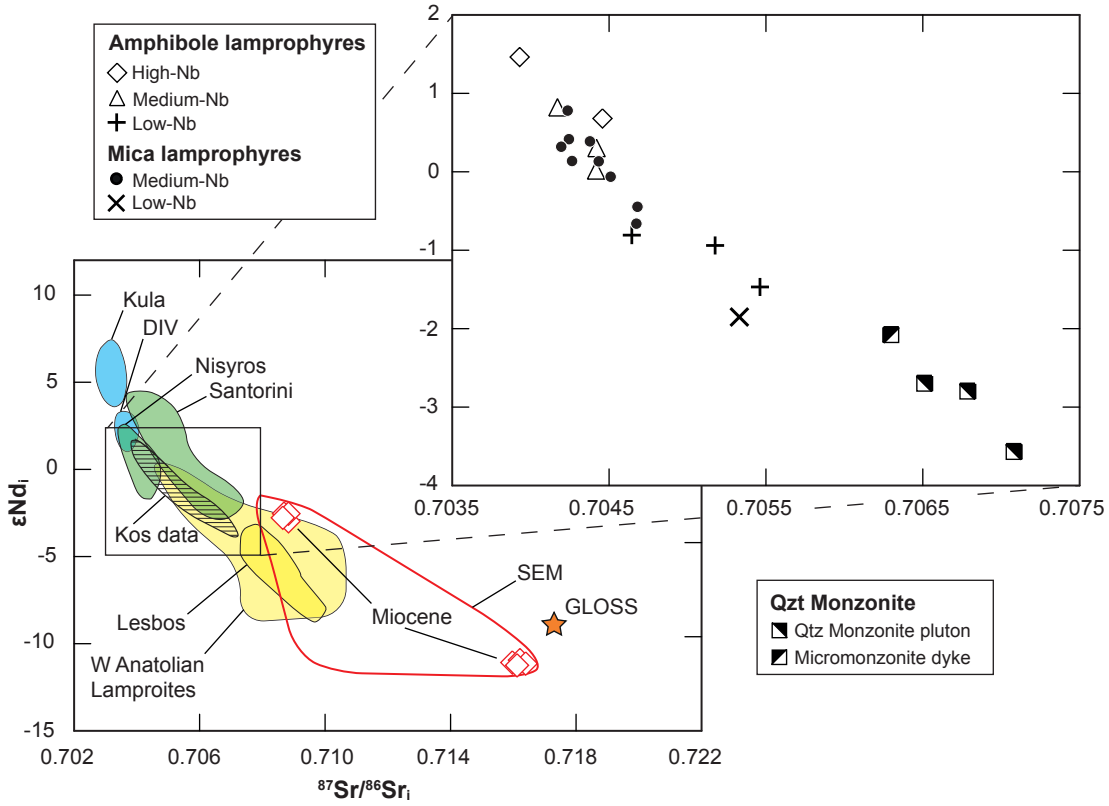

Fig. 2.6. Nd–Sr isotopic compositions (εNd vs $^{87}Sr/^{86}Sr_i$) of the Kos lamprophyres and the quartz monzonitic intrusion. Initial values were calculated for an age of 8 Ma (lamprophyres) and of 12 Ma (quartz monzonite) (see section on geological setting). The inset shows a detailed excerpt with symbols as shown in the legend. Fields of Kula basalts from Alıcı *et al.* (2002), Chakrabarti *et al.* (2012) and Ersoy *et al.* (2012). W Anatolian lamproite data from Ersoy *et al.* (2012) and Prelević *et al.* (2012) (excluding DIV localities Bucak and Denizli). DIV (Bucak: Prelević *et al.*, 2012; Denizli: Yılmaz, 2010,Prelević *et al.*, 2012; Gölcük-Isparta: Chakrabarti *et al.*, 2012). Data for Lesbos from Pe-Piper *et al.* (2014) and for Santorini from Bailey *et al.* (2009) and Kirchenbaur *et al.* (2012). Nisyros data from Buettner *et al.* (2005), Braschi *et al.* (2012) and Klaver *et al.* (2016). The field for southeastern Mediterranean sediments (SEM) is from Weldeab *et al.* (2002) and Klaver *et al.* (2015)). Compositions of Miocene sediment samples from ODP Leg 160 to the south of Crete (see Fig. 2.1a for locations) are given, as well as globally subducted sediment (GLOSS) from Plank & Langmuir (1998). The Sr–Nd isotope data of the quartz monzonite samples are from Juteau *et al.* (1986) and Altherr & Siebel (2002). The micromonzonite dyke is sample KW8 from Altherr & Siebel (2002). Note, the Sr–Nd isotope data of the quartz monzonite on Kos plot at the high-$^{87}Sr/^{86}Sr$ extension of the trend of the lamprophyres. The micromonzonite dykes are chemically, spatially and temporally closely associated with the main intrusion and are cut by the lamprophyres. The quartz monzonite additionally hosts mafic microgranular enclaves, which are very abundant in some parts of the intrusion. Although the lamprophyres have no direct chemical connection to the quartz-monzonitic intrusion, the Sr and Nd isotopic composition of the pluton indicates the involvement of a mantle-derived component, which could be similar to the lamprophyres.

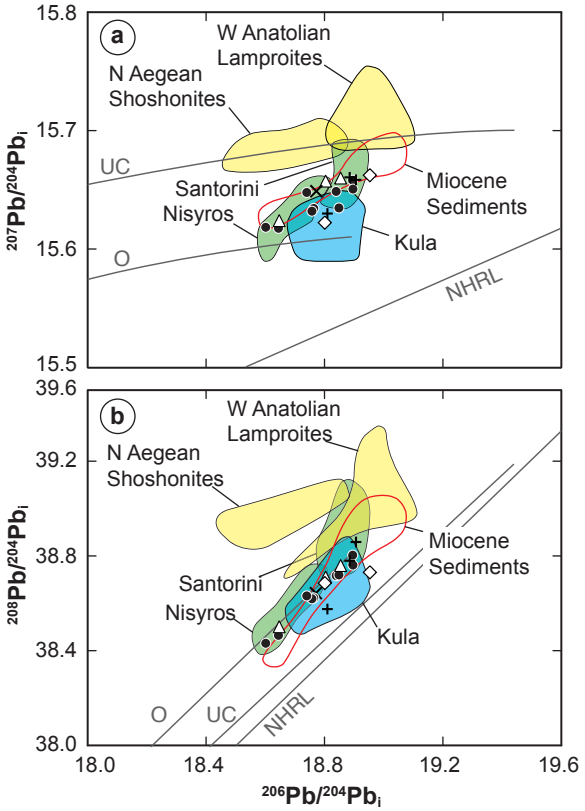

Fig. 2.7. Pb isotopic composition of the lamprophyres from Kos. Data field for volcanic rocks from nearby Nisyros island (basaltic andesites to andesites) was taken from Buettner *et al.* (2005) and Klaver *et al.* (2016). The field for Santorini is from Bailey *et al.* (2009) and Kirchenbaur *et al.* (2012). The field for N Aegean shoshonites includes samples from Chios, Lesbos and Samothraki (Pe-Piper, 1994; Pe-Piper *et al.*, 2014). W Anatolian Lamproites data from Prelević *et al.* (2012) (excluding DIV localities Bucak and Denizli). Field for Na-alkaline Kula basalts after Alıcı *et al.* (2002), Chakrabarti *et al.* (2012) and Ersoy *et al.* (2012). Field for sediments includes data for river Nile delta sediments (Pe-Piper, 1994) and Miocene sediments from ODP Leg 160, site 971B south of Crete (see Fig. 2.1 for location) from Klaver *et al.* (2015). The northern hemisphere reference line (NHRL) is drawn according to Hart (1984). Pb evolution curves for orogenic crust (O) and upper crust (UC) after Zartman & Doe (1981). Symbols as in Fig. 2.3.

Table 2.1. Strontium and Nd isotopic composition of lamprophyres from Kos, Greece.

Sample	$^{87}Sr/^{86}Sr$	$^{87}Sr/^{86}Sr_i$	$^{143}Nd/^{144}Nd$	$^{143}Nd/^{144}Nd_i$	εNd
KL02	0.704178±6	0.70417	0.512674±2	0.512670	0.82
KL07	0.705184±4	0.70518	0.512585±3	0.512580	-0.94
KL14	0.703941±5	0.70393	0.512707±2	0.512703	1.46
KL22	0.704720±9	0.70468	0.512610±2	0.512605	-0.45
KL27	0.704509±3	0.70443	0.512640±2	0.512635	0.13
KL28	0.704716±4	0.70467	0.512599±2	0.512594	-0.66
KL36	0.705484±5	0.70546	0.512558±2	0.512552	-1.47
KL37	0.704526±4	0.70451	0.512630±2	0.512624	-0.06
KL41	0.704466±3	0.70446	0.512667±3	0.512663	0.68
KL45	0.704261±4	0.70424	0.512654±4	0.512649	0.42
KL52	0.704425±4	0.70442	0.512648±3	0.512643	0.30
KL54	0.705359±4	0.70533	0.512538±3	0.512533	-1.86
KL59	0.704418±6	0.70438	0.512653±3	0.512648	0.39
KL63	0.704207±7	0.70419	0.512649±3	0.512644	0.32
KL64	0.704435±4	0.70442	0.512633±2	0.512629	0.02
KL66	0.704252±4	0.70424	0.512673±3	0.512668	0.78
KL78	0.704668±9	0.70465	0.512592±3	0.512586	-0.81
KL80	0.704279±3	0.70426	0.512640±2	0.512635	0.14

$^{87}Sr/^{86}Sr_i$ $^{143}Nd/^{144}Nd_i$ and εNd_i were calculated for the emplacement age of 8 Ma using the contents of Rb, Sr, Sm and Nd (Table C.1) and $\lambda^{87}Rb$ = 1.3972E-11 a^{-1}, $\lambda^{147}Sm$ = 6.54E-12 a^{-1}, $(^{147}Sm/^{144}Nd)^0_{CHUR}$ = 0.1967 and $(^{143}Nd/^{144}Nd)^0_{CHUR}$ = 0.512638, respectively.

Table 2.2. Lead isotopic composition of lamprophyres from Kos, Greece.

Sample	$^{206}Pb/^{204}Pb$	$^{207}Pb/^{204}Pb$	$^{208}Pb/^{204}Pb$	$^{206}Pb/^{204}Pb_i$	$^{207}Pb/^{204}Pb_i$	$^{208}Pb/^{204}Pb_i$
KL02	18.637	15.579	38.423	18.65	15.62	38.50
KL07	18.791	15.584	38.476	18.81	15.63	38.58
KL14	18.784	15.577	38.595	18.80	15.62	38.69
KL22	18.865	15.612	38.694	18.90	15.66	38.80
KL27	18.732	15.586	38.516	18.76	15.63	38.62
KL28	18.876	15.605	38.660	18.90	15.65	38.76
KL36	18.867	15.615	38.688	18.89	15.66	38.78
KL37	18.860	15.605	38.665	18.84	15.65	38.72
KL41	18.953	15.617	38.660	18.95	15.66	38.73
KL45	18.649	15.573	38.402	18.64	15.62	38.46
KL52	18.783	15.611	38.616	18.80	15.66	38.71
KL54	18.749	15.603	38.544	18.77	15.65	38.64
KL59	18.739	15.603	38.558	18.74	15.65	38.63
KL63	18.572	15.572	38.329	18.60	15.62	38.43
KL64	18.854	15.615	38.680	18.85	15.66	38.76
KL66	18.746	15.588	38.529	18.76	15.63	38.62
KL78	18.886	15.612	38.758	18.91	15.66	38.86
KL80	18.822	15.588	38.619	18.85	15.63	38.72

Lead isotope data recalculated to the emplacement age (8 Ma) using the contents of Pb, Th, and U (Table C.1) and the constants recommended by IUGS ($\lambda^{232}Th$ = 4.9475E-11 a^{-1}, $\lambda^{235}U$ = 9.8485E-10 a^{-1}, and $\lambda^{238}U$ = 1.55125E-10 a^{-1}), $\lambda^{238}U$ = 1.55125E-10 a^{-1}).

2.5. Discussion

2.5.1. Fractional crystallisation and crustal contamination

Bulk-rock Mg# values [= 100×Mg/(Mg+0.9 Fe_{tot})] of the lamprophyres from Kos range from 72 to 54, which indicates that the magmas were initially equilibrated with mantle peridotite and that most of them were affected by fractional crystallisation during ascent. The petrographically determined crystallisation sequence is olivine + clinopyroxene ± Cr-Al-spinel → phlogopite/amphibole + apatite → K-feldspar + plagioclase + Fe-Ti oxides. This agrees with experimental crystallisation studies performed on K-rich lamprophyres (minettes) that have found multiple saturation of olivine + clinopyroxene + phlogopite ± spinel (Esperança & Holloway, 1987; Righter & Carmichael, 1996).

The initial SiO_2 content of the lamprophyres is highly variable (see below), therefore, the Mg# is used to illustrate the differentiation processes (Fig. 2.8a). The relatively low abundances of Ni and Cr correlate with the Mg# (Fig. 2.8e, f) and reflect fractionation of olivine, Cr-Al-spinel, and possibly clinopyroxene, phlogopite or amphibole that all have high D_{Ni} and/or D_{Cr}.

Clinopyroxene fractionation is geochemically indicated by a decrease of CaO, Sc and CaO/Al_2O_3 with decreasing Mg# (e.g. Adam & Green, 2006). While Sc is compatible in clinopyroxene, the partitioning behaviour of V strongly depends on the oxygen fugacity (e.g. Lee *et al.*, 2005). Concentrations of V are roughly constant during differentiation resulting in a general increase of V/Sc from $\sim 5.5-12$ in amphibole and mica lamprophyres. The continuous increase of V/Sc with decreasing Mg# indicates simultaneous crystallisation of olivine and clinopyroxene.

Fractionation of amphibole would additionally reduce the Ti concentrations and should produce a negative slope in HREE patterns with a decreasing Dy/Yb value (Davidson *et al.*, 2007). These two features are not observed though. Increasing K_2O with decreasing Mg# rules out significant fractionation of phlogopite. The presence of large apatite phenocrysts is reflected by the high P_2O_5 contents (up to 1.78 wt%) in the high-Nb lamprophyres. Despite the fractionated character of these rocks, no negative P anomaly is present, excluding significant apatite fractionation (Fig. 2.5). Plagioclase phenocrysts are only present in some differentiated amphibole lamprophyres (Mg# = 53–51). The absence of a negative Eu anomaly in these rocks excludes plagioclase fractionation. A weak negative Eu anomaly is present in the low-Nb lamprophyres, which are near primary melts devoid of plagioclase phenocrysts. Therefore, the Eu anomaly may be inherited from the mantle source.

The strong variations of high field-strength element (HFSE) ratios such as Zr/Hf (34–51) and Nb/Ta (16–31) call for an explanation. Fractionation of clinopyroxene and amphibole causes an increase of Zr/Hf in the melt as both minerals have $D_{Zr_{min/melt}} \sim 0.5 \times D_{Hf_{min/melt}} < 1$ (e.g. Tiepolo *et al.*, 2000, 2001; Klemme *et al.*, 2002; Salters *et al.*, 2002; Adam & Green (2006)). The low-Nb amphibole lamprophyres (Mg# ~ 70) have Zr/Hf of $\sim 35-37$, i.e. values that are only slightly higher than those of chondrites (34.3 ± 0.3; Münker *et al.*, 2003) and Nb/Ta ratios as low as 16. In marked contrast,

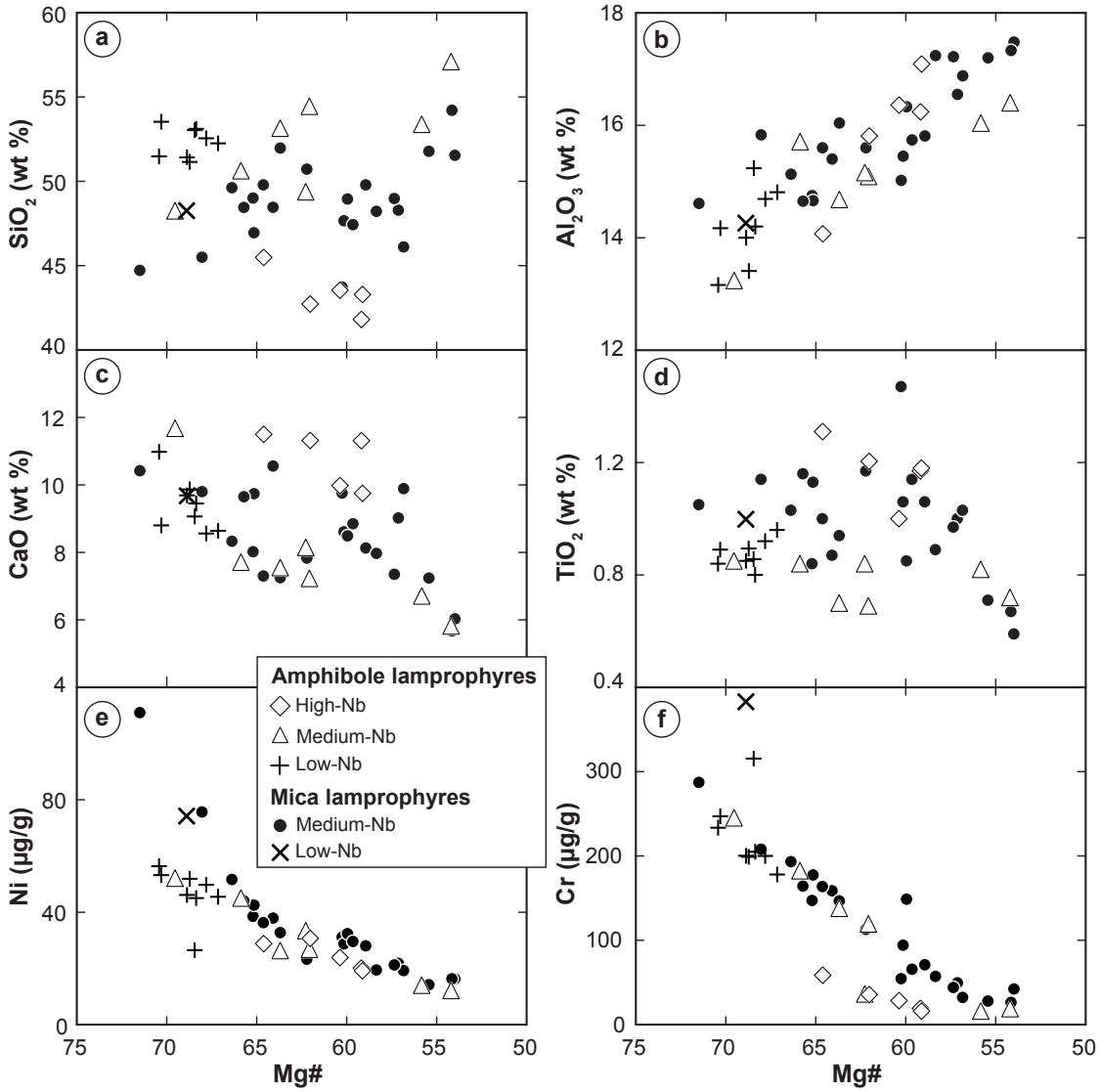

Fig. 2.8. Differentiation diagrams for some major and trace elements. Mg# = 100×Mg/(Mg + 0.9 Fe_{tot}).

the high-Nb amphibole and mica lamprophyres show strongly superchondritic values of Zr/Hf (up to $\sim$ 51) and Nb/Ta (up to $\sim$ 31). Although some of them are clearly differentiated (high-Nb lamprophyres have Mg# = 65–59), such high ratios cannot be obtained by fractionation of clinopyroxene, amphibole, and/or biotite, as Zr and Hf are incompatible to moderately compatible and the fractionating phases have $D_{Nb}/D_{Ta} < 1$ (Münker *et al.*, 2004 and references therein). Samples that were affected more strongly by fractional crystallisation are excluded from the following discussion.

Crustal contamination is documented within some samples by the presence of quartz xenocrysts that are mantled by clinopyroxene and show undulatory extinction. However, the high primary content of incompatible trace elements makes lamprophyric magmas little sensitive to contamination by average crustal lithologies (e.g. Conticelli, 1998). The most differentiated group of quartz xenocryst-bearing plagioclase-phyric lamprophyres (Mg# = 51.6) lies in the center of the Sr–Nd isotopic array (εNd = 0.02). A correlation between Mg# and Sr or Nd isotopic composition is not observed. Xenocrysts of mantle minerals are absent from the studied dykes. But, the presence of green-core clinopyroxenes may indicate crystallisation at depth.

Autometasomatic processes are ubiquitous features of lamprophyric dyke rocks (e.g. Rock, 1991). Fluid release upon solidification of the melts may lead to replacement of primary magmatic minerals and crystallisation of secondary minerals typical for greenschist-facies metamorphism (e.g. epidote, chlorite, actinolite). Especially Cs and Pb may show unsystematic concentration variations within different lamprophyre groups. These fluid-mobile elements are predominantly stored in the feldspathic groundmass that is affected by hydrothermal alteration to a variable extent. The slight deviation of the Pb isotopic composition of two samples (KL07, KL41) from the linear array in Fig. 2.7b may be related to secondary alteration. However, as several samples do not show the geochemical signature that could be expected if particular minerals were fractionated or altered, it is obvious that the observed geochemical and isotopic variation is largely inherited from the mantle source.

2.5.2. Mantle source and source components

The generation of lamprophyres with extreme incompatible trace element enrichment requires a previously enriched mantle source. The geochemical characteristic of these rocks is best explained by melting of a hybrid mantle source, comprising veins of non-peridotitic enriched material hosted by a depleted mantle (Foley, 1992). Although the mantle is dominantly peridotitic, low-degree melting preferentially mobilizes material from the non-peridotitic veins, which have a lower solidus compared to the surroundings. Therefore, the incompatible trace element budget of the lamprophyres is strongly controlled by the composition of the enriched component(s). These incipient melts induce partial melting of the depleted mantle, which introduces material with high Cr and Ni contents and a high Mg#. Higher degrees of partial melting will more strongly dilute the metasomatic signal by increasing contributions from the ambient mantle. The ambient mantle, however, is isotopically not distinctive and only mantle-compatible elements may

serve as proxys for the degree of mantle depletion. High-Mg# phenocrystic olivine and Cr-rich spinel, which usually appear as the first liquidus phases in potassic and ultrapotassic melts, along with high whole-rock Mg# are robust tracers for the depleted source (e.g. Prelević & Foley, 2007). Yet, most of the Kos lamprophyres are at least slightly fractionated. Additionally, olivine is hydrothermally altered, which is typical for lamprophyric dyke rocks (Rock, 1991). Thus, the degree of depletion of the mantle source is poorly known. A refractory ambient mantle, however, facilitates the preferential mobilisation of the veined metasomes and seems to be a likely prerequisite for the generation of strongly enriched melts such as the Kos lamprophyres.

The tightly constrained mixing trend in the εNd vs $^{87}Sr/^{86}Sr$ diagram (Fig. 2.6) demonstrates that two isotopically distinct endmembers are involved. The two endmembers are geochemically highly enriched and, therefore, related to different metasomatic components. The Sr–Nd isotope-mixing array does not rule out additional isotopically distinct endmembers, but implies that such reservoirs do not contribute significantly to the Sr and Nd budget of the lamprophyres. For instance, contributions from the depleted mantle would variably dilute the metasomatic signal from the veins, but would not disturb the correlation in the Sr–Nd isotope-mixing array.

The geochemical and isotopic compositions of the Kos lamprophyres clearly indicate a subduction-related component. The Pb isotopic composition is relatively homogeneous and has values typical for continental crust. Subducted terrigenous sediment dominates the Pb isotopic composition of the lamprophyres, reflecting that average continental crust has two orders of magnitude higher Pb contents than the mantle (Hofmann, 1988; Rudnick & Gao, 2003). The presence of a second enriched component may be related to the particular situation of the island of Kos at the eastern end of the volcanic arc, where rollback may have caused tearing or rupturing of the downgoing slab, eventually creating small-scale pathways for ascending melts from the asthenosphere below the subducting lithosphere. Low-degree incipient melting of the asthenospheric mantle will particularly mobilize low-T melting domains such as carbonated or hydrated sections (Thibault *et al.*, 1992; Green & Falloon, 1998; Gudfinnsson & Presnall, 2005). The resulting melts migrate upwards and potentially metasomatize the lithospheric mantle above the subducting plate. Infiltration and metasomatism of the lithospheric mantle by asthenosphere-derived low-degree melts has been proposed for oceanic and intracontinental alkaline magmatic provinces (e.g. Harte *et al.*, 1993; McKenzie & O'Nions, 1995; Tappe *et al.*, 2006).

The variable contribution from the two metasomatic components to the lamprophyre melts accounts for the mixing trend in the Sr–Nd isotope diagram (Fig. 2.6). Excluding more differentiated lamprophyres (Mg# < 60), this mixing is also seen in correlations between various trace element ratios (e.g. Nb/Ta, Th/La, Ba/Th, Eu/Eu*, Nb/U) (Fig. 2.9a). Nb/U ratios of the Kos lamprophyres vary from 2.7 to 23.6 with a systematic increase with rising Nb concentrations, i.e. they range from typical crustal values towards mantle compositions (Nb/U of 47 $\pm$ 10 of MORB and OIB; Hofmann *et al.*, 1986). In addition, near linear relationships between some element abundances (e.g. SiO_2, P_2O_5, Nb, V, Y) (Fig. 2.9b–d) are not the result of fractional crystallisation, but reflect differences in the mineralogy of the participating mantle source components.

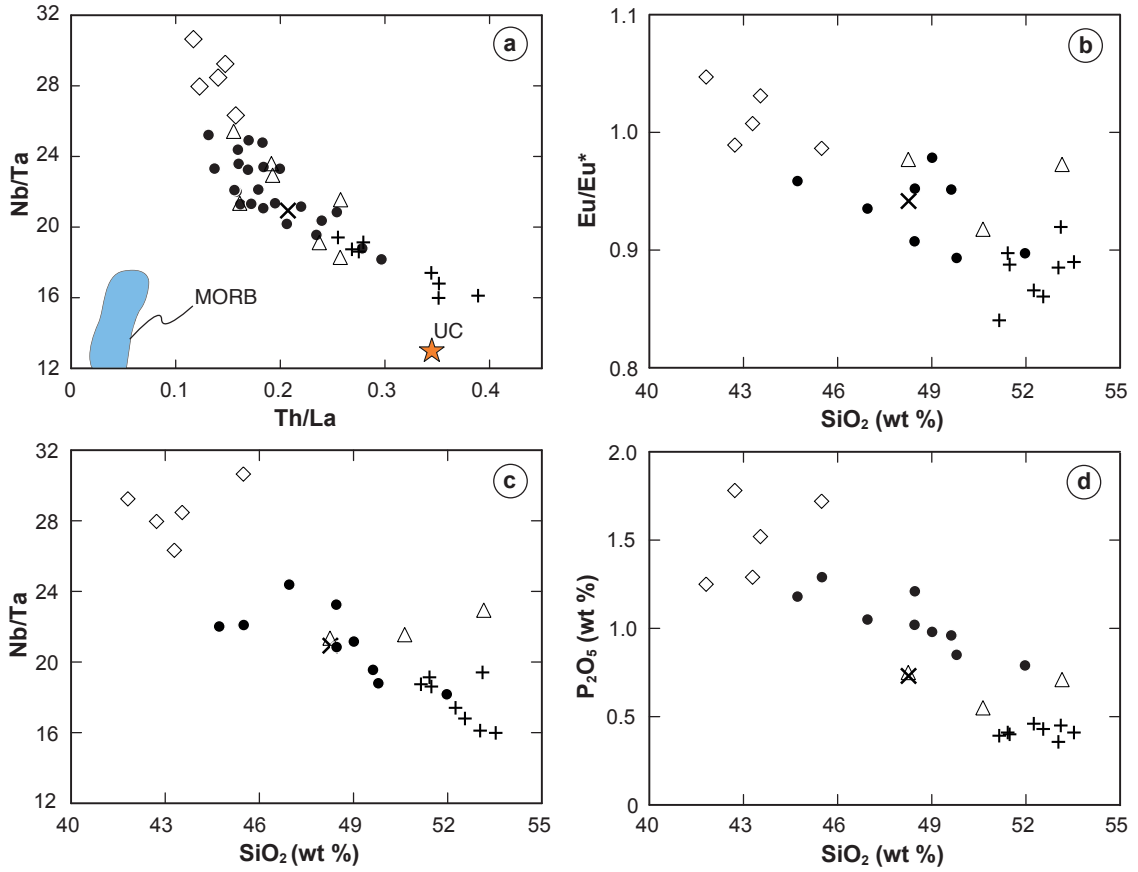

Fig. 2.9. Variation diagrams for Kos lamprophyres illustrating the mixing relationship between two enriched mantle-derived melt components. (a) Nb/Ta vs Th/La with MORB field (data compilation of Class & Lehnert, 2012) and average upper continental crust (UC) from Rudnick & Gao (2003). (b) Eu/Eu* vs SiO_2 with Eu/Eu* = $Eu_{cn}/(Sm_{cn} \times Gd_{cn})^{0.5}$ and chondrite normalisation (cn) with values of Sun & McDonough (1989). (c) Nb/Ta vs SiO_2. (d) P_2O_5 vs SiO_2. Symbols as in Fig. 2.3.

The level of enrichment of LIL elements is variable and strongly depends on the degree of partial melting of the non-peridotitic vein assemblages. To account for the high K_2O content of the melts, a K-bearing phase is required in the mantle source of the lamprophyres, which could be phlogopite or amphibole. As Ba is moderately compatible to incompatible in amphibole and phlogopite, the breakdown of these minerals will yield melts with high Ba, but contrasting K_2O contents. The high K_2O content of up to 7 wt% and the high K_2O/Na_2O of the minettes require phlogopite in the source (Conticelli *et al.*, 2009). The high- and medium-Nb amphibole lamprophyres are heavily enriched in LREE and LILE, but have only moderate K_2O contents. Thus, the high Ba contents at low K_2O of these rocks may reflect low-degree partial melting of an amphibole-bearing mantle source (Fig. 2.10a). Discrimination between phlogopite- and amphibole-bearing mantle sources may be possible using the Rb/Sr vs Ba/Rb diagram (Fig. 2.10b) (Furman & Graham, 1999). The different trends, however, also could be related to higher Ba contents

within the mantle-derived metasomatic agent.

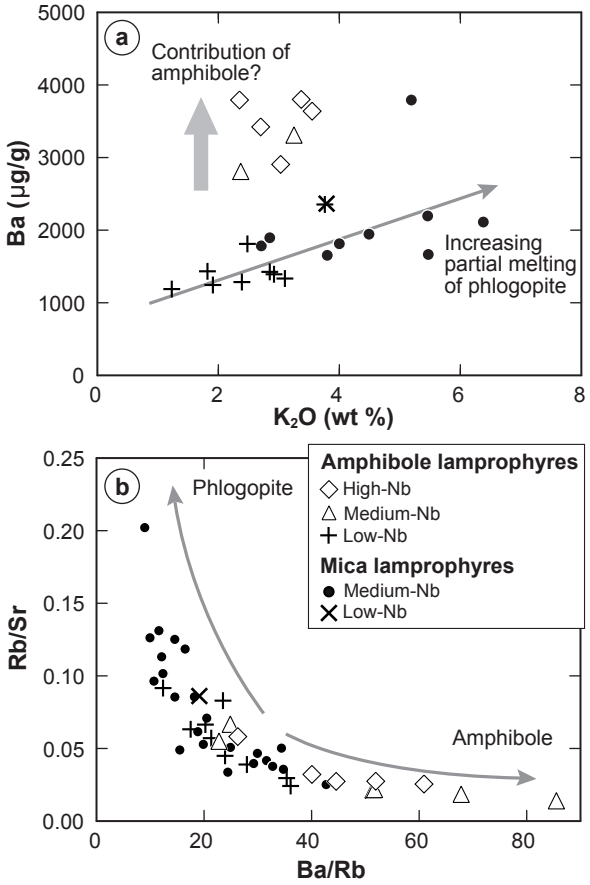

Fig. 2.10. Systematics of large-ion lithophile elements (LILE) in Kos lamprophyres. Both amphibole and phlogopite may play a major role in controlling the LILE budget of the mantle source of the lamprophyres. Samples with Mg# < 60 are excluded. Melts generated in equilibrium with amphibole are expected to have low Rb/Sr (< 0.1) and high Ba/Rb (> 20), while melts coexisting with phlogopite are thought to be characterised by high Rb/Sr and low Ba/Rb (Furman & Graham, 1999).

The variable major element compositions of the lamprophyre groups indicate that the two metasomatic components are hosted within mineralogically distinct metasomes within the lithospheric mantle. Variable degrees of partial melting affecting these two components and subsequent mixing in different proportions result in scattered data pattern in trace element or isotope diagrams (Fig. 2.12), as the various mixtures are defined by mixing hyperbola of contrasting curvature (Fig. 2.12c, inset). Thus, the entire chemical heterogeneity can be explained by the two enriched endmembers and variable contributions of the depleted mantle. To better characterize the metasomatic components, the focus is set on the low- and high-Nb groups, which most closely reflect the two geochemical endmembers.

2.5.3. Subduction-related low-Nb component

Incompatible trace element patterns of the Kos lamprophyres and especially those of the low-Nb groups exhibit strong positive Pb anomalies and negative anomalies for Nb, Ta, and Ti (Fig. 2.5), which are typical for both subduction-related magmatic rocks and the average continental crust. Among the studied dykes, the low-Nb lamprophyres resemble geochemically the average mantle-derived rocks erupted along the SAVA, for instance on Santorini or Nisyros (Fig. 2.4 and Fig. 2.5), although they show a stronger enrichment of incompatible trace elements. Furthermore, the low-Nb lamprophyres form the crustal-like isotopic endmember of the Sr–Nd array and have more radiogenic $^{87}Sr/^{86}Sr$ and less radiogenic εNd values than the SAVA lavas (Fig. 2.6), indicating a more pronounced role of subducted continental crust in their source.

Although sediments only represent a volumetrically minor component during oceanic subduction, their recycling into the mantle has the potential to control the budget of many incompatible trace elements in arc magmas due to the trace element enrichment of the continental crust, whereas altered oceanic crust (AOC) commonly contributes to a smaller extent (Plank & Langmuir, 1998; Peate *et al.*, 1997; Elliott, 2003). The thick sedimentary pile of the Mediterranean accretionary complex covers the trench of the Hellenic subduction zone (Kopf *et al.*, 2003). These sediments are heterogeneous but fluvial input of river Nile sediments and aeolian Sahara dust are the main components of the tectono-sedimentary succession, both having a 'Pan-African' crustal provenance (Weldeab *et al.*, 2002; Klaver *et al.*, 2015). It is most likely that small or even large amounts of this sedimentary material enters the steeply dipping subduction zone (Kopf *et al.*, 2003) and is recycled via arc magmatism, as documented in the isotopic and trace element composition of mantle-derived lavas that erupted along the Pliocene–Quaternary SAVA (Bailey *et al.*, 2009; Kirchenbaur & Münker, 2015). The Kos lamprophyres have crustal Pb isotopic compositions that are indistinguishable from the SAVA lavas, indicating a similar crustal component. Furthermore, they overlap with Miocene sediments drilled from the Mediterranean Ridge and the Nile delta (Fig. 2.7). In contrast, the North Aegean shoshonitic rocks or West Anatolian lamproites have higher $^{207}Pb/^{204}Pb$ for a given $^{206}Pb/^{204}Pb$, demonstrating a different crustal source (Fig. 2.7).

During retreat of the subduction zone, mantle domains in the hanging plate get impregnated with material released from the subducted lithosphere. In a diagram of Ba/Th vs La/Sm, global arc basalts form a mixture between variably depleted mantle and material released from the subducted crust. Arc basalts with high Ba/Th and low La/Sm ratios are thought to be derived from a depleted mantle source that was modified by hydrous fluids released from subducting AOC. In contrast, high La/Sm and low Ba/Th ratios are attributed to source enrichment by partial melts from subducted sediments (Woodhead *et al.*, 2001; Elliott, 2003; Hanyu *et al.*, 2006; Handley *et al.*, 2007). This distinction is based on the fact that the solubility of Th in aqueous fluids is very low (Bali *et al.*, 2011), whereas LIL elements like Ba are mobile. Both mantle-derived lavas erupted along the SAVA and the low-Nb Kos lamprophyres are characterised by low Ba/Th ratios and high ratios of La/Sm (Fig. 2.11a), suggesting that the LILE and LREE–Th–U budgets of these

magmas are dominated by melts from subducted sediments. In fact, compared to many other arcs, the basaltic lavas from the SAVA predominantly plot near the sediment-melt endmember in Fig. 2.11a, likely due to high amounts of sediment entering the steeply dipping subduction zone, leading to the production of correspondingly high amounts of slab melt. During downthrusting into the mantle prograde metamorphism of sediments results in the breakdown of hydrous minerals such as phengite which may cause partial melting. Additionally, release of water from dehydration of underlying serpentinised mantle or AOC can induce fluid-fluxed melting in the metasediments (Skora & Blundy, 2010). Hydrous silicate melts (and supercritical fluids) effectively transport incompatible elements from the slab to the mantle wedge (Hermann *et al.*, 2006; Spandler *et al.*, 2007; Hermann & Spandler, 2008). These melts may migrate into the mantle peridotite of the hanging wall and cause metasomatic reactions or induce partial melting.

Some geochemical features in the lamprophyres, such as the slight negative Eu anomaly of the low-Nb lamprophyres, are inherited from the metasediments. Whether the crustal trace element signature is transferred unchanged or not into these melts largely depends on the behaviour of accessory phases that sequester significant amounts of incompatible trace elements, as for instance zircon, rutile or monazite. The Th/La ratio in arc magmas may be inherited from the subducting sediment (Plank, 2005). In a diagram of Th/La vs Sm/La (Fig. 2.11b), primitive basalts erupted along an island arc typically show a 'linear' relationship between a high-(Th/La)/low-(Sm/La) sedimentary and a low-(Th/La)/high-(Sm/La) mantle component (Plank, 2005; Singer *et al.*, 2007). The orientation of the array depends on the composition of the components involved, i.e. the degree of mantle depletion and the geochemical signature of the subducted sediment. Marine sediments have variable Th/La ratios between 0.05 and 0.45, whereby the higher ratios (> 0.25) are typical for terrigenous sediments and the lower ratios (< 0.15) are found in metalliferous and phosphatic clays. The average global subducting sediment (GLOSS) has a Th/La ratio of 0.24 (Plank & Langmuir, 1998; Plank, 2005), while the values of the bulk and the upper continental crust are estimated to 0.27 ± 0.05 and 0.33 ± 0.05, respectively (Rudnick & Gao, 2003). The existing data on SE Mediterranean sediments show typical terrigenous values of 0.20–0.34 (Kirchenbaur & Münker, 2015; Klaver et al., 2015). The low-Nb lamprophyres show variable Th/La values (0.24–0.46). These values overlap with data from Nisyros and Santorini (Fig. 2.11b) and cover the range reported for terrigenous sediments, but exceed the range reported for SE Mediterranean sediments. This broader range may be related to initial sedimentary heterogeneity, or highlight the role of fractionation of accessories like monazite, which is able to fractionate the Th/La ratio during melting of the metasedimentary rocks (inset in Fig. 2.11b). The Th/U ratios of the investigated lamprophyres range from 3.5 to 5.8, whereby the low-Nb amphibole lamprophyres show the lowest ratios. These values are similar to those of basaltic rocks from Santorini and Nisyros and resemble those of average upper continental crust and the immature continental detritus of the SE Mediterranean sediments. In contrast, pelagic clays typically have high Th/U ratios ($\sim 6 - 14$) (Plank & Langmuir, 1998). The similarity of this ratio between the low-Nb lamprophyres and subducted sediments and average upper crust implies that fractionation of accessories like monazite or allanite, which incorporate

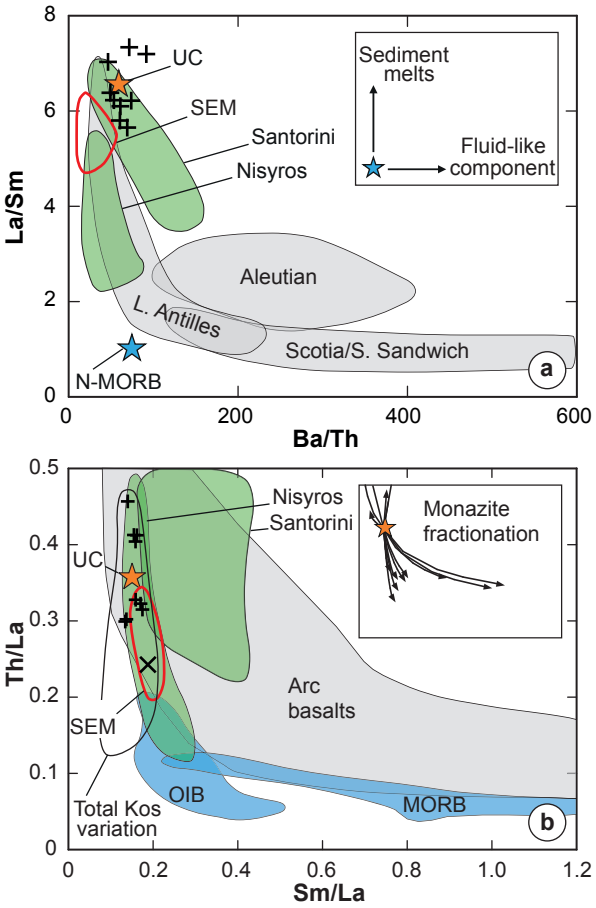

Fig. 2.11. Characterisation of subduction-related endmember based on low-Nb lamprophyres (symbols as in Fig. 2.3). (a) Ba/Th vs La/Sm diagram highlights that mantle source enrichment of the Kos lamprophyres is dominated by melts from subducted sediment rather than by aqueous fluids. Many island arcs show broadly asymptotic trends to both axes. Fields for Scotia/South Sandwich and Lesser Antilles are representative for high Ba/Th and high La/Sm arcs, respectively. Arcs showing 'intermediate' values, are represented by data for the Aleutian arc. Data for basaltic lavas from the SAVA (Santorini and Nisyros) are shown for reference. (b) Plot of Th/La vs Sm/La. The low-Nb lamprophyre data is in the range of terrigenous sediments and scatters around the value for average upper crust (UC). The high-Nb lamprophyres trend towards an enriched low-(Th/La)–low-(Sm/La) component while the depleted/ambient mantle does not contribute significantly to the incompatible element inventory of the lamprophyres. The arc basalt field is taken from Plank (2005). Low-Th/La values are characteristic for intra-oceanic arcs (e.g. Tonga, Marianas) with subducted deep-sea sediments. The highest Th/La values are found in arcs that are dominated by the subduction of continent-derived material. Data fields for OIB, MORB (Singer *et al.*, 2007) and SEM (Klaver *et al.*, 2015; Kirchenbaur & Münker, 2015) are shown for reference. Inset showing effect of Rayleigh fractionation of monazite (Hermann & Rubatto, 2009; Skora & Blundy, 2010; Stepanov *et al.*, 2012) on Th/La and Sm/La of intial average upper crust. The published partition coefficients between monazite and silicic melt are heterogeneous.

Th in preference of U (Klimm *et al.*, 2008; Stepanov *et al.*, 2012), is insignificant. High amounts of Th, U and LREE suggest effective dissolution of accessories from initially heterogeneous metasediments into the anatectic liquids.

Partial melts derived from subducted metasediments have SiO_2-rich quartz saturated compositions. These melts may rise into the mantle wedge and react with the peridotite, leading to the formation of orthopyroxene and phlogopite at the expense of olivine, which lowers the SiO_2 content of the melt. Assimilation of peridotite increases the Mg and Fe content of the melt and the concentrations of mantle-compatible trace elements like Cr or Ni. Depending on the previous depletion of the peridotite (harzburgite vs lherzolite), Na-rich clinopyroxene, garnet and amphibole may form additional phases in the hybridised mantle rock (Sekine & Wyllie, 1982a; Sudo & Tatsumi, 1990; Ertan & Leeman, 1996; Rapp *et al.*, 1999; Wunder & Melzer, 2003; Malaspina *et al.*, 2006; Fumagalli *et al.*, 2009; Mallik *et al.*, 2015). Fractional crystallisation of these phases may significantly change the trace element patterns of the uprising melts. However, channelised flow will cause the formation of orthopyroxene-rich reaction zones between quartz-saturated melt and peridotite causing very limited further interaction (Pirard & Hermann, 2015). Thus, the melts may rise to the surface or freeze in colder regions of the mantle lithosphere.

Lamprophyres originate from low-degree melting of a mantle source enriched by slab-derived sediment melts with no discernible contribution of an aqueous fluid (high-Ba/Th component). In fact, high amounts of aqueous slab fluids would induce significant partial melting of peridotite, therefore, diluting the sediment-derived component and preventing the generation of strongly enriched lamprophyric or shoshonitic melts. Consequently, lamprophyres or similar rocks with comparable geochemical features rarely occur above oceanic subduction zones. Instead, they are more common in post-collisional settings, where the lithospheric mantle contaminated by a preceding stage of subduction is decompressed and the metasomatic domains are preferentially affected by partial melting.

2.5.4. Asthenosphere-derived high-Nb component

The systematics of large-ion lithophile elements (LILE) indicate that amphibole might have played a major role in the generation of the high-Nb lamprophyres during partial melting of the metasomatically overprinted mantle (Fig. 2.10). In mantle rocks, Ca-amphibole is stable at pressures below 3.2 GPa and temperatures between 750 and 1070°C (Niida & Green, 1999; Fumagalli *et al.*, 2009; Tumiati *et al.*, 2013; Green *et al.*, 2014). The solidus of amphibole-rich mantle domains is always lower than that of the enclosing peridotite. Crossing the stability limit of amphibole causes a high degree of melting in these rocks. The resulting melts have Si-undersaturated nephelinitic compositions and may grade towards basanitic to alkali basaltic compositions upon reaction with surrounding peridotite (Médard *et al.*, 2006; Pilet *et al.*, 2008; Pilet, 2015). Such a vein-plus-wallrock melting relationship is in accordance with the low silica contents of the high-Nb lamprophyres. Primitive shoshonitic (orogenic) lamprophyres, such as the low-Nb amphibole lamprophyres, tend to have much higher silica concentrations (~ 50 wt% SiO_2; Fig. 2.3, Fig. 2.9). In addition, the high-Nb lamprophyres show higher CaO/Al_2O_3 ratios

for a given Mg#, which is in line with melting of amphibole-rich lithologies.

The amphibole structure accommodates significant amounts of REE and can incorporate HFSE in large quantities (Vannucci *et al.*, 1995; Tiepolo *et al.*, 2000). As the high-Nb lamprophyres show $HFSE^{4+}$ depletion and superchondritic Zr/Hf and Nb/Ta values, amphibole fractionation has to be taken into consideration. In the proposed vein-plus-wallrock melting mechanism, a high degree of partial melting affects the veins and will readily consume amphibole-rich lithologies without significant trace element fractionation. However, amphibole fractionation may influence the melt composition during ascent of the metasomatizing fluid phase in the mantle ('percolative fractional crystallisation' sensu Harte *et al.*, 1993). It has been experimentally shown that the major element composition of amphibole strongly influences the trace element partitioning behaviour (Tiepolo *et al.*, 2001). Amphiboles precipitated in veins cutting peridotites generally have lower Mg# than amphiboles disseminated in peridotite. These amphiboles preferentially incorporate Nb over Zr, leading to lower Zr/Nb ratios in the vein assemblages (Tiepolo *et al.*, 2001). This is also reported for natural amphibole-rich mantle veins (e.g. Ionov & Hofmann, 1995). Furthermore, low TiO_2 concentrations and high f_{O_2} increases $D_{Nb_{amp/liq}}$, supporting the decoupling of $HFSE^{4+}$ from $HFSE^{5+}$ (Tiepolo *et al.*, 2001). One could argue that melting of such amphibole 'cumulates' causes the observed trace element patterns. However, in low-Mg# amphiboles, D_{Nb}/D_{Ta} is ~ 1 or slightly higher but both elements are still moderately incompatible. Therefore, amphibole fractionation is unlikely to cause the very high $HFSE^{5+}$ concentrations and strongly superchondritic Nb/Ta ratios. In addition, amphibole crystallisation cannot explain superchondritic Zr/Hf ratios, as Hf is more compatible than Zr (Tiepolo *et al.*, 2001). Melting of amphibole cumulates seems not to be the origin of the observed trace element patterns. Instead, it is more plausible, that the trace element patterns are largely inherited from the metasomatic vein-forming agents.

The respective metasomatizing fluids were strongly enriched in incompatible elements and must originate from a fertile source with a mantle-like Sr–Nd isotopic signature. One of the most striking features is the superchondritic Nb/Ta ratio (Fig. 2.12d). Low-degree melts from an eclogitic source are characterised by high Nb/Ta ratios but have very low Nb concentrations, as $HFSE^{5+}$ are strongly compatible in restitic rutile (Green & Pearson, 1987; Klemme *et al.*, 2005). Moreover, melts from an eclogitic source will be characterised by high SiO_2 contents (Rapp *et al.*, 1999) and steep chondrite-normalised HREE patterns, unlike those of the Kos lamprophyres. Thus, subducted oceanic crust cannot account for the geochemical peculiarities shown by the lamprophyres from Kos.

Superchondritic Nb/Ta is rarely observed in mantle-derived melts and most accessible terrestrial reservoirs show subchondritic values. The range of Nb/Ta values in OIB is $\sim 14-16$ while the average continental crust has Nb/Ta of 12–14, which taken together represents the spread observed in MORB (Münker *et al.*, 2003). Higher ratios of up to 19.1 were observed in continental intraplate basalts (Pfänder *et al.*, 2012), while dominantly superchondritic ratios were reported for kimberlites (Becker & Roex, 2006) and calciocarbonatites (average Nb/Ta ~ 35; Chakhmouradian, 2006). Elevated Nb/Ta and

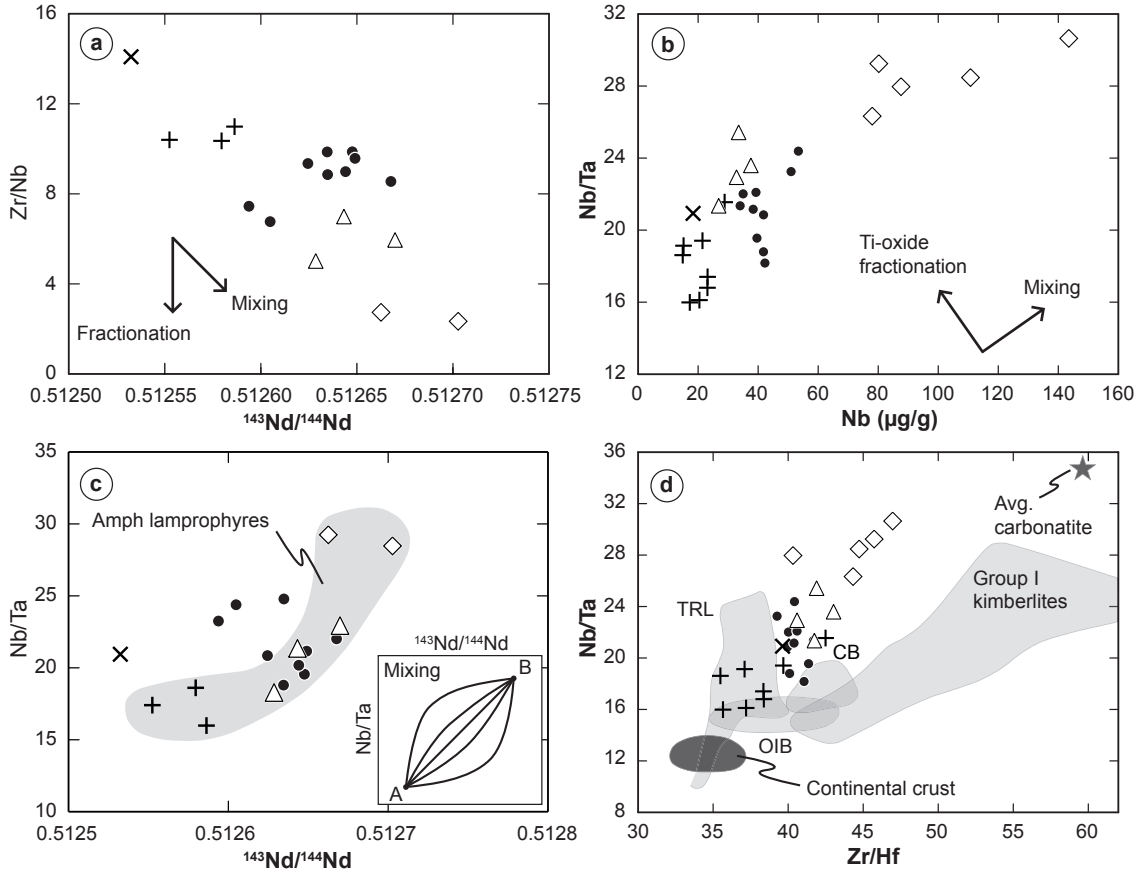

Fig. 2.12. High field-strength element (HFSE) systematics for Kos lamprophyres. (a) Zr/Nb vs $^{143}Nd/^{144}Nd$. (b) Nb/Ta vs Nb. (c) Nb/Ta vs $^{143}Nd/^{144}Nd$. (d) Nb/Ta vs Zr/Hf. Schematic inset for two–component mixing in frame (c) reflects the dependence of mixing trends on the Nd concentration in the two endmembers. Data sources for reference fields: Average carbonatite (Chakhmouradian, 2006), Tethyan realm lamproites (TRL; Prelević *et al.*, 2008), South African Group I kimberlites (Becker & Roex, 2006), ocean island basalts (OIB), continental basalts (CB) and continental crust (Münker *et al.*, 2003). Considerably fractionated samples are not shown to minimize the effect of cpx fractionation on the Zr/Hf ratio. Symbols as in Fig. 2.3. Except for the low-Nb amphibole lamprophyres, all other groups are characterised by Nb/Ta values (18.3–30.7) that are mostly higher than those of chondrites (19.9 ± 0.6, 1σ; Münker *et al.*, 2003). Zr/Hf values (34.8–50.2) are generally higher than the value of 34.3 ± 0.3 for bulk silicate earth (BSE) as given by Münker *et al.* (2003). In terms of Nb/Ta vs Zr/Hf (Fig. 2.12d), the least fractionated samples (Mg# $\geq$ 60) of the five lamprophyre groups define a steep positive correlation.

Zr/Hf values in continental intraplate basaltic rocks were attributed to carbonatite metasomatism, which may be a widespread feature in the subcontinental lithospheric mantle (Pfänder *et al.*, 2012). This is supported by mantle xenoliths metasomatised by such fluids (Ionov *et al.*, 1993; Rudnick *et al.*, 1993; Yaxley *et al.*, 1998; van Achterbergh *et al.*, 2004; Aulbach *et al.*, 2011). Further typical features are negative $HFSE^{4+}$-anomalies (e.g. low Ti/Eu and Hf/Sm), high P contents and high amounts of Sr, LREE, Th and U, i.e. features that are characteristic for the high-Nb lamprophyres.

Incipient melting of a fertile asthenospheric mantle may produce trace element-enriched low-degree silicate or primary magnesiocarbonatitic melts (e.g. Thibault *et al.*, 1992; Tappe *et al.*, 2006; Brey *et al.*, 2008). Primary carbonatites are generated in the dolomite peridotite stability field and experimental mineral-melt partition coefficients predict the development of strongly trace element-enriched melts with negative $HFSE^{4+}$ anomalies (Sweeney *et al.*, 1995; Klemme *et al.*, 1995; Blundy & Dalton, 2000; Adam & Green, 2001; Dasgupta *et al.*, 2009). Carbonatitic liquids have low viscosities and, therefore, are highly mobile and represent effective metasomatic agents that may easily percolate through the mantle (Hammouda & Laporte, 2000). At shallow levels (< 2.2 GPa), such melts are consumed by metasomatic reactions, resulting in clinopyroxene and possibly amphibole crystallisation at the expense of orthopyroxene (formation of wherlites) (Green & Wallace, 1988; Thibault *et al.*, 1992).

Trace element patterns with negative $HFSE^{4+}$ anomalies may, however, also develop in low-degree silicate melt fractions from a garnet-bearing peridotite. As $HFSE^{4+}$ are moderately incompatible to compatible in garnet and clinopyroxene (Salters *et al.*, 2002; Klemme *et al.*, 2002; Adam & Green, 2003, Adam & Green, 2006; Pertermann *et al.*, 2004; Hill *et al.*, 2011), this may also result in low Hf/Sm or Ti/Eu. Inconsistencies in published partition coefficients regarding the fractionation behaviour of garnet and clinopyroxene on Zr/Hf and Nb/Ta hinders an unambiguous distinction between carbonatite and silicate melt metasomatism. However, similar trace element patterns as observed in the high-Nb lamprophyres are known from igneous rocks that involve carbonate-bearing peridotite in their genesis, like kimberlites or ultramafic lamprophyres, making carbonatite metasomatism a likely candidate (Becker & Roex, 2006; Tappe *et al.*, 2006, Tappe *et al.*, 2007; Woodard *et al.*, 2014).

The asthenospheric mantle below the subducting lithosphere is the potential source of the anorogenic signature, most probably transported in the form of carbonatitic melts (though low-degree silicate melts cannot fully be excluded). These metasomatic agents infiltrated the lithospheric mantle and possibly migrated along zones of weakness such as the pre-existing subduction-related vein-network to cause modal and cryptic metasomatism. The presence of a fertile source with an asthenospheric geochemical fingerprint above an active subduction zone requires gaps in the subducting slab to allow the inflow into the lithospheric mantle. Such gaps may have developed at the eastern margin of the Aegean back-arc basin, where the slab presumably was stretched and possibly torn apart due to contrasting rollback rates.

2.6. Conclusions

Lamprophyres rarely occur in active arc settings, what makes the presence of numerous amphibole and mica lamprophyres of Kos at the eastern end of the South Aegean Volcanic Arc (SAVA) an unusual example. The dykes intruded into the crystalline basement of the island in an 'en-échelon' style along a sinistral shear zone. As the Aegean back-arc basin extends faster than western Anatolia, the two crustal domains are separated by a lithosphere-scale transition zone that accommodates differential motion and creates pathways for mantle-derived melts. Melting took place in the lithospheric mantle and was probably triggered by decompression during extensional thinning of the Aegean lithosphere.

The composition of the lamprophyres from Kos was controlled by at least three components, two of them being enriched and one depleted. The enriched components originated from (i) subduction-related mantle metasomatism, geochemically dominated by sediments and (ii) incipient melts from the asthenosphere below the subducting slab. The depleted component is derived from the lithospheric mantle of the upper plate that was variably impoverished by former subduction-related melting processes. The two fertile components showed variable contributions from the ambient mantle and subsequent mixing among the components happened in different proportions.

The crust-like component was introduced into the mantle by the Hellenic subduction zone and is dominated by terrigenous sediments of Pan-African provenance. Upon descending into the mantle, the metasediments released K-rich silicic melts that migrated into and reacted with the depleted peridotite producing phlogopite pyroxenites. Lamprophyres dominated by this component have geochemical similarities with basalts erupted along magmatic arcs with high input of continental crust-derived sediments. Despite isotopic and geochemical similarities with lavas erupted along the South Aegean Volcanic Arc, the sediment signatures are (much) stronger in the lamprophyres. In general, lamprophyres appear during post-collisional extension, when partial melting takes place in the previously enriched lithospheric mantle. The basic differences to arc basalts may be the scarcity of free aqueous fluid, preventing significant partial melting of the ambient peridotite that would cause a dilution of the enriched signature.

The second fertile mantle component is introduced into the lithospheric mantle by low-degree melts originating in the asthenosphere below the subducting slab, and was introduced into the supra-subduction mantle through slab ruptures that were formed due to transtensional tectonics at the edge of the retreating subduction zone. These melts reacted with the lithospheric mantle and caused the crystallisation of clinopyroxene-rich and, most probably, amphibole-bearing lithologies. Even though some of the chemical characteristics of the second enriched component may be attributed to amphibole fractionation during metasomatism, the signature is essentially inherited from the asthenosphere-derived incipient melts that show a carbonatite-like signature.

3. Post-collisional potassic–ultrapotassic magmatism of the Variscan orogen: mantle source enrichment caused by continental subduction

3.1. Introduction

Continental collision zones differ from oceanic subduction zones by a striking absence of characteristic arc basalts (Rumble *et al.*, 2003). The generation of arc basalts above oceanic subduction zones involves partial melting of the mantle wedge, fluxed by large amounts of water released from subducted altered oceanic crust and mantle serpentinite. In contrast, continental collision zones show voluminous granitic intrusions and subordinate mantle-derived K-rich, dominantly shoshonitic to ultrapotassic rocks. The main hydrous phase in subducted continental crust or continent-derived clastic sediments is phengite. Breakdown of phengite at mantle depth induces partial melting of the crustal rocks and may release hydrous silicate melts (or supercritical liquids) to the mantle peridotite of the hanging wall of the subducting slab (e.g. Hermann & Green, 2001; Schmidt *et al.*, 2004). These metasomatic agents interact with peridotite resulting in hybrid melts with both high contents of mantle compatible and incompatible elements. Most of these melts crystallize in the mantle lithosphere. During post-collisional equilibration of the crust or regional extension these enriched domains may re-melt preferentially and eventually be transported into the upper crust. A number of processes controls the geochemical signature of the K-rich melts. When the subducted continental crust reaches its solidus, the trace element pattern of the resulting melt is essentially controlled by the stability of accessory phases that may sequester significant amounts of incompatible trace elements. Interaction between granitic melt and peridotite eventually results in the consumption of olivine and precipitation of orthopyroxene (e.g. Mallik *et al.*, 2015). Sequestration of trace elements in metasomatic minerals like garnet, phlogopite or amphibole may additionally strongly influence the trace element inventory of the melt.

The Variscan orogen is an ideal site for studying the effect of crustal recycling in collision zones, causing mantle metasomatism and diverse syn- to post-collisional magmatism. A striking feature of the Variscides is the wide distribution of felsic high- to ultrahigh-pressure nappes that are commonly associated with garnet peridotites and locally may contain diamond, testifying for deep continental subduction (Kotková *et al.*, 2011). The emplacement of potassic–ultrapotassic mantle-derived melts (durbachites) forming major intrusive bodies around 340–335 Ma immediately follows the exhumation of (U)HP crustal nappes (Janoušek & Holub, 2007) and repeatedly thereafter. Countless lamprophyre dykes were emplaced across the internal parts of the orogen during post-collisional extension between ∼330–325 Ma and 300 Ma. Post-collisional lamprophyre dykes were

systematically sampled along a traverse across the various Variscan tectonic units in SW Germany and NE France. Major- and trace element and Sr–Nd–Pb isotopic compositions of lamprophyres were investigated in order to trace the nature of the subducted material and investigate how the multi-stage petrogenesis affects composition of the K-rich melts. The advantage of studying lamprophyre dykes is that usually several independent magmatic pulses are present within a co-genetic suite of dykes with little to highly enriched trace element contents, allowing to investigate the interaction between subducted continental crust and mantle peridotite as well as the final melting process and generation of lamprophyres within the lithospheric mantle. It is important to divide between primary compositions of subducted lithology and processes like fluid vs melt transfer.

3.2. Geological setting

The Variscan orogen is the result of the Paleozoic convergence of Laurussia and Gondwana during the closure of the Rheic Ocean, eventually leading to the assembly of Pangaea (e.g. Stampfli *et al.*, 2002; Winchester *et al.*, 2002; Nance *et al.*, 2012; Kroner & Romer, 2013). In SW Germany and easternmost France, Variscan basement is exposed in two belts that are separated by the Cenozoic rift of the Upper Rhine Graben. The study area includes the Rheno-Hercynian Zone, the Mid-German Crystalline Zone (MGCZ), the Saxo-Thuringian Zone and the Moldanubian Zone of the Variscan orogen (Fig. 3.1). The Rheno-Hercynian Zone is part of Avalonia (Laurussia), whereas the Saxo-Thuringian Zone and Moldanubian Zone are part of Gondwana (Franke, 2000). The MGCZ probably hosts the obscured Rheic suture (Zeh & Gerdes, 2010).

The MGCZ is exposed in the Odenwald–Spessart area and represents a basement wedge within the Saxo-Thuringian Zone, dominated by granitoid plutons that are bordered by medium- to high-grade schists and gneisses (Altherr *et al.*, 1999a; Zeh & Will, 2010). Orthogneisses with Silurian–Devonian protolith ages are possibly remnants of the Rheic magmatic arc (e.g. Dombrowski *et al.*, 1995; Reischmann *et al.*, 2001; Franke, 2000). They additionally contain relictic eclogites (Will & Schmädicke, 2001). The MGCZ separates very low- to low-grade metasediments and volcanic rocks from the Northern Phyllite Zone (NPZ) and Rhenohercynian Zone in the northwest and low- to medium-grade metamorphics of the Saxo-Thuringian Zone in the southeast. The Saxo-Thuringian volcano-sedimentary succession in the N Vosges and N Schwarzwald area comprises a SE dipping wedge of lower Palaeozoic metasediments and meta-igneous rocks and Upper Devonian to lower Carboniferous synorogenic volcanics and clastics. The Lalaye-Lubine/Baden Baden shear zone separates the Saxo-Thuringian/MGCZ from the Moldanubian zone to the south, where a double-vergent (bivergent) basement wedge of dominantly medium- to high-grade gneisses and granitoids is exposed in the Vosges and the Central Schwarzwald Gneiss Complex and the Southern Gneiss Complex of the Schwarzwald (e.g. Eisbacher *et al.*, 1989). Relict basic and felsic granulites are present within the metamorphic basement of the Vosges and Schwarzwald as well as retrogressed eclogites and Spl-, Grt–Spl- and Grt-peridotites (e.g. Hanel *et al.*, 1993; Altherr

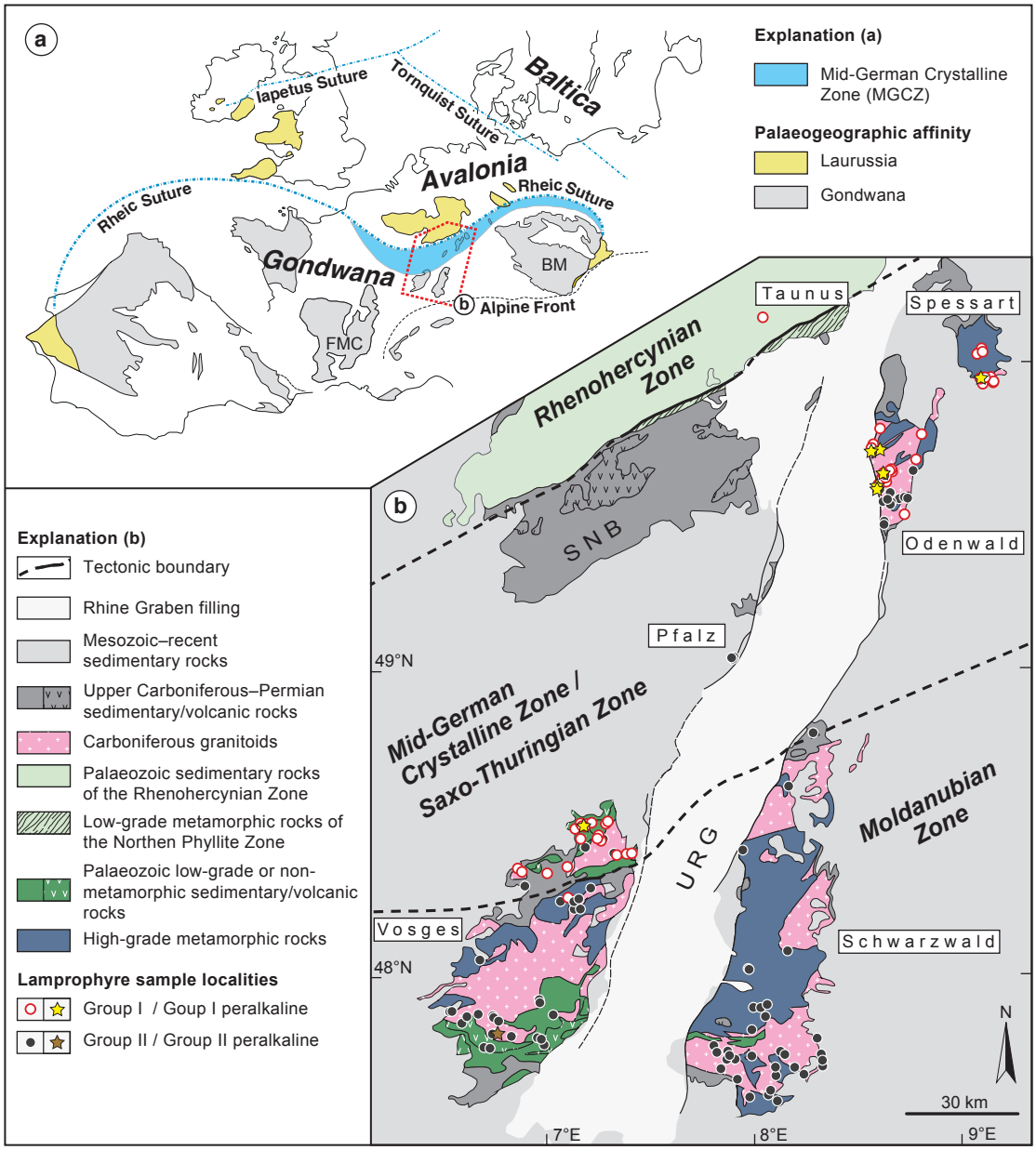

Fig. 3.1. (a) Map showing the exposed Variscan basement of Europe, palaeogeographic affinities of crustal domains and the location of the Rheic suture zone (after Linnemann *et al.*, 2007; Franke, 2000). BM = Bohemian Massif, FMC = French Massif Central. (b) Simplified geological map of the study area (modified after Lahner & Toloczyki, 2004) with sample localities along the basement units (Taunus, Odenwald-Spessart, Pfalz, Schwarzwald and Vosges) exposed along the Cenozoic Upper Rhine Graben (URG). SNB = Permo-Carboniferous Saar-Nahe basin. In cases of high density of sample locations, only representative ones are shown.

& Kalt, 1996; Marschall *et al.*, 2003; Skrzypek *et al.*, 2012). High-pressure granulites are a widespread lithology in the Central European Variscides. The discovery of diamond within felsic granulites of the Saxo-Thuringian Zone in the Bohemian Massif testifies for deep continental subduction around 340 Ma (Kotková *et al.*, 2011; Kotková *et al.*, 2016). UHP conditions (about 4–6 GPa and 1000–1100°C; Altherr & Kalt, 1996) are recorded in garnet peridotites enclosed in gneisses of the Vosges Mountains and indicate that continental crust was subducted to mantle depths during the final stages of the Variscan collision, similar to the Bohemian Massif. Zircon U–Pb dating of gneisses and granulites yielded ages of $\sim 335 - 342$ Ma (Hanel *et al.*, 1993; Schaltegger *et al.*, 1999; Kober *et al.*, 2004; Skrzypek *et al.*, 2012). Additionally, abundant syn- to postkinematic granitoid magmatism affected both domains during the Late Visean (e.g. Schaltegger *et al.*, 1996; Altherr *et al.*, 1999b, Altherr *et al.*, 2000; Tabaud *et al.*, 2014, Tabaud *et al.*, 2015).

K-rich Variscan magmatism K-rich mantle-derived magmatism is widespread in the Variscides and recurrently formed during the at least 50 Ma following the peak of the Variscan orogeny at 340 Ma. The exhumation of the HP granulites around 340–335 Ma is followed by the emplacement of potassic–ultrapotassic mantle-derived melts (durbachites), forming independent intrusive bodies or co-magmatic enclaves within granitoids of the Bohemian massif or the External Massifs of the Alps, for instance (e.g. Gerdes *et al.*, 2000; Kotková *et al.*, 2010). A next pulse of K-rich mantle-derived magmatism between 330–320 Ma follows the widespread post-collisional granitoid magmatism and is scattered across the entire internal zones of the Variscan orogen (e.g. Abdelfadil *et al.*, 2014). Finally, another activation of the lithospheric mantle resulted in the eruptions of K-rich lavas within Upper Carboniferous–Permian basins (e.g. SW England; Saar-Nahe basin) and the emplacement of a third generation of lamprophyre dykes (e.g. von Seckendorff *et al.*, 2004).

All stages are present in the study area where the earliest K-rich mantle-derived melts are amphibole-biotite quartz-melasyenite intrusions (durbachites), which are present in the Central and Southern Vosges (as part of the Crêtes and Ballon intrusions), dated around 340 Ma (Schaltegger *et al.*, 1996; Tabaud *et al.*, 2015) and the Schwarzwald (the type locality near Durbach, Central Schwarzwald). Following Late Visean post-collisional granitoid magmatism, a large number of lamprophyre dykes were emplaced throughout the study area between 332–325 Ma and around 300 Ma (Boutin *et al.*, 1995; Hess & Schmidt, 1989; Hess *et al.*, 1995; Hegner *et al.*, 1998; von Seckendorff *et al.*, 2004; Turpin *et al.*, 1988).

Lamprophyre dykes from the Variscan basement massifs along the shoulders of the Cenozoic Upper Rhine Graben (Fig. 3.1) typically form steeply dipping dykes that have a thickness in the m–dm range. In the southern Vosges and the Schwarzwald, mica lamprophyres (minettes and kersantites) prevail, whereas hornblende-lamprophyres (spessartites) are common in the northern outcrop areas, and even dominate in some regions (e.g. Spessart). Furthermore, peralkaline minettes were identified from the Spessart–

Odenwald, Northern Vosges and Southern Vosges areas, earlier only known for the descriptions of 'blue–green hornblende' in minettes from the Odenwald (Schottler, 1906; Klemm, 1924) and crocidolite (fibrous riebeckite) in a minette dyke from the N Vosges (Delesse, 1856). The described peralkaline minettes are geochemically and mineralogically closely related to orogenic lamproites, as occurring along the Alpine-Himalayan belt, for instance (e.g. Conticelli *et al.*, 2009).

3.3. Results

The lamprophyres of the study area include a range of petrographically and mineralogically different rocks. According to the IUGS classification scheme (Le Maitre, 2002), mica lamprophyres are kersantites or minettes (alkali feldspar < plagioclase in kersantites et vice versa) and amphibole lamprophyres are spessartites (plagioclase > alkali feldspar). Vogesites were not observed (although originally defined in the Vosges mountains; Rosenbusch, 1887) in which Ca-amphibole is more abundant than biotite and alkali feldspar is more abundant than plagioclase. Rare peralkaline varieties of minette dykes were identified in the Odenwald–Spessart, the N Vosges and the S Vosges areas. Based on their mineralogy, mineral chemistry and whole rock geochemistry, these peralkaline dykes are lamproites as defined by Mitchell & Bergman (1991). Two geochemically defined lamprophyre groups are present in the study area. Unambiguous distinction between both groups is possible based on a combination of isotopic and several trace element ratios, although some overlap between both groups exists for most ratios (Table 3.1).

Table 3.1. Geochemical characterisation of Group I and Group II lamprophyres.

	Group I	**Group II**
$^{87}Sr/^{86}Sr_i$	0.70531 – 0.71107	0.70591 – 0.71572
εNd	-3.4 – -0.6	-7.4 – -1.4
Th/La	0.15 – 0.55	0.22 – 1.96
Eu/Eu*	0.89 ± 0.07	0.74 ± 0.16
Nb/Ta	17.2 ± 3.9	14.4 ± 3.9
K/Rb	307 ± 152	187 ± 70
Cr/Ni	1.8 ± 0.4	4.0 ± 3.1

Mean values given ± 2σ SD.

Most characteristic features are the contrasting shapes of the REE patterns and the different Sr–Nd isotopic compositions. Group I lamprophyres occur mainly in the northwest, i.e. in the Odenwald–Spessart, the Taunus, and the N-Vosges. Group II dominantly occur in the southeast, i.e. the Schwarzwald and the Vosges, but they also show a spatial overlap with Group I lamprophyres at the southern margin of the MGCZ, i.e., the S-Odenwald and the N-Vosges–Pfalz areas (Fig. 3.1). Group II lamprophyres are dominantly mica lamprophyres while Group I dykes also comprise abundant amphibole lamprophyres.

3.3.1. Petrography and mineral chemistry

The dykes studied usually range from cm to several m in width. They have a melanocratic to mesocratic appearance and show porphyritic textures. The groundmass is commonly fine-grained due to rapid crystallisation in the upper crust. Larger dykes usually show a textural zonation with a submicron-sized matrix along chilled margins and a fine-grained matrix with conspicuous quench textures, such as spherulitic to sheave-like crystallisation of the feldspathic matrix and dendritic growth of mafic minerals, with a coarsening towards the center of the dyke, where poikilitic textures may be developed.

Major phenocryst phases are clinopyroxene and phlogopite/biotite (Fig. 3.2a–d) and/or Ca-amphibole (Fig. 3.2e). Many dykes additionally contain phenocrysts of (altered) olivine. Some also contain apatite (micro-) phenocrysts. The groundmass is made up of feldspars, titanite, magnetite (more rarely ilmenite), apatite and interstitial precipitates of calcite, REE-bearing epidote group minerals and in many cases interstitial quartz. These late-stage phases sometimes fill ocelli (biotite-rimmed globular structures) (Fig. 3.2f).

Rare peralkaline minettes in the Spessart–Odenwald and Northern Vosges areas contain eye-catching colourful alkali amphiboles (Fig. 3.2a, b and d). These minette dykes usually are porphyritic with up to 1 cm long phlogopite laths and phenocrysts of clinopyroxene and apatite. Euhedral alkali amphibole (arfvedsonite in Odenwald–Spessart dykes and magnesio-riebeckite in Vosges minette) and numerous tiny crystals of titanite form microphenocrysts. Some rare larger magnetite grains are present. The matrix is dominated by mostly euhedral, lath-shaped or sheave-like alkali-feldspar that enclose the phenocryst phases. Plagioclase is generally absent or occurs together in subordinate amount with a late-stage interstitial mass of alkali-feldspar, quartz, allanite/REE-rich epidote, zircon and some calcite enclosing early crystallised minerals. The alkali amphiboles are overgrown by a second generation of chemically heterogeneous Na- and Na–Ca- to Ca-amphiboles (magnesio-arfvedsonite, magnesio-riebeckite, K-richterite, winchite, actinolite) that also form acicular interstitial grains. Clinopyroxene phenocrysts are rimmed by Zr-rich aegirine.

Autometasomatic processes, due to exsolution of volatiles, affected all dykes. Late magmatic to hydrothermal minerals form greenschist- to subgreenschist-facies assemblages, including chlorite, albite, actinolite, epidote, prehnite, analcime, phengite, calcite, baryte, fluorite and hematite. Olivine phenocrysts are completely transformed to secondary phases (calcite–chlorite, calcite–chlorite–actinolite, talc). Melts rich in CO_2 show replacement of clinopyroxene by calcite. Although chlorite is commonly present in small quantities in the matrix, phlogopite phenocrysts of the analysed lamprophyres are not chloritised.

Phlogopite phenocrysts of kersantites and 'normal' minettes are characterised by high Al_2O_3 contents $\sim$14–18 wt%, typical of shoshonitic lamprophyres (Fig. 3.3b). Phlogopite phenocrysts in peralkaline minettes differ from those of metaluminous minettes/kersantites by lower Al_2O_3 contents ($\sim$10–14 wt%) and fall in the compositional range known from lamproitic rocks (Mitchell & Bergman, 1991). Although these micas show elevated Si content, there is not sufficient Al present to fill the tetrahedral sites and

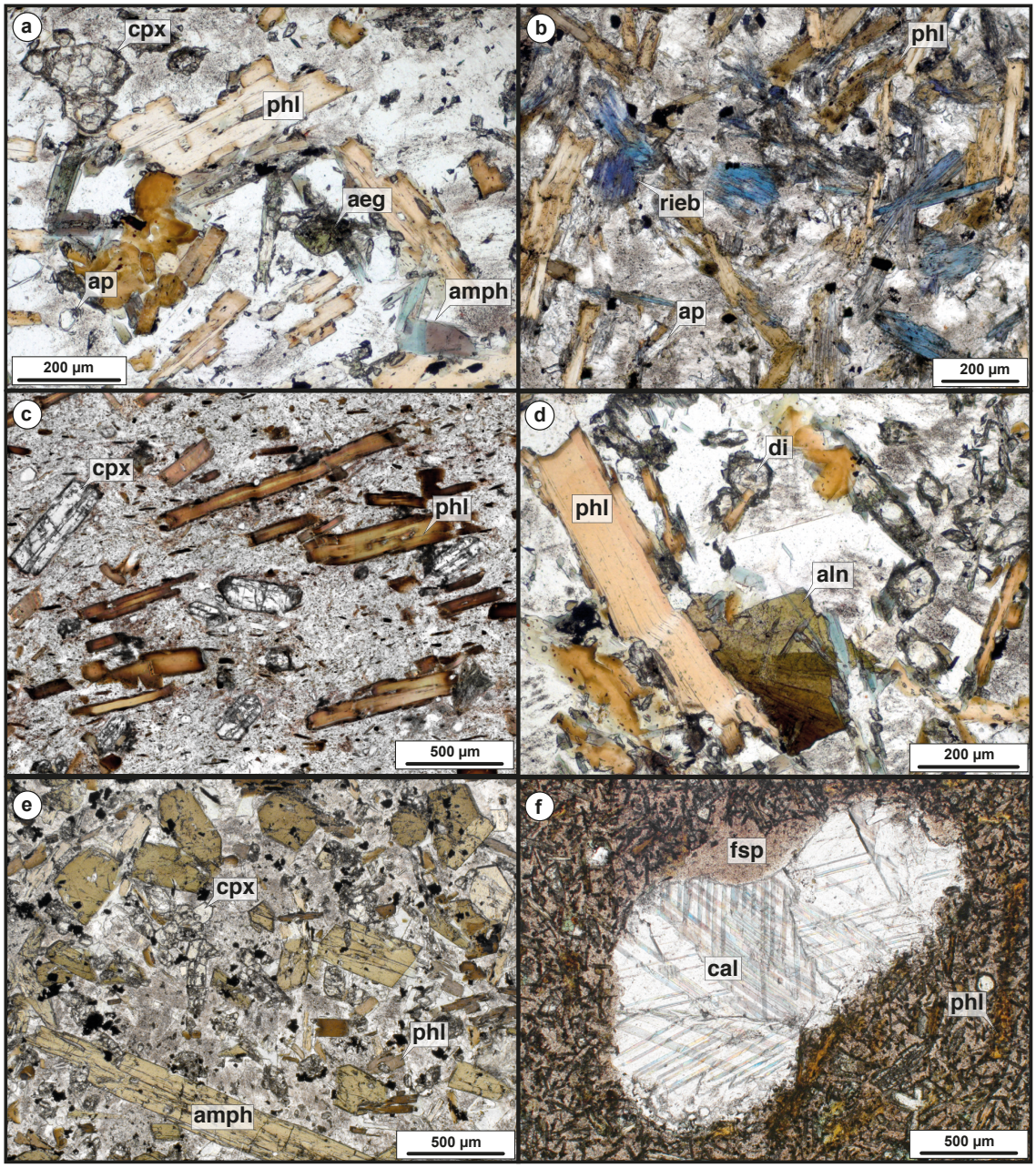

Fig. 3.2. Photomicrographs of lamprophyres. (a) Peralkaline minette (sample OD153) with phlogopite (phl), diopside-rich clinopyroxene (di), apatite (ap), aegirine (aeg), zoned alkali amphibole (dirty violet–blue arfvedsonite core rimmed by blue magnesio-riebeckite–winchite), embedded in a groundmass of K-feldspar ± qtz and tiny euhedral titanite. (b) Peralkaline minette from N Vosges (sample VO03) with phlogopite and blue–violet magnesio-riebeckite ('crocidolite minette' from Delesse, 1856). (c) Minette (sample VO64B) with phenocrysts of clinopyroxene and phlogopite (with dark Fe-rich rims) embedded into a fine-gained quartzofeldspathic matrix from S Vosges. (d) Peralkaline minette (sample OD153) with interstitial (late-stage) allanite (aln), quartz and blue amphibole (magnesio-riebeckite–winchite). (e) Spessartite–Kersantite (sample PF04) with large amphibole phenocrysts along with clinopyroxene and some biotite/phlogopite. (f) Minette (sample OD019) with ocelli filled by calcite and fine-grained, sheave-like feldspar.

some Fe^{3+} may compensate this deficiency (as tetra-ferriphlogopite component). Phlogopite shows a rimward decrease in the Mg# that is accompanied by decreasing Al and increasing Ti and Ba. Some phlogopite has up to 1.20 wt% Cr_2O_3.

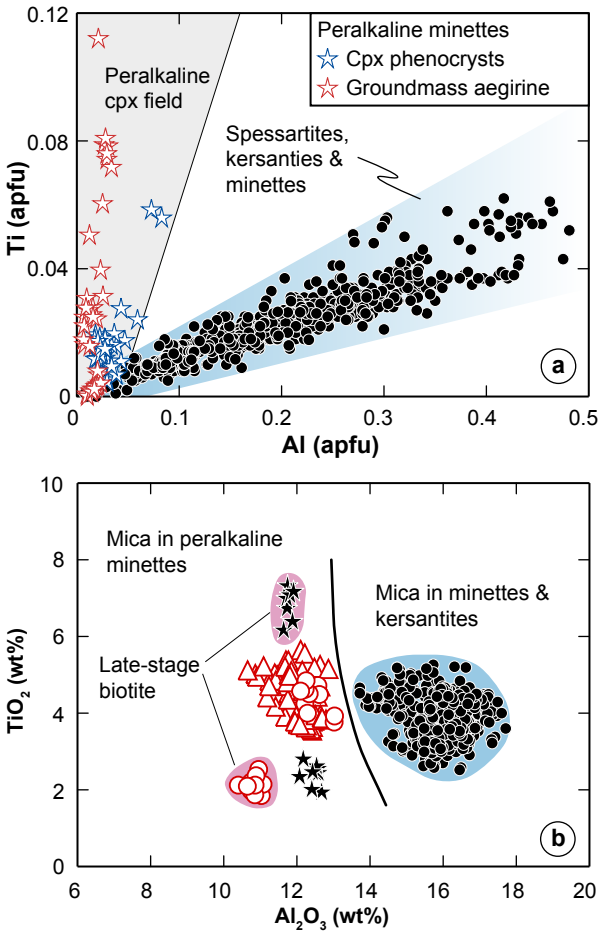

Fig. 3.3. Mineral chemistry diagrams for clinopyroxene (a) and mica (b) illustrate that peralkaline minettes show deficiencies in Al compared to metaluminous-peraluminous spessartites, kersantites and minettes. The mineralogy and mineral chemistry of peralkaline minettes resemble those of orogenic lamproites. (a) Clinopyroxene compositions are given in atoms per formula unit (apfu). (b) Late-stage biotite commonly is enriched in Ba, Ti and F compared to phenocrysts. An exception is the late-stage biotite from the N-Vosges peralkaline minette, which shows low Ti contents. Analyses are documented in Table D.2.

Clinopyroxene phenocrysts have diopsidic compositions and show Fe-enrichment towards the margins (X_{Mg} = 0.89–0.62; Ca = 0.812–0.963 apfu). Oscillatory and sector zoning is locally present. Some dykes contain reversely zoned crystals, commonly with sieve structures partly replacing more Fe-rich domains. Chromium concentrations are typically below detection limit but values of up to 1.6 wt% can be found. TiO_2 increases towards the margins and ranges between 0.26–2.2 wt% TiO_2. Clinopyroxene in peralkaline minettes is Al-poor diopside (Fig. 3.3a) and may show Fe^{3+} in the tetrahedral site. Aegirine/acmite is present in some samples as late rim around diopside phenocrysts. The

amount of aegirine component ranges between 26 and 92 %. Clinopyroxene shows variable but high content of TiO_2 and ZrO_2, with maximum values of 3.9 wt% and 4.2 wt%, respectively.

Amphibole is present as phenocryst and groundmass phase in spessartites. The composition of Ca-amphiboles mostly ranges from magnesio-hastingsite to pargasite. Additionally, late stage actinolitic amphibole is frequently present. In contrast, peralkaline minettes contain microphenocrysts and late-stage sodic to sodic-calcic amphiboles. These Si-rich amphiboles fall in the compositional range of arfvedsonite–richterite–winchite–riebeckite. Most peralkaline minettes contain two generations of alkali amphibole (Fig. 3.2a). The N-Vosges minettes contain microphenocrysts of magnesio-riebeckite, which is also a late-stage phase and replaces clinopyroxene.

Feldspar is present in the groundmass of all lamprophyres. Spessart–Odenwald peralkaline minettes contain no or only very little plagioclase. Alkali feldspar in peralkaline minettes ($Or_{88-93}Ab_{2-8}$) is characterised by elevated contents of Fe^{3+}, which increases from core to rim to max. 5.0 wt% Fe_2O_3 (18% Fe-orthoclase component). These alkali-feldspar phenocrysts are surrounded by small amounts of late stage interstitial alkali feldspar with <0.3 wt% Fe_2O_3. BaO content of alkali feldspar is variable and may in some cases reach up to 2 wt%. Alkali feldspar from the Vosges peralkaline minette ($Or_{72-93}Ab_{17}$Fe-$Or_{1.0-5.5}$) contains up to 4 wt% BaO.

3.3.2. Major and trace element geochemistry and Sr–Nd–Pb isotopic composition

The lamprophyres span a wide range in major and trace element compositions (Fig. 3.4 and Fig. 3.5). Samples with high Mg# [= molar $Mg/(Mg+0.9\times Fe_{tot})\times 100$] show highly variable MgO (5–14 wt%), SiO_2 (45–64 wt%) or K_2O concentrations (1.0–10.1 wt%; Fig. 3.4, Fig. 3.5a). Most of the dykes plot in the shoshonitic field of Peccerillo & Taylor (1976). About half of the samples are ultrapotassic (with K_2O >3 wt%, MgO >3 wt% and K_2O/Na_2O >2). The remaining samples dominantly fall in the shoshonitic field and only some dykes are calc-alkaline according to Fig. 3.4. Most of the dykes are metaluminous while some Si-Al-rich lamprophyres are peraluminous. The most K-rich dykes are mildly peralkaline with a maximum peralkaline index of 1.11 [= molar $(K_2O+Na_2O)/Al_2O_3$] and Na_2O contents as low as 0.2 wt% (Fig. 3.4b; max. K_2O/Na_2O of 52 in unweathered samples).

The chondrite-normalised REE patterns of the lamprophyres (Fig. 3.6a and c) show high $(La/Yb)_{cn}$ and flat HREE patterns between Er und Lu. Group II lamprophyres additionally show a conspicuous flattening in their LREE patterns, becoming more pronounced with increasing trace element enrichment. Furthermore, Group II lamprophyres show a clear negative Eu-anomaly. Primitive mantle-normalised element abundance patterns of all lamprophyres are characterised by strong enrichments in large ion lithophile elements (LILE) and are characterised by negative anomalies of high field strength elements (HFSE) Nb, Ta and Ti and positive anomalies of Pb (Fig. 3.6b and d). Peralkaline minettes show similar patterns but have higher contents of incompatible elements compared to other petrographic varieties of cogenetic dykes. However, they differ in having

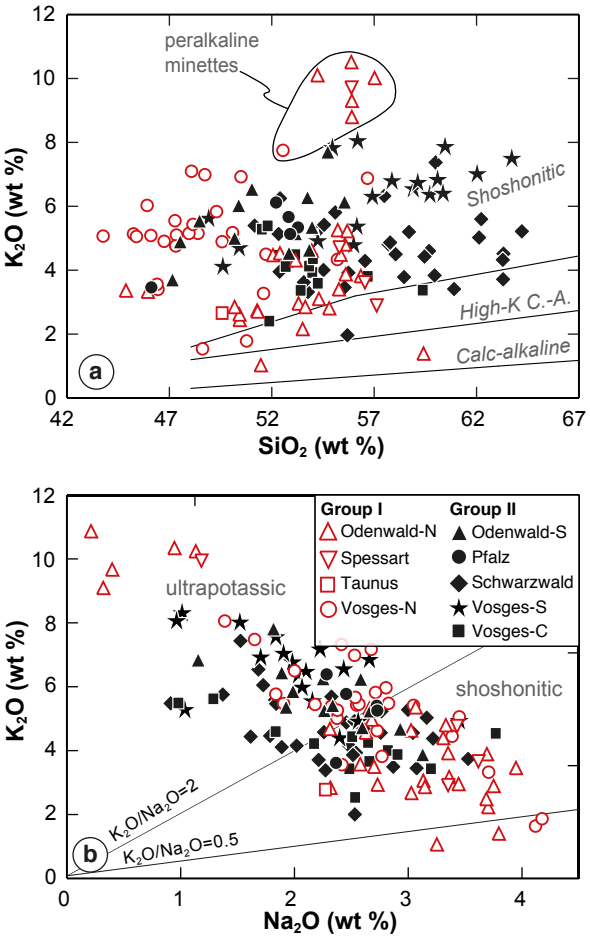

Fig. 3.4. (a) K_2O vs SiO_2 content of Variscan mantle-derived lamprophyres with fields from Peccerillo & Taylor, 1976. (b) Samples show a rough negative correlation in the diagram of K_2O vs Na_2O with ultrapotassic, shoshonitic and calc-alkaline fields (not labelled) from Turner *et al.* (1996).

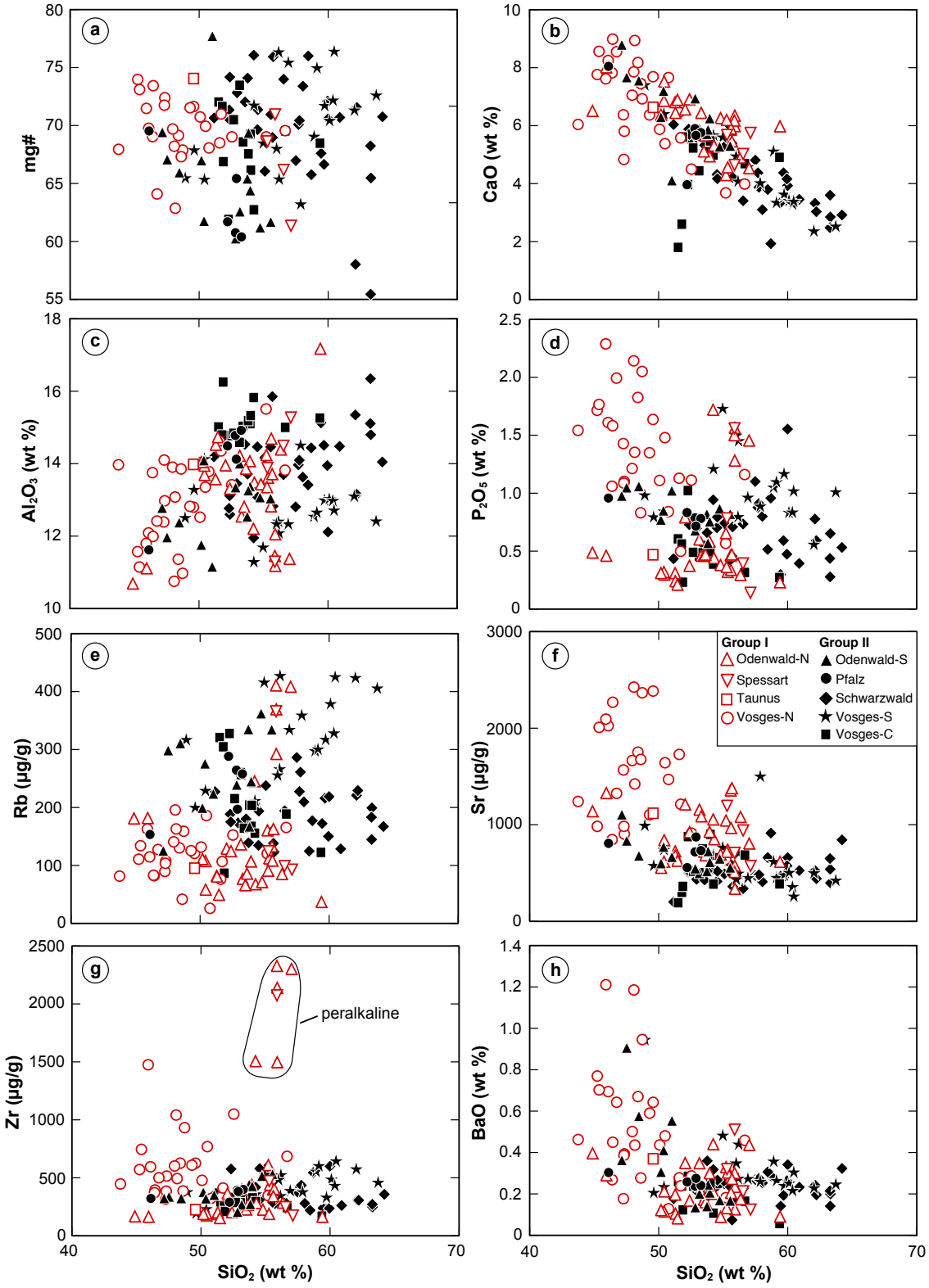

Fig. 3.5. Harker variation diagrams illustrate major and trace element variability. The Mg# in (a) is defined as molar $Mg/(Mg+Fe^{2+})$ with $Fe^{2+}=0.9\times Fe_{tot}$.

strongly positive anomalies of Zr and Hf and smaller negative Ti-anomalies (Fig. 3.6b). Both lamprophyre groups and their regional varieties are on average equally enriched in Pb and some outliers are related to secondary mobilisation of highly fluid-mobile Pb.

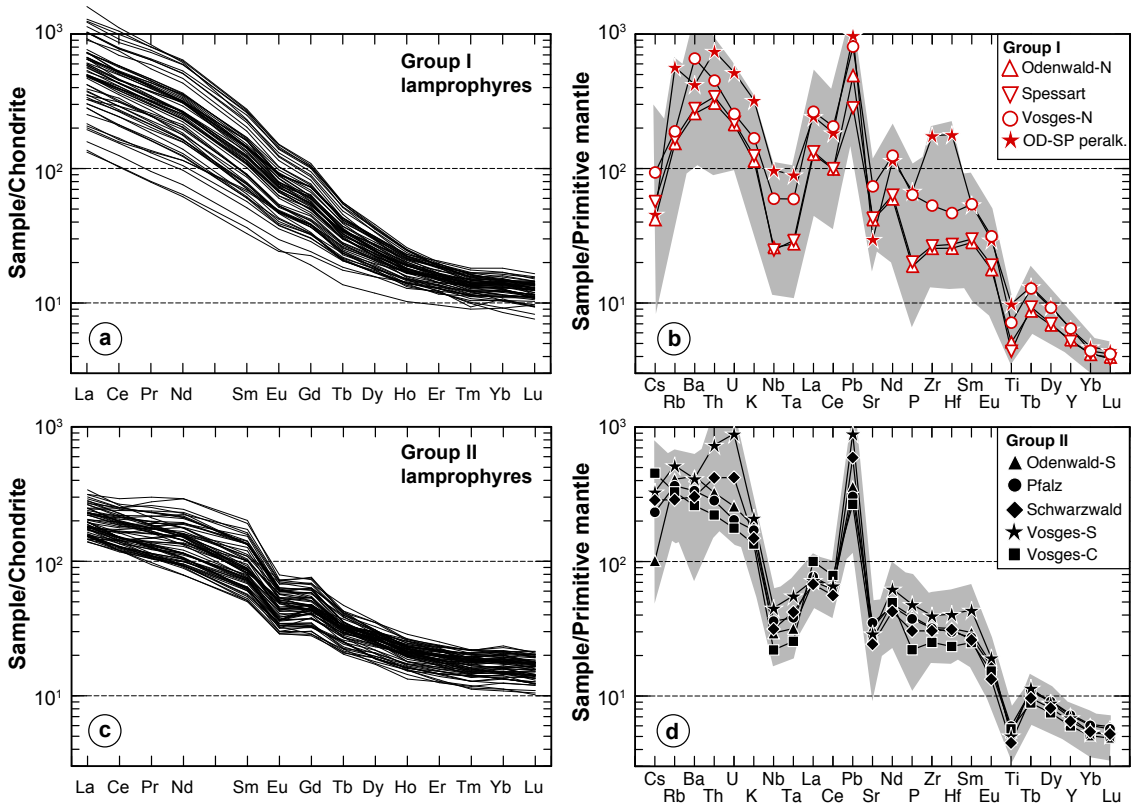

Fig. 3.6. Chondrite-normalised rare earth element patterns for (a) Group I and (c) Group II lamprophyres (normalisation values from McDonough & Sun, 1995). Average primitive mantle-normalised trace element concentration patterns (normalisation values from Sun & McDonough, 1989) for regional varieties of (b) Group I and (d) Group II lamprophyres. The grey reference fields give the total variation of each group. Additional chondrite-normalised rare earth element patterns and primitive mantle-normalised element concentration diagrams for individual regions are given in Fig. C.1 (Group I) and Fig. C.2 (Group II).

Some differences are present between the various dyke swarms of each group. Group I lamprophyres from the N-Vosges, for instance, show on average higher trace element contents compared to those from other regions. N-Vosges dykes are furthermore characterised by the lowest SiO_2 and very high Sr, Ba and P_2O_5 concentrations (Fig. 3.5d, f and h). They also define a different array in Sr–Nd space than the dykes from the Odenwald–Spessart (Fig. 3.7). The Nb/U ratios of Group I and Group II lamprophyres are <10 (6.1±2.3 and 3.2±1.5, respectively) and in the range of average continental crust but significantly lower compared to OIBs (Nb/U = 47±10; Hofmann *et al.*, 1986). However, a limited number of samples from the Pfalz and N-Vosges (i.e. PF04, VO37, VO88, VO91) show increased Nb/U (up to 21). This possibly indicates the contribution of an additional geochemical component to the source of the lamprophyres, possibly derived

from the convecting mantle.

Strontium, Nd and Pb isotopic compositions of representative lamprophyres are given in Table 3.2 and Table 3.3. The lamprophyres have negatively correlated initial $^{143}Nd/^{144}Nd$ and $^{87}Sr/^{86}Sr$ isotopic compositions. The $\varepsilon Nd_{(330Ma)}$ values of the lamprophyres range from slightly negative to distinctly negative. They show compositions similar to the local average continental crust, as represented by post-collisional Variscan granitoids (Fig. 3.7). Group I lamprophyres show only small variations in $^{87}Sr/^{86}Sr_i$ (0.70531–0.70821) and $^{143}Nd/^{144}Nd_i$ (0.51202–0.51219), whereas Group II lamprophyres extend to more radiogenic $^{87}Sr/^{86}Sr_i$ (0.70591–0.71572) and have a broader range in $^{143}Nd/^{144}Nd_i$ (0.51184–0.51215).

The Pb isotopic composition of Group I and Group II lamprophyres defines overlapping fields and, therefore shows no regional differences. The Pb isotopic composition of both groups falls in the range of typical crustal rocks (Fig. 3.8). As most radiogenic ^{207}Pb formed early in Earth's history (due to the relatively short half-live of ^{235}U), the high $^{207}Pb/^{204}Pb$ values at a given $^{206}Pb/^{204}Pb$ value of Group I and Group II lamprophyres indicates that the Pb from these rocks is derived from old continental crust and that contribution of mantle Pb must be subordinate. The range in $^{207}Pb/^{204}Pb$ at comparable $^{206}Pb/^{204}Pb$, however, does not reflect one single old crustal source, but instead may be due to two different crustal sources. For instance, an old craton has higher $^{207}Pb/^{204}Pb$ than a younger magmatic arc. Lead of lamprophyres from the Saxo-Thuringian Zone, including all samples from this study, has higher $^{207}Pb/^{204}Pb$ values than lamprophyres from the Moldanubian Zone of the Bohemian Massif, indicating that there are regional differences in the Pb isotopic composition of the metasomatised mantle beneath different zones of the Variscan orogen.

3.4. Discussion

The most striking whole-rock geochemical features of orogenic (shoshonitic) lamprophyres are high contents of potassium and incompatible trace elements with Sr–Nd–Pb isotopic compositions reflecting the involvement of continental crust. These characteristics are coupled with whole rock Mg# and mantle compatible elements contents (e.g. Cr and Ni) that are sufficiently high to be in equilibrium with mantle peridotite. This hybrid nature results from the melting of a lithospheric mantle source contaminated by melts or fluids derived from subducted continental crust or crust-derived sediments (Peccerillo, 1999; Prelević *et al.*, 2008; Conticelli *et al.*, 2009; Leslie *et al.*, 2009; Soder *et al.*, 2016).

In contrast to subduction of oceanic lithosphere where serpentine and chlorite carry large amounts of water to mantle depths, subducted continental crust is relatively dry as water is essentially stored in hydrous phases like phengite or biotite (e.g. Hermann & Green, 2001; Schmidt *et al.*, 2004). Unlike in oceanic settings where dehydration of serpentinite, altered oceanic crust or mélange rocks induces fluid-fluxed melting in subducted sediments, significant partial melting in subducted continental crust will first take place at elevated temperatures due to breakdown of hydrous phases. Slab temperatures

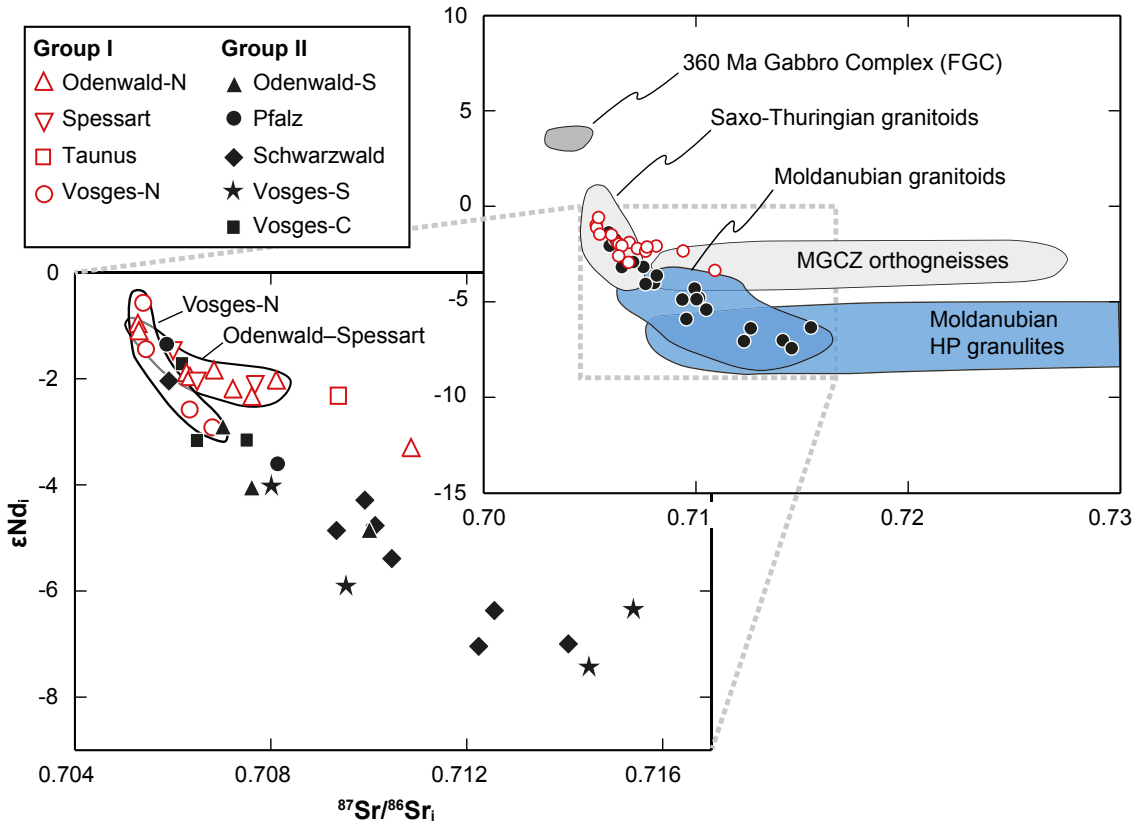

Fig. 3.7. Sr–Nd isotopic composition of lamprophyres were corrected for post-emplacement radiogenic growth based on an average age of 330 Ma (see geology section). Saxo-Thuringian and Moldanubian crustal fields are drawn for granitoids from Liew & Hofmann, 1988, Altherr *et al.*, 1999b, Altherr *et al.*, 1999a, Altherr *et al.*, 2000), Siebel *et al.*, 2012 and Tabaud *et al.*, 2015. Data for orthogneisses from the MGCZ are from Reischmann *et al.*, 2001. Data of Moldanubian HP granulites from the Bohemian Massif are from Becker *et al.*, 1999 and Janoušek *et al.*, 2004. HP granulites from the Vosges Mountains plot in the same range as the Moldanubian HP granulites (see Fig. 3 in Hasalová *et al.*, 2015). The 360 Ma old Frankenstein Gabbro Complex (FGC) of the northern Odenwald possibly represents the best estimate for the isotopic composition of the mantle prior to metasomatism by continental subduction. Group I lamprophyres from Vosges and Odenwald–Spessart area are outlined. The Taunus sample and one peralkaline minette from the Odenwald are outliers. Sample VO37 has an elevated Nb/U ratio and is characterised by the highest εNd value observed in this study. This is possibly related to the presence of an additional geochemical component derived from the convecting mantle, which is only documented in a subordinate amount of samples.

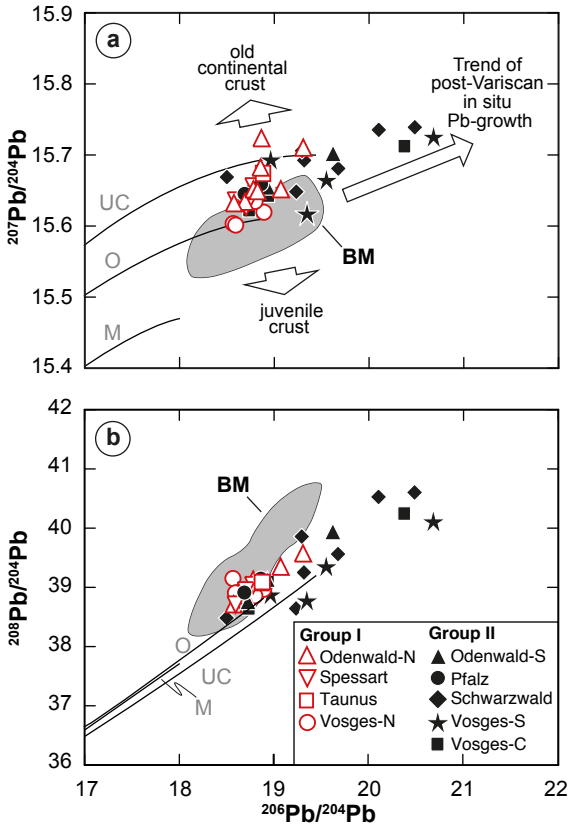

Fig. 3.8. The Pb isotopic composition of the lamprophyres is not corrected for post-emplacement ('in-situ') growth of Pb as several samples show significant overcorrection due to Pb loss relative to U and/or Th due to the formation of secondary minerals (Pb released during alteration is largely lost, whereas U and Th rather are adsorbed on Fe-oxyhydroxides, which results in higher U/Pb and Th/Pb ratios). Reference fields for lamprophyric dykes from the Bohemian Massif are given [covering lamprophyres from the Moldanubian Zone (Krmíček *et al.*, 2016) and the Saxo-Thuringian Zone (Abdelfadil *et al.*, 2014)]. Pb evolution curves for mantle (M), orogen (O) and upper crust (UC) from Zartman & Doe (1981).

during continental subduction in the Variscides may exceed 1000°C, which is documented within the Variscan belt by exhumed (U)HP–UHT metamorphic crustal rocks (e.g. Massonne, 2003; Kotková & Janák, 2015; Haifler & Kotková, 2016). Thus, subducted continental rocks locally were subjected to conditions exceeding phengite stability. Melts produced at high pressure by phengite dehydration may rise into the upper mantle above the subducting slab and there assimilate mantle material and metasomatize the ambient peridotite. Melts from the slab may rise to the crust or become completely consumed by metasomatic reactions in the mantle wedge. It is this metasomatised mantle that may melt during later events – such as post-collisional extension of the crust – to generate lamprophyric magmas.

The signatures of incompatible elements and the isotopic compositions of the lamprophyres reflect the material derived from the slab. Local differences in the composition of the subducted crust, therefore, are likely to be reflected in the incompatible element signature of these potassic melts. The transfer of material from the slab to potassic and ultrapotassic rocks that have been emplaced in the upper crust involves a series of processes that obliterate to some extent the original nature of the contributions from the subducted material. These processes include (i) material loss during progressive metamorphism of the subducted material, (ii) selective mobilisation from the slab, whereby the metasomatic agent and restite may show different incompatible element signatures and contrasting Sr, Nd, and Pb isotopic compositions, (iii) reactive melt transport into the lithospheric mantle with intense interaction with the peridotitic mantle to form mineralogically and chemically zoned veins within the lithospheric mantle, (iv) partial melting of sections of the veined mantle with variable assimilation of pyroxenitic and peridotitic mantle material, and (v) modification of these melts during fractional crystallisation, crustal assimilation, and later alteration. Note, metasomatism of the mantle and extraction of melts from the metasomatised lithospheric mantle may be related to different events that are widely separated in time and are related to different tectonic settings. As later processes may modify geochemical signatures acquired during earlier processes, the role of the various processes from the latest processes to the earliest ones are discussed in the following.

3.4.1. Fractional crystallisation, crustal contamination and alteration

Lamprophyres with low Mg# and low contents of mantle compatible elements do not represent primitive magma compositions but were modified by low-pressure processes such as fractional crystallisation or crustal assimilation. The strongly porphyritic nature of lamprophyres makes them sensitive to fractional crystallisation. High-Mg varieties of all petrographic lamprophyre groups show a crystallisation sequence starting with olivine containing minute inclusions of Cr-spinel, followed by clinopyroxene and finally phlogopite and/or amphibole. Some dykes, rich in phosphorus, (mostly minettes) additionally have phenocrysts of apatite. Fractional crystallisation of olivine, spinel and clinopyroxene is indicated by covariations between Mg# and Cr, Ni and Sc contents (e.g. Fig. 3.9). There is no geochemical indication for significant fractionation of amphibole, phlogopite or apatite. Feldspars do not form phenocryst phases. Negative Eu anomalies, which are

Table 3.2. Strontium and Nd isotopic composition of Variscan lamprophyres.

Sample	Region	$^{87}Sr/^{86}Sr$	$^{87}Sr/^{86}Sr_i$	$^{143}Nd/^{144}Nd$	$^{143}Nd/^{144}Nd_i$	εNd_i
Group I lamprophyres						
OD153B	Odenwald	0.709845±8	0.70684	0.512203±2	0.51202	-3.8
OD154	Odenwald	0.724709±7	0.71086	0.512262±6	0.51204	-3.3
OD169R	Odenwald	0.714681±5	0.70811	0.512327±6	0.51211	-2.0
OD175	Odenwald	0.713785±9	0.70722	0.512294±8	0.51210	-2.2
OD178	Odenwald	0.718006±6	0.70761	0.512293±4	0.51209	-2.3
OD043	Odenwald	0.707055±7	0.70528	0.512349±3	0.51216	-1.0
OD064	Odenwald	0.706322±7	0.70531	0.512386±4	0.51216	-1.1
OD151C	Odenwald	0.707766±3	0.70628	0.512310±2	0.51212	-1.9
OD156B	Odenwald	0.707798±3	0.70635	0.512315±3	0.51211	-2.0
SP12	Spessart	0.714355±8	0.70768	0.512297±4	0.51210	-2.1
SP15	Spessart	0.708091±6	0.70600	0.512363±7	0.51214	-1.5
SP19	Spessart	0.707852±5	0.70649	0.512306±3	0.51211	-2.0
TA01	Taunus	0.710476±3	0.70938	0.512295±5	0.51209	-2.3
VO86	N-Vosges	0.707850±5	0.70681	0.512246±3	0.51206	-2.9
VO33A	N-Vosges	0.705679±4	0.70545	0.512325±3	0.51214	-1.4
VO36	N-Vosges	0.707814±5	0.70634	0.512284±4	0.51208	-2.6
VO37	N-Vosges	0.707554±5	0.70539	0.512376±8	0.51218	-0.6
Group II lamprophyres						
OD152	Odenwald	0.709997±8	0.70702	0.512326±4	0.51206	-2.9
OD157B	Odenwald	0.717790±6	0.71001	0.512208±8	0.51196	-4.8
OD163	Odenwald	0.711949±8	0.70761	0.512276±3	0.51201	-4.0
PF01	Pfalz	0.712907±6	0.70814	0.512288±6	0.51203	-3.6
PF04	Pfalz	0.708332±7	0.70587	0.512372±5	0.51214	-1.3
SCH06	Schwarzwald	0.715629±9	0.71047	0.512227±3	0.51194	-5.4
SCH09	Schwarzwald	0.708423±8	0.70592	0.512336±2	0.51211	-2.0
SCH12	Schwarzwald	0.716534±4	0.71224	0.512130±5	0.51185	-7.0
SCH17	Schwarzwald	0.720344±9	0.71256	0.512182±4	0.51189	-6.4
SCH29	Schwarzwald	0.716851±6	0.71013	0.512208±6	0.51197	-4.8
SCH32A	Schwarzwald	0.712485±4	0.70992	0.512236±3	0.51199	-4.3
SCH38	Schwarzwald	0.713737±5	0.70934	0.512205±2	0.51196	-4.9
VO10	C-Vosges	0.710602±8	0.70751	0.512296±4	0.51205	-3.2
VO14	C-Vosges	0.709658±4	0.70649	0.512264±3	0.51205	-3.2
VO52	C-Vosges	0.711017±4	0.70619	0.512314±4	0.51213	-1.7
VO05	S-Vosges	0.719062±4	0.70953	0.512225±5	0.51191	-5.9
VO64B	S-Vosges	0.726743±8	0.71449	0.512174±5	0.51183	-7.4
VO66	S-Vosges	0.711987±8	0.70801	0.512291±4	0.51201	-4.0
VO83	S-Vosges	0.736281±4	0.71540	0.512181±3	0.51189	-6.3

$^{87}Sr/^{86}Sr_i$, $^{143}Nd/^{144}Nd_i$ and εNd_i were calculated for the emplacement age of 325 Ma using $\lambda^{87}Rb$= 1.3972E-11 y^{-1}, $\lambda^{147}Sm$ = 6.54E-12 y^{-1}, $(^{147}Sm/^{144}Nd)^0_{CHUR}$= 0.1967 and $(^{143}Nd/^{144}Nd)^0_{CHUR}$ = 0.512638, respectively.

Table 3.3. Lead isotopic composition of Variscan lamprophyres.

Sample	Region	$^{206}Pb/^{204}Pb$	$^{207}Pb/^{204}Pb$	$^{208}Pb/^{204}Pb$
Group I lamprophyres				
OD153B	Odenwald	19.069	15.652	39.349
OD154	Odenwald	18.864	15.724	39.114
OD169R	Odenwald	22.605	15.845	43.881
OD175	Odenwald	18.854	15.682	39.087
OD178	Odenwald	19.305	15.710	39.573
OD043	Odenwald	18.690	15.634	38.862
OD064	Odenwald	18.574	15.632	38.715
OD151C	Odenwald	18.780	15.652	39.132
OD156B	Odenwald	18.823	15.649	39.107
SP12	Spessart	18.594	15.636	38.709
SP15	Spessart	18.779	15.656	39.039
SP19	Spessart	18.703	15.627	38.949
TA01	Taunus	18.881	15.674	39.080
VO86	N-Vosges	18.566	15.603	39.149
VO33A	N-Vosges	18.890	15.619	38.967
VO36	N-Vosges	18.592	15.601	38.907
VO37	N-Vosges	18.797	15.635	38.857
Group II lamprophyres				
OD152	Odenwald	18.725	15.649	38.761
OD157B	Odenwald	19.620	15.702	39.941
OD163	Odenwald	18.929	15.655	39.137
PF01	Pfalz	18.860	15.659	39.147
PF04	Pfalz	18.686	15.645	38.912
SCH06	Schwarzwald	19.315	15.692	39.252
SCH09	Schwarzwald	19.675	15.681	39.562
SCH12	Schwarzwald	26.834	16.081	50.608
SCH17	Schwarzwald	20.483	15.739	40.603
SCH29	Schwarzwald	19.292	15.706	39.859
SCH32A	Schwarzwald	18.499	15.669	38.482
SCH38	Schwarzwald	20.103	15.735	40.527
VO10	C-Vosges	18.733	15.622	38.644
VO14	C-Vosges	18.936	15.643	39.090
VO52	C-Vosges	20.373	15.712	40.246
VO05	S-Vosges	20.681	15.726	40.117
VO64B	S-Vosges	18.962	15.694	38.882
VO66	S-Vosges	19.345	15.618	38.781
VO83	S-Vosges	19.550	15.665	39.357

especially prominent in Group II lamprophyres (Fig. 3.6c, Table 3.1), are interpreted to be inherited from the mantle source, as the lamprophyric melts originate from depth, exceeding the stability field of plagioclase in mantle and crustal rocks. Samples more strongly affected by fractional crystallisation (low Mg#) were excluded from the discussion of source signatures in cases trace element ratios sensitive to fractional crystallisation are used.

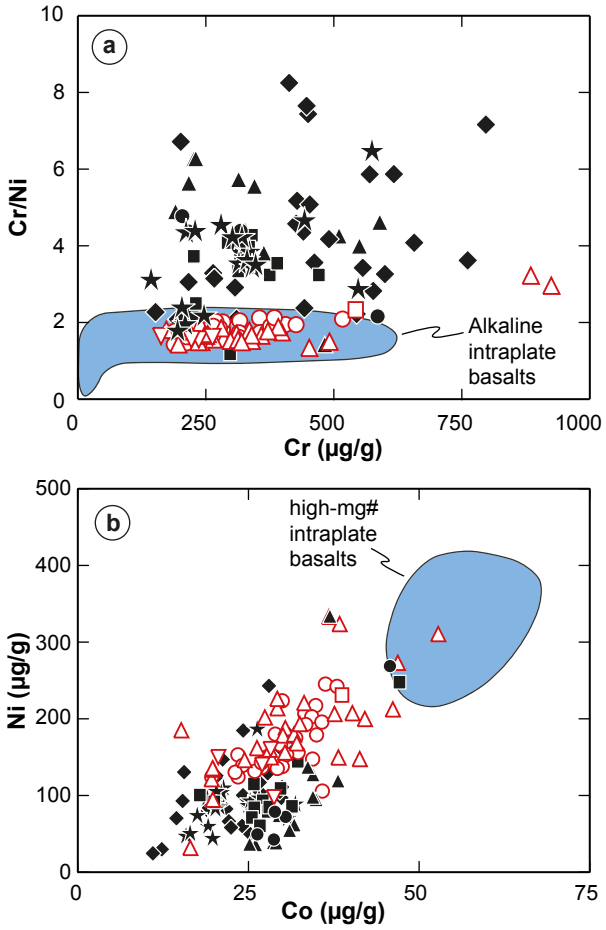

Fig. 3.9. Mantle-compatible elements of the lamprophyres are dominantly controlled by (1) low-pressure crystal fractionation of olivine and clinopyroxene and (2) the mineralogical composition of the mantle source. Data for intraplate basalt reference fields from Lustrino & Wilson (2007). Only samples with Mg# $\geq$ 69 used for reference field in (b).

Group I and Group II lamprophyres show striking differences in their Cr/Ni ratios. Group I lamprophyres show nearly constant Cr/Ni (Fig. 3.9a), unaffected by fractional crystallisation. Therefore, the ratio of olivine/spinel was constant in the course of crystal fractionation. This is possibly resulting from the coupled removal of olivine with inclusions of spinel, which are the major hosts of Ni and Cr, respectively. In contrast, Group II lamprophyres typically show high and variable Cr/Ni. These higher ratios are essen-

tially the result of lower Ni contents in Group II lamprophyres at similar Cr contents. A possible explanation is the removal of olivine prior to spinel crystallisation. For instance, decreasing f_{O_2} increases the Cr solubility of basaltic melts, thereby inhibiting the crystallisation of Cr-spinel (Roeder & Reynolds, 1991). The strong variability in Ni contents of high-MgO and high-Mg# samples, however, indicates that the variable Cr/Ni also may be inherited from the source, either in terms of heterogeneous source composition or as a result of the melting processes (see below).

Upper mantle and crustal xenoliths rarely occur in the lamprophyres studied. Dykes with xenoliths were excluded from this study. Every sample was investigated petrographically in thin section. Some dykes contain xenocrystic material (e.g., cpx-rimmed undulose quartz) indicating at least some crustal contamination. Assimilation of small amounts of crustal material, however, does not significantly change the trace element patterns of the lamprophyres due to their high primary incompatible trace element contents. Some composite dykes from the Schwarzwald with a porphyry granite core grading into lamprophyre margins may reflect hybridisation (Wimmenauer, 1972). Some Group II lamprophyres with a high Mg# (>70) are mesocratic with high SiO_2 contents and therefore lack olivine phenocrysts. In these dykes, clinopyroxene and phlogopite phenocrysts show normal zonation patterns and no signs of mingling and mixing with crustal melts. Therefore, some of the major element variability is interpret as 'primary' feature derived from melting of the metasomatically overprinted mantle.

Only samples with minimal visible secondary alteration were used for analysis. Fluid-mobile elements like Pb, Ba or Cs are preferentially stored in the feldspathic groundmass and may be mobilised during autometasomatism or secondary alteration. This is most clearly demonstrated by Pb and its isotopic composition: (i) Alteration of feldspar releases Pb, which may be redistributed by fluids and may account for the large scatter in Ce/Pb (0.26–43) and U/Pb (0.01–1.9) ratios. (ii) Alteration of feldspar makes U and Th (in inclusions and on defects) and Pb (in the crystal lattice) available for redistribution. The elements Th and U may be scavenged by Fe-oxyhydroxides or other secondary minerals, whereas Pb may be lost to some extent. Such a fractionation of Th and possibly U from Pb generates an open system and results in an overcorrection of in situ Pb growth (i.e., the calculated initial Pb isotopic composition yields too low values) if the alteration does not represent a late magmatic autometasomatic alteration, but reflects a much younger process. A few lamprophyre samples have low calculated initial $^{206}Pb/^{204}Pb$ values, which unequivocally demonstrates that these samples have been affected by late alteration, possibly during Jurassic–Early Cretaceous hydrothermal activity that affected the entire study area (e.g. Lippolt & Kirsch, 1994; Pfaff *et al.*, 2009 and references therein). The Pb isotopic composition is used as a highly sensitive tracer for fluid-mediated secondary alteration and do not use the concentrations of fluid-mobile elements like Pb, Ba or Cs for petrogenetic interpretation for samples that show anomalous calculated initial Pb isotopic compositions.

3.4.2. Metasomatism of the lithospheric mantle and later partial melting

There is a general understanding that orogenic lamprophyres and lamproites result from partial melting of metasomatically overprinted mantle lithologies rich in pyroxene and hydrous K-rich phases like phlogopite or K-richterite. These non-peridotitic lithologies are produced by the reaction between peridotitic mantle and melts and/or fluids released from the subducting slab and may form vein-like structures in the lithospheric mantle (e.g. Foley, 1992; Prelević *et al.*, 2008; Conticelli *et al.*, 2009). For instance, phlogopite-bearing pyroxenites, described from veined ultramafic xenoliths associated with subduction zone processes, have been interpreted to result from hybridisation between silicate melts released from subducted crust and peridotite (e.g. Ertan & Leeman, 1996; Grégoire *et al.*, 2001; Downes *et al.*, 2004; Bianchini *et al.*, 2011). Silica-rich melts are not in equilibrium with peridotite and will cause metasomatic crystallisation of pyroxene at the expense of olivine. Such reactions were successfully reproduced in hybridisation experiments between siliceous melts and peridotite (Sekine & Wyllie, 1982a; Sekine & Wyllie, 1982b; Sekine & Wyllie, 1982c; Sekine & Wyllie, 1983; Wyllie & Sekine, 1982; Wunder & Melzer, 2003; Pirard & Hermann, 2015; Mallik *et al.*, 2015; Mallik *et al.*, 2016). Complete consumption of these metasomatic liquids will result in the crystallisation of additional phases to accommodate the alkalis (e.g. Fumagalli *et al.*, 2009).

Later remelting preferentially mobilised such domains due to their lower solidus compared to ambient peridotite. The very high K_2O contents (up to 10 wt% K_2O) of some lamprophyres (minettes) clearly demonstrate the presence of a potassic phase in their source region, most likely phlogopite. The commonly high silica (SiO_2 >50 wt%) and low Al_2O_3 and CaO contents of ultrapotassic orogenic lamprophyres and lamproites reflect mantle sources enriched in orthopyroxene, which is in line with the proposed silicic melt–peridotite interaction process (e.g. Condamine & Médard, 2014). Mantle-compatible trace elements could provide information on the mineralogical composition of the source for rocks not affected by secondary processes like fractional crystallisation. For instance, the highly variable and elevated Cr/Ni of most Group II lamprophyres are reflecting deficiencies in Ni (Fig. 3.9), which seem to be related to mantle source processes rather than to fractional crystallisation (see below). If melts in equilibrium with olivine-rich mantle lithologies are buffered in Ni, elevated Cr/Ni ratios could be related to the lack of residual olivine. On the other hand, Group I lamprophyres and alkaline intraplate basalts that have constant Cr/Ni ratios at similar levels may be derived from a source with higher amounts of olivine, which is in line with the generally higher Co concentrations of these rocks (Fig. 3.9b).

Hybridisation experiments between peridotite and hydrous rhyolitic melt showed, that olivine is absent in experiments performed at low H_2O concentrations and higher pressures (3 GPa), but olivine forms in experiments performed at low-pressure runs (<2 GPa) or at high amounts of water independent of pressure (Mallik *et al.*, 2015; Mallik *et al.*, 2016). Thus, availability of H_2O may control the formation of olivine-rich and olivine-poor domains and eventually contribute to the difference between Group I and Group II lamprophyres. The availability of H_2O in turn may reflect the contrasting H_2O content of

subducted continental lithologies.

A second factor that may contribute to differences could be related to contrasting compositions of the metasomatic agents, causing variable vein paragenesis. For instance, the formation of olivine-rich domains may be related to the recycling of carbonate-bearing crustal material, as carbonate-rich liquids with low silica activity may react with orthopyroxene to form clinopyroxene and olivine (e.g. Ammannati *et al.*, 2016). Such a process might be involved in the source of lamprophyres from the N-Vosges that show low SiO_2 concentrations and high amounts of calcite disseminated within the matrix and in ocelli. Whatever caused these mineralogical heterogeneity of the lamprophyre source, it is likely to have contributed to the considerable major element variability even in lamprophyres without effects of fractional crystallisation (Mg# >70, 5–14 wt% MgO, or 45–64 wt% SiO_2; Fig. 3.5a).

Distinct petrographic lamprophyre varieties may be present within cogenetic dyke swarms ranging from spessartite, kersantite to minette with increasing K_2O content. The amount of K_2O is roughly positively correlated with many incompatible trace elements. Covariation between Sr–Nd isotope ratios and K_2O/Na_2O (Fig. 3.10a) or negative correlation of K_2O vs. Na_2O (Fig. 3.4b) reflect variable contributions from at least two reservoirs to both lamprophyre groups. High-K_2O/Na_2O melts are dominantly derived from melting of phlogopite-rich mantle lithologies, whereas the source of Na-rich and K-poor lamprophyres has higher contributions from the lithospheric peridotite, which is depleted with respect to incompatible element concentrations. The relative contribution of peridotite and the metasomatic assemblage to the melts is possibly controlled by the degree of melting. Higher degrees of melting could result in a stronger dilution of the metasomatic component due to fluxing of ambient peridotite (e.g. Foley, 1992). However, it is important to understand how the interaction process with the peridotite changes the geochemical signature of the metasomatic agents. Compared to porous flow, the extent of melt–peridotite interaction of channelised flow is limited (Pirard & Hermann, 2015). The formation of orthopyroxene-rich reaction walls causes little modification of the trace element pattern of the metasomatic melts, which may assimilate mantle-compatible elements like Mg, Fe, Ni, Cr or Co, but lowers the SiO_2 contents and increases the Mg# of the melts. The melts may finally freeze within the lithospheric mantle and form mineralogically and chemically zoned veins consisting of earlier-formed metasomatic rims and phlogopite–pyroxene-rich interiors. Initial melting of the veined lithospheric mantle mobilizes phlogopite-rich portions that crystallised from highly evolved residual melts, strongly enriched in incompatible elements and possibly peralkaline in composition. Higher contributions from wall-rock (phlogopite-poor) pyroxenites that crystallised from by-passing metasomatic melts are less enriched in crust-derived trace elements and should have more contributions from the ambient peridotite, resulting in less enriched, less K-rich lamprophyres. Thus, the apparent dilution the crustal trace element signature does not necessarily reflect the influence of the ambient mantle, but instead may reflect the melting of diverse hybridisation products created during channelised reactive transport of the slab-derived melts into the mantle wedge, which also may generate the observed spread in major and trace element and isotopic compositions. In other words, the influence of the ambient mantle was in-

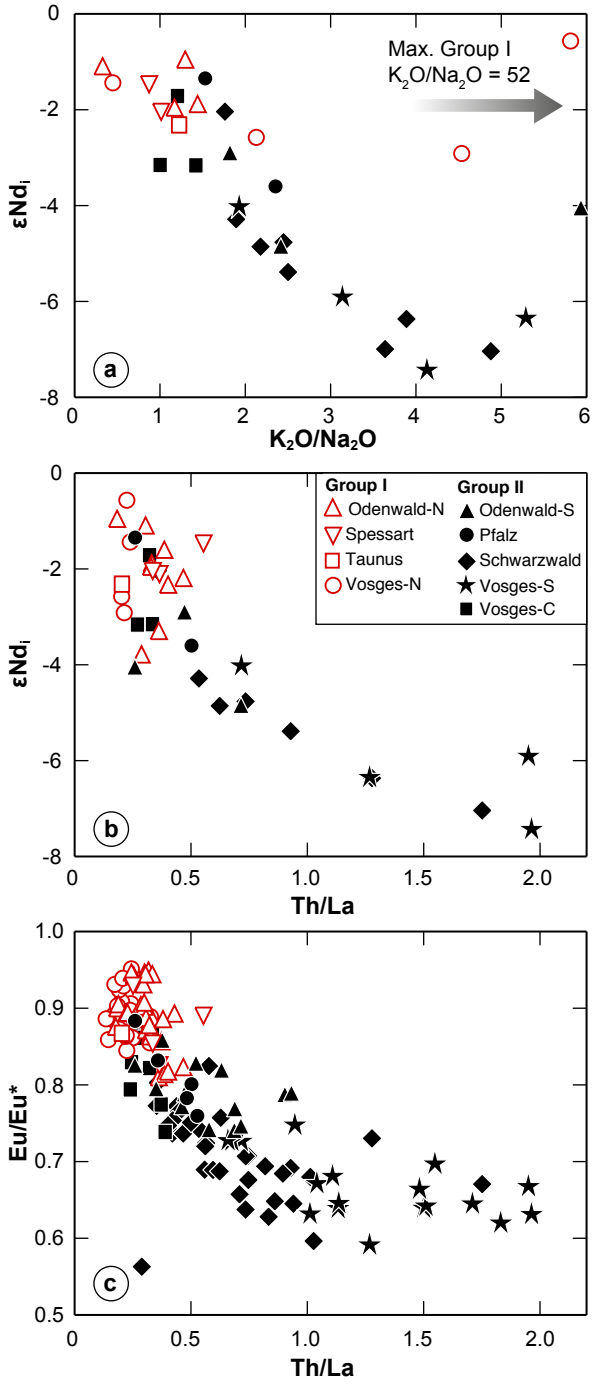

Fig. 3.10. Variations between Sr–Nd isotopic compositions and trace element ratios indicate mixing between source components: mantle peridotite and two distinct crust-derived hybrid metasomatic domains, in Group I and II lamprophyres, respectively. Mixing trends are pronounced in Group II lamprophyres due to end members with contrasting trace element signatures and isotopic compositions. Mixing trends for Group I lamprophyres are less obvious. This is basically due to a more evolved Sr–Nd isotopic composition of the Group II crustal endmember that furthermore has some distinctive trace element signatures, such as high Th/La, Sm/La or a marked negative Eu anomaly [$Eu/Eu^* = Eu_{cn}/Sm_{cn} \times Gd_{cn})^{0.5}$].

troduced during the formation of the metasomatic assemblages rather than during their mobilisation.

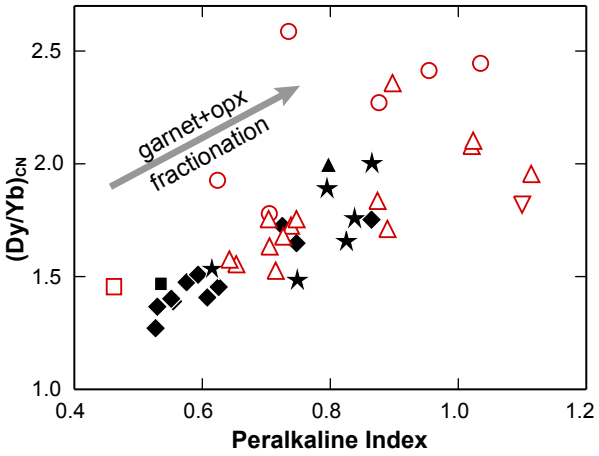

Fig. 3.11. Formation of orthopyroxene + garnet due to melt–peridotite interaction during channelised flow increases $(Dy/Yb)_{cn}$ and removes Al_2O_3 from the melt, thereby increases the Alumina Saturation Index (not shown) and the Peralkaline Index. Only samples with Mg# >70 are shown. Symbols used as in Fig. 3.10. Chondrite normalisation values (cn) are from McDonough & Sun (1995).

In a co-genetic dyke swarm, the most K-rich lamprophyres (minettes) form the crust-like Sr–Nd isotopic endmember (e.g. Owen, 2008; Fig. 3.10a) and, therefore, their Sr and Nd budget are dominated by the crustal component. Peralkaline compositions do, however, not represent the initial partial melts from continental crust (pelitic to greywacke in composition), as these have peraluminous to metaluminous compositions, independently whether they formed at low or ultrahigh-pressure (Auzanneau *et al.*, 2006; Hermann & Spandler, 2008; Stepanov *et al.*, 2016). Therefore, peralkalinity is likely a result of melt–peridotite interaction or partial melting of metasomatic domains. The products of hybridisation between silica-rich melt and ambient peridotite during channelised flow are orthopyroxene and garnet (e.g. Sekine & Wyllie, 1982b; Johnston & Wyllie, 1989; Rapp *et al.*, 1999; Malaspina *et al.*, 2006; Pirard & Hermann, 2015). Reactive transport through the lithospheric mantle may result in fractional crystallisation of orthopyroxene + garnet, which removes Al_2O_3 from the melts. Garnet fractionation additionally removes HREE and increases Dy/Yb, causes covariations between alkalinity and Dy/Yb (Fig. 3.11) and may result in peralkaline melt compositions. The peralkaline dykes are furthermore shifted away from the silicate differentiation line in the Nb/Ta–Zr/Hf space towards lower Zr/Hf ratios (Fig. 3.12). Both elements show partition coefficients for garnet ~ 1 and have $D_{Zr/Hf}>1$. Therefore, removal of garnet decreases Zr/Hf. The lowest observed Mn concentrations are present in peralkaline lamprophyres and are also attributed to garnet fractionation. A conceptual illustration of the vein-like metasomatic domain hosted within the lithospheric mantle is given in Fig. 3.13.

Peralkaline lamprophyres show extreme trace element enrichment, several times higher than average continental crust. Beside enrichment effects of the double-stage melting pro-

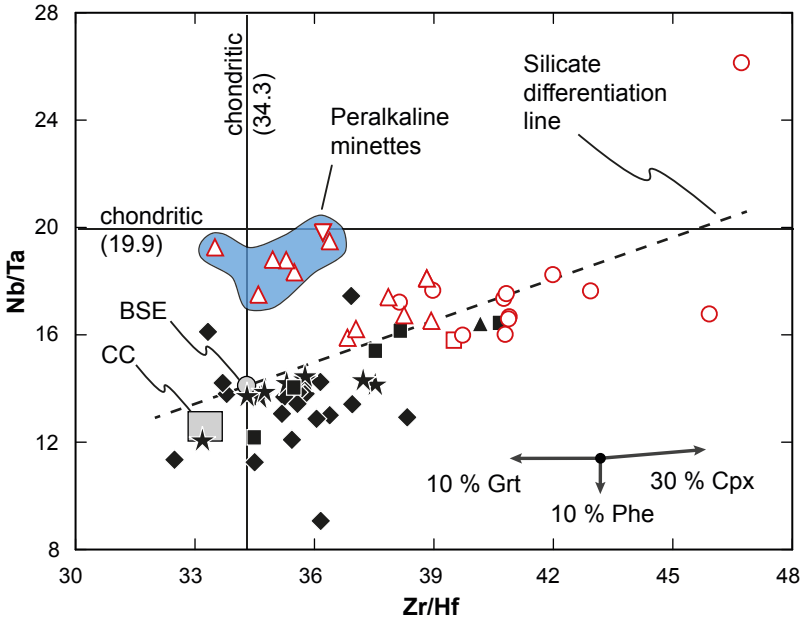

Fig. 3.12. The lamprophyres of Group I and II differ with respect to their Nb/Ta–Zr/Hf compositions (samples with Mg# <70 are excluded due to effect of cpx fractionation on Zr/Hf). The silicate differentiation line in the diagram is taken from Münker *et al.*, 2003 and indicates first order coupling of Nb/Ta–Zr/Hf due to fractionation of the silicate mantle by melting processes. The average composition of the continental crust (CC) is taken from Barth *et al.* (2000). Vector for garnet (Grt) is given to illustrate fractionation during melt–peridotite interaction with partition coefficients from Rubatto & Hermann (2007); 1000°C run). Vector for phengite (Phe) is given to illustrate the effect of buffering mica on Nb/Ta during partial melting of subducted continental crust (Stepanov & Hermann, 2013; 1000°C run). Rutile may counteract the decrease in Nb/Ta caused by fractionation of mica. However, the unknown primary composition of subducted crustal material hinders an evaluation of the respective process.

cess (melting of continental crust and melting of metasomatic mantle lithologies), wall-rock fractional crystallisation causes additional passive enrichment of most incompatible trace elements in the metasomatic melts. In general, the whole rock concentration of K_2O is roughly positively correlated with many incompatible trace elements. However, at very high K_2O and peralkaline compositions, a deviation from the linear trend observed for some trace elements (most pronounced for $HFSE^{4+}$) towards exceptionally high concentrations (Fig. 3.14a). Experimental studies show that solubility of $HFSE^{4+}$ strongly depends on peralkalinity (Watson, 1979; Watson & Harrison, 1983). Consequently, many incompatible trace element ratios are strongly fractionated in peralkaline lamprophyres, e.g. Hf/Sm, Zr/Nb or Lu/Hf (Fig. 3.14b). However, some chemical features could be either related to the protolith compositions or related to the process of partial melting of subducted continental crust.

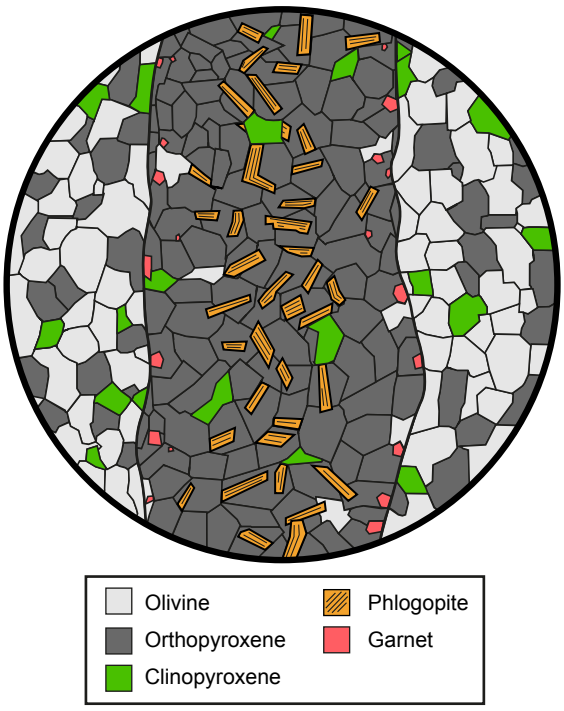

Fig. 3.13. Conceptual sketch of a vein-like metasomatic domain hosted within the lithospheric mantle. Garnet-orthopyroxene-rich reaction zones result from interaction between SiO_2-rich melts, originating in the subducted continental crust, and peridotite during channelised flow through the lithosphere.

3.4.3. (U)HP partial melting of continental crust

During thrusting into the mantle, the continental crust is affected by prograde metamorphism eventually resulting in partial melting due to the breakdown of hydrous phases like phengite or biotite (Schreyer *et al.*, 1987; Hermann & Green, 2001; Schmidt *et al.*, 2004, Stepanov *et al.*, 2014; Stepanov *et al.*, 2016). Corresponding hydrous silicate melts (or supercritical liquids) therefore have high K_2O/Na_2O ratios and are enriched in elements like K, Rb and Ba, that are predominantly hosted in mica. Whether the crustal trace element signature is transferred unchanged into these melts or not depends on the behaviour of accessory phases, which sequester important amounts of incompatible trace elements during partial melting. Residual phases may strongly influence the trace element inventory of the metasomatic melts released from the subducting slab. The high temperatures required for phengite dehydration melting during continental subduction may additionally result in partial or complete consumption of other trace element controlling accessory phases (e.g. Klimm *et al.*, 2008; Skora & Blundy, 2010; Stepanov *et al.*, 2012).

Striking differences concerning the Th–U–LREE characteristics are present between both lamprophyre groups. A distinctive feature of the crustal endmember of Group II lamprophyres is the depletion in LREE relative to similarly incompatible elements, resulting in a positive coupling between Sm/La and Th/La (Fig. 3.15a). Potential repositories of these elements in subducted lithologies are lawsonite, monazite and epidote-group

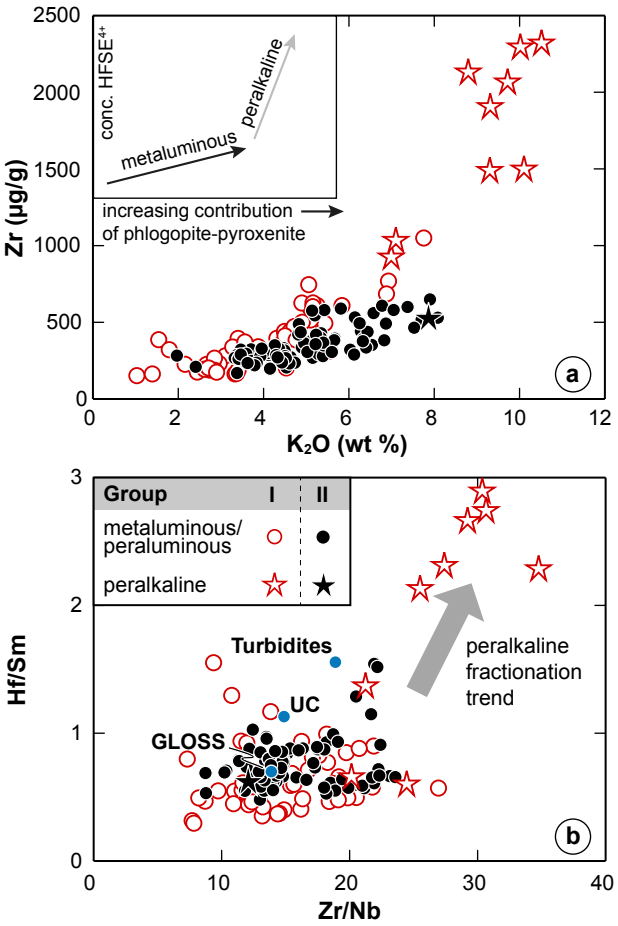

Fig. 3.14. Influence of metaluminous–peralkaline transition on geochemical trace element signatures observed in lamprophyres. (a) K_2O versus Zr of metaluminous and peralkaline lamprophyres from the study area. (b) Both Zr/Nb and Hf/Sm ratios are strongly affected by peralkaline melt fractionation. 'Average' turbidite (Prelević *et al.*, 2012 and references therein), upper continental crust (UC; Rudnick & Gao, 2003) and average global subducting sediment (GLOSS; Plank & Langmuir, 1998) are shown for comparison. Turbiditic continental-derived zircon-rich detritus has higher Zr/Nb and Hf/Sm compared to pelagic deep-sea sediments. Peralkaline dykes show fractionated pattern due to changing solubilities for HFSE (see text).

minerals (zoisite, epidote, allanite). Lawsonite and zoisite are restricted to cold subduction zones and may produce LREE-enriched fluids upon breakdown or, instead, stabilize allanite or monazite. According to experimental studies, both monazite and allanite incorporate Th in preference over U (Hermann, 2002; Klimm *et al.*, 2008; Hermann & Rubatto, 2009; Skora & Blundy, 2010; Stepanov *et al.*, 2012; Carter *et al.*, 2015). According to Stepanov *et al.*, 2012, monazite in granitic systems has $D_{\mathrm{Th/La}}$ >1. In contrast, allanite has $D_{\mathrm{Th/La}}$ and $D_{\mathrm{Sm/La}}$ <1 (Hermann, 2002; Klimm *et al.*, 2008). Thus, monazite and allanite define contrasting fractionation trends. The Sr content in Group II lamprophyres is lower than in Group I lamprophyres. This could be related to contrasting protolith chemistry or, alternatively, to residual allanite in the source of the metasomatic melts, as allanite is an important carrier of Sr in plagioclase- and titanite-free (U)HP rocks (e.g. Nagasaki & Enami, 1998).

Although the upper thermal stability of allanite depends on the LREE–Th budget of the rock, REE-rich epidote and allanite may be stable at phengite-breakdown melting conditions similar to conditions encountered by Variscan (U)HP granulites (at 1000°C, 4.0 and 5.0 GPa; 900°C, 3.0 GPa; e.g., Stepanov *et al.*, 2012). Tiny amounts of residual allanite during partial melting of the subducted crust may generate metasomatic melts with the features observed in Group II lamprophyres (Fig. 3.15). Such residual allanite could be obtained in metagranitoids or metagreywackes by a reaction that consumes REE-poor epidote to produce allanite and melt (Klimm *et al.*, 2008), whereas monazite rather would form in Ca-poor metapelites. Melts that formed with residual allanite will have reduced Th and LREE contents. If the stability of allanite is surpassed after such melts have been lost from the subducting slab, later melts may be strongly enriched in Th and LREE and markedly depleted in elements released during phengite breakdown. The absence of these trace element features in Group I lamprophyres reflects the absence or complete consumption of allanite during partial melting of continental crust.

The solubility of LREE-bearing accessories depends on melt composition (Montel, 1986; Klimm *et al.*, 2008), which is affected by the degree of melting, protolith composition and temperature, whereas the trace element contents of the protoliths control whether the melt may reach saturation in LREE. Possibly, the levels of LREE-enrichment or the degree of partial melting in the crustal protoliths for the metasomatic melt for Group I and Group II lamprophyres were different, resulting in complete or incomplete dissolution of allanite. For instance, the very high LREE and Sr concentrations and the exceptionally high Th/U ratios (max. Th/U $\sim$ 11) of Group I lamprophyres from the N-Vosges may reflect the complete dissolution of significant amounts of (residual) allanite.

The trace element pattern of all lamprophyres are characterised by negative Nb-Ta-Ti anomalies, reflecting both the composition of the subducted crustal protoliths and the nature of residual phases during partial melting. The budget of the $HFSE^{5+}$ in partial melts may be controlled by the stability of biotite and phengite in rocks having low TiO_2 and high K_2O contents and by Ti-oxides in rocks with high TiO_2 contents. Biotite and phengite have D_{Nb}>D_{Ta} and their presence during partial melting would lower Nb/Ta ratios in coexisting melts, whereas Ti-oxides would increase Nb/Ta (Stepanov & Hermann, 2013). Therefore, micas and Ti-oxides may account for contrasting signatures in coex-

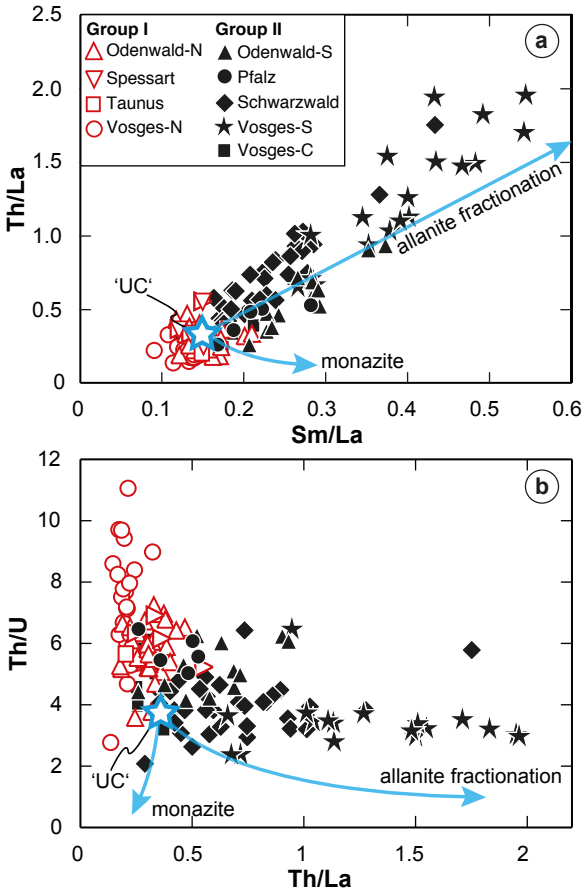

Fig. 3.15. LREE–Th–U systematics of the lamprophyres. Both allanite and monazite cause strong fractionations between La, Sm, Th and U. (a) Fractionation of small amounts of allanite during partial melting are assumed to explain the positive correlation between Sm/La and Th/La of Group II lamprophyres. The allanite fractionation vectors starting from the composition of average upper continental crust (UC) of Rudnick & Gao (2003) are calculated by Rayleigh fractionation with partition coefficients of Klimm *et al.*, 2008; run 19). Monazite also fractionates both ratios. Published monazite partition coefficients are not fully consistent (e.g. Hermann & Rubatto (2009); Skora & Blundy, 2010; Stepanov *et al.*, 2012) but dominantly show $D_{\mathrm{Th/La}}$ >1, as represented by the vector. (b) Allanite and monazite incorporate U in preference of Th.

isting melts. Thus, the low Nb/Ta values of Group II lamprophyres (below the silicate differentiation line in Fig. 3.12) might reflect to the buffering role of mica during crustal melting. The buffering role of micas is also reflected by fractionation of LIL elements.

Group I lamprophyres have systematically higher K/Rb ratios compared to Group II lamprophyres (310 $\pm$ 79 vs. 186 $\pm$ 35; 2σ SD; Fig. 3.16a). The average K/Rb ratio of Group I lamprophyres is in the range of average upper continental crust. The low and relatively constant K/Rb of Group II lamprophyres potentially are related to a mineralogically controlled fractionation process during lamprophyre petrogenesis. Group II lamprophyres additionally show higher Cs/Rb compared to Group I lamprophyres (Fig. 3.16b). Experimentally determined partition coefficients for mica indicate, that Cs is more incompatible than Rb and than K (e.g. Wunder & Melzer, 2003; Stepanov *et al.*, 2016). Therefore, the LILE systematics of Group II are in accordance with a buffering effect of mica during (U)HP anatexis. However, that the differences between Group I and II lamprophyres are inherited from the subducted lithologies undergoing partial melting (no mica buffering) cannot fully be rule out. In this case, The LILE systematics of Group II lamprophyres is indicative of a more strongly differentiated crustal composition.

3.4.4. Regional implications

Systematic sampling of lamprophyres across the tectonic zones of the Variscan orogen in the SW Germany and E France revealed to two fundamentally distinct crustal signatures hosted within the lithospheric mantle, resulting in two groups of lamprophyres. Though some spatial overlap between lamprophyres of both groups exists, Group I lamprophyres are primarily distributed across the northern (Saxo-Thuringian Zone/Mid-German Crystalline Zone; MGCZ) and those of Group II along southern (Moldanubian Zone) crustal segments. The Sr–Nd isotopic composition of the two groups resembles the local crust as represented by late Variscan hornblende-, biotite- and two-mica-granitoids, i.e. the MGCZ/Saxo-Thuringian Zone (Group I) and the Moldanubian Zone (Group II), respectively (Fig. 3.7). The MGCZ to the north of the Saxo-Thuringian Zone is interpreted to be the suture zone of the Rheic Ocean. The lower $^{87}Sr/^{86}Sr_i$ and higher εNd of the MGCZ are possibly related to rejuvenation of this crustal segment by the addition of mantle-derived melts along the Silurian to early Devonian magmatic arc (Franke, 2000). Orthogneissses with HP metamorphic history (Will & Schmädicke, 2001) from the eastern Odenwald are remnants of this magmatic arc and have Sr–Nd isotopic compositions similar to the crustal endmember of the Group I lamprophyres (Reischmann *et al.*, 2001; Fig. 3.7). Compared to Group I lamprophyres, sediments from the Rhenohercynian Zone and from the Saxo-Thuringian Zone show lower $\varepsilon Nd_{(340Ma)}$ (Küstner, 2000; Romer & Hahne, 2010). Group II lamprophyres overlap isotopically with Variscan felsic HP granulites. Consequently, the timing of mantle metasomatism for Group II lamprophyres is placed around 340 Ma (Schaltegger *et al.*, 1996; Schaltegger *et al.*, 1999). Such a scenario has been proposed for source enrichment of durbachites of the Bohemian Massif, that show close spatial and temporal relationships to HP granulites (Janoušek & Holub, 2007). The tectonic framework and timing of mantle metasomatism of the source of Group I lamprophyres is less

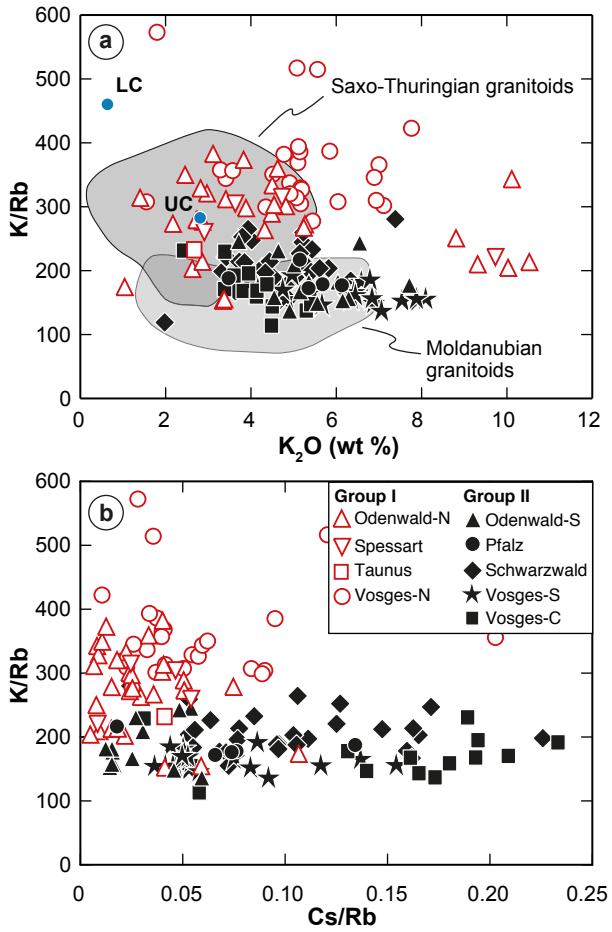

Fig. 3.16. LILE systematics of Group I and II lamprophyres. (a) The compositions of average upper continental crust (UC) and lower continental crust (LC) are from Rudnick & Gao, 2003. Reference fields are based on whole rock data of post-collisional granitoids from the study area (Henes-Klaiber, 1992; Altherr *et al.*, 1999b; Altherr *et al.*, 1999a; Altherr *et al.*, 2000; Tabaud *et al.*, 2014; Tabaud *et al.*, 2015). (b) Lamprophyres of Group II show scattered but on average higher Cs/Rb compared to those of Group I.

clear, as the MGCZ has a long-lived history and a wide range of different rocks may have been deeply subducted and produced melts that enriched the mantle wedge. The $\sim$ 360 Ma old calc-alkaline Frankenstein gabbroic complex in the northern Odenwald is interpreted to have originated from a depleted, subduction-modified mantle source (Altherr *et al.*, 1999a). The post-collisional lamprophyres exhibit a much stronger trace element-enrichment than the gabbros and distinctly more continental crust-like Sr–Nd isotopic compositions. This indicates that the lamprophyres and gabbros were derived from a different mantle source or metasomatism of the lamprophyre mantle source post-dated the extraction of the gabbros from the mantle. In the second case, mantle source contamination for Group I lamprophyres may be related to the final Variscan collision at c. 340 Ma, which reactivated crustal-scale boundaries as strike-slip zones (e.g., Kroner & Romer, 2013; Stephan *et al.*, 2016). Down-thrusting of crustal material or along transpressive fault zones also may result in metasomatism of the lithospheric mantle (Campbell *et al.*, 2014). Thus, the lithospheric mantle beneath the study area has been affected by material derived from at least two stages subduction. The subducting oceanic slab of the Rheic Ocean and by material derived from deeply subducted continental material.

A feature of the Variscan post-collisional evolution is the rare contribution of a geochemical signal derived from the convecting mantle to the mantle-derived magmatism. Asthenospheric contributions are common in post-collisional scenarios with on-going oceanic subduction, where rupturing and tearing of retreating slabs allows the incursion of the convecting mantle (Prelević *et al.*, 2012; Soder *et al.*, 2016). As a consequence of the retreating oceanic slab the asthenospheric contribution becomes spatially and temporally systematically more important and locally mantle-derived magmatism even may show a transition from K-dominated rocks to Na-dominated rocks. Instead post-collisional magmatism in the Variscan orogen was related to repeated decompression due to regional extension, which is the result of post-collisional reorganisation of the plate movement and concomitantly the regional stress-field (cf. Kroner & Romer, 2013) that culminated in the development of the Permian Oslo Rift and Permian volcano-sedimentary basins in Variscan Europe (Wilson *et al.*, 2004). Subordinate asthenospheric input is possibly related to lithosphere-scale strike-slip tectonics allowing limited incursion of the convecting mantle.

3.5. Conclusions

Post-collisional mantle-derived magmatism is widespread across the internal parts of the Variscan belt where a large number of dominantly potassic–ultrapotassic lamprophyre dykes were emplaced during the final stages of the orogeny and later periods of regional extension. The detailed whole-rock Sr–Nd–Pb isotopic and trace element data set gives insights into the multi-stage process of mantle-source enrichment.

1. Systematic sampling across various tectonic zones revealed geochemically and isotopically distinct lamprophyre groups, related to downthrusting of crustal rocks with contrasting compositions into the mantle.

2. Exhumed Variscan (U)HP crustal segments demonstrate that crustal rocks had been subducted to mantle depth and reached temperatures sufficient for dehydration melting of phengite (and possibly biotite). The trace element signature of partial melts released from the subducted continental crust may be strongly affected by the stability of phases that sequester particular groups of trace elements and thereby control the trace element budget of the subducted crustal material. Group II lamprophyres show high Th/La, Sm/La and low Th/U ratios that may reflect stable residual allanite in the subducted crustal rocks, whereas reduced Nb/Ta, Rb/Cs and K/Rb may be related to the buffering role of mica during partial melting.

3. Interaction between granitic melts derived from deeply subducted continental crust and mantle peridotite causes hybrid reaction zones, rich in orthopyroxene and phlogopite that are hosted within the lithospheric mantle. Compatible trace elements suggest that Group II lamprophyres dominantly are derived from melting olivine-poor/-free metasomatic mantle lithologies and that these melts did not react extensively with the ambient mantle.

4. Formation of orthopyroxene + garnet during melt–peridotite interaction increases Dy/Yb, decreases Zr/Hf and removes Al from the melt, eventually resulting in peralkaline compositions. Peralkalinity changes solubility of $HFSE^{4+}$ in the melt, eventually resulting in selective enrichment of $HFSE^{4+}$.

The chemical composition of lamprophyres gives insights into the process of recycling of deeply subducted continental crust in collision zones. Regional variation in part are related to the nature and source of the subducted continental material, in part to the conditions of partial melting and the nature of residual phases that may uncouple groups of incompatible trace element from each other.

4. Crustal xenoliths in post-collisional Variscan lamprophyres: records of continental collision and orogenic extension

4.1. Introduction

During orogenesis, the lithosphere is affected by a massive chemical and physical disturbance. In the course of continental subduction and collision, upper continental lithologies are deeply buried to lower crustal depth or are juxtaposed against hot mantle peridotite. Downthrusted felsic lithologies may undergo partial melting, causing weakening and providing a lubrication for rapid tectonic exhumation. Alternatively, a density reduction compared to the average upper crust, caused by decompression melting and melt extraction, may result in a relamination at the base of the crust (Hacker *et al.*, 2011). Consequently, felsic lithologies may have a significant contribution to the composition of the lower crust.

The processing of the lower crust, however, is difficult to study. Outcrops of high-grade metamorphic rocks exposed in the course of collisional tectonics may provide valuable information. However, these units are usually affected by significant recrystallisation and overprinting during their exhumation. Instead, xenoliths erupted from high-pressure settings may provide direct insights into the deeper reaches of the orogen. During and after continental collision, considerable amounts of granitoids are emplaced. This is usually accompanied by volumetrically subordinate (ultra)potassic mantle-derived magmatism. Following the peak of the orogeny, extensional forces, supported by the weakening effect of partial melting, cause the thickened crust to return to stable conditions. Extension also affects the underlying mantle lithosphere, resulting in 'cleansing' of contaminated (metasomatised) portions, thereby triggering the generation of K-rich lamprophyres (see Chapter 3). These mantle-derived melts may entrain xenoliths that record a snapshot of processes coevally operating in the crust and, at best, provide a full profile through the lithosphere.

In this study, lower crustal xenoliths entrained in post-collisional lamprophyres from the Variscan orogen were investigated. Samples were taken in the Mid-German Crystalline Zone (MGCZ). Although this structural zone hosts the Rheic suture, which is the principal oceanic suture of the Variscan orogen (e.g. Zeh & Gerdes, 2010), surprisingly little is known about its metamorphic evolution. High-pressure xenoliths found in the crystalline Odenwald record the processing of continental crust during orogenesis under eclogite-facies conditions. Further, the xenoliths are partly characterised by chemical and textural disequilibria, providing information on the crystallisation, melting and deformation conditions in the deeper reaches of a collisional belt.

4.2. Geological setting

The crystalline Odenwald is part of the Mid-German Crystalline Zone (MGCZ) of the Variscan orogen (Fig. 4.1). The MGCZ is positioned at the northern margin of the Saxothuringian Zone and is bordered to the north by low- to non-metamorphic sedimentary and volcanic rocks of the Northern Phyllite Zone and the Rhenohercynian Zone. The Variscan collisional belt resulted from the convergence between Laurussia and Gondwana during the closure of the Rheic Ocean in Devonian to Carboniferous times, finally leading to the assembly of Pangaea (e.g. Kroner & Romer, 2013; Franke *et al.*, 2017 and references therein). The obscured Rheic suture is hosted by the MGCZ (Zeh & Gerdes, 2010).

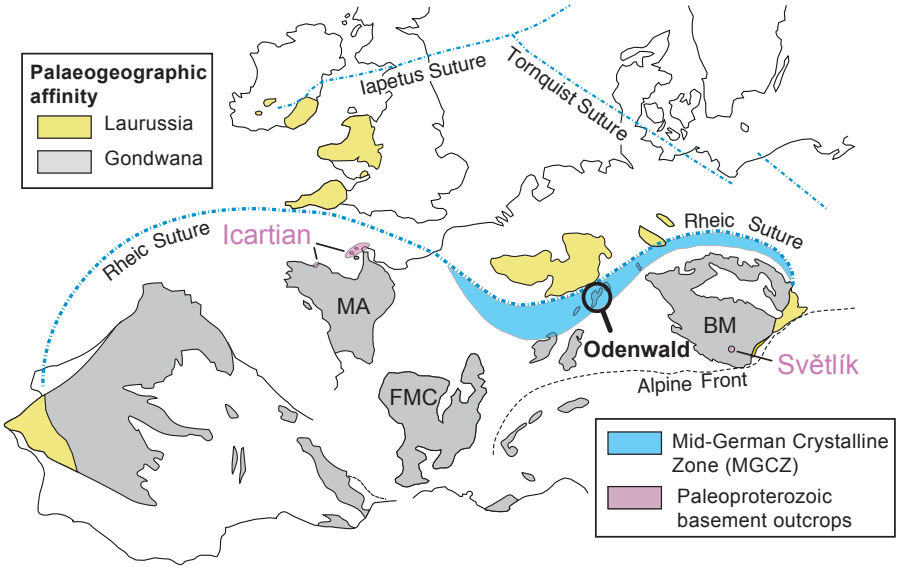

Fig. 4.1. Map showing the exposed Variscan basement of Europe, palaeogeographic affinities of crustal domains and the location of the Rheic suture zone (after Linnemann *et al.*, 2007; Franke, 2000). Rare occurrences of Paleoproterozoic basement outcrops are indicated. BM = Bohemian Massif, FMC = French Massif Central, MA = Massif Armoricain.

The Odenwald Crystalline Complex is composed of two distinct structural units. The eastern part ('Böllsteiner Odenwald'), is composed of an antiformal orthogneiss, surrounded by greenschist to lower amphibolite-facies metasedimentary lithologies (e.g. Altenberger & Besch, 1993; Dörr *et al.*, 2017). Silurian/Early Devonian protolith ages are reported for the orthogneisses (Reischmann *et al.*, 2001). Some meta-basic intercalations show amphibolite-facies parageneses but preserve relicts of an eclogite-facies metamorphic event of possible Devonian age (Will & Schmädicke, 2001, 2003 and references therein).

This western part ('Bergsträßer Odenwald') is tectonically juxtaposed against the eastern segment and is dominated by calc-alkaline granitoid plutons, dated around 340–330 Ma, and a gabbro complex emplaced at ∼360 Ma (Altherr *et al.*, 1999a; Kirsch *et al.*,

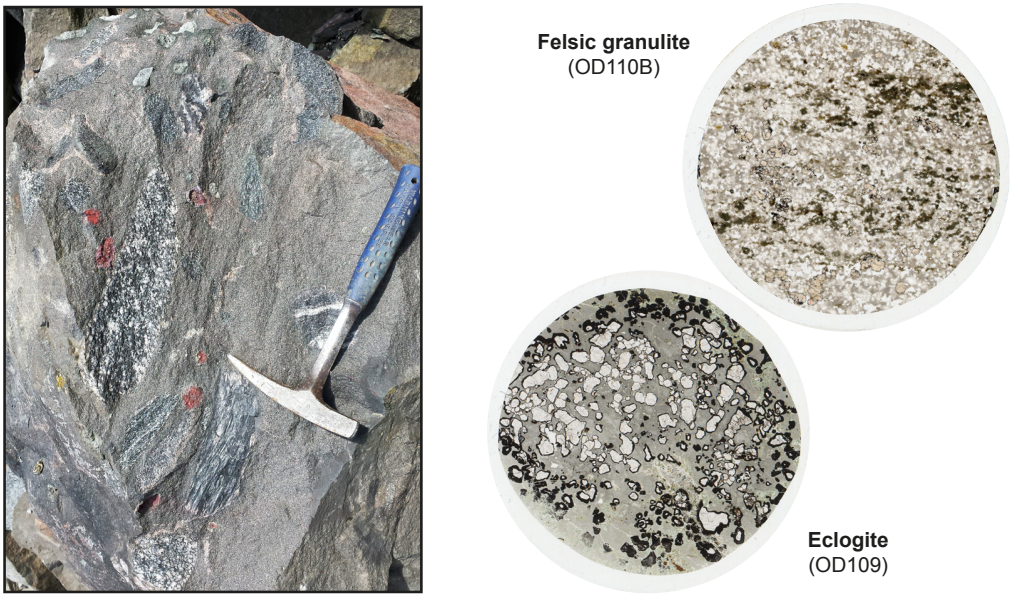

Fig. 4.2. Left: Outcrop photograph showing a block of lamprophyre (quarry Sonderbach, Heppenheim; Röhrig Granit GmbH; N 49° 37' 56.91" E 8° 41' 44.54") with abundant crust- and upper mantle-derived xenoliths, as well as inclusions of probable cognate origin. All xenoliths are affected by autometasomatic alteration to a variable degree. For instance, olivine-rich xenoliths (dunites) are transformed to Cr-spinel-bearing talc-rich lithologies (dark-red portions). Right: Thin sections (Ø 2.5 cm) of samples investigated in this study. The opaque, extremely fine-grained kelyphite rims around garnet in the eclogite sample are more strongly developed towards the host magma (until complete replacement), giving clear evidence for a breakdown during uprise in the lamprophyre melt. Please note the irregular shape and heterogeneous grain-size distribution of garnet in both lithologies.

1988). Subordinate metamorphic rocks bordering the intrusives record a low- to medium-pressure metamorphic event at high temperatures (Willner *et al.*, 1991; Okrusch, 1995; Todt *et al.*, 1995; Will & Schmädicke, 2003). Emplacement of the granitoids has been related to syn- to post-collisional tectonics between ~340–333 Ma. Metamorphic evidence for a Carboniferous high-pressure event in the MGCZ, documenting subduction or collision, is missing. However, the geochemistry of some intrusives is indicative of marked crustal thickening (Altherr *et al.*, 1999a).

Post-collisional, mantle-derived potassic–ultrapotassic magmatism is a typical feature of the internal parts of the Variscan orogen. Lamprophyre dykes are part of this magmatism and are particularly abundant across the crystalline basement of the Odenwald (cf. Fig. 3.1 in Chapter 3). The age of lamprophyre magmatism in the Odenwald–Spessart area is dated around 330–320 Ma (Hess & Schmidt, 1989; von Seckendorff *et al.*, 2004). The xenoliths discussed in this study were taken from a lamprophyre dyke cutting the Weschnitz pluton (Fig. 4.2), a quartz-bearing biotite-hornblende monzodiorite to granodiorite containing numerous metric to decimetric mafic enclaves of quartz dioritic to quartz monzodioritic compositions (Altherr *et al.*, 1999a). The lamprophyre is biotite- and amphibole-phyric and petrographically classified as kersantite, locally grading into

spessartite. High Mg# and high contents of Cr and Ni are indicative of near-primitive melt composition and little fractional crystallisation during uprise (see analyses of chemically closely related, though, uncontaminated samples OD25/OD27 from the same quarry given in Table C.2). The dykes are of variable thickness, ranging from a few centimetres to 2 m. The amount of xenolithic material varies and may reach up to one third of the dykes' volume. The xenoliths range in size from < 1 cm to ∼50 cm. The larger xenoliths are crustal lithologies, comprising gneisses, amphibolites, gabbros and granitoids. The smaller fragments usually have rounded shapes and comprise retrograde eclogites, felsic and basic granulites, phl-clinopyroxenites, phl-orthopyroxenites, hornblendites and strongly altered olivine-rich lithologies.

4.3. Petrography

Two xenolith samples were investigated in detail. A retrogressed eclogite (OD109) and a felsic granulite (OD110) measure 7 cm and 15 cm in diameter, respectively. Both high-pressure (HP) metamorphic lithologies show granoblastic to porphyroblastic textures with garnet crystals of up to 3 mm in size (Fig. 4.2). Additionally, both samples show strong signs of retrogression. As discussed below, three metamorphic stages can be distinguished: (i) peak conditions in the eclogite facies, (ii) a short-lived overprint, possibly related to decompression in the course of crustal thinning and (iii) retrogression during transport in the mantle-derived volatile-rich host magma. The latter caused complex replacement textures involving plenty of mineral phases. It is important to distinguish between the secondary (pyrometamorphic) processes and the primary features of the rocks. Secondary features are more intensely developed along the xenoliths margins but decrease towards the center of the xenolith, such as the development of kelyphite rims around garnet (Fig. 4.2). A summary of the metamorphic evolutionary stages is given in Table 4.1.

Table 4.1. Samples investigated in this study.

Sample	**Rock type**	**Stage I** **Peak assemblage**	**Stage II** **Short-lived overprint**	**Stage III** **Pyrometamorphism***
OD110	Felsic granulite	Grt, Qtz, Afs, Plg, Bt, Omp, Rt, Aln, Zrn, **melt**	Omp+Plg symplectites Grt, Bt(?)	Cpx, Bt, Fsp, Spl, Ilm, Ttn, melt
OD109	Retrogressed eclogite	Grt, Omp, Ky, Rt, Czo, Qtz, Phe, Ap, Zrn	Grt, Omp, Plg, Amp, Qtz, Rt, Spl, Czo(?), **melt**	Spr, Pgt, Cpx, Fsp, Bt, Spl, Amp, Ilm, Ttn, melt

*Phases are present in symplectites and local sub-systems.
Mineral abbreviations: Afs, alkali feldspar; Aln, alanite; Amp, Amphibole; Ap, apatite; Bt, biotite; Czo, clinozoisite; Grt, garnet; Ilm, ilmenite; Phe, phengite; Pgt, pigeonite; Plg, plagioclase; Qtz, quartz; Rt, rutile; Spl, spinel; Spr, sapphirine; Ttn, titanite; Omp, omphacite; Zrn, zircon.

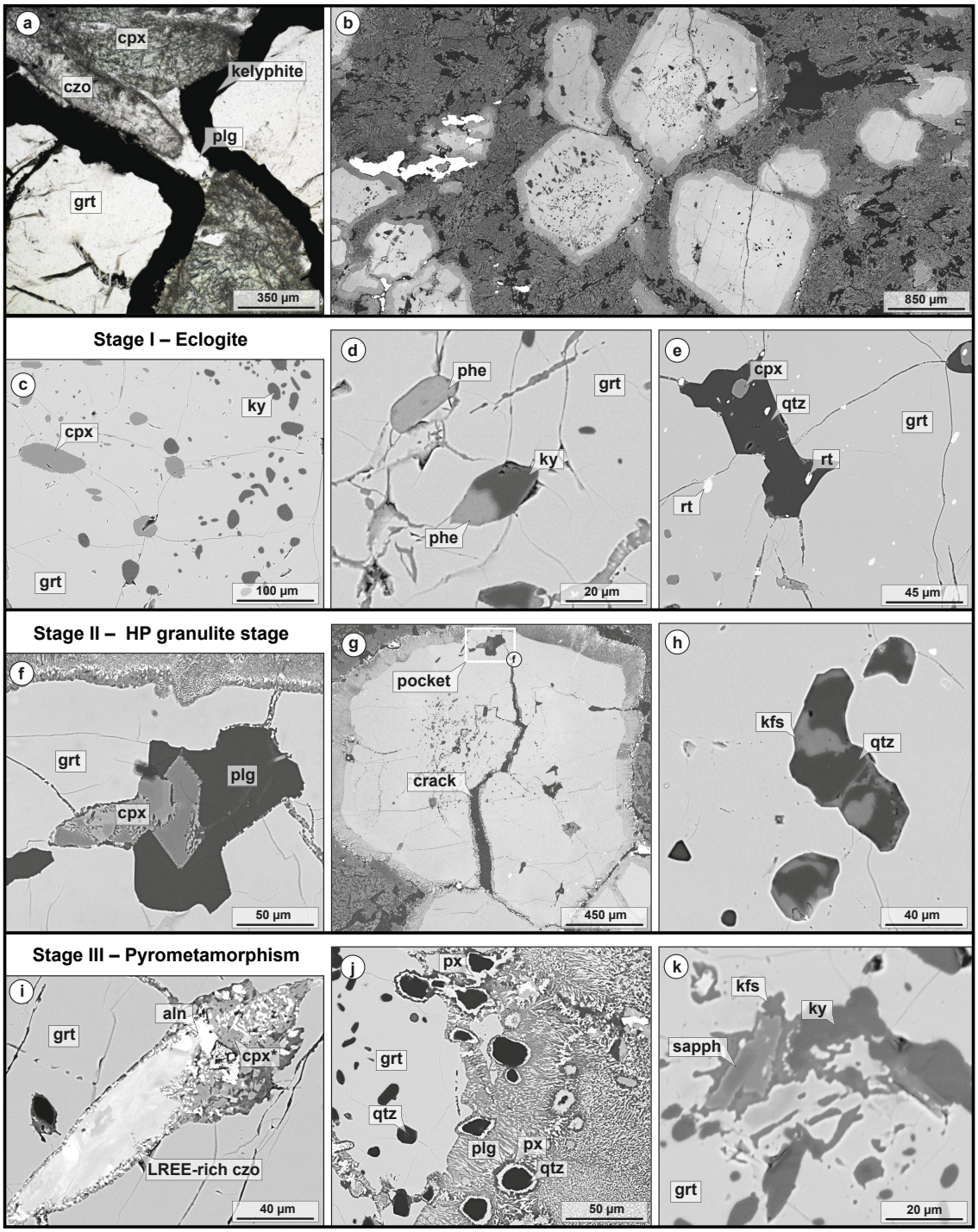

Fig. 4.3. Some characteristic petrographic features outlining the polymetamorphic history of the retrogressed eclogite are shown in a–k. (a) Photomicrograph of xenolith (plane-polarised light) with garnet and pseudomorphs after clinozoisite (Czo) and Omphacite (Cpx). (b) Garnet crystals with abundant inclusions hosted within a matrix dominated by symplectites of clinopyroxene and plagioclase (former omphacite). (c–e) Eclogite assemblage preserved as inclusions in garnet (phe, phengite; ky, kyanite; grt, garnet; qtz, quartz; rt, rutile). (f, g) Stage II paragenesis filling cracks and pockets of garnet. (h) The rock contains subordinate amounts of phengite that breaks down to K-feldspar and quartz. (i–k) Various subsystems develop during Stage III (pyrometamorphism). LREE-rich clinozoisite (czo) is replaced by near-endmember Ca-tschermak's pyroxene and allanite (i). Garnet + quartz react to pigeonite + plagioclase (j). Inclusions consisting of phengite + kyanite in garnet are transformed to sapphirine + k-feldspar (k).

4.3.1. Retrogressed eclogite

Eclogite stage Garnet porphyroblasts in the metabasic xenoliths are rich in minute inclusions. These provide evidence for an eclogite-facies peak metamorphic paragenesis (stage I) (Fig. 4.3c–e), among which kyanite and omphacite are most common. Furthermore, quartz, rutile, (partly LREE-enriched) clinozoisite and, more rarely, phengite are present. Although the matrix is nearly completely retrogressed, textural relicts of the eclogite-facies paragenesis are preserved. The garnet porphyroblasts are embedded in a matrix dominated by pseudomorphs after large omphacite grains. Except for some relict cores, these are mostly transformed to symplectites consisting of secondary clinopyroxene and plagioclase. Some pseudomorphs consisting of fine-grained secondary phases replace oriented, prismatic, in part LREE-enriched clinozoisite. Additionally, quartz, rutile (rimmed by ilmenite) and apatite occur (Fig. 4.3a,b).

Short-lived overprint Prior (unrelated) to entrainment into the lamprophyre magma, the eclogite was overprinted in the presence of a K-poor melt phase. The latter crystallised along grain boundaries and cracks crossing stage I mineral phases. This second mineral assemblage comprises garnet, omphacite, plagioclase, amphibole, rutile, quartz and possibly epidote (stage II paragenesis). Na-rich plagioclase (oligoclase) is present along the grain boundaries of omphacite and garnet and fills cracks crossing garnet grains (Fig. 4.3g). Garnet in contact to plagioclase seems to be resorbed and may show marginal patchy zonation patterns. Stage II minerals along garnet cracks and in melt pockets may show euhedral crystals faces (Fig. 4.3f). Due to the Na-rich plagioclase-bearing assemblage containing omphacite but lacking orthopyroxene and the presence of only minor amounts of hydrous phases, this stage is referred to as the high-pressure (HP) granulite stage (e. g. O'Brien & Rötzler, 2003). Phengite did not form during overprinting of the eclogite. Phengite inclusions in garnet partly show decomposition. However, this is most probably related to pyrometamorphism (see below).

Pyrometamorphism Additionally, a plethora of fine-grained reaction textures is present. The development of these features is related to the pyrometamorphic overprint within the mantle-derived lamprophyre magma. The assignment to this stage is based on textural relationships to the host magma and phase stabilities. Several types and generations of reaction textures can be identified. Their mineralogy basically depends on the local subsystem (the primary phases replaced) as well as the changing P–T conditions during uprise and cooling of the host magma. These structures can be briefly summarised as follows: Omphacite is replaced by symplectites of clinopyroxene and plagioclase with small amounts of amphibole. Garnet I/II is marginally replaced by (a) coarse-grained spinel + plagioclase + clinopyroxene ± garnet, (b) spinel + plagioclase + clinopyroxene + pigeonite ± amphibole, (c) submicron-sized kelyphite (plagioclase + spinel + orthopyroxene/pigeonite) which appears opaque in transmitted light due to the fine-grained nature, (d) subordinate chlorite related to fluid exsolution during autometasomatism of the lamprophyre. The coarse-grained assemblage partly shows euhedral crystal shapes and

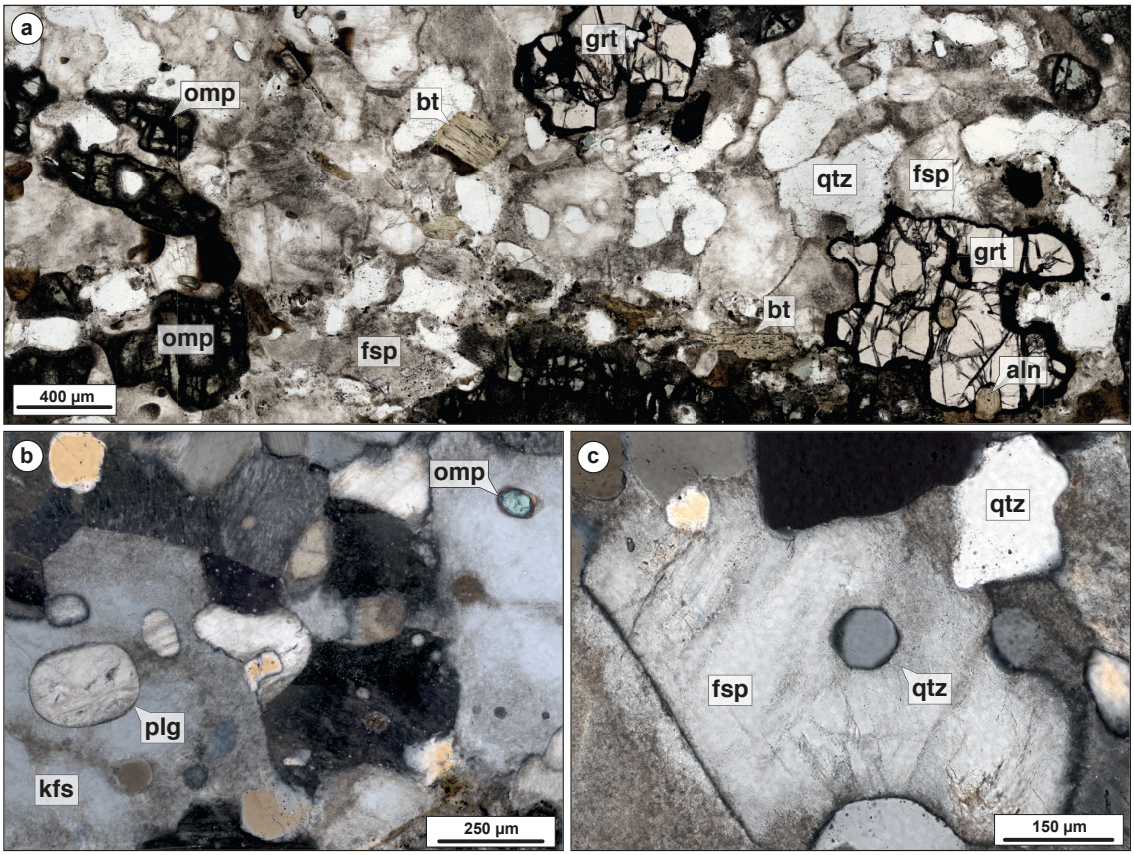

Fig. 4.4. Photomicrographs of felsic granulite in plane-polarised (a) and crossed-polarised light (b,c). (a) Large garnet and omphacite grains are embedded in a biotite-bearing, quartzofeldspathic matrix. The garnet crystal to the lower right contains several large grains of allanite. Metamictisation causes radial fractures in enclosing garnet. The cloudy appearance of some grains is related to partial decomposition of feldspar. (b) Large K-feldspar grains enclosing plagioclase and omphacite. (c) Feldspar with inclusion of euhedral quartz (marked with blue arrow) and small angle grain boundaries (red arrow) are indicative for crystallisation from a melt.

preferentially forms 'pockets' between contacting garnet grains. This assemblage probably indicates crystallisation from a melt. Garnet and its mineral inclusions may form several secondary subsystems:

- Quartz is rimmed by pigeonite and plagioclase. This reaction texture may result from the pressure-sensitive reaction garnet + quartz → pigeonite + plagioclase. (Fig. 4.3j).
- Kyanite is replaced by spinel, plagioclase and sometimes sapphirine. The coexistence of sapphirine with K-feldspar indicates that phengite breakdown is related to the appearance of sapphirine (Fig. 4.3k).
- LREE-enriched clinozoisite reacts to strongly subsilicic clinopyroxene (calcium tschermak's pyroxene) and allanite (Fig. 4.3i). The subsilicic clinopyroxene may

later be retrogressed to secondary epidote. Some pseudomorphs after clinozoisite within the matrix additionally contain grossular.

- Garnet inclusions with negative crystal shapes consisting of quartz and K-feldspar (Fig. 4.3h) are indicative of in-situ breakdown of phengite (cf. Liu *et al.*, 2013). This is supported by a common association with preserved phengite or partly decomposed grains. Alternatively, phengite dehydration could have already occurred during metamorphic stage II.

4.3.2. Felsic granulite

Similar to the eclogite, the felsic granulite is also retrogressed, yet it preserves relatively abundant relicts of the peak assemblage consisting of garnet, quartz, K-feldspar, plagioclase, omphacite, biotite, rutile and (metamict) allanite. Zircon and apatite occur as accessory phases. The xenolith is medium grained and shows a weakly developed gneissic texture due to omphacite-rich layers. Quartzofelspathic domains have isotropic fabrics and contain isometric to irregularly shaped garnet crystals (Fig. 4.2, 4.4a). Some textural features suggest the presence of partial melt during crystallisation of the peak assemblage (though less obvious compared to stage II in the eclogite). Abundant small angle grain boundaries are indicative for partial melting, as subsolidus recrystallisation tends to form triple junctions (120° angles). Further, crystallisation in the presence of a melt phase favours development of euhedral crystal shapes, as observed for quartz or biotite, for instance (Fig. 4.4).

Compared to the eclogite, a metamorphic overprint of the peak assemblage, unrelated to pyrometamorphism, is less obvious. However, some features could be related to regional processes rather than pyrometamorphism. Secondary jadeite-bearing clinopyroxenes are present in relatively coarse grained symplectites replacing stage I omphacite. These textures could be related to crystallisation of stage I melt. Garnet at some places shows marginal replacement caused by dissolution/reprecipitation.

The coarse-grained symplectites are succeeded by a second generation of more fine-grained intergrowths of plagioclase and clinopyroxene. These are more intensely developed towards the xenolith margin and related to pyrometamorphism. Garnet is rimmed by fine-grained symplectites of variable thickness similar to those in the garnet-bearing metabasic xenoliths. Plagioclase and alkali feldspar are replaced by fine-grained intergrowths of secondary feldspar minerals and biotite shows dark rims. Rutile is rimmed by ilmenite (and may contain fine ilmenite lamellae), sometimes followed by a rim of titanite.

4.4. Mineral chemistry

Garnet in the retrogressed eclogite Millimeter-sized garnet porphyroblasts formed during the eclogite stage. Apparent 'prograde' zonation is indicated by increasing Mg and decreasing Mn, Fe^{2+} and Ca content towards the rim (Fig. 4.6). While garnet is

Table 4.2. Whole-rock compositions (wt %) of xenolith samples.

	OD110B Felsic granulite		OD109 Eclogite
	XRF	model*	XRF
SiO_2	67.45	67.45	49.39
TiO_2	0.56	0.56	0.80
Al_2O_3	13.76	13.76	15.00
Fe_2O_3	4.15	0.21	9.95
FeO	n. d.	3.64	n. d.
MnO	0.10	–	0.15
MgO	2.39	2.39	8.81
CaO	2.53	2.46	11.34
Na_2O	3.43	3.43	2.52
K_2O	4.32	4.32	1.01
P_2O_5	0.19	–	0.12
LOI	1.21	0.50	0.81
Sum	100.09	98.73	99.90

Analyses given in wt%. LOI = loss on ignition.
*used for thermodynamic modelling

concentrically zoned in Ca, the elements Mg, Fe^{2+} and Mn show marked sector zonation. The trivalent cations Al and Fe^{3+} do not show any zonation trend. Please note that nicely developed and sectioned examples such as the one presented in Fig. 4.5 are rarely found in the sample. This is related to the large grain size of garnet, the development of irregular crystal shapes as well as the partly severe overprinting during stage II and III.

The second generation of garnet developed during stage II. Although garnet is dominantly consumed during this metamorphic stage, some new garnet formed at the expense of garnet I. Garnet II compositions are found along an outer rim or along fractures crossing the porphyroblasts (Fig. 4.3g). While some garnet I is unaffected by recrystallisation, others are extensively transformed. The patchy and schlieren-like zonation patterns, as well as sharp interfaces between garnet II and garnet I, argue for a dissolution/reprecipitation process (e.g. Hames & Menard (1993); Erambert & Austrheim, 1993; Putnis, 2002; Feenstra *et al.*, 2007). The irregular replacement of garnet I suggests recrystallisation due to interaction with a fluid phase. Most probably this was a melt phase migrating along grain boundaries and newly formed cracks. The composition of garnet II is characterised by a marked drop in the grossular content (<20, mostly ∼15 mol% Grs; Fig. 4.7) compared to garnet I. Either, Ca was transported away for plagioclase formation, or the introduction of a melt phase caused metasomatic alteration resulting in different garnet compositions.

During early (high-pressure) pyrometamorphism rare, newly formed garnet is characterised by high Mg# (Fig. 4.7). Additionally, Ca-rich garnet is formed in proximity to clinozoisite breakdown domains. Some garnet grains contain melt pockets formed during pyrometamorphism. Such grains commonly are metasomatically altered, showing patchy structures. During low-pressure pyrometamorphism, garnet is replaced by kelyphite. Secondary grossular (X_{Grs}>0.9) is present in large pseudomorphs after clinozoisite in the rock matrix. It is unclear, whether it formed during stage II or III.

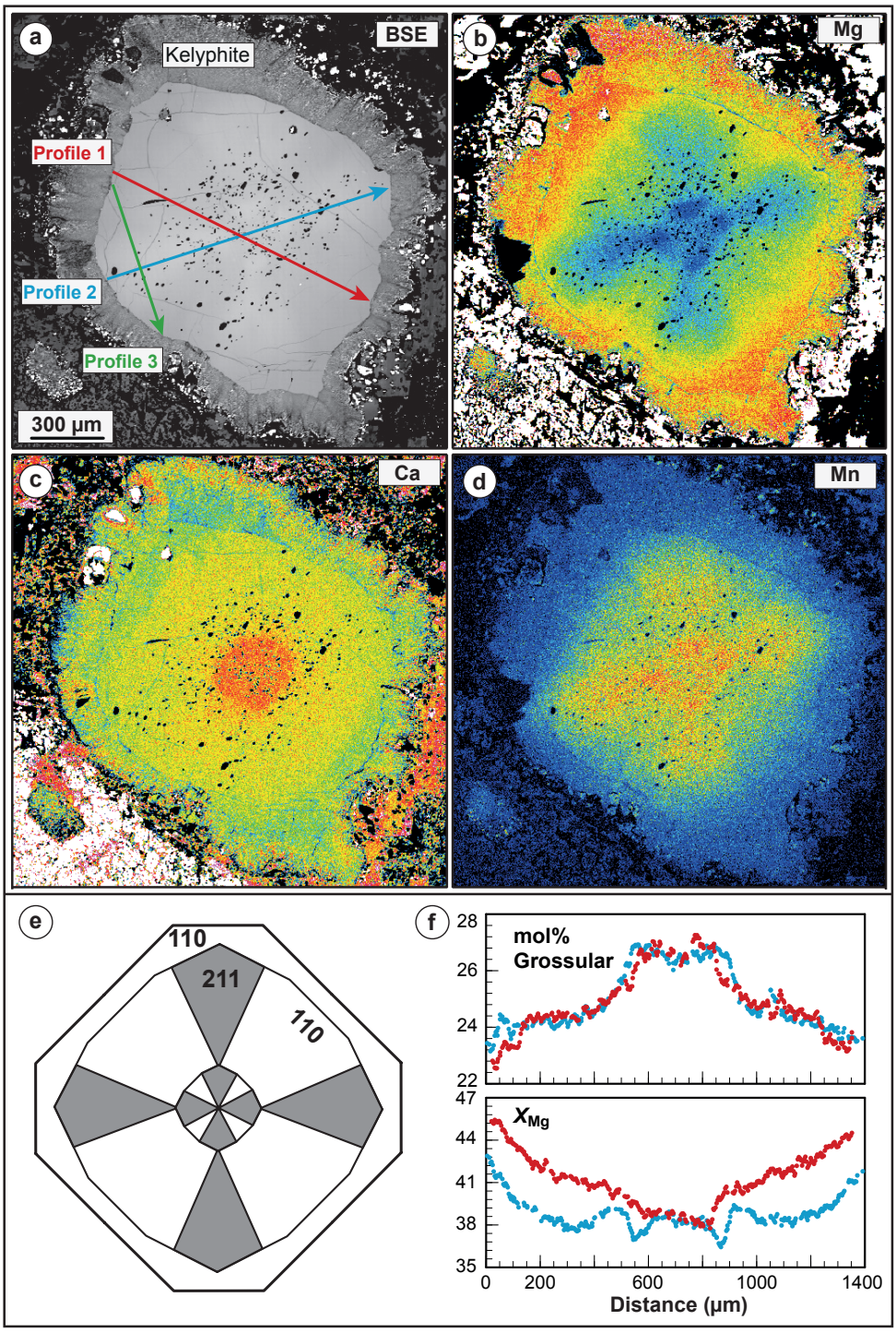

Fig. 4.5. (a–d) Microprobe element distribution (X-ray) maps of a sector zoned garnet in the eclogite (OD109) for Mg (b), Ca (c) and Mn (d) as well as a BSE image (a). The dark spots in garnet are tiny inclusions of kyanite. (e) Conceptual sketch of the sector-zoned garnet, showing the two growth generations. The presence of distinct crystal faces during rapid growth is necessary for the development of compositional sector zonation. The {110} crystal faces are clearly indicated by external morphology, whereas presence of {211} is very likely but not proven (by morphology or electron backscatter diffraction, for instance). (f). Comparison of concentration profiles across both sectors.

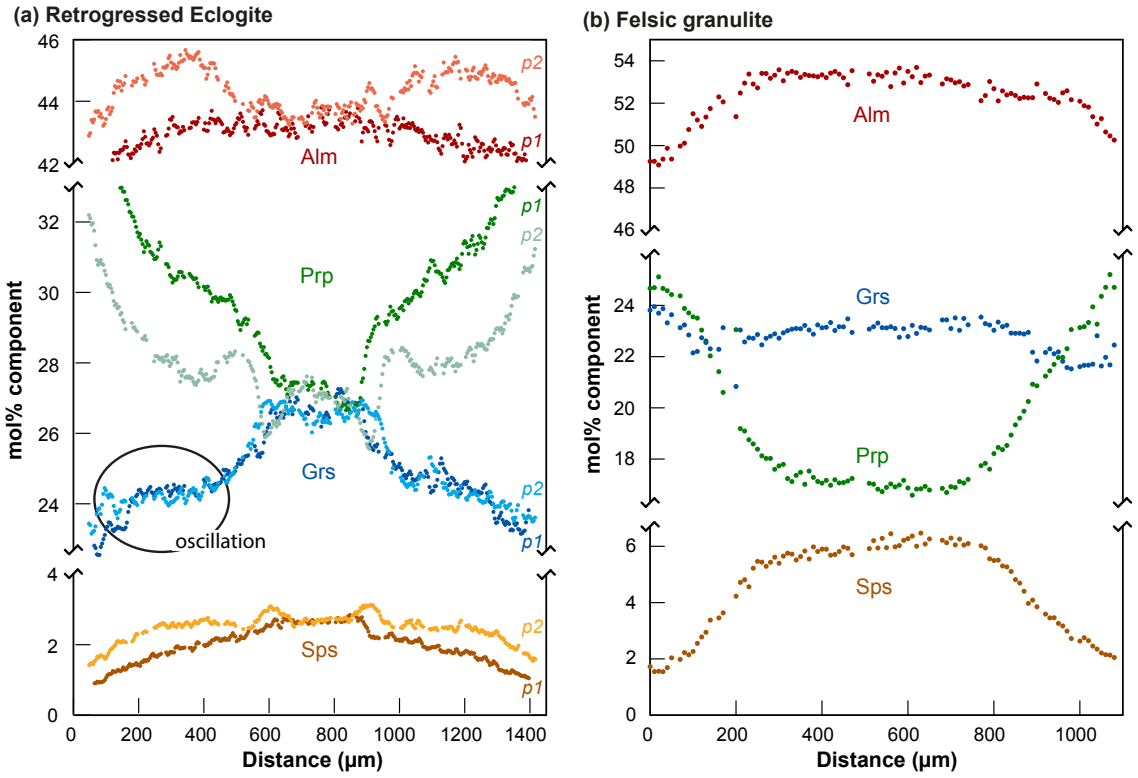

Fig. 4.6. Compositional profile across sector zoned garnet in the eclogite (sample OD109; profile position p1 and p2 shown in Fig. 4.5) and across garnet of the felsic granulite (sample OD110). Garnet of the felsic granulite has an older, initially unzoned core overgrowth by a rim with distinct composition. Incipient diffusion between both regions causes the observed concentration gradient. In contrast, smaller garnet grains without core have flat concentration patterns (not shown).

Garnet in the felsic granulite Garnet in the felsic granulite is characterised by irregular crystal shapes (Fig. 4.2). Larger grains preserve a chemical zonation having plateau-like cores enriched in Mn (5.0–6.5 mole% spessartine) and an overgrowth rim with less Mn (1.0–2.8 mole% Sps). Core regions are characterised by Mg# = 23.9–26.5, while rims and smaller grains have Mg# = 29.5–35.5. Cores and rims have similar grossular content. Core regions are homogeneous with 22.5–23.5 mole% grossular. On average, the rims have very similar grossular content but show some scatter with an overall range of 21.0–26.0 mole% (Fig. 4.6, 4.7). The cores and the rims preserve flat concentration pattern, with (limited) diffusional relaxation between the domains. Smaller garnet without older cores have flat patterns, as they are not influenced by diffusional influx from the interiors.

Clinopyroxene Clinopyroxene crystallised during all three stages in both lithologies (Fig. 4.8a,b). Stage I omphacite in the felsic granulite is characterised by 0.42–0.38 apfu Na (apfu = atoms per formula unit), which corresponds to Jd_{33-30}. A considerable amount of ferric iron (Fe^{3+}) is indicated by structural formula calculation (14–36 % of total Fe, Table D.5). Stage II clinopyroxene (Jd_{14}) is present in coarse symplectites, followed by

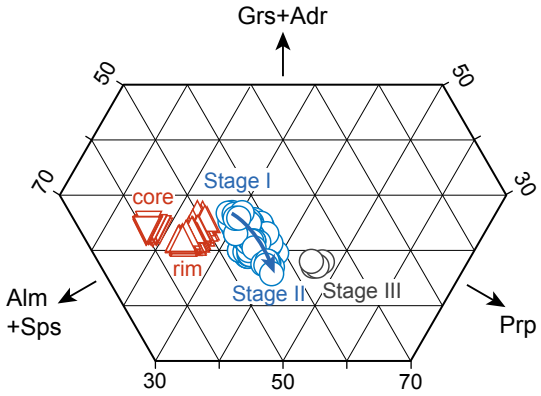

Fig. 4.7. Garnet compositions in eclogite (circles) and felsic granulite (triangles).

fine-grained (stage III) symplectic clinopyroxene free of Jd. Stage I omphacite in the eclogite has 0.43–0.35 apfu Na corresponding to Jd_{39-29} (Table D.6). Some rare, small omphacite inclusions in garnet have up to 0.52 apfu Na. During stage II, a second omphacite generation coexisting with plagioclase develops and has $\leq$ 0.35 apfu Na ($Jd_{\leq 30}$). Omphacite I grains may be marginally adjusted towards omphacite II compositions, resulting in the more-or-less compositional continuum of omphacite I–II in Fig. 4.8a.

During pyrometamorphism (stage III), omphacite I and II is replaced by symplectites consisting of plagioclase and clinopyroxene ($Jd_{<10}$). Additionally, a large spectrum of other clinopyroxene compositions developed during stage III. For instance, clinopyroxene in proximity to garnet has higher amounts of hedenbergite–ferrosilite component. Pigeonite (together with plagioclase) replaces the paragenesis garnet + quartz. Pyroxene rich in Ca-tschermaks component (up to 70 % CATS) is present in pseudomorphs replacing clinozoisite.

Epidote-group minerals Garnet of the eclogite contains primary inclusions of clinozoisite (X_{Czo}=0.82–0.88, Table D.10). Some grains show enrichment in LREE (ΣLREE up to 8 wt%). During pyrometamorphism, these grains may be replaced by allanite + sub-silicic clinopyroxene (Fig. 4.3i). Additionally, secondary clinozoisite–epidote forms during late-stage metasomatism by the lamprophyre.

Mica Biotite in the felsic granulite is part of the peak assemblage. It is chemically homogeneous with TiO_2 concentrations of around 4 wt% and Mg# ~0.66. It is marginally replaced by biotite with variable, but on average higher TiO_2 and lower Mg# (Table D.8).

Phengite is present in small amounts as inclusions in stage I garnet of the retrogressed eclogite. It is characterised by very high celadonite contents with 3.51–3.70 Si apfu (Table D.8). Cation sums on the octahedral position are in excess of 2 with $\Sigma_{Y-pos.}$ = 2.07–2.12, assuming only ferrous iron (with Mg# of 58–75). Excess remains even for formula calculations taking only ferric iron, implying that some solution towards trioctahedral

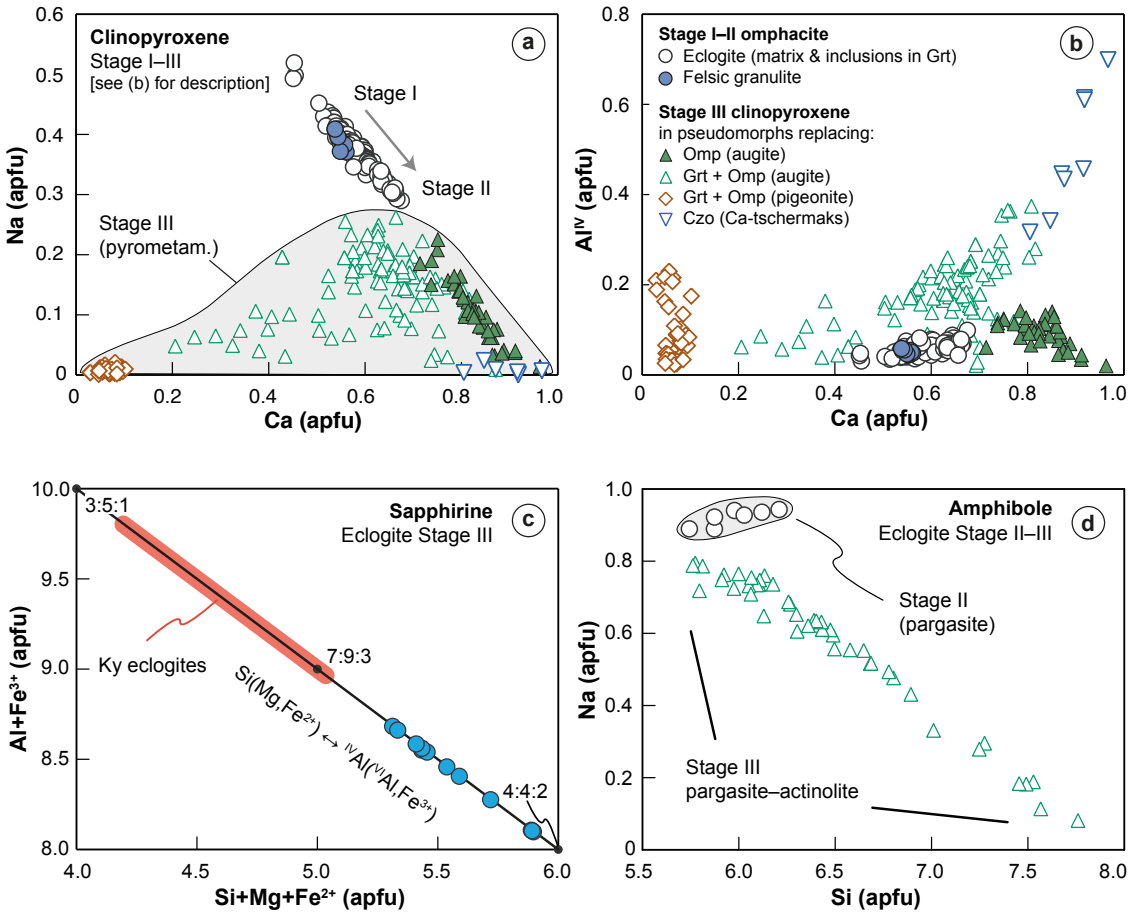

Fig. 4.8. Composition clinopyroxene (a, b) in eclogite and felsic granulite and composition of sapphirine (c) and amphibole (d) of in the retrogressed eclogite.

mica is present. Some of these phengites are affected by chloritisation during late-stage metasomatism by the lamprophyre.

Rutile Rutile grains in both lithologies were measured for their Zr concentrations, which revealed to be very homogeneous. Average values are 385±47 µg/g (2σ SD; n = 18) and 998±103 µg/g (2σ SD; n = 18) for the eclogite and felsic granulite, respectively (see also Fig. 4.9). Rutile belongs to stage I paragenesis. Some grains within the eclogite are situated within the stage II assemblage. These show similar Zr concentrations compared to grains in contact to stage I paragenesis.

Amphibole Amphibole is present in minor amounts during stage II and stage III within the retrogressed eclogite (Fig. 4.8d; Table D.10). Stage II amphibole is chemically relatively homogeneous and corresponds to pargasite and magnesiohastingsite according to Hawthorne *et al.* (2012). Amphibole III is chemically heterogeneous and corresponds to

pargasite, edenite, magnesiohornblende and actinolite. It may replace symplectic intergrowths of clinopyroxene and plagioclase formed during stage III. Further, it crystallises from aluminous melt pools (together with spinel and felspar).

Feldspar In the felsic granulite, two chemically homogeneous feldspars are present during stage I. K-feldspar and plagioclase have the composition $Or_{64-65}Ab_{33-34}An_{1.5-2.0}$ and $Ab_{79}An_{12}Or_9$, respectively (Fig. 4.9b, Table D.9). In the eclogite, plagioclase appears during stage II (HP granulite stage) and has the composition $Ab_{78-83}An_{15-19}Or_{2-4}$ (Fig. 4.9b). K-feldspar is present in small amounts during stage II as a product of phengite breakdown (Fig. 4.3h) and has near endmember composition ($Or_{>99}$). Both lithologies contain plagioclase (and K-feldspar) during stage III that occurs in various symplectites and crystallises from small melt pools. It is chemically heterogeneous with the general formula $Ab_{76-43}An_{21-55}Or_{1-6}$. Fe concentration is lower in stage II plagioclase ($\sim$0.2 wt% Fe_2O_3) compared to stage III plagioclase (0.4–0.8 wt% Fe_2O_3). Both feldspars show marginal to complete replacement by secondary feldspar compositions, while relict grains are very homogeneous in composition.

Spinel The eclogite contains spinel replacing kyanite and euhedral octahedrons in melt pockets between garnet grains. Spinel has high amounts of hercynite–spinel, and shows, as the analyses suggest, a considerable solubility towards the magnetite-magnesioferrite series with $Fe^{3+}/(Fe^{3+}+Al)$ of 0.15–0.35 (Table D.11). It is characterised by Mg# = 22–59. Minor elements (given in wt% of the oxide) are ZnO ($\leq$0.35), NiO ($\leq$0.2), MnO (0.3–1.0), Cr_2O_3 ($\leq$1.0) and TiO_2 (0.1–1.2). This spinel grains show commonly a marginal to complete replacement by fine-grained lamellar intergrowths (possibly exsolution of magnetite).

Sapphirine Tiny grains of sapphirine (<50 μm) are present as inclusions within embayed and chemically modified garnet. The composition ranges between the 7:9:3 and 4:4:2 endmembers of sapphirine with 1.646–1.937 apfu Si (Fig. 4.8c and Table D.11). The grains show chemical zonation with a core-to-rim decrease of the Mg# (86–76). Sapphirine is surrounded by Kfs that again occurs in proximity to kyanite (Fig. 4.3k). The textural relationship and chemical zonation pattern indicate growth from a melt phase, replacing inclusions of kyanite + phengite in garnet due to phengite dehydration. In comparison, sapphirine described from Grt-Ky-breakdown domains in orogenic eclogites is usually 'peraluminous' ranging between the 3:5:1 and 7:9:3 endmembers of sapphirine (e.g. Liati & Seidel, 1996; Godard & Mabit, 1998; Möller, 1999).

4.5. Metamorphic evolution

In order to constrain the *P–T* conditions experienced by the rocks, several thermobarometric methods including Zr-in-rutile thermometry, thermodynamic modelling and 'classical'

thermobarometric methods (exchange thermometry, net-transfer reactions, solvus thermometry) were applied. The results of the classical and trace element thermobarometry are summarised in Table 4.3. The results of Zr-in-rutile thermometry and ternary feldspar solvus thermometry are presented in Fig. 4.9. Calculated equilibrium phase diagrams are shown in Fig. 4.10 and Fig. 4.11.

Equilibrium phase diagrams ('pseudosections') were calculated in the Na_2O–CaO–K_2O–FeO–MgO–Al_2O_3–SiO_2–H_2O–TiO_2–O_2 (NCKFMASHTO) system. Calculations were performed with the software package THERIAK-DOMINO (version 03.01.2012, Capitani & Petrakakis, 2010) using the updated internally consistent thermodynamic dataset of Holland & Powell (1998). The following solution models were used: garnet (White *et al.*, 2007), omphacite (Green *et al.*, 2007, updated by Diener & Powell, 2012), white mica (Coggon & Holland, 2002), biotite (White *et al.*, 2007), amphibole (Diener *et al.*, 2007, updated by Diener & Powell, 2012), spinel (White *et al.*, 2007), orthopyroxene (White *et al.*, 2002), epidote (Holland & Powell, 1998), feldspar (Holland & Powell, 2003) and melt (White *et al.*, 2007). The chemical composition used for modelling is given in Table 4.2. XRF analyses were obtained from rock chips used for thin section preparation. These were carefully controlled for contamination by the host lamprophyre.

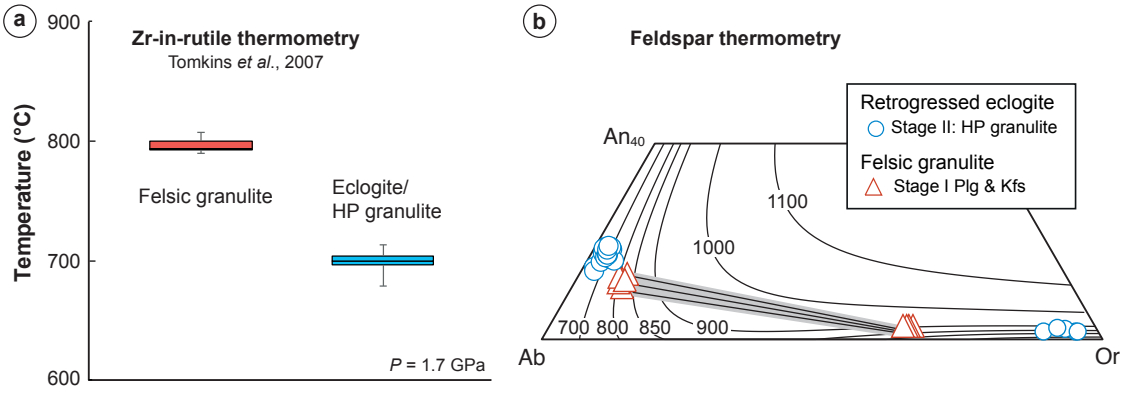

Fig. 4.9. Zr-in-rutile and feldspar thermometry. (a) Average Zr-in-rutile temperatures for the felsic granulite are 791±11°C (2σ SD; n = 18). Rutile in the retrogressed eclogite records temperatures of 701±10°C (2σ SD; n = 18) using the calibration of Tomkins *et al.* (2007). The results of Zr-in-rutile thermometry are summarised in boxplot-type diagrams. The box represents the interquartile range (middle half) of the data. The horizontal line represents the median of the data. The vertical line connects the minimum and maximum values. (b) The felspar compositions are plotted in the ternary system anorthite (An) – albite (Ab) – orthoclase (Or). Isotherms were calculated with THERIAK-DOMINO using the ternary felspar model of Holland & Powell (2003), updated by Nahodilová *et al.* (2011) at 1.7 GPa.

4.5.1. Felsic granulite

Rutile grains have uniform Zr concentrations and have no core-to-rim zonation. Using the calibration of Tomkins *et al.* (2007) gives a temperature of 791±11°C at 1.7 GPa. The preservation of homogeneous Zr concentrations indicates a rapid exhumation process with

Table 4.3. Results of application of various geothermobarometric calibrations

Method (Calibration)		Stage	Felsic granulite		Retrogressed eclogite	
			T (°C)	*P* (GPa)	*T* (°C)	*P* (GPa)
Grt–Cpx Fe^{2+}-Mg exchange	(1)	I	**815±25**	1.7	**730±30**	1.7
	(1)	II	–	–	**695±20**	1.4
	(1)	III	–	–	**1150±50**	1.0
GADS (Grt–Cpx–Plg–Qtz)	(2)	I	800	**1.7–1.9**	–	–
	(2)	II	–	–	700	**1.2±0.2**
Zr-in-rutile	(3)	I	**791±11**	1.7	**701±10**	1.7

P–T calculations using the calibrations of (1) Krogh Ravna, 2000, (2) Eckert *et al.*, 1991, and (3) Tomkins *et al.* (2007).

no diffusional overprint during retrograde cooling (Cherniak *et al.*, 2007). The temperature range derived from Zr-in-rutile is supported by ternary feldspar solvus thermometry (Fig. 4.9b).

During metamorphic mineral growth, element fractionation into refractory mineral phases (such as garnet) and sluggish intracrystalline diffusion results in the preservation of chemical zonations. In this case, fractionation-corrected bulk compositions have to be used for calculating equilibrium phase diagrams (e.g. Konrad-Schmolke *et al.*, 2008). The felsic granulite is characterised by the absence of strongly zoned phases, except for some decrease in the Mg# of garnet towards the rims. Furthermore, compositions of different mineral grains are uniform across thin sections. Therefore, the effective bulk-rock composition is very likely to be similar to the bulk-rock composition, which is therefore used for modelling.

According to the calculated phase diagram (Fig. 4.10a), the high-pressure granulite-facies mineral assemblage, together with partial melt, is stable at temperatures above 750°C at 1.5 GPa and up to conditions of 900°C and 2.0 GPa. The solidus curve has a positive slope above 1.5 GPa and a negative slope below 1.5 GPa down to 1.2 GPa. Phengite is the stable hydrous phase at subsolidus conditions. The phengite-out reaction is positioned at temperatures only slightly below 800°C at 1.7 GPa. Biotite is stable up to temperatures in excess of 900°C at 1.7 GPa. Orthopyroxene is stable below 1.0 GPa at 800°C. The pressure conditions of formation are inferred using isopleths of jadeite content in clinopyroxene and grossular in garnet as well as Mg# of both phases. Jadeite content of omphacite indicates pressures of 1.7–1.8 GPa at 800°C. Intersection of the grossular (25–30 mol% Grs) and Mg# isopleths (Mg#=25–35) occurs at slightly higher temperatures of 850°C, however, the modelling results are in good agreement with the *P–T* estimates summarised in Table 4.3. The preferred *P–T* conditions for the peak paragenesis are 800°C at 1.7 GPa.

For thermodynamic modelling, assumptions concerning the H_2O concentration have to be made. The stability of hydrous phases such as biotite during peak conditions as well as petrographic indications for the presence of partial melt require at least 0.3 wt% H_2O at 800°C and 1.7 GPa to reach the wet solidus (Fig. 4.11). A further increase of the H_2O content does not significantly change the topology of the calculated phase diagrams or the mineral compositions, but it causes an increase in the amount of partial melt.

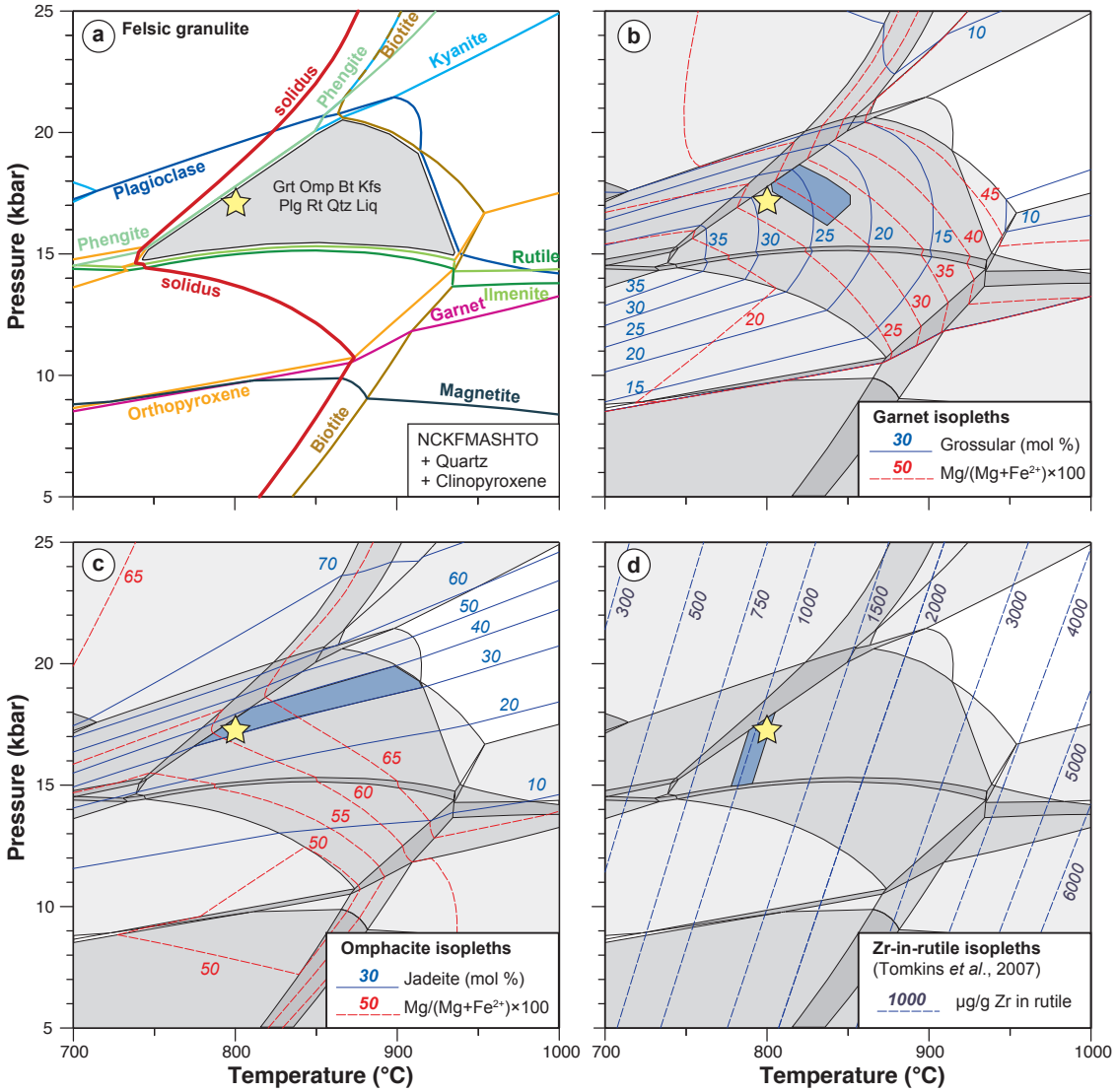

Fig. 4.10. Results of thermodynamic modelling for the felsic granulite (sample OD110B). The chemical composition used is given in Table 4.2. The $Fe^{3+}/\Sigma Fe$ ratio was set to 0.1 and a water content of 0.5 wt% was used. (a) Phase stability limits are outlined. The grey-shaded field indicates the high-pressure granulite-facies mineral assemblage of the granodioritic rock sample (garnet, omphacite, plagioclase, K-feldspar, biotite, quartz and rutile), together with partial melt. (b–d) Phase stability limits from (a) and mineral composition isopleths are shown. Fields are filled according to their variance with increasing shades of grey indicating increasing variance. The analysed compositions of garnet (b), omphacite (c) and rutile (d) plot in the blue-shaded regions. The star is positioned at 800°C, 1.7 GPa and indicates the preferred peak *P*–*T* conditions.

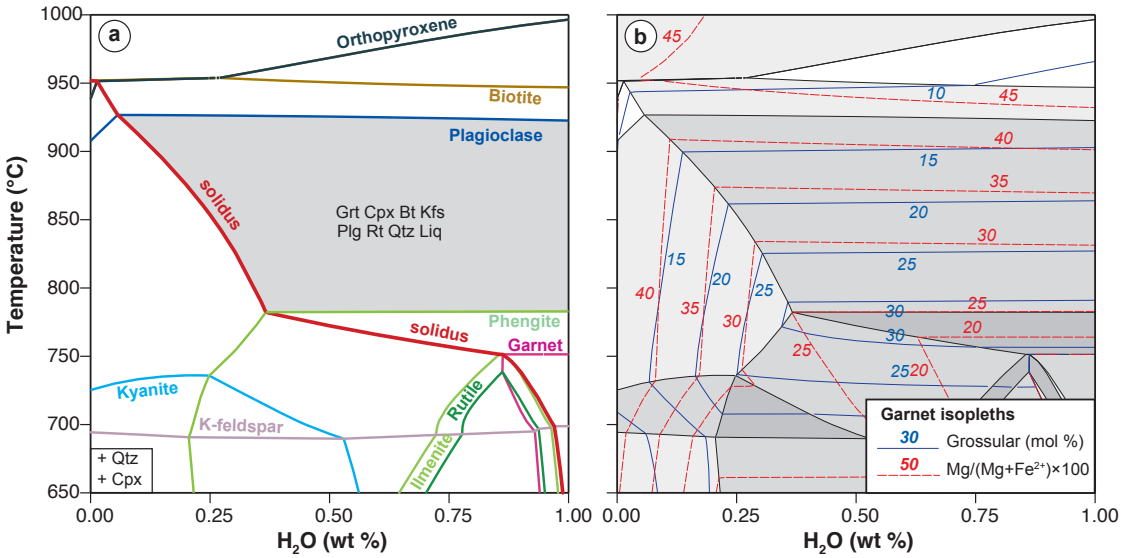

Fig. 4.11. Binary T–H_2O (wt%) diagram calculated at 1.7 GPa for the felsic granulite (sample OD110B) illustrating the effect of the water content on the (a) stable mineral assemblage and (b) chemical composition of garnet.

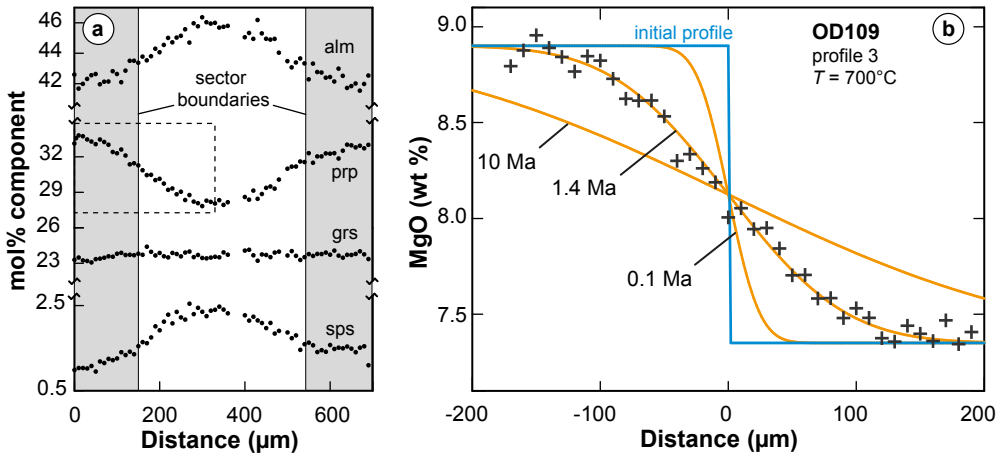

Fig. 4.12. (a) Electron microprobe profiles (10 mm spot distance) across a sector boundary in the rim region of the large garnet grain (see Fig. 4.5a for loaction of the profile (profile 3). Please note the axis breaks. The inset represents the part of the profile used for diffusion modelling. (b) Diffusion modelling of the MgO zonation (crosses). The curves display the results of diffusion modelling assuming an initial step function between both sector domains. The temperature of 700°C was derived from Zr-in-rutile thermometry. The one-dimensional semi-infinite diffusion model is a strong simplification (see text), however, a rough estimation of the duration between crystal growth and cooling is possible. Diffusion coefficient was taken from Chakraborty & Ganguly (1992).

4.5.2. Retrogressed eclogite

Thermobarometric calculations for the retrogressed eclogite are problematic due to potential chemical disequilibrium caused by rapid crystal growth. First of all, garnet sector zonation is indicative of reaction overstepping (see below). Mineral nucleation requires sufficient overstepping of the respective metamorphic reaction to overcome the kinetic nucleation barrier. The composition of a garnet nucleating during overstepping of the garnet-forming reaction differs from garnet that crystallises under equilibrium conditions. This compositional difference increases with increasing overstepping (e.g. Pattison *et al.*, 2011; Gaidies *et al.*, 2011; Spear *et al.*, 2014). The growing garnet approaches equilibrium compositions only if volume diffusion and diffusion in the growth medium (the rock matrix) are efficient.

Garnet compositional profiles mimic an apparent 'prograde' trend. However, a rapid growth mechanism might cause element fractionation and produce such zonations under constant *P–T* conditions. Pseudosection calculations can be used to model chemical fractionation. However, it is difficult to reconstruct the effective bulk-rock composition.

The most reliable temperature estimates are most probably provided by Zr-in-rutile thermometry, yielding 701±10°C (2σ SD; n = 18). Nevertheless, an attempt was made to derive temperatures using Grt-Cpx Fe^{2+}-Mg exchange thermometry on coexisting garnet cores and high-Jd omphacite inclusions, yielding values of around 700°C (Table 4.3).

Pressures for the eclogite stage were at least 1.7 GPa according to the maximum jadeite content of omphacite (Holland, 1980). Pressures calculated based on the silica content of phengite yield unrealistically high values within the diamond stability field. A prograde path (pre-stage I) is not documented in the eclogite (similar to the felsic granulite). Except for zircon, nearly all other mineral record was obliterated during the rapid metamorphic crystallisation event. The rare phengite grains with extremely high Si-content and very rare omphacite of unusual composition (e.g. higher jadeite content with 0.5 apfu Na) could be 'inherited' from the precursor. No coesite was detected. Polycrystalline quartz aggregates in garnet surrounded by radial cracks, indicating the former presence of coesite, are also absent (e.g. Chopin, 1984).

The plagioclase-bearing HP assemblage filling cracks in garnet yielded pressure values of 1.2±0.2 GPa, according to the net-transfer reaction anorthite + diopside = pyrope + grossular + quartz (Eckert *et al.*, 1991). Isothermal decompression is indicated by Grt-Cpx Fe^{2+}-Mg exchange temperatures similar to the eclogite-facies stage (Table 4.3). Petrographic observations suggest that this second assemblage crystallised from a melt phase. The eclogite-facies metamorphism is located slightly below the wet solidus of H_2O-saturated qtz-eclogite (e.g. Lambert & Wyllie, 1972; Poli & Fumagalli, 2003). However, isothermal decompression and supply of aqueous fluids result in partial melting as the solidus is crossed (fluid-fluxed melting).

Temperatures during pyrometamorphism were in excess of 1100°C as indicated by Grt-Cpx Fe^{2+}-Mg thermometry on the assemblage Grt + Plg + Cpx + Spl, which is locally developed between contacting grains of garnet I/II. Furthermore, the presence of pigeonite or the stabilisation of allanite + strongly subsilicic clinopyroxene (calcium tschermak's

pyroxene) at the expense of LREE-bearing clinozoisite also suggest high temperatures.

4.5.3. Timescale between HP metamorphism and xenolith extraction

The well preserved growth zonation of garnet indicates a relative fast exhumation process. During garnet growth, step profiles developed between two neighbouring sectors. The concentration profiles measured across these zones are flat for Ca, confirming analysis within a growth shell. The concentraion profiles of Mg, Fe^{2+} and Mn, instead, indicate some diffusive relaxation. Diffusion modelling may provide a rough estimation for the duration the metabasite remained at peak temperatures until the extraction by the lamprophyre occured (Fig. 4.12).

Mg, Mn and Fe^{2+} show diffusion profiles. However, only Mg shows regions with a plateau-like, homogeneous concentration. Based on an initial Mg step function profile and using a one-dimensional, semi-infinite diffusion model (Crank, 1975), an error function was fitted to the measured concentration profile. A one-dimensional model is an over-simplification. Additional to the diffusional relaxation across sectors, radial diffusion along the prograde zonation took place, requiring a more complex diffusion model. However, the simple model used is sufficient to determine the order of magnitude of the maximum time range the lithology remained at peak temperatures. In any case, a precise determination is difficult, regarding the discrepancies in experimentally determined diffusion coefficients and coefficients determined from diffusion profiles in natural garnet (e.g. Chakraborty & Ganguly, 1992; Carlson, 2006; Chu & Ague, 2015). Using the diffusion coefficients of Chakraborty & Ganguly (1992) and a temperature of 700°C results in a time range of $\sim$1 Ma (Fig. 4.12).

4.6. U-Pb zircon geochronology

SIMS U-Pb zircon dating of the felsic granulite and the retrogressed eclogite was performed in order to determine metamorphic and protolith ages, respectively. The results are presented in Fig. 4.13 and Table E.1.

4.6.1. Felsic granulite

Zircon grains from the felsic granulite commonly have rounded shapes but elongated, prismatic habits. Three distinct domains can be distinguished. The zircons are characterised by oscillatory zoned cores. These are surrounded by structureless mantles with low luminescence. Additionally, a thin (<10 μm), discontinuous brightly-luminescent rim is developed. The fine oscillatory zonation of the cores along with high Th/U ratios is indicative of a magmatic origin. The mantle domains are dark, partly crosscutting the magmatic zonation and show strong enrichment in U as well as very low Th/U ratios (<0.01). The presence of 'ghost' primary oscillatory zoning is caused by remnants of the initial magmatic trace element distribution and is indicative of solid-state recrystallisation

in contrast to overgrowth or fluid dissolution. Metamorphic zircon growth is limited to a narrow and incomplete overgrowth rim.

Old zircon grains with high U contents (several thousand µg/g) are likely to suffer a breakdown of the zircon lattice by metamictisation. Subsequent recrystallisation in the course of a thermal event may reset these domains. This interpretation is supported by analyses of mantle domains that gave a ^{238}U-^{206}Pb concordia age of 332±7.2 Ma (Fig. 4.13b), which is interpreted as the age of eclogite-facies peak metamorphism. During recrystallisation, Th dominantly moved into allanite, which is part of the metamorphic mineral assemblage and present in high amounts. The outer, CL-bright metamorphic rim is spatially not resolvable.

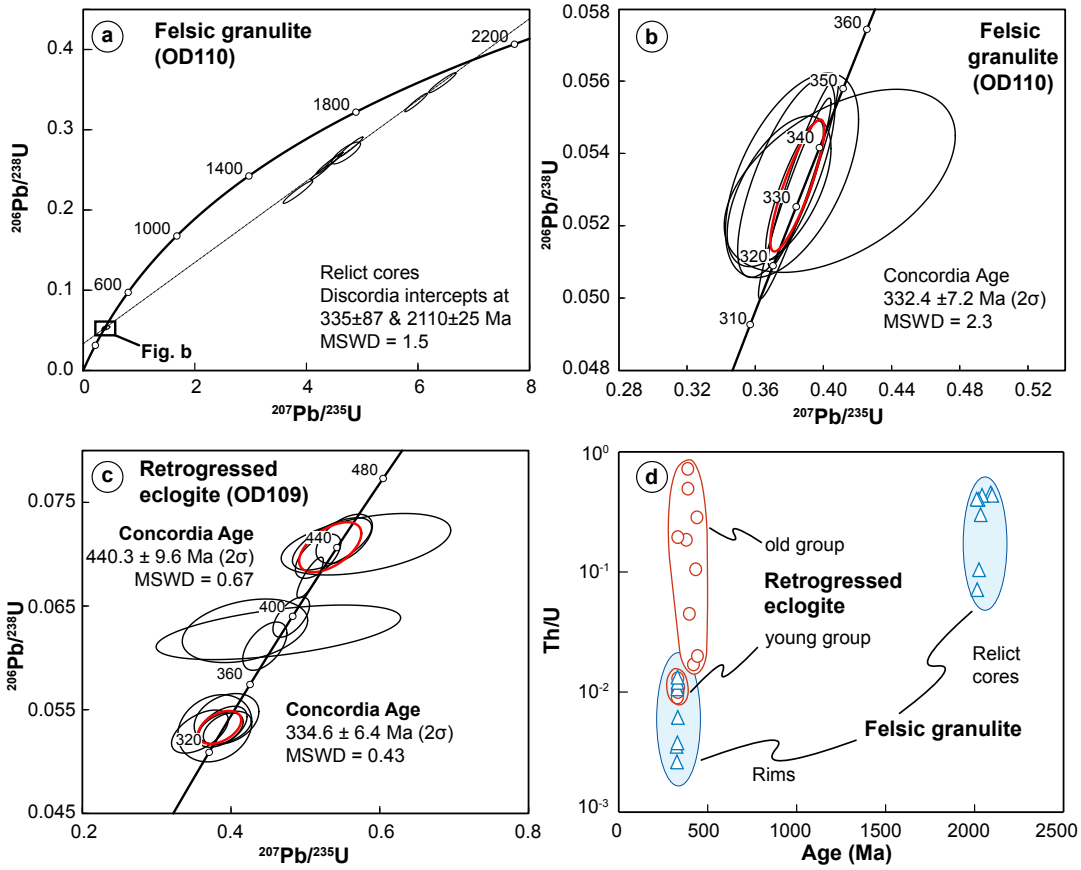

Fig. 4.13. (a–c) Concordia diagrams for SIMS U-Pb zircon analyses of the felsic granulite (a,b) and the retrogressed eclogite (c). Ellipses represent 2σ errors. Red ellipses mark pooled concordia ages. (d) Th/U vs age diagram showing analyses of relict magmatic cores (^{207}Pb/^{206}Pb age) and metamorphic zircon mantle domains (^{206}Pb/^{238}U age) of the felsic granulite.

Analyses on oscillatory-zoned cores lie on a discordia with an upper intercept age of 2110±25 Ma (Fig. 4.13a). The weighted mean ^{207}Pb/^{206}Pb age of the cores is 2041±13. Discordance in the magmatic fraction is more likely related to annealing of metamict high-U oscillatory zones during high-grade metamorphism, rather than to volume diffusion in

intact zircon. Zircon in the felsic granulite does not record a second metamorphic event. Possibly, the protolith was below annealing temperature just until the collisional event in the Visean. Some rim analyses gave young ages (<300 Ma), which are attributed to post-metamorphic lead loss due to metamictisation, as indicated by the development of radial fractures.

4.6.2. Retrogressed eclogite

Zircon grains in the retrogressed eclogite are relatively small (usually < 50µm). At least two age groups were identified, resulting in concordia ages of 334.6±6.4 Ma and 440.3±9.6 Ma, respectively (Fig. 4.13c). Zircons of the younger age group are characterised by low Th/U ratios (mostly ∼0.01) in accordance with a metamorphic origin. Within 2σ error the age is identical with the metamorphic age derived from the felsic granulite and interpreted to date the eclogite-facies metamorphism. The older age group could possibly date the age of the magmatic protolith. The Th/U ratios are higher and range from 0.02–0.73 (Table E.1). A third age group (∼370–400 Ma) is present, showing intermediate ages, possibly indicating another metamorphic event. Only homogeneous domains identified by cathodoluminescence and BSE imaging were analysed. However, mixed ages cannot fully be ruled out.

4.7. Discussion

4.7.1. Chemical disequilibrium during garnet growth

Sector zoning in garnet is rarely seen in regional metamorphic rocks (e.g. Shirahata & Hirajima, 1995; Medaris *et al.*, 2003; Stowell *et al.*, 2011). However, the process of selective enrichment of cations into distinct sectors is well known from other minerals like staurolite, Ti-augite or zircon, for instance (e.g. Hollister, 1970; Nakamura, 1973; Watson & Liang, 1995). Compositional sector zonation (≠ textural sector zonation; e.g. Wilbur & Ague, 2006) can be caused by rapid growth of a crystal, developing different faces with distinct, crystallographically-controlled partitioning behaviour for specific cations. Selective partitioning is governed by the geometry of an exposed cation site (or protosite) in the boundary layer surrounding the growing crystal, from which components are incorporated during rapid growth (e.g. Nakamura, 1973). Despite the isotropic character of garnet, structural differences concerning one cation site may exist, depending on the respective crystal form exposed to the growth medium. These differences may result from a different number of bonds below the surface in the partly exposed cation site, which influences the partitioning behaviour. The number of bonds, in turn, is governed by the spatial relationship between the form and the crystal lattice.

The HP garnet of the retrogressed eclogite sample shows strong intersectoral differences in Mg, Fe^{2+} and Mn concentrations, whereas Ca and tri-/tetravalent cations are concentrically zoned. The external morphology of the crystals is characterised if well developed and preserved, by {110} faces (rhombic dodecahedrons). To account for the

sector zonation, an additional crystal form must have been present during most of the garnet growth history, having a different exposure of the X-site, which is occupied by divalent cations. These were most likely {211} faces (deltoidal icositerahedron). Judging from the concentration profiles in Fig. 4.6a, the {211} faces preferentially incorporate Mn and Fe^{2+} over Mg.

The rapid growth process is supported by the large number of tiny trapped mineral inclusions. Furthermore, a fine oscillatory zonation is nicely preserved in the Ca profile. Small-scale oscillatory zoning occurs concentrically parallel to both crystal faces and is inferred to result from matrix processes. These could be related to (i) externally controlled cyclic changes (e.g. T, P, X_{fluid}) or, (ii) to the kinetics of rapid crystal growth, causing depletion of reactant elements in the surrounding matrix (e.g. Kohn, 2004; Stowell *et al.*, 2011). The latter seems more realistic. The presence of two generations of sector zoned growth shells (Fig. 4.5) suggests at least two rapid growth pulses. The overall growth zonation with decreasing Mn, Ca and Fe but increasing Mg is most probably a result of fractional crystallisation.

4.7.2. Post-collisional processing of lower crust

During metamorphism, reaction onset may be significantly delayed and may not begin at equilibrium P–T conditions. Dry protoliths and moderate temperatures may result in sluggish nucleation of reaction products and slow diffusion rates. Therefore, mineral assemblages and compositions may lag behind changing P, T, and X. A high degree of reaction overstepping may have a supersaturation as a consequence that ist likely to be equalised by sudden, rapid crystal growth. Once initiated, overstepped reactions can proceed rapidly. This may result from a certain amount of heating. Inflow of fluids may enhance reactivities and promote nucleation. Alternatively, deformation processes can initiate metamorphic reactions by increasing the reactive surface areas as well as rates of nucleation and reaction, under both, wet and dry conditions (Austrheim, 1998; de Ronde & Stünitz, 2007).

Temperatures of $\sim$700°C may result in sluggish recrystallisation of relatively lower crustal lithologies, providing a possible scenario to explain rapid crystal growth observed in the retrogressed eclogite. Preservation of stage I garnet zonation patterns in both the felsic granulite and the retrogressed eclogite indicates a short-lived overprint (stage II), otherwise compositional zoning would be erased by intracrystalline diffusion. It is therefore most likely that these two consecutive events (rapid crystal growth and partial melting in case of the retrogressed eclogite) are related to a single geologic process (or tectonic event). According to the inferred P–T conditions, both events are linked by near-isothermal decompression.

Nucleation may be caused by the commencement of deformation during incipient extensional tectonics, resulting in the crystallisation of an eclogite-facies assemblage. Reaction could also be related to fluid input at subsolidus conditions and/or heating. Progressive post-collisional crustal thinning at isothermal conditions leads to a crossing of the water-saturated solidus. Eventually, water access results in partial melting.

Experimental deformation tests show that very low amounts of partial melt (melt fractions < 10 %) cause a drastic reduction in rock strength (e.g. Rosenberg & Handy, 2005). Weakening has been attributed to brittle failure. However, the deformation experiments cause microtectonic features that are rarely seen in high-grade metamorphic terrains. Such features are, for instance, inter- and intragranular microcracks. These structures are very nicely developed and preserved in the retrogressed eclogite (Fig. 4.3). Rigid-body rotation of grains, accommodated by frictional sliding or by movement along incipient melt pockets, results in a strong decrease of viscosity (Rosenberg & Handy, 2005 and references therein).

Due to the effect of rheological weakening, sites of partial melting in the crust may therefore coincide with the localisation of deformation if non-lithostatic stresses are active. Crust-scale shear zones may accommodate orogenic extension, provide pathways and trigger the ascend of the mantle-derived magmas. In this scenario, mass-transfer resulting in metasomatic processes is expected to occur along these high-strain zones. This may also have an impact on the geochemistry of by-passing mantle-derived melts due to the high assimilation potential.

4.7.3. Regional implications

The xenoliths entrained in post-collisional lamprophyres are lower crustal documents of the Variscan collision process affecting the MGCZ during the Visean. The HP metamorphic peak assemblages indicate marked crustal thickening to ∼60 km. U-Pb zircon dating gives a young age for a Variscan HP metamorphic event, similar to the age of post-collisional granitoid magmatism. The xenoliths document a thickened and thermally disturbed crust on its way to the attainment of structural and thermal equilibrium. Partial melting during post-collisional extension clearly has an impact on the rheological properties and tectonic processes of the lithosphere. However, partial melting affected the crust also during peak conditions, as suggested by petrographic signs and thermodynamic modelling results of the felsic granulite. Syn- to post-tectonic granitoids are very abundant across the MGCZ. Indeed, significant melting of garnet-rich HP crustal lithologies is indicated by distinct trace element signatures in post-collisional granitoids (Altherr *et al.*, 1999a). Among the post-collisional intrusives of the MGCZ, some granitoids are characterised by adakite-like signatures (e.g. low Y concentrations and high Sr/Y ratios).

The protolith age of the felsic granulite indicates that at least some of the lower crust of the MGCZ formed during the Paleoproterozoic. This finding is supported by some inherited Paleoproterozoic zircons previously found in Silurian orthogneisses of the MGCZ (e.g. Dombrowski *et al.*, 1995). The metamorphic and magmatic rocks in Central and Western Europe show dominantly Neoproterozoic–Paleozoic ages (e.g. Melleton *et al.*, 2010). Older basement has solely been identified in the gneisses of the Icartian basement in the North Armorican Massif (e.g. Vidal *et al.*, 1981) and the Svtlik gneiss in the Bohemian Massif (Wendt *et al.*, 1993; see Fig. 4.1). Both units have similar protolith ages compared to the felsic granulite, dated at ∼2.1 Ga. Paleoproterozoic ages of the meta-igneous xenolith are comparable to those of the West Africa craton (e.g.

Abouchami *et al.*, 1990; Boher *et al.*, 1992). Paleoproterozoic detrital zircons are abundant in Neoproterozoic–Paleozoic sediments of the Variscides with a likely provenance in the West Africa craton (e.g. Zeh & Gerdes, 2010).

4.8. Conclusions

Two lithologies entrained as xenoliths in post-collisional lamprophyres from the Odenwald crystalline complex (MGCZ) were studied in detail. A felsic granulite and a retrogressed eclogite record a HP metamorphic event. While the felsic granulite is well equilibrated, the eclogite records strong textural disequilibria in terms of (i) rapid eclogite-facies metamorphic crystallisation causing sector and oscillatory zonation of garnet, followed by (ii) incipient partial melting resulting in intra- and intercrystalline fracturing. Yet, it is possible to derive *P–T* informations from both lithologies. A combination of different thermobarometric methods indicates that the eclogite and the felsic granulite record peak conditions of $\sim$700°C and $\sim$800°C, respectively, at pressures around 1.7 GPa. No prograde *P–T* path is documented in the samples. *P–T* conditions of melt-mediated overprinting of the retrogressed eclogite suggest isothermal decompression to 1.2$\pm$0.2 GPa.

Preservation of chemical zonation in garnet and homogeneous Zr-in-rutile temperatures in both samples indicate limited diffusional overprint, demanding a rapid exhumation process without prolonged retrograde cooling. Therefore, the melt-mediated partial recystallisation of the retrogressed eclogite must have occurred shortly before extraction by the lamprophyre melts. These results are supported by SIMS U-Pb zircon dating, giving a relatively young age for the Variscan HP metamorphic event, similar to the age of post-collisional granitoid magmatism.

Sector zonation in garnet suggests rapid crystal growth due to reaction overstepping, caused by sluggish nucleation rates. Nucleation is possibly related to shearing and fluid-inflow. During continuing decompression, the wet solidus is crossed, resulting in incipient partial melting. Small amounts of partial melt cause a drastic reduction in the rock strength due to brittle failure. A consequence of rheological weakening may be a localization of deformation, resulting in crust-scale shears zones. Such shear zones may accommodate orogenic extension, provide pathways and trigger the ascend of the mantle-derived lamprophyres.

During transport in the mantle-derived melt, multiple parageneses in local subsystems developed, involving partial melting at $T > 1100$°C. HT phases such as sapphirine or pigeonite crystallised from small melt pockets. Allanite is stabilised at the expense of LREE-poorer epidote-group minerals.

The xenoliths document Variscan collision during the Visean with marked crustal thickening to at least 60 km. They give rare insights into the process of destabilisation of the lower orogenic crust during post-collisional extension. Furthermore, magmatic protolith ages indicate mantle-derived magmatism during the Silurian and identify Paleoproterozoic basement within the MGCZ.

5. Conclusions

Potassium-rich mantle-derived magmatic rocks from two geodynamic settings were studied in this thesis. First, lamprophyres were sampled from the Island of Kos at the eastern end of the South Aegean Volcanic Arc, where numerous late Neogene amphibole and mica lamprophyres crop out. Second, a detailed dataset of post-collisional lamprophyre dykes of the Variscan orogen in SW Germany and E France was obtained.

In both cases, mantle-derived potassic–ultrapotassic magmatism is related to partial melting of a subduction-modified upper mantle. Lamprophyre magmatism is commonly decoupled in time from the event of subduction and mantle metasomatism. Partial melting is related to thermal adjustment of the lithospheric mantle during extensional processes. In the Variscan case, a large number of lamprophyres is scattered across the internal zones of the orogen. These dykes were emplaced during post-collisional extension (330–320 Ma) or even later events of lithospheric thinning (300–290 Ma).

Lamprophyres commonly intruded 'en-échelon' in several parallel-arranged fissures. The orientation of such structures on the Island of Kos indicates magma uprise and dyke emplacement during sinistral shear which is in accordance with the tectonic stress field between the Aegean and western Anatolia. The Aegean back-arc basin extends faster than western Anatolia and the two crustal domains are separated by a lithosphere-scale transition zone that accommodates differential motion. Partial melting of the lithospheric mantle was probably triggered by decompression due to extensional thinning of the Aegean lithosphere during slab rollback.

The lamprophyres have crust-like trace element pattern and elevated $^{87}Sr/^{86}Sr$ and $^{207}Pb/^{204}Pb$ as well as low $^{143}Nd/^{144}Nd$ ratios. Further, they are characterised by high concentrations of mantle-compatible elements, which reflects equilibration between the melts and mantle peridotite. Lamprophyres from Kos are outstanding, as they are positioned above an active oceanic subduction zone. In contrast, the fossil example of the Variscan belt is related to deep continental subduction. In the Variscan belt, subduction of continental crust during continent-continent collision at around 340 Ma (e.g. Kotková *et al.*, 2011) is responsible for the metasomatic alteration of the mantle lithosphere. Mantle source enrichment beneath Kos is related to subduction of large amounts of sediments. Therefore, both examples involve subduction of upper continental crustal material.

The isotopic compositions of the lamprophyres indicate that at least two geochemical components are present in their source: depleted lithospheric mantle and subducted crustal material. The trace element patterns are strongly controlled by the metasomatic (crustal) component due to much higher contents of incompatible trace element compared to the ambient lithospheric mantle peridotite. However, an additional metasomatic component is present in the source of the lamprophyres from Kos. The lamprophyre suite from Kos shows geochemical evidence for a significant chemical contribution from the astheno-

spheric mantle. This component is characterised by a marked enrichment in incompatible elements and has a carbonatite-like trace element signature. This component is derived from the fertile asthenosphere, infiltrating the Aegean mantle wedge along ruptures that developed in the retreating slab. Concerning the Variscan lamprophyres, a chemical contribution from the asthenospheric mantle can be detected only in rare cases. Juvenile input derived from melting of upwelling asthenospheric (convecting) mantle is very rare in orogens and is largely restricted to strike-slip zones. The mantle-derived lavas indicate that juvenile mantle-input to the crust is negligible during continent-continent collision and magmatism is basically restricted to recycling of older crust with assimilation of mantle during melt-peridotite interaction.

The crust-like signature of the Kos lamprophyres can be linked to the addition of subducted SE Mediterranean sediments, that are dominated by a terrigenous component of Pan-African provenance. In case of the Variscan belt, continental collision resulted in subduction of felsic lithologies to mantle depth. These lithologies are potentially responsible for the enrichment of the mantle source. Systematic sampling of dyke rocks across tectonic zones of the Variscan orogen reveals different crustal signatures with distinct isotopic compositions, resembling the local average composition of the upper crust. Mantle-derived rocks have trace element patterns and isotopic compositions that allow for tracing different compositions of subducted crust and show regional distributions following major tectonic zones of the orogen. Systematic sampling across various tectonic zones revealed geochemically and isotopically distinct lamprophyre groups, related to downthrusting of crustal rocks with contrasting compositions into the mantle.

In part, regional variations are related to the nature and source of the subducted continental material, or the conditions of mobilisation from the subducting slab and the interaction processes between metasomatic agents and the ambient mantle. A petrogenetic model was developed to explain the large chemical heterogeneity observed in local mantle-derived magmatic suites, which range from high-K basalts, shoshonitic lamprophyres to lamproites. The model describes (i) material loss during progressive metamorphism of the subducted material, (ii) selective mobilisation from the slab, whereby the metasomatic agent and restite may show different incompatible element signatures and contrasting Sr, Nd, and Pb isotopic compositions, (iii) reactive melt transport into the lithospheric mantle with intense interaction with the peridotitic mantle to form mineralogically and chemically zoned veins within the lithospheric mantle (c.f. Fig. 3.13), (iv) partial melting of sections of the veined mantle and (v) modification of these melts during fractional crystallisation.

Exhumed Variscan (U)HP crustal segments demonstrate that crustal rocks had been subducted to mantle depth and reached temperatures sufficient for dehydration melting of phengite. The trace element signature of partial melts released from the subducted continental crust may be strongly affected by the stability of phases that sequester particular groups of trace elements and thereby control the trace element budget of the subducted crustal material. Some lamprophyres show high Th/La, Sm/La and low Th/U ratios that may reflect stable residual allanite in the subducted crustal rocks, whereas reduced Nb/Ta, Rb/Cs and K/Rb may be related to the buffering role of phengite during partial melting.

Interaction between granitic melts derived from deeply subducted continental crust and mantle peridotite causes hybrid reaction zones, rich in orthopyroxene and phlogopite that are hosted within the lithospheric mantle. Later remelting during post-collisional extension preferentially mobilizes these metasomatic portions. Compatible trace elements suggest that some lamprophyres are dominantly derived from melting of olivine-poor/-free metasomatic domains and that these melts did not react extensively with the ambient mantle. Formation of orthopyroxene + garnet during melt–peridotite interaction increases Dy/Yb, decreases Zr/Hf and removes Al from the melt, resulting in peralkaline compositions. Peralkalinity changes solubility of $HFSE^{4+}$ in the melt, eventually resulting in selective enrichment of $HFSE^{4+}$. This model may therefore explain the wide geochemical and mineralogical variability observed in post-collisional mantle-derived magmatism, including the exotic and rare lamproites, which were previously not described from the study area.

In some cases, lamprophyres contain xenoliths, which are disintegrated wall-rock fragments entrained during magma ascent. A dyke from the Variscan Odenwald is outstanding, as it contains a wealth of rock fragments representing a section from the upper mantle through the continental crust. Some of the material is possibly related to the described mantle-metasomatism (e.g. phlogopite-othopyroxenites), it could represent the ambient depleted lithospheric mantle (dunites), or it could represent cognate cumulates (hornblendites, phlogopite-clinopyroxenites). However, most of the ultramafic xenoliths are intensely altered due to metasomatism by the lamprophyre. Instead, two lower crustal xenoliths were investigated.

High-grade metamorphic lower crustal xenoliths (retrogressed eclogites and HP granulites) record the processing of continental crust during orogenesis under eclogite-facies conditions. *P–T*-information derived from thermodynamic modelling and classical phase and trace element thermobarometry demonstrates that these lithologies record crustal thickening to $\sim$60 km and subsequent isothermal decompression, which resulted in partial melting at still elevated pressures (1.2$\pm$0.2 GPa). The preservation of growth zonation features in garnet indicates that eclogite-facies metamorphism, the overprint during decompression and the entrainment into the lamprophyre were closely followed in time and possibly are tectonically related to each other. Consequently, this is the first direct evidence for a Lower Carboniferous eclogite-facies metamorphism in this part of the orogen (the Mid-German Crystalline Zone). Furthermore, the xenoliths provide a snapshot of the lower orogenic crust during continental collisional and record the dynamics of regional extension. A Lower Carboniferous age of metamorphism is supported by SIMS U-Pb zircon dating, which gave ages of 332$\pm$7 Ma (felsic granulite) and 335$\pm$6 Ma (eclogite). An age of 440$\pm$10 Ma is interpreted to date the magmatic precursor of the eclogite. This age is well established for metagranitic rocks within the Mid-German Crystalline Zone and is related to arc magmatism above the cryptic Rheic subduction zone. Oscillatory zoned zircon cores in the felsic granulite are discordant with an upper intercept at 2110$\pm$25 Ma. This age is interpreted as the crystallisation age of a granitic protolith. Paleoproterozoic basement was previously unknown in the Mid-German Crystalline Zone and is generally very rare in the european Variscides.

Bibliography

Abdelfadil KM, Romer RL, Glodny J (2014) Mantle wedge metasomatism revealed by Li isotopes in orogenic lamprophyres. *Lithos* 196: 14–26

Abouchami W, Boher M, Michard A, Albarede F (1990) A major 2.1 Ga event of mafic magmatism in West Africa: an early stage of crustal accretion. *Journal of Geophysical Research: Solid Earth* 95: 17 605–17 629

van Achterbergh E, Griffin WL, Ryan CG, O'Reilly SY, Pearson NJ, Kivi K, Doyle BJ (2004) Melt inclusions from the deep Slave lithosphere: implications for the origin and evolution of mantle-derived carbonatite and kimberlite. *Lithos* 76: 461–474

van Achterbergh ES, Ryan CG, Griffin WL (2000) On-line interactive data reduction for the LA-ICP-MS microprobe. *Sydney, Australia, Macquarie Research Limited* 62 pp.

Adam J, Green T (2001) Experimentally determined partition coefficients for minor and trace elements in peridotite minerals and carbonatitic melt, and their relevance to natural carbonatites. *European Journal of Mineralogy* 13: 815–827

Adam J, Green T (2003) The influence of pressure, mineral composition and water on trace element partitioning between clinopyroxene, amphibole and basanitic melts. *European Journal of Mineralogy* 15: 831–841

Adam J, Green T (2006) Trace element partitioning between mica-and amphibole-bearing garnet lherzolite and hydrous basanitic melt: 1. Experimental results and the investigation of controls on partitioning behaviour. *Contributions to Mineralogy and Petrology* 152: 1–17

Agostini S, Doglioni C, Innocenti F, Manetti P, Tonarini S, Savaşçin MY (2007) The transition from subduction-related to intraplate Neogene magmatism in the Western Anatolia and Aegean area. *Geological Society of America Special Papers* 418: 1–15

Aldanmaz E, Pearce JA, Thirlwall MF, Mitchell JG (2000) Petrogenetic evolution of late Cenozoic, post-collision volcanism in western Anatolia, Turkey. *Journal of Volcanology and Geothermal Research* 102: 67 – 95

Alıcı P, Temel A, Gourgaud A (2002) Pb–Nd–Sr isotope and trace element geochemistry of Quaternary extension-related alkaline volcanism: a case study of Kula region (western Anatolia, Turkey). *Journal of Volcanology and Geothermal Research* 115: 487 – 510

Altenberger U, Besch T (1993) The Böllstein Odenwald: evidence for pre-to Early Variscan plate convergence in the Central European Variscides. *Geologische Rundschau* 82: 475–488

Altherr R, Kalt A (1996) Metamorphic evolution of ultrahigh-pressure garnet peridotites from the Variscan Vosges Mts. (France). *Chemical Geology* 134: 27–47

Altherr R, Siebel W (2002) I-type plutonism in a continental back-arc setting: Miocene granitoids and monzonites from the central Aegean Sea, Greece. *Contributions to Mineralogy and Petrology* 143: 397–415

Altherr R, Keller J, Kott K (1976) Der jungtertiäre Monzonit von Kos und sein Kontakthof (Ägäis, Griechenland). *Bulletin de la Société Géologique de France* 7: 403–412

Altherr R, Kreuzer H, Wendt I, Lenz H, Wagner GA, Keller J, Harre W, Höhndorf A (1982) A late Oligocene/ early Miocene high temperature belt in the Attic–Cycladic crystalline complex (SE Pelagonian, Greece). *Geologisches Jahrbuch* E23: 97–164

Altherr R, Henjes-Kunst F, Matthews A, Friedrichsen H, Hansen BT (1988) O-Sr isotopic variations in Miocene granitoids from the Aegean: evidence for an origin by combined assimilation and fractional crystallization. *Contributions to Mineralogy and Petrology* 100: 528–541

Altherr R, Henes-Klaiber U, Hegner E, Satir M, Langer C (1999a) Plutonism in the Variscan Odenwald (Germany): from subduction to collision. *International Journal of Earth Sciences* 88: 422–443

Altherr R, Henjes-Kunst F, Langer C, Otto J (1999b) Interaction between crustal-derived felsic and mantle-derived mafic magmas in the Oberkirch Pluton (European Variscides, Schwarzwald, Germany). *Contributions to Mineralogy and Petrology* 137: 304–322

Altherr R, Holl A, Hegner E, Langer C, Kreuzer H (2000) High-potassium, calc-alkaline I-type plutonism in the European Variscides: northern Vosges (France) and northern Schwarzwald (Germany). *Lithos* 50: 51–73

Altherr R, Meyer HP, Holl A, Volker F, Alibert C, McCulloch MT, Majer V (2004) Geochemical and Sr-Nd-Pb isotopic characteristics of late cenozoic leucite lamproites from the east European alpine belt (Macedonia and Yugoslavia). *Contributions to Mineralogy and Petrology* 147: 58–73

Ammannati E, Jacob DE, Avanzinelli R, Foley SF, Conticelli S (2016) Low Ni olivine in silica-undersaturated ultrapotassic igneous rocks as evidence for carbonate metasomatism in the mantle. *Earth and Planetary Science Letters* 444: 64–74

Aulbach S, O'Reilly SY, Pearson NJ (2011) Constraints from eclogite and MARID xenoliths on origins of mantle Zr/Hf–Nb/Ta variability. *Contributions to Mineralogy and Petrology* 162: 1047

Austrheim H (1998) Influence of fluid and deformation on metamorphism of the deep crust and consequences for the geodynamics of collision zones. In: Hacker BR, Liou JG (eds.) *When continents collide: geodynamics and geochemistry of ultrahigh-pressure rocks*, no. 10 in Petrology and Structural Geology, 297–323, Springer

Auzanneau E, Vielzeuf D, Schmidt MW (2006) Experimental evidence of decompression melting during exhumation of subducted continental crust. *Contributions to Mineralogy and Petrology* 152: 125–148

Avigad D, Garfunkel Z, Jolivet L, Azañón JM (1997) Back arc extension and denudation of Mediterranean eclogites. *Tectonics* 16: 924–941

Bachmann O, Deering CD, Ruprecht JS, Huber C, Skopelitis A, Schnyder C (2012) Evolution of silicic magmas in the Kos-Nisyros volcanic center, Greece: a petrological cycle associated with caldera collapse. *Contributions to Mineralogy and Petrology* 163: 151–166

Bailey JC, Jensen ES, Hansen A, Kann ADJ, Kann K (2009) Formation of heterogeneous magmatic series beneath North Santorini, South Aegean island arc. *Lithos* 110: 20–36

Bali E, Audétat A, Keppler H (2011) The mobility of U and Th in subduction zone fluids: an indicator of oxygen fugacity and fluid salinity. *Contributions to Mineralogy and Petrology* 161: 597–613

Barth MG, McDonough WF, Rudnick RL (2000) Tracking the budget of Nb and Ta in the continental crust. *Chemical Geology* 165: 197–213

Bassias Y, Triboulet C (1994) Tectono-metamorphic evolution of blueschist formations in the Peloponnesus (Parnon and Taygetos Massifs, Greece): a model of nappe stacking during Tertiary orogenesis. *The Journal of Geology* 102: 697–708

Becker H, Wenzel T, Volker F (1999) Geochemistry of glimmerite veins in peridotites from Lower Austria—implications for the origin of K-rich magmas in collision zones. *Journal of Petrology* 40: 315–338

Becker M, Roex APL (2006) Geochemistry of South African on-and off-craton, Group I and Group II kimberlites: petrogenesis and source region evolution. *Journal of Petrology* 47: 673–704

Bianchini G, Beccaluva L, Nowell GM, Pearson DG, Siena F (2011) Mantle xenoliths from Tallante (Betic Cordillera): insights into the multi-stage evolution of the south Iberian lithosphere. *Lithos* 124: 308–318

Bijwaard H, Spakman W, Engdahl ER (1998) Closing the gap between regional and global travel time tomography. *Journal of Geophysical Research: Solid Earth* 103: 30 055–30 078

Biryol B, Beck SL, Zandt G, Özacar AA (2011) Segmented African lithosphere beneath the Anatolian region inferred from teleseismic P-wave tomography. *Geophysical Journal International* 184: 1037

Blundy J, Dalton J (2000) Experimental comparison of trace element partitioning between clinopyroxene and melt in carbonate and silicate systems, and implications for mantle metasomatism. *Contributions to Mineralogy and Petrology* 139: 356–371

Böger H (1983) Stratigraphische und tektonische verknüpfungen kontinentaler Sedimente des Neogens im Ägäis-Raum. *Geologische Rundschau* 72: 771–813

Boher M, Abouchami W, Michard A, Albarede F, Arndt NT (1992) Crustal growth in west Africa at 2.1 Ga. *Journal of Geophysical Research: Solid Earth* 97: 345–369

Bolhar R, Ring U, Allen CM (2010) An integrated zircon geochronological and geochemical investigation into the Miocene plutonic evolution of the Cyclades, Aegean Sea, Greece: Part 1: Geochronology. *Contributions to Mineralogy and Petrology* 160: 719–742

de Boorder H, Spakman W, White S, Wortel M (1998) Late Cenozoic mineralization, orogenic collapse and slab detachment in the European Alpine Belt. *Earth and Planetary Science Letters* 164: 569 – 575

Boutin R, Montigny R, Thuizat R (1995) Chronologie K-Ar et $^{40}Ar/^{39}Ar$ du métamorphisme et du magmatisme des Vosges. Comparison avec les massifs varisques avoisinants. *Géologie de la France* 1: 3–25

Braschi E, Francalanci L, Vougioukalakis GE (2012) Inverse differentiation pathway by multiple mafic magma refilling in the last magmatic activity of Nisyros Volcano, Greece. *Bulletin of volcanology* 74: 1083–1100

Brey GP, Bulatov VK, Girnis AV, Lahaye Y (2008) Experimental melting of carbonated peridotite at 6–10 GPa. *Journal of Petrology* 49: 797–821

Brun JP, Sokoutis D (2010) 45 my of Aegean crust and mantle flow driven by trench retreat. *Geology* 38: 815–818

Buettner A, Kleinhanns IC, Rufer D, Hunziker JC, Villa IM (2005) Magma generation at the easternmost section of the Hellenic arc: Hf, Nd, Pb and Sr isotope geochemistry of Nisyros and Yali volcanoes (Greece). *Lithos* 83: 29–46

Campbell IH, Stepanov AS, Liang HY, Allen CM, Norman MD, Zhang YQ, Xie YW (2014) The origin of shoshonites: new insights from the Tertiary high-potassium intrusions of eastern Tibet. *Contributions to Mineralogy and Petrology* 167: 1–22

Capitani Cd, Petrakakis K (2010) The computation of equilibrium assemblage diagrams with Theriak/Domino software. *American Mineralogist* 95: 1006–1016

Carlson WD (2006) Rates of Fe, Mg, Mn, and Ca diffusion in garnet. *American Mineralogist* 91: 1–11

Carter LB, Skora S, Blundy JD, De Hoog JCM, Elliott T (2015) An experimental study of trace element fluxes from subducted oceanic crust. *Journal of Petrology* 56: 1585–1606

Chakhmouradian AR (2006) High-field-strength elements in carbonatitic rocks: geochemistry, crystal chemistry and significance for constraining the sources of carbonatites. *Chemical Geology* 235: 138–160

Chakrabarti R, Basu AR, Ghatak A (2012) Chemical geodynamics of western Anatolia. *International Geology Review* 54: 227–248

Chakraborty S, Ganguly J (1992) Cation diffusion in aluminosilicate garnets: experimental determination in spessartine-almandine diffusion couples, evaluation of effective binary diffusion coefficients, and applications. *Contributions to Mineralogy and petrology* 111: 74–86

Cherniak DJ, Manchester J, Watson EB (2007) Zr and Hf diffusion in rutile. *Earth and Planetary Science Letters* 261: 267–279

Chopin C (1984) Coesite and pure pyrope in high-grade blueschists of the Western Alps: a first record and some consequences. *Contributions to Mineralogy and Petrology* 86: 107–118

Chu X, Ague JJ (2015) Analysis of experimental data on divalent cation diffusion kinetics in aluminosilicate garnets with application to timescales of peak Barrovian metamorphism, Scotland. *Contributions to Mineralogy and Petrology* 170: 25

Class C, Lehnert K (2012) PetDB expert MORB (mid-ocean ridge basalt) compilation. *EarthChem Library* doi:10.1594/IEDA/100060

Coggon R, Holland TJB (2002) Mixing properties of phengitic micas and revised garnet-phengite thermobarometers. *Journal of Metamorphic Geology* 20: 683–696

Condamine P, Médard E (2014) Experimental melting of phlogopite-bearing mantle at 1 GPa: Implications for potassic magmatism. *Earth and Planetary Science Letters* 397: 80–92

Conticelli S (1998) The effect of crustal contamination on ultrapotassic magmas with lamproitic affinity: mineralogical, geochemical and isotope data from the Torre Alfina lavas and xenoliths, Central Italy. *Chemical Geology* 149: 51–81

Conticelli S, Guarnieri L, Farinelli A, Mattei M, Avanzinelli R, Bianchini G, Boari E, Tommasini S, Tiepolo M, Prelević D, Venturelli G (2009) Trace elements and Sr–Nd–Pb isotopes of K-rich, shoshonitic, and calc-alkaline magmatism of the Western Mediterranean Region: genesis of ultrapotassic to calc-alkaline magmatic associations in a post-collisional geodynamic setting. *Lithos* 107: 68–92

Coyle DA, Wagner GA (1998) Positioning the titanite fission-track partial annealing zone. *Chemical Geology* 149: 117–125

Crank J (1975) *The mathematics of diffusion*. Oxford University Press. 414 pp.

Dasgupta R, Hirschmann MM, McDonough WF, Spiegelman M, Withers AC (2009) Trace element partitioning between garnet lherzolite and carbonatite at 6.6 and 8.6 GPa with applications to the geochemistry of the mantle and of mantle-derived melts. *Chemical Geology* 262: 57–77

Davidson J, Turner S, Handley H, Macpherson C, Dosseto A (2007) Amphibole "sponge" in arc crust? *Geology* 35: 787–790

Delesse A (1856) Mémoire sur la minette. *Annales des Mines* 10: 317–379

Diener JFA, Powell R (2012) Revised activity–composition models for clinopyroxene and amphibole. *Journal of Metamorphic Geology* 30: 131–142

Diener JFA, Powell R, White RW, Holland TJB (2007) A new thermodynamic model for clino- and orthoamphiboles in the system Na_2O–CaO–FeO–MgO–Al_2O_3–SiO_2–H_2O–O. *Journal of Metamorphic Geology* 25: 631–656

Dilek Y, Altunkaynak Ş (2009) Geochemical and temporal evolution of Cenozoic magmatism in western Turkey: mantle response to collision, slab break-off, and lithospheric tearing in an orogenic belt. In: Van Hinsbergen DJJ, Edwards MA, Govers R (eds.) *Collision and Collapse at the Africa–Arabia–Eurasia Subduction Zone*, vol. 311 of *Special Publications*, 213–233, Geological Society, London

Dinter DA (1998) Late Cenozoic extension of the Alpine collisional orogen, northeastern Greece: Origin of the north Aegean basin. *Geological Society of America Bulletin* 110: 1208–1230

Dombrowski A, Okrusch M, Richter P, Henjes-Kunst F, Höhndorf A, Kröner A (1995) Orthogneisses in the Spessart Crystalline Complex, north-west Bavaria: Silurian granitoid magmatism at an active continental margin. *Geologische Rundschau* 84: 399–411

Dörr W, Zulauf G, Gerdes A, Loeckle F (2017) Provenance of Upper Devonian clastic (meta)sediments of the Böllstein Odenwald (Mid-German-Crystalline-Zone, Variscides). *International Journal of Earth Sciences* doi:10.1007/s00 531–017–1473–x

Downes H, Macdonald RAY, Upton BGJ, Cox KG, Bodinier Jl, Mason PRD, James D, Hill PG, Hearn BC (2004) Ultramafic xenoliths from the Bearpaw Mountains, Montana, USA: Evidence for multiple metasomatic events in the lithospheric mantle beneath the Wyoming craton. *Journal of Petrology* 45: 1631–1662

Duda A, Schmincke HU (1985) Polybaric differentiation of alkali basaltic magmas: evidence from green-core clinopyroxenes (Eifel, FRG). *Contributions to Mineralogy and Petrology* 91: 340–353

Duggen S, Hoernle K, van den Bogaard P, Garbe-Schönberg D (2005) Post-collisional transition from subduction- to intraplate-type magmatism in the Westernmost Mediterranean: Evidence for continental-edge delamination of subcontinental lithosphere. *Journal of Petrology* 46: 1155

Eckert JO, Newton RC, Kleppa OJ (1991) The ΔH of reaction and recalibration of garnet-pyroxene-plagioclase-quartz geobarometers in the CMAS system by solution calorimetry. *American Mineralogist* 76: 148–160

Eisbacher GH, Lüschen E, Wickert F (1989) Crustal-scale thrusting and extension in the Hercynian Schwarzwald and Vosges, central Europe. *Tectonics* 8: 1–21

Elitok Ö, Özgür N, Drüppel K, Dilek Y, Platevoet B, Guillou H, Poisson A, Scaillet S, Satır M, Siebel W, Bardintzeff JM, Deniel C, Yılmaz K (2010) Origin and geodynamic evolution of late Cenozoic potassium-rich volcanism in the Isparta area, southwestern Turkey. *International Geology Review* 52: 454–504

Elliott T (2003) Tracers of the slab. In: Eiler J (ed.) *Inside the subduction factory*, vol. 138 of *Geophysical Monograph*, 23–45, American Geophysical Union, Washington, D. C

Erambert M, Austrheim H (1993) The effect of fluid and deformation on zoning and inclusion patterns in poly-metamorphic garnets. *Contributions to Mineralogy and Petrology* 115: 204–214

Ersoy EY, Palmer MR (2013) Eocene-Quaternary magmatic activity in the Aegean: Implications for mantle metasomatism and magma genesis in an evolving orogeny. *Lithos* 180–181: 5 – 24

Ersoy YE, Helvacı C, Palmer MR (2012) Petrogenesis of the Neogene volcanic units in the NE–SW-trending basins in western Anatolia, Turkey. *Contributions to Mineralogy and Petrology* 163: 379–401

Ertan IE, Leeman WP (1996) Metasomatism of Cascades subarc mantle: evidence from a rare phlogopite orthopyroxenite xenolith. *Geology* 24: 451–454

Esperança S, Holloway JR (1987) On the origin of some mica-lamprophyres: experimental evidence from a mafic minette. *Contributions to Mineralogy and Petrology* 95: 207–216

Faccenna C, Jolivet L, Piromallo C, Morelli A (2003) Subduction and the depth of convection in the Mediterranean mantle. *Journal of Geophysical Research: Solid Earth* 108, 2099

Faccenna C, Piromallo C, Crespo-Blanc A, Jolivet L, Rossetti F (2004) Lateral slab deformation and the origin of the western Mediterranean arcs. *Tectonics* 23, tC1012

Feenstra A, Petrakakis K, Rhede D (2007) Variscan relicts in Alpine high-P pelitic rocks from Samos (Greece): evidence from multi-stage garnet and its included minerals. *Journal of Metamorphic Geology* 25: 1011–1033

Ferrari L (2004) Slab detachment control on mafic volcanic pulse and mantle heterogeneity in central Mexico. *Geology* 32: 77–80

Foley S (1992) Vein-plus-wall-rock melting mechanisms in the lithosphere and the origin of potassic alkaline magmas. *Lithos* 28: 435–453

Foley SF, Venturelli G, Green DH, Toscani L (1987) The ultrapotassic rocks: Characteristics, classification, and constraints for petrogenetic models. *Earth-Science Reviews* 24: 81 – 134

Francalanci L, Vougioukalakis GE, Perini G, Manetti P (2005) A West-East Traverse along the magmatism of the south Aegean volcanic arc in the light of volcanological, chemical and isotope data. In: Fytikas M, Vougioukalakis GE (eds.) *The South Aegean Active Volcanic ArcPresent Knowledge and Future Perspectives*, vol. 7 of *Developments in Volcanology*, 65 – 111, Elsevier

Franke W (2000) The mid-European segment of the Variscides: tectonostratigraphic units, terrane boundaries and plate tectonic evolution. In: Franke W, Haak V, Oncken O, Tanner D (eds.) *Orogenic Processes: Quantification and Modeling in the Variscan Belt*, vol. 179 of *Special Publications*, 35–61, Geological Society, London

Franke W, Cocks LRM, Torsvik TH (2017) The Palaeozoic Variscan oceans revisited. *Gondwana Research* 48: 257–284

Fumagalli P, Zanchetta S, Poli S (2009) Alkali in phlogopite and amphibole and their effects on phase relations in metasomatized peridotites: a high-pressure study. *Contributions to Mineralogy and Petrology* 158: 723

Furman T, Graham D (1999) Erosion of lithospheric mantle beneath the East African Rift system: geochemical evidence from the Kivu volcanic province. *Lithos* 48: 237–262

Fytikas M, Innocenti F, Manetti P, Peccerillo A, Mazzuoli R, Villari L (1984) Tertiary to Quaternary evolution of volcanism in the Aegean region. *Geological Society, London, Special Publications* 17: 687–699

Gaidies F, Pattison DRM, De Capitani C (2011) Toward a quantitative model of metamorphic nucleation and growth. *Contributions to Mineralogy and Petrology* 162: 975

Gasperini D, Blichert-Toft J, Bosch D, Del Moro A, Macera P, Albarède F (2002) Upwelling of deep mantle material through a plate window: Evidence from the geochemistry of Italian basaltic volcanics. *Journal of Geophysical Research: Solid Earth* 107: B12, 2367

Gerdes A, Wörner G, Finger F (2000) Hybrids, magma mixing and enriched mantle melts in post-collisional Variscan granitoids: the Rastenberg Pluton, Austria. *Geological Society, London, Special Publications* 179: 415–431

Gerstenberger H, Haase G (1997) A highly effective emitter substance for mass spectrometric Pb isotope ratio determinations. *Chemical Geology* 136: 309 – 312

Godard G, Mabit JL (1998) Peraluminous sapphirine formed during retrogression of a kyanite-bearing eclogite from Pays de Léon, Armorican Massif, France. *Lithos* 43: 15–29

Govers R, Wortel MJR (2005) Lithosphere tearing at STEP faults: response to edges of subduction zones. *Earth and Planetary Science Letters* 236: 505 – 523

Govindaraju K (1994) 1994 compilation of working values and sample description for 383 geostandards. *Geostandards Newsletter* 18: 1–158

Green DH, Falloon TJ (1998) Pyrolite: a Ringwood concept and its current expression. In: Jackson I (ed.) *The Earth's mantle: composition, structure, and evolution*, 311–378, Cambridge University Press

Green DH, Wallace ME (1988) Mantle metasomatism by ephemeral carbonatite melts. *Nature* 336: 459–462

Green DH, Hibberson WO, Rosenthal A, Kovács I, Yaxley GM, Falloon TJ, Brink F (2014) Experimental study of the influence of water on melting and phase assemblages in the upper mantle. *Journal of Petrology* 55: 2067–2096

Green E, Holland T, Powell R (2007) An order-disorder model for omphacitic pyroxenes in the system jadeite-diopside-hedenbergite-acmite, with applications to eclogitic rocks. *American Mineralogist* 92: 1181–1189

Green TH, Pearson NJ (1987) An experimental study of Nb and Ta partitioning between Ti-rich minerals and silicate liquids at high pressure and temperature. *Geochimica et Cosmochimica Acta* 51: 55–62

Grégoire M, McInnes BI, O'Reilly SY (2001) Hydrous metasomatism of oceanic sub-arc mantle, Lihir, Papua New Guinea: Part 2. Trace element characteristics of slab-derived fluids. *Lithos* 59: 91–108

Gudfinnsson GH, Presnall DC (2005) Continuous gradations among primary carbonatitic, kimberlitic, melilititic, basaltic, picritic, and komatiitic melts in equilibrium with garnet lherzolite at 3–8 GPa. *Journal of Petrology* 46: 1645–1660

Gvirtzman Z, Nur A (1999) The formation of Mount Etna as the consequence of slab rollback. *Nature* 401: 782–785

Hacker BR, Kelemen PB, Behn MD (2011) Differentiation of the continental crust by relamination. *Earth and Planetary Science Letters* 307: 501–516

Haifler J, Kotková J (2016) UHP–UHT peak conditions and near-adiabatic exhumation path of diamond-bearing garnet–clinopyroxene rocks from the Eger Crystalline Complex, North Bohemian Massif. *Lithos* 248: 366–381

Hames WE, Menard T (1993) Fluid-assisted modification of garnet composition along rims, cracks, and mineral inclusion boundaries in samples of amphibolite facies schists. *American Mineralogist* 78: 338–344

Hammouda T, Laporte D (2000) Ultrafast mantle impregnation by carbonatite melts. *Geology* 28: 283–285

Handley HK, Macpherson CG, Davidson JP, Berlo K, Lowry D (2007) Constraining fluid and sediment contributions to subduction-related magmatism in Indonesia: Ijen Volcanic Complex. *Journal of Petrology* 48: 1155–1183

Hanel M, Lippolt HJ, Kober B, Wimmenauer W (1993) Lower carboniferous granulites in the Schwarzwald basement near Hohengeroldseck (SW Germany). *Naturwissenschaften* 80: 25–28

Hanyu T, Tatsumi Y, Nakai S, Chang Q, Miyazaki T, Sato K, Tani K, Shibata T, Yoshida T (2006) Contribution of slab melting and slab dehydration to magmatism in the NE Japan arc for the last 25 Myr: Constraints from geochemistry. *Geochemistry, Geophysics, Geosystems* 7: Q08 002

Hart SR (1984) A large-scale isotope anomaly in the Southern Hemisphere mantle. *Nature* 309: 753–757

Harte B, Hunter RH, Kinny PD (1993) Melt geometry, movement and crystallization, in relation to mantle dykes, veins and metasomatism. *Philosophical Transactions of the Royal Society of London A: Mathematical, Physical and Engineering Sciences* 342: 1–21

Hasalová P, Schulmann K, Tabaud AS, Oliot E (2015) Microstructural evidences for mineralogical inheritance in partially molten rocks: example from the Vosges Mts. *Bulletin de la Société Géologique de France* 186: 131–143

Hawthorne FC, Oberti R, Harlow GE, Maresch WV, Martin RF, Schumacher JC, Welch MD (2012) Nomenclature of the amphibole supergroup. *American Mineralogist* 97: 2031–2048

Hegner E, Kölbl-Ebert M, Loeschke J (1998) Post-collisional Variscan lamprophyres (Black Forest, Germany): $^{40}Ar/^{39}Ar$ phlogopite dating, Nd, Pb, Sr isotope, and trace element characteristics. *Lithos* 45: 395–411

Henes-Klaiber U (1992) *Zur Geochemie der variszischen Granitoide des Bergsträsser Odenwalds*. Dissertation, Universität Karlsruhe. 264 pp.

Hermann J (2002) Allanite: thorium and light rare earth element carrier in subducted crust. *Chemical Geology* 192: 289–306

Hermann J, Green DH (2001) Experimental constraints on high pressure melting in subducted crust. *Earth and Planetary Science Letters* 188: 149–168

Hermann J, Rubatto D (2009) Accessory phase control on the trace element signature of sediment melts in subduction zones. *Chemical Geology* 265: 512–526

Hermann J, Spandler CJ (2008) Sediment melts at sub-arc depths: an experimental study. *Journal of Petrology* 49: 717–740

Hermann J, Spandler C, Hack A, Korsakov AV (2006) Aqueous fluids and hydrous melts in high-pressure and ultra-high pressure rocks: implications for element transfer in subduction zones. *Lithos* 92: 399–417

Hess JC, Schmidt G (1989) Zur Altersstellung der Kataklasite im Bereich der Otzberg-Zone, Odenwald. *Geol Jb Hessen* 117: 69–77

Hess JC, Lippolt HJ, Kober B (1995) The age of the Kagenfels granite (northern Vosges) and its bearing on the intrusion scheme of late Variscan granitoids. *Geologische Rundschau* 84: 568–577

Hill E, Blundy JD, Wood BJ (2011) Clinopyroxene–melt trace element partitioning and the development of a predictive model for HFSE and Sc. *Contributions to Mineralogy and Petrology* 161: 423–438

van Hinsbergen DJJ, Boekhout F (2009) Neogene brittle detachment faulting on Kos (E Greece): implications for a southern break-away fault of the Menderes metamorphic core complex (western Turkey). *Geological Society, London, Special Publications* 311: 311–320

Hofmann AW (1988) Chemical differentiation of the Earth: the relationship between mantle, continental crust, and oceanic crust. *Earth and Planetary Science Letters* 90: 297–314

Hofmann AW, Jochum KP, Seufert M, White WM (1986) Nb and Pb in oceanic basalts: new constraints on mantle evolution. *Earth and Planetary Science Letters* 79: 33–45

Holland T, Powell R (2003) Activity–composition relations for phases in petrological calculations: an asymmetric multicomponent formulation. *Contributions to Mineralogy and Petrology* 145: 492–501

Holland TJB (1980) The reaction albite= jadeite+ quartz determined experimentally in the range 600-1200!' C. *American Mineralogist* 65: 129–134

Holland TJB, Powell R (1998) An internally consistent thermodynamic data set for phases of petrological interest. *Journal of metamorphic Geology* 16: 309–343

Hollister LS (1970) Origin, mechanism, and consequences of compositional sector-zoning in staurolite. *American Mineralogist* 55: 742–766

Horn I, Hinton RW, Jackson SE, Longerich HP (1997) Ultra-Trace Element Analysis of NIST SRM 616 and 614 using Laser Ablation Microprobe-Inductively Coupled Plasma-Mass Spectrometry (LAM-ICP-MS): a Comparison with Secondary Ion Mass Spectrometry (SIMS). *Geostandards Newsletter* 21: 191–203

Ionov DA, Hofmann AW (1995) Nb-Ta-rich mantle amphiboles and micas: Implications for subduction-related metasomatic trace element fractionations. *Earth and Planetary Science Letters* 131: 341–356

Ionov DA, Dupuy C, O'Reilly SY, Kopylova MG, Genshaft YS (1993) Carbonated peridotite xenoliths from Spitsbergen: implications for trace element signature of mantle carbonate metasomatism. *Earth and Planetary Science Letters* 119: 283–297

Janoušek V, Holub FV (2007) The causal link between HP-HT metamorphism and ultrapotassic magmatism in collisional orogens: case study from the Moldanubian Zone of the Bohemian Massif. *Proceedings of the Geologists' Association* 118: 75–86

Janoušek V, Finger F, Roberts M, Frỳda J, Pin C, Dolejš D (2004) Deciphering the petrogenesis of deeply buried granites: whole-rock geochemical constraints on the origin of largely undepleted felsic granulites from the Moldanubian Zone of the Bohemian Massif. *Geological Society of America Special Papers* 389: 141–159

Johnston AD, Wyllie PJ (1989) The system tonalite-peridotite-H_2O at 30 kbar, with applications to hybridization in subduction zone magmatism. *Contributions to Mineralogy and Petrology* 102: 257–264

Jolivet L (2001) A comparison of geodetic and finite strain pattern in the Aegean, geodynamic implications. *Earth and Planetary Science Letters* 187: 95–104

Juteau M, Michard A, Albarede F (1986) The Pb-Sr-Nd isotope geochemistry of some recent circum-Mediterranean granites. *Contributions to Mineralogy and Petrology* 92: 331–340

Kalt A, Altherr R, Ludwig T (1998) Contact metamorphism in pelitic rocks on the island of Kos (Greece, Eastern Aegean Sea): a test for the Na-in-cordierite thermometer. *Journal of Petrology* 39: 663–688

Kemp AIS, Hawkesworth CJ (2003) Granitic Perspectives on the Generation and Secular Evolution of the Continental Crust. In: Holland HD, Turekian KK (eds.) *The crust*, vol. 3 of *Treatise on Geochemistry*, 349–410, Elsevier Ltd

Kirchenbaur M, Münker C (2015) The behaviour of the extended HFSE group (Nb, Ta, Zr, Hf, W, Mo) during the petrogenesis of mafic K-rich lavas: The Eastern Mediterranean case. *Geochimica et Cosmochimica Acta* 165: 178–199

Kirchenbaur M, Münker C, Schuth S, Garbe-Schönberg D, Marchev P (2012) Tectonomagmatic Constraints on the Sources of Eastern Mediterranean K-rich Lavas. *Journal of Petrology* 53: 27

Kirsch H, Kober B, Lippolt HJ (1988) Age of intrusion and rapid cooling of the Frankenstein gabbro (Odenwald, SW-Germany) evidenced by $^{40}Ar/^{39}Ar$ and single-zircon $^{207}Pb/^{206}Pb$ measurements. *Geologische Rundschau* 77: 693–711

Klaver M, Djuly T, de Graaf S, Sakes A, Wijbrans J, Davies G, Vroon P (2015) Temporal and spatial variations in provenance of Eastern Mediterranean Sea sediments: Implications for Aegean and Aeolian arc volcanism. *Geochimica et Cosmochimica Acta* 153: 149–168

Klaver M, Davies GR, Vroon PZ (2016) Subslab mantle of African provenance infiltrating the Aegean mantle wedge. *Geology* 44: 367–370

Klemm G (1924) Über die Minetten, Vogesite und Kersantite des Odenwaldes. *Notizblatt des Vereins für Erdkunde und der Hessischen Geologischen Landesanstalt zu Darmstadt* 5: 5–27

Klemme S, Van der Laan SR, Foley SF, Günther D (1995) Experimentally determined trace and minor element partitioning between clinopyroxene and carbonatite melt under upper mantle conditions. *Earth and Planetary Science Letters* 133: 439–448

Klemme S, Blundy JD, Wood BJ (2002) Experimental constraints on major and trace element partitioning during partial melting of eclogite. *Geochimica et Cosmochimica Acta* 66: 3109–3123

Klemme S, Prowatke S, Hametner K, Günther D (2005) Partitioning of trace elements between rutile and silicate melts: implications for subduction zones. *Geochimica et Cosmochimica Acta* 69: 2361–2371

Klimm K, Blundy JD, Green TH (2008) Trace element partitioning and accessory phase saturation during H_2O-saturated melting of basalt with implications for subduction zone chemical fluxes. *Journal of Petrology* 49: 523–553

Kober B, Kalt A, Hanel M, Pidgeon RT (2004) SHRIMP dating of zircons from high-grade metasediments of the Schwarzwald/SW-Germany and implications for the evolution of the Moldanubian basement. *Contributions to Mineralogy and Petrology* 147: 330–345

Kohn MJ (2004) Oscillatory-and sector-zoned garnets record cyclic (?) rapid thrusting in central Nepal. *Geochemistry, Geophysics, Geosystems* 5

Konrad-Schmolke M, O'Brien PJ, de Capitani C, Carswell DA (2008) Garnet growth at high-and ultra-high pressure conditions and the effect of element fractionation on mineral modes and composition. *Lithos* 103: 309–332

Kopf A, Mascle J, Klaeschen D (2003) The Mediterranean Ridge: A mass balance across the fastest growing accretionary complex on Earth. *Journal of Geophysical Research: Solid Earth* 108

Kotková J, Janák M (2015) UHP kyanite eclogite associated with garnet peridotite and diamond-bearing granulite, northern Bohemian Massif. *Lithos* 226: 255–264

Kotková J, Schaltegger U, Leichmann J (2010) Two types of ultrapotassic plutonic rocks in the Bohemian Massif—Coeval intrusions at different crustal levels. *Lithos* 115: 163–176

Kotková J, O'Brien PJ, Ziemann MA (2011) Diamond and coesite discovered in Saxony-type granulite: Solution to the Variscan garnet peridotite enigma. *Geology* 39: 667–670

Kotková J, Whitehouse M, Schaltegger U, D'Abzac FX (2016) The fate of zircon during UHT–UHP metamorphism: isotopic (U/Pb, δ18O, Hf) and trace element constraints. *Journal of Metamorphic Geology* 34: 719–739

Krmíček L, Romer RL, Ulrych J, Glodny J, Prelević D (2016) Petrogenesis of orogenic lamproites of the Bohemian Massif: Sr–Nd–Pb–Li isotope constraints for Variscan enrichment of ultra-depleted mantle domains. *Gondwana Research* 35: 198–216

Krogh Ravna E (2000) The garnet–clinopyroxene Fe^{2+}–Mg geothermometer: an updated calibration. *Journal of metamorphic Geology* 18: 211–219

Kroner U, Romer RL (2013) Two plates–many subduction zones: the Variscan orogeny reconsidered. *Gondwana Research* 24: 298–329

Küstner W (2000) K-Ar-Datierungen an detritischen Muskoviten und Sm-Nd-Modellalter prä- und synorogener schwach metamorpher Sedimente im Rhenoherzynikum-Grundlegende Daten zur Quantifizierung orogener Prozesse am Beispiel der Varisziden. *Unpublished PhD Thesis, Göttingen: p* 85

Lahner L, Toloczyki M (2004) Geowissenschaftliche Karte der Bundesrepublik Deutschland 1: 2.000. 000. *Geologie, Bundesanstalt für Geowissenschaften und Rohstoffe, Hannover*

Lambert IB, Wyllie PJ (1972) Melting of gabbro (quartz eclogite) with excess water to 35 kilobars, with geological applications. *The Journal of Geology* 80: 693–708

Le Maitre RW (2002) *Igneous rocks: A classification and glossary of terms*. Cambridge University Press. 236 pp.

Le Pichon X, Angelier J (1979) The Hellenic arc and trench system: a key to the neotectonic evolution of the eastern Mediterranean area. *Tectonophysics* 60: 1–42

Lee CTA, Leeman WP, Canil D, Li ZXA (2005) Similar V/Sc systematics in MORB and arc basalts: implications for the oxygen fugacities of their mantle source regions. *Journal of Petrology* 46: 2313–2336

Leslie RAJ, Danyushevsky LV, Crawford AJ, Verbeeten AC (2009) Primitive shoshonites from Fiji: Geochemistry and source components. *Geochemistry, Geophysics, Geosystems* 10: Q07 001

Liati A, Seidel E (1996) Metamorphic evolution and geochemistry of kyanite eclogites in central Rhodope, northern Greece. *Contributions to Mineralogy and Petrology* 123: 293–307

Liew TC, Hofmann AW (1988) Precambrian crustal components, plutonic associations, plate environment of the Hercynian Fold Belt of central Europe: indications from a Nd and Sr isotopic study. *Contributions to Mineralogy and Petrology* 98: 129–138

Linnemann U, Gerdes A, Drost K, Buschmann B (2007) The continuum between Cadomian orogenesis and opening of the Rheic Ocean: Constraints from LA-ICP-MS U-Pb zircon dating and analysis of plate-tectonic setting (Saxo-Thuringian zone, northeastern Bohemian Massif, Germany). *Geological Society of America Special Papers* 423: 61–96

Lippolt HJ, Kirsch H (1994) Ar^{40}/Ar^{39}–Untersuchungen an serizitisierten Plagioklasen des Frankenstein-Gabbros (NW-Odenwald) in Hinblick auf ihren Alterations-Zeitpunkt. *Geologisches Jahrbuch Hessen* 122: 123–142

Liu Q, Hermann J, Zhang J (2013) Polyphase inclusions in the Shuanghe UHP eclogites formed by subsolidus transformation and incipient melting during exhumation of deeply subducted crust. *Lithos* 177: 91–109

Ludwig K (2012) User's manual for Isoplot version 3.75: a geochronological toolkit for Microsoft Excel. *Berkley Geochronological Center Special Publication* 5

Lustrino M, Wilson M (2007) The circum-Mediterranean anorogenic Cenozoic igneous province. *Earth-Science Reviews* 81: 1–65

Luvizotto GL, Zack T, Meyer HP, Ludwig T, Triebold S, Kronz A, Münker C, Stockli DF, Prowatke S, Klemme S, Jacob DE, von Eynatten H (2009) Rutile crystals as potential trace element and isotope mineral standards for microanalysis. *Chemical Geology* 261: 346–369

Makris J, Stobbe C (1984) Physical properties and state of the crust and upper mantle of the Eastern Mediterranean Sea deduced from geophysical data. *Marine Geology* 55: 347–363

Malaspina N, Hermann J, Scambelluri M, Compagnoni R (2006) Polyphase inclusions in garnet–orthopyroxenite (Dabie Shan, China) as monitors for metasomatism and fluid-related trace element transfer in subduction zone peridotite. *Earth and Planetary Science Letters* 249: 173–187

Mallik A, Nelson J, Dasgupta R (2015) Partial melting of fertile peridotite fluxed by hydrous rhyolitic melt at 2–3 GPa: implications for mantle wedge hybridization by sediment melt and generation of ultrapotassic magmas in convergent margins. *Contributions to Mineralogy and Petrology* 169: 1–24

Mallik A, Dasgupta R, Tsuno K, Nelson J (2016) Effects of water, depth and temperature on partial melting of mantle-wedge fluxed by hydrous sediment-melt in subduction zones. *Geochimica et Cosmochimica Acta* 195: 226–243

Marschall HR, Kalt A, Hanel M (2003) P–T evolution of a Variscan lower-crustal segment: a study of granulites from the Schwarzwald, Germany. *Journal of Petrology* 44: 227–253

Massonne HJ (2003) A comparison of the evolution of diamondiferous quartz-rich rocks from the Saxonian Erzgebirge and the Kokchetav Massif: are so-called diamondiferous gneisses magmatic rocks? *Earth and Planetary Science Letters* 216: 347–364

Matsuda J, Senoh K, Maruoka T, Sato H, Mitropoulos P (1999) K-Ar ages of the Aegean volcanic rocks and their implication for the arc-trench system. *Geochemical Journal* 33: 369–377

McDonough WF, Sun SS (1995) The composition of the Earth. *Chemical geology* 120: 223–253

McKenzie D, O'Nions RK (1995) The source regions of ocean island basalts. *Journal of petrology* 36: 133–159

Médard E, Schmidt MW, Schiano P, Ottolini L (2006) Melting of amphibole-bearing wehrlites: an experimental study on the origin of ultra-calcic nepheline-normative melts. *Journal of Petrology* 47: 481–504

Medaris G, Ducea M, Ghent E, Iancu V (2003) Conditions and timing of high-pressure Variscan metamorphism in the South Carpathians, Romania. *Lithos* 70: 141–161

Melleton J, Cocherie A, Faure M, Rossi P (2010) Precambrian protoliths and Early Paleozoic magmatism in the French Massif Central: U–Pb data and the North Gondwana connection in the west European Variscan belt. *Gondwana Research* 17: 13–25

Meulenkamp JE, Wortel MJR, Van Wamel WA, Spakman W, Strating EH (1988) On the Hellenic subduction zone and the geodynamic evolution of Crete since the late Middle Miocene. *Tectonophysics* 146: 203–215

Mitchell RH, Bergman SC (1991) *Petrology of lamproites*. Springer Science & Business Media. 447 pp.

Möller C (1999) Sapphirine in SW Sweden: a record of Sveconorwegian (-Grenvillian) late-orogenic tectonic exhumation. *Journal of Metamorphic Geology* 17: 127–141

Montel JM (1986) Experimental determination of the solubility of Ce-monazite in SiO_2-Al_2O_3-K_2O-Na_2O melts at 800 °C, 2 kbar, under H_2O-saturated conditions. *Geology* 14: 659–662

Münker C, Pfänder JA, Weyer S, Büchl A, Kleine T, Mezger K (2003) Evolution of planetary cores and the Earth-Moon system from Nb/Ta systematics. *Science* 301: 84–87

Münker C, Wörner G, Yogodzinski G, Churikova T (2004) Behaviour of high field strength elements in subduction zones: constraints from Kamchatka–Aleutian arc lavas. *Earth and Planetary Science Letters* 224: 275–293

Nagasaki A, Enami M (1998) Sr-bearing zoisite and epidote in ultra-high pressure (UHP) metamorphic rocks from the Su-Lu province, eastern China: An important Sr reservoir under UHP conditions. *American Mineralogist* 83: 240–247

Nahodilová R, Faryad SW, Dolejš D, Tropper P, Konzett J (2011) High-pressure partial melting and melt loss in felsic granulites in the Kutná Hora complex, Bohemian Massif (Czech Republic). *Lithos* 125: 641–658

Nakamura Y (1973) Origin of sector-zoning of igneous clinopyroxenes. *American Mineralogist* 58: 986–990

Nance RD, Gutiérrez-Alonso G, Keppie JD, Linnemann U, Murphy JB, Quesada C, Strachan RA, Woodcock NH (2012) A brief history of the Rheic Ocean. *Geoscience Frontiers* 3: 125–135

Niida K, Green DH (1999) Stability and chemical composition of pargasitic amphibole in MORB pyrolite under upper mantle conditions. *Contributions to Mineralogy and Petrology* 135: 18–40

Niu Y, O'Hara MJ (2003) Origin of ocean island basalts: A new perspective from petrology, geochemistry, and mineral physics considerations. *Journal of Geophysical Research: Solid Earth* 108

O'Brien PJ, Rötzler J (2003) High-pressure granulites: Formation, recovery of peak conditions and implications for tectonics. *Journal of Metamorphic Geology* 21: 3–20

Okrusch M (1995) IV.E. Metamorphic evolution. In: Dallmeyer RD, Franke W, Weber K (eds.) *Pre-Permian Geology of Central and Eastern Europe*, 201–213, Springer, Berlin Heidelberg

Owen JP (2008) Geochemistry of lamprophyres from the Western Alps, Italy: implications for the origin of an enriched isotopic component in the Italian mantle. *Contributions to Mineralogy and Petrology* 155: 341–362

Papanikolaou D, Nomikou PV (1998) The Palaeozoic of Kos: A low grade metamorphic unit of the basement of the External Hellenides Terrane. *Special Publications of the Geological Society of Greece* 3: 155–166

Pattison DRM, De Capitani C, Gaidies F (2011) Petrological consequences of variations in metamorphic reaction affinity. *Journal of Metamorphic Geology* 29: 953–977

Pe-Piper G (1994) Lead isotopic compositions of Neogene volcanic rocks from the Aegean extensional area. *Chemical Geology* 118: 27–41

Pe-Piper G, Moulton B (2008) Magma evolution in the Pliocene–Pleistocene succession of Kos, South Aegean arc (Greece). *Lithos* 106: 110 – 124

Pe-Piper G, Zhang Y, Piper DJ, Prelević D (2014) Relationship of Mediterranean type lamproites to large shoshonite volcanoes, Miocene of Lesbos, NE Aegean Sea. *Lithos* 184–187: 281 – 299

Pearce NJG, Perkins WT, Westgate JA, Gorton MP, Jackson SE, Neal CR, Chenery SP (1997) A compilation of new and published major and trace element data for NIST SRM 610 and NIST SRM 612 glass reference materials. *Geostandards Newsletter* 21: 115–144

Peate DW, Pearce JA, Hawkesworth CJ, Colley H, Edwards CMH, Hirose K (1997) Geochemical variations in Vanuatu arc lavas: the role of subducted material and a variable mantle wedge composition. *Journal of Petrology* 38: 1331–1358

Peccerillo A (1999) Multiple mantle metasomatism in central-southern Italy: geochemical effects, timing and geodynamic implications. *Geology* 27: 315–318

Peccerillo A, Taylor SR (1976) Geochemistry of Eocene calc-alkaline volcanic rocks from the Kastamonu area, northern Turkey. *Contributions to mineralogy and petrology* 58: 63–81

Pertermann M, Hirschmann MM, Hametner K, Günther D, Schmidt MW (2004) Experimental determination of trace element partitioning between garnet and silica-rich liquid during anhydrous partial melting of MORB-like eclogite. *Geochemistry, Geophysics, Geosystems* 5

Pfaff K, Romer RL, Markl G (2009) U-Pb ages of ferberite, chalcedony, agate, 'U-mica' and pitchblende: constraints on the mineralization history of the Schwarzwald ore district. *European Journal of Mineralogy* 21: 817–836

Pfänder JA, Jung S, Münker C, Stracke A, Mezger K (2012) A possible high Nb/Ta reservoir in the continental lithospheric mantle and consequences on the global Nb budget–Evidence from continental basalts from Central Germany. *Geochimica et Cosmochimica Acta* 77: 232–251

Pilet S (2015) Generation of low-silica alkaline lavas: Petrological constraints, models, and thermal implications. *Geological Society of America Special Papers* 514: SPE514–17

Pilet S, Baker MB, Stolper EM (2008) Metasomatized lithosphere and the origin of alkaline lavas. *Science* 320: 916–919

Pirard C, Hermann J (2015) Focused fluid transfer through the mantle above subduction zones. *Geology* 43: 915–918

Piromallo C, Morelli A (2003) P wave tomography of the mantle under the Alpine-Mediterranean area. *Journal of Geophysical Research: Solid Earth* 108, b2, 2065

Plank T (2005) Constraints from thorium/lanthanum on sediment recycling at subduction zones and the evolution of the continents. *Journal of Petrology* 46: 921–944

Plank T, Langmuir CH (1998) The chemical composition of subducting sediment and its consequences for the crust and mantle. *Chemical geology* 145: 325–394

Poli S, Fumagalli P (2003) Mineral assemblages in ultrahigh pressure metamorphism: a review of experimentally determined phase diagrams. In: Carswell DA, Compagnoni R (eds.) *Ultrahigh pressure metamorphism*, vol. 5 of *Notes in Mineralogy*, 307–340, European Mineralogical Union

Pouchou JL, Pichoir F (1984) A new model for quantitative analyses. I. Application to the analysis of homogeneous samples. *La Recherche Aérospatiale* 3: 13–38

Pouchou JL, Pichoir F (1985) PAP correction procedure for improved quantitative microanalysis. *Microbeam Analysis* 104–106

Prelević D, Foley SF (2007) Accretion of arc-oceanic lithospheric mantle in the Mediterranean: evidence from extremely high-Mg olivines and Cr-rich spinel inclusions in lamproites. *Earth and Planetary Science Letters* 256: 120–135

Prelević D, Foley SF, Romer R, Conticelli S (2008) Mediterranean Tertiary lamproites derived from multiple source components in postcollisional geodynamics. *Geochimica et Cosmochimica Acta* 72: 2125–2156

Prelević D, Akal C, Foley SF, Romer RL, Stracke A, Van Den Bogaard P (2012) Ultrapotassic Mafic Rocks as Geochemical Proxies for Post-collisional Dynamics of Orogenic Lithospheric Mantle: the Case of Southwestern Anatolia, Turkey. *Journal of Petrology* 53: 1019

Prelević D, Akal C, Romer RL, Mertz-Kraus R, Helvaci C (2015) Magmatic Response to Slab Tearing: Constraints from the Afyon Alkaline Volcanic Complex, Western Turkey. *Journal of Petrology* 56: 527

Putnis A (2002) Mineral replacement reactions: from macroscopic observations to microscopic mechanisms. *Mineralogical Magazine* 66: 689–708

Rapp RP, Shimizu N, Norman MD, Applegate GS (1999) Reaction between slab-derived melts and peridotite in the mantle wedge: experimental constraints at 3.8 GPa. *Chemical Geology* 160: 335–356

Reischmann T, Anthes G, Jaeckel P, Altenberger U (2001) Age and origin of the Böllsteiner Odenwald. *Mineralogy and Petrology* 72: 29–44

Righter K, Carmichael ISE (1996) Phase equilibria of phlogopite lamprophyres from western Mexico: biotite-liquid equilibria and PT estimates for biotite-bearing igneous rocks. *Contributions to Mineralogy and Petrology* 123: 1–21

Ring U, Laws S, Bernet M (1999) Structural analysis of a complex nappe sequence and late-orogenic basins from the Aegean Island of Samos, Greece. *Journal of Structural Geology* 21: 1575–1601

Ring U, Glodny J, Will T, Thomson S (2010) The Hellenic subduction system: high-pressure metamorphism, exhumation, normal faulting, and large-scale extension. *Annual Review of Earth and Planetary Sciences* 38: 45–76

Robert U, Cantagrel JM (1977) Le volcanisme basaltique dans le Sud-Est de la Mer Egee. Donnees geochronologiques et relations avec la tectonique. In: *Proceedings of the VI Colloquium on the Geology of the Aegean Region, Athens*, vol. 3, 961–967

Robert U, Foden J, Varne R (1992) The Dodecanese Province, SE Aegean: a model for tectonic control on potassic magmatism. *Lithos* 28: 241–260

Rock NMS (1991) *Lamprophyres*. Blackie. 285 pp.

Roeder PL, Reynolds I (1991) Crystallization of chromite and chromium solubility in basaltic melts. *Journal of Petrology* 32: 909–934

Romer RL, Hahne K (2010) Life of the Rheic Ocean: scrolling through the shale record. *Gondwana Research* 17: 236–253

de Ronde AA, Stünitz H (2007) Deformation-enhanced reaction in experimentally deformed plagioclase-olivine aggregates. *Contributions to Mineralogy and Petrology* 153: 699–717

Rosenbaum G, Gasparon M, Lucente FP, Peccerillo A, Miller MS (2008) Kinematics of slab tear faults during subduction segmentation and implications for Italian magmatism. *Tectonics* 27, tC2008

Rosenberg CL, Handy MR (2005) Experimental deformation of partially melted granite revisited: implications for the continental crust. *Journal of metamorphic Geology* 23: 19–28

Rosenbusch H (1887) *Mikroskopische Physiographie der Mineralien und Gesteine. Band II, Massige Gesteine*. Schweizerbart, Stuttgart. 877 pp., 2nd edn.

Rosenbusch H (1896) *Mikroskopische Physiographie der Mineralien und Gesteine. Band II, Massige Gesteine*. Schweizerbart, Stuttgart. 1360 pp., 3rd edn.

Rubatto D, Hermann J (2007) Experimental zircon/melt and zircon/garnet trace element partitioning and implications for the geochronology of crustal rocks. *Chemical Geology* 241: 38 – 61

Rudnick RL, Gao S (2003) Composition of the continental crust. In: Holland HD, Turekian KK (eds.) *The crust*, vol. 3 of *Treatise on geochemistry*, 1–64, Elsevier Ltd

Rudnick RL, McDonough WF, Chappell BW (1993) Carbonatite metasomatism in the northern Tanzanian mantle: petrographic and geochemical characteristics. *Earth and Planetary Science Letters* 114: 463–475

Rumble D, Liou JG, Jahn BM (2003) Continental crust subduction and ultrahigh pressure metamorphism. In: Holland HD, Turekian KK (eds.) *The crust*, vol. 3 of *Treatise on Geochemistry*, 293–319, Elsevier Ltd

Salters VJM, Longhi JE, Bizimis M (2002) Near mantle solidus trace element partitioning at pressures up to 3.4 GPa. *Geochemistry, Geophysics, Geosystems* 3: 1–23

Saunders P, Priestley K, Taymaz T (1998) Variations in the crustal structure beneath western Turkey. *Geophysical Journal International* 134: 373–389

Schaltegger U, Schneider JL, Maurin JC, Corfu F (1996) Precise U-Pb chronometry of 345–340 Ma old magmatism related to syn-convergence extension in the Southern Vosges (Central Variscan Belt). *Earth and Planetary Science Letters* 144: 403–419

Schaltegger U, Fanning CM, Günther D, Maurin JC, Schulmann K, Gebauer D (1999) Growth, annealing and recrystallization of zircon and preservation of monazite in high-grade metamorphism: conventional and in-situ U-Pb isotope, cathodoluminescence and microchemical evidence. *Contributions to Mineralogy and Petrology* 134: 186–201

Schmidt MW, Vielzeuf D, Auzanneau E (2004) Melting and dissolution of subducting crust at high pressures: the key role of white mica. *Earth and Planetary Science Letters* 228: 65–84

Schmitz MD, Bowring SA, Ireland TR (2003) Evaluation of Duluth Complex anorthositic series (AS3) zircon as a U-Pb geochronological standard: New high-precision isotope dilution thermal ionization mass spectrometry results. *Geochimica et Cosmochimica Acta* 67: 3665–3672

Schottler W (1906) *Erläuterungen zur geologischen Karte des Großherzogtums Hessen im Maßstabe 1 : 25 000, Blatt Viernheim (Käfertal).* Darmstadt. 116 pp.

Schreyer W, Massonne HJ, Chopin C (1987) Continental crust subducted to depths near 100 km: implications for magma and fluid genesis in collision zones. In: Mysen BO (ed.) *Magmatic Processes: Physicochemical Principals*, no. 1 in Special Publication, 155–163, The Geochemical Society of America

Schumacher JC (1997) The estimation of ferric iron in electron analysis of amphiboles. *European Journal of Mineralogy* 9: 643—651

von Seckendorff V, Timmerman MJ, Kramer W, Wrobel P (2004) New $^{40}Ar/^{39}Ar$ ages and geochemistry of late Carboniferous-early Permian lamprophyres and related volcanic rocks in the Saxothuringian Zone of the Variscan Orogen (Germany). In: Wilson M, Neumann ER, Davies GR, Timmermann MJ, Heeremans M, Larsen BT (eds.) *Permo-Carboniferous Magmatism and Rifting in Europe*, vol. 223 of *Special Publications*, 335–359, Geological Society, London

Seidel E, Kreuzer H, Harre W (1982) A late Oligocene/early Miocene high pressure belt in the external Hellenides. *Geologisches Jahrbuch E* 23: 165–206

Sekine T, Wyllie PJ (1982a) Phase relationships in the system $KAlSiO_4$-Mg_2SiO_4-SiO_2-H_2O as a model for hybridization between hydrous siliceous melts and peridotite. *Contributions to Mineralogy and Petrology* 79: 368–374

Sekine T, Wyllie PJ (1982b) Synthetic systems for modeling hybridization between hydrous siliceous magmas and peridotite in subduction zones. *The Journal of Geology* 90: 734–741

Sekine T, Wyllie PJ (1982c) The system granite-peridotite-H_2O at 30 kbar, with applications to hybridization in subduction zone magmatism. *Contributions to Mineralogy and Petrology* 81: 190–202

Sekine T, Wyllie PJ (1983) Experimental simulation of mantle hybridization in subduction zones. *The Journal of Geology* 91: 511–528

Shand P, Gaskarth JW, Thirlwall MF, Rock NMS (1994) Late Caledonian lamprophyre dyke swarms of south-eastern Scotland. *Mineralogy and Petrology* 51: 277–298

Shirahata K, Hirajima T (1995) Chemically sector-zoned garnet in Sanbagawa schists; its mode of occurrence and growth timing. *Journal of Mineralogy, Petrology and Economic Geology* 90: 69–79

Siebel W, Eroğlu S, Shang C, Rohrmüller J (2012) Zircon geochronology, elemental and Sr-Nd isotope geochemistry of two Variscan granitoids from the Odenwald-Spessart crystalline complex (mid-German crystalline rise). *Mineralogy and Petrology* 105: 187–200

Singer BS, Jicha BR, Leeman WP, Rogers NW, Thirlwall MF, Ryan J, Nicolaysen KE (2007) Along-strike trace element and isotopic variation in Aleutian Island arc basalt: Subduction melts sediments and dehydrates serpentine. *Journal of Geophysical Research: Solid Earth* 112

Skora S, Blundy J (2010) High-pressure hydrous phase relations of radiolarian clay and implications for the involvement of subducted sediment in arc magmatism. *Journal of Petrology* 51: 2211–2243

Skrzypek E, Štípská P, Cocherie A (2012) The origin of zircon and the significance of U–Pb ages in high-grade metamorphic rocks: a case study from the Variscan orogenic root (Vosges Mountains, NE France). *Contributions to Mineralogy and Petrology* 164: 935–957

Smith DC (1984) Coesite in clinopyroxene in the Caledonides and its implications for geodynamics. *Nature* 310: 641–644

Soder C, Altherr R, Romer RL (2016) Mantle metasomatism at the edge of a retreating subduction zone: Late Neogene lamprophyres from the Island of Kos, Greece. *Journal of Petrology* 57: 1705–1728

Spandler C, Mavrogenes J, Hermann J (2007) Experimental constraints on element mobility from subducted sediments using high-P synthetic fluid/melt inclusions. *Chemical Geology* 239: 228–249

Spear FS, Thomas JB, Hallett BW (2014) Overstepping the garnet isograd: a comparison of QuiG barometry and thermodynamic modeling. *Contributions to Mineralogy and Petrology* 168: 1–15

Stacey JS, Kramers JD (1975) Approximation of terrestrial lead isotope evolution by a two-stage model. *Earth and Planetary Science Letters* 26: 207–221

Stampfli GM, von Raumer JF, Borel GD (2002) Paleozoic evolution of pre-Variscan terranes: from Gondwana to the Variscan collision. *Special Papers-Geological Society of America* 263–280

Stepanov AS, Hermann J (2013) Fractionation of Nb and Ta by biotite and phengite: Implications for the "missing Nb paradox". *Geology* 41: 303–306

Stepanov AS, Hermann J, Rubatto D, Rapp RP (2012) Experimental study of monazite/melt partitioning with implications for the REE, Th and U geochemistry of crustal rocks. *Chemical Geology* 300: 200–220

Stepanov AS, Hermann J, Korsakov AV, Rubatto D (2014) Geochemistry of ultrahigh-pressure anatexis: fractionation of elements in the Kokchetav gneisses during melting at diamond-facies conditions. *Contributions to Mineralogy and Petrology* 167: 1–25

Stepanov AS, Hermann J, Rubatto D, Korsakov AV, Danyushevsky LV (2016) Melting history of an ultrahigh-pressure paragneiss revealed by multiphase solid inclusions in garnet, Kokchetav massif, Kazakhstan. *Journal of petrology* 57: 1531–1554

Stephan T, Kroner U, Hahn T, Hallas P, Heuse T (2016) Fold/cleavage relationships as indicator for late Variscan sinistral transpression at the Rheno-Hercynian–Saxo-Thuringian boundary zone, Central European Variscides. *Tectonophysics* 681: 250–262

Stöckhert B, Brix MR, Kleinschrodt R, Hurford AJ, Wirth R (1999) Thermochronometry and microstructures of quartz–a comparison with experimental flow laws and predictions on the temperature of the brittle–plastic transition. *Journal of Structural Geology* 21: 351–369

Stowell H, Zuluaga C, Boyle A, Bulman G (2011) Garnet sector and oscillatory zoning linked with changes in crystal morphology during rapid growth, North Cascades, Washington. *American Mineralogist* 96: 1354–1362

Sudo A, Tatsumi Y (1990) Phlogopite and K-amphibole in the upper mantle: Implication for magma genesis in subduction zones. *Geophysical Research Letters* 17: 29–32

Sun SS, McDonough WF (1989) Chemical and isotopic systematics of oceanic basalts: implications for mantle composition and processes. *Geological Society, London, Special Publications* 42: 313–345

Sweeney RJ, Prozesky V, Przybylowicz W (1995) Selected trace and minor element partitioning between peridotite minerals and carbonatite melts at 18–46 kb pressure. *Geochimica et Cosmochimica Acta* 59: 3671–3683

Tabaud AS, Whitechurch H, Rossi P, Schulmann K, Guerrot C, Cocherie A (2014) Devonian–Permian magmatic pulses in the northern Vosges Mountains (NE France): Result of continuous subduction of the Rhenohercynian Ocean and Avalonian passive margin. *Geological Society, London, Special Publications* 405: SP405–12

Tabaud AS, Janoušek V, Skrzypek E, Schulmann K, Rossi P, Whitechurch H, Guerrot C, Paquette JL (2015) Chronology, petrogenesis and heat sources for successive Carboniferous magmatic events in the Southern–Central Variscan Vosges Mts (NE France). *Journal of the Geological Society* 172: 87–102

Tappe S, Foley SF, Jenner GA, Heaman LM, Kjarsgaard BA, Romer RL, Stracke A, Joyce N, Hoefs J (2006) Genesis of ultramafic lamprophyres and carbonatites at Aillik Bay, Labrador: a consequence of incipient lithospheric thinning beneath the North Atlantic craton. *Journal of Petrology* 47: 1261–1315

Tappe S, Foley SF, Stracke A, Romer RL, Kjarsgaard BA, Heaman LM, Joyce N (2007) Craton reactivation on the Labrador Sea margins: $^{40}Ar/^{39}Ar$ age and Sr–Nd–Hf–Pb isotope constraints from alkaline and carbonatite intrusives. *Earth and Planetary Science Letters* 256: 433–454

Thibault Y, Edgar AD, Lloyd FE (1992) Experimental investigation of melts from a carbonated phlogopite lherzolite: implications for metasomatism in the continental lithospheric mantle. *American Mineralogist* 77: 784–794

Tiepolo M, Vannucci R, Oberti R, Foley S, Bottazzi P, Zanetti A (2000) Nb and Ta incorporation and fractionation in titanian pargasite and kaersutite: crystal–chemical constraints and implications for natural systems. *Earth and Planetary Science Letters* 176: 185–201

Tiepolo M, Bottazzi P, Foley SF, Oberti R, Vannucci R, Zanetti A (2001) Fractionation of Nb and Ta from Zr and Hf at mantle depths: the role of titanian pargasite and kaersutite. *Journal of Petrology* 42: 221–232

Todt WA, Altenberger U, Von Raumer JF (1995) U-Pb data on zircons for the thermal peak of metamorphism in the Variscan Odenwald, Germany. *Geologische Rundschau* 84: 466–472

Tomkins H, Powell R, Ellis D (2007) The pressure dependence of the zirconium-in-rutile thermometer. *Journal of metamorphic Geology* 25: 703–713

Triantaphyllis M (1998) *Geological map of Greece, Eastern Kos sheet 1:50000.* Institute of Geology and Mineral Exploration (IGME)

Tumiati S, Fumagalli P, Tiraboschi C, Poli S (2013) An experimental study on COH-bearing peridotite up to 3.2 GPa and implications for crust–mantle recycling. *Journal of Petrology* 54: 453–479

Turner S, Arnaud N, LIU J, Rogers N, Hawkesworth C, Harris N, Kelley S, Van Calsteren P, Deng W (1996) Post-collision, shoshonitic volcanism on the Tibetan Plateau: implications for convective thinning of the lithosphere and the source of ocean island basalts. *Journal of petrology* 37: 45–71

Turpin L, Velde D, Pinte G (1988) Geochemical comparison between minettes and kersantites from the Western European Hercynian orogen: trace element and PbSrNd isotope constraints on their origin. *Earth and Planetary Science Letters* 87: 73–86

Vannucci R, Piccardo GB, Rivalenti G, Zanetti A, Rampone E, Ottolini L, Oberti R, Mazzucchelli M, Bottazzi P (1995) Origin of LREE-depleted amphiboles in the subcontinental mantle. *Geochimica et Cosmochimica Acta* 59: 1763–1771

Vidal P, Auvray B, Charlot R, Cogné J (1981) Precadomian relicts in the Armorican Massif: their age and role in the evolution of the Western and Central European Cadomian-Hercynian Belt. *Precambrian Research* 14: 1–20

Wagner C, Velde D (1985) Mineralogy of two peralkaline, arfvedsonite-bearing minettes. A new occurrence of Zn-rich chromite. *Bulletin de minéralogie* 108: 173–187

Watson EB (1979) Zircon saturation in felsic liquids: experimental results and applications to trace element geochemistry. *Contributions to Mineralogy and Petrology* 70: 407–419

Watson EB, Harrison TM (1983) Zircon saturation revisited: temperature and composition effects in a variety of crustal magma types. *Earth and Planetary Science Letters* 64: 295–304

Watson EB, Liang Y (1995) A simple model for sector zoning in slowly grown crystals: Implications for growth rate and lattice diffusion, with emphasis on accessory minerals in crustal rocks. *American Mineralogist* 80: 1179–1187

Weldeab S, Emeis KC, Hemleben C, Siebel W (2002) Provenance of lithogenic surface sediments and pathways of riverine suspended matter in the Eastern Mediterranean Sea: evidence from $^{143}Nd/^{144}Nd$ and $^{87}Sr/^{86}Sr$ ratios. *Chemical Geology* 186: 139–149

Wendt JI, Kröner A, Fiala J, Todt W (1993) Evidence from zircon dating for existence of approximately 2.1 Ga old crystalline basement in southern Bohemia, Czech Republic. *Geologische Rundschau* 82: 42–50

White RW, Powell R, Clarke GL (2002) The interpretation of reaction textures in Fe-rich metapelitic granulites of the Musgrave Block, central Australia: constraints from mineral equilibria calculations in the system K_2O–FeO–MgO–Al_2O_3–SiO_2–H_2O–TiO_2–Fe_2O_3. *Journal of metamorphic Geology* 20: 41–55

White RW, Powell R, Holland TJB (2007) Progress relating to calculation of partial melting equilibria for metapelites. *Journal of Metamorphic Geology* 25: 511–527

Wiedenbeck MAPC, Alle P, Corfu F, Griffin WL, Meier M, Oberli F, Quadt Av, Roddick JC, Spiegel W (1995) Three natural zircon standards for U-Th-Pb, Lu-Hf, trace element and REE analyses. *Geostandards newsletter* 19: 1–23

Wilbur DE, Ague JJ (2006) Chemical disequilibrium during garnet growth: Monte Carlo simulations of natural crystal morphologies. *Geology* 34: 689–692

Will TM, Schmädicke E (2001) A first find of retrogressed eclogites in the Odenwald Crystalline Complex, Mid-German Crystalline Rise, Germany: evidence for a so far unrecognised high-pressure metamorphism in the Central Variscides. *Lithos* 59: 109–125

Will TM, Schmädicke E (2003) Isobaric cooling and anti-clockwise P–T paths in the Variscan Odenwald Crystalline Complex, Germany. *Journal of Metamorphic Geology* 21: 469–480

Williams IS (1998) U-Th-Pb geochronology by ion microprobe. In: McKibben M, WC S, Ridley W (eds.) *Applications of microanalytical techniques to understanding mineralizing processes*, vol. 7 of *Reviews in Economic Geology*, 1–35, Society of Economic Geologists, Inc.

Willner AP, Massonne HJ, Krohe A (1991) Tectono-thermal evolution of a part of a Variscan magmatic arc: the Odenwald in the Mid-German Crystalline Rise. *Geologische Rundschau* 80: 369–389

Wilson M, Neumann ER, Davies GR, Timmerman MJ, Heeremans M, Larsen BT (2004) Permo-Carboniferous magmatism and rifting in Europe: introduction. *Geological Society, London, Special Publications* 223: 1–10

Wimmenauer W (1972) Die Lamprophyre des Schwarzwaldes. *Fortschritte der Mineralogie* 50: 34–37

Wimmenauer W (1977) Lamprophyres and associated rocks in the dyke suite of the Dikeos monzonite, Kos (Greece). *Annales Géologiques des Pays Helléniques* 28: 427–435

Winchester JA, Pharaoh TC, Verniers J (2002) Palaeozoic amalgamation of Central Europe: an introduction and synthesis of new results from recent geological and geophysical investigations. *Geological Society, London, Special Publications* 201: 1–18

Woodard J, Kietäväinen R, Eklund O (2014) Svecofennian post-collisional shoshonitic lamprophyres at the margin of the Karelia Craton: Implications for mantle metasomatism. *Lithos* 205: 379–393

Woodhead JD, Hergt JM, Davidson JP, Eggins SM (2001) Hafnium isotope evidence for 'conservative' element mobility during subduction zone processes. *Earth and Planetary Science Letters* 192: 331–346

Wortel MJR, Spakman W (2000) Subduction and slab detachment in the Mediterranean-Carpathian region. *Science* 290: 1910–1917

Wunder B, Melzer S (2003) Experimental evidence on phlogopitic mantle metasomatism induced by phengite dehydration. *European Journal of Mineralogy* 15: 641–647

Wyllie PJ, Sekine T (1982) The formation of mantle phlogopite in subduction zone hybridization. *Contributions to Mineralogy and Petrology* 79: 375–380

Yaxley GM, Green DH, Kamenetsky V (1998) Carbonatite metasomatism in the southeastern Australian lithosphere. *Journal of Petrology* 39: 1917–1930

Yılmaz K (2010) Origin of anorogenic 'lamproite-like' potassic lavas from the Denizli region in Western Anatolia Extensional Province, Turkey. *Mineralogy and Petrology* 99: 219–239

Zartman RE, Doe BR (1981) Plumbotectonics–the model. *Tectonophysics* 75: 135–162

Zeh A, Gerdes A (2010) Baltica- and Gondwana-derived sediments in the Mid-German Crystalline Rise (Central Europe): Implications for the closure of the Rheic ocean. *Gondwana Research* 17: 254–263

Zeh A, Will TM (2010) The mid-German crystalline zone. In: Linnemann U, Romer RL (eds.) *Pre-Mesozoic Geology of Saxo-Thuringia–from the Cadomian Active Margin to the Variscan Orogen*, 195–220, Schweizerbart, Stuttgart

A. Analytical methods

A.1. Sample preparation

Rock samples were collected in the field and every sample was examined in thin section for signs of alteration using a polarisation microscope equipped with a digital camera. Polished thin sections with a thickness of $\sim 40\,\mu m$ were prepared from selected samples for electron probe microanalysis (EPMA). Thin sections were pre-analysed with a back-scattered electron (BSE) and energy dispersive X-ray fluorescence detector (EDS) using a Leo 440 scanning electron microscope (SEM; Institut für Geowissenschaften, Universität Heidelberg). For SEM analyses samples were cleaned with isopropanol and coated with carbon.

For whole rock analysis, hand specimens were treated in a rock splitter to remove alteration along joints and produce pieces of a few cubic centimetres in size. These were processed in a jaw crusher and powdered in an agate ring mill. For X-ray fluorescence analysis (XRF) and laser-ablation-ICP-MS, rock powders were dried at 110 °C for 24 hours. 1 g of sample powder was used to produce fused glass discs with di-lithium tetraborate (Merck Spectromelt A 1000; $Li_2B_4O_7$ + 0.07 wt% LiBr). Homogeneous beads were produced using a low sample-to-fluxing agent ratio of 1:10. The powders were homogenised with an agate mortar and pestle and fused using an automatic fusion apparatus (Claisse Fluxer). Loss on ignition (LOI) was determined from mass loss after heating of 2 g sample powder to 1050 °C for 8 h.

A.2. X-ray fluorescence analysis – XRF

Major elements (SiO_2, TiO_2, Al_2O_3, $Fe_2O_3{}^{tot}$, MnO, MgO, CaO, Na_2O, K_2O, P_2O_5) were determined by wavelength-dispersive X-ray fluorescence spectrometry (WD-XRF) using lithium borate fusion disks. International reference samples were used for calibration and run as unknowns. Measurements were performed with a Bruker AXS S8 Tiger at Terrachem Analytical Laboratory (Mannheim, Germany) and a Bruker AXS S4 Explorer instrument at the Institut für Geowissenschaften, Universität Heidelberg. The precision was better than 0.3 %.

A.3. Electron probe microanalysis – EPMA

Mineral analyses were carried out at the Institut für Geowissenschaften at Heidelberg using a CAMECA SX51 electron microprobe in wavelength-dispersion mode. Operating

conditions were 20 nA beam current and a 15 kV acceleration voltage and a beam diameter of $\sim 1\,\mu m$.

To minimize loss of alkalis and halogens during measurement, the electron beam was defocused for analysing feldspar (10 µm) and phlogopite/biotite (5 µm). PAP correction was applied to the raw data (Pouchou & Pichoir, 1984, 1985). Peak counting times were 20 s for major elements (except 10 s for K, Na) and 40 s for minor elements (Ba, Zr, Sr). Background counting times were half the counting times of the peak on each side. Natural and synthetic oxide and silicate standards were used for calibration. Table A.1 shows standards, crystals, counting times and detection limits.

Zr-in-rutile The concentration of Zr in rutile was determined in cooperation with Hans-Peter Meyer and Johannes Grimm (Heidelberg). A calibration curve was obtained by counting on the Zr$L\alpha$ peak of well-characterised rutile crystals. Four standard grains with variable Zr concentration were measured at the beginning, the middle and the end of each session [we used the synthetic (Syn, Zr-free) and natural (Diss, 128 µg/g Zr; R19, 249 µg/g Zr; R10, 759 µg/g Zr) rutile standards of Luvizotto *et al.*, 2009]. No background correction or matrix correction were applied as standards and samples are nearly pure TiO_2.

Operation conditions of the EPMA were 200 nA beam current and 15 kV acceleration voltage with a focused beam resulting in a spot diameter of $\sim 5-10\,\mu m$. The counting time of each analysis was set to 1000 seconds, while the beam current was checked every 10 seconds. Intensities of Zr $L\alpha$ were measured on two spectrometers using TAP crystals. Additionally, the Si $K\alpha$ (PET) and Fe $K\alpha$ (LIF) lines were checked to test for homogeneity and to rule out excitation in neighbouring grains of silicates or ilmenite, for instance.

A.4. Laser ablation-ICP-MS – LA-ICP-MS

The laser ablation ICP-MS technique was used for whole rock concentration determinations of trace elements on XRF fusion glass discs. The analyses were performed at the GeoZentrum Nordbayern (GZN), Universität Erlangen-Nürnberg in cooperation with Helene Brätz using an Agilent 7500i single collector ICP-MS with a quadrupole mass analyser. The system is equipped with New Wave (Merchantek) LUV 266x Nd:YAG (neodymium-doped yttrium aluminium garnet) ultraviolet laser (266 nm). Ablation occurred in an Ar atmosphere. 1.35 L/min Ar was used as carrier gas and 14.9 L/min and 0.9 L/min Ar as plasma and auxiliary gas, respectively. The plasma power was 1350 W. The laser was adjusted to a scan speed of 40 µm/s at an energy of 1.0 mJ and a repetition rate of 20 Hz. It was traced along four $\sim 1200\,\mu m$ long and 50 µm wide extraction lines on each fusion glass disc resulting in an energy density of $51\,J/cm^2$.

Each analysis lasted 50 seconds with 20 s counting time for gas background and 30 s for sample ablation, respectively. The integration time for ^{29}Si and ^{55}Mn was set to 10 ms while for trace element 25 ms were chosen, resulting in a duration of 1.0582 s per mass

scan with the following isotopes being measured: ^{9}Be, ^{45}Sc, ^{51}V, ^{53}Cr, ^{59}Co, ^{60}Ni, ^{63}Cu, ^{66}Zn, ^{69}Ga, ^{71}Ga, ^{85}Rb, ^{88}Sr, ^{89}Y, ^{90}Zr, ^{93}Nb, ^{118}Sn, ^{121}Sb, ^{133}Cs, ^{137}Ba, ^{139}La, ^{140}Ce, ^{141}Pr, ^{146}Nd, ^{147}Sm, ^{153}Eu, ^{157}Gd, ^{159}Tb, ^{163}Dy, ^{165}Ho, ^{166}Er, ^{169}Tm, ^{172}Yb, ^{175}Lu, ^{178}Hf, ^{181}Ta, ^{208}Pb, ^{232}Th, ^{238}U.

The NIST SRM 612 standard glass was used for external calibration of the trace elements with the values of Pearce *et al.* (1997). SiO_2 concentrations from XRF analysis were used for internal standardisation. Raw data were processed externally with the GLITTER Version 3.0 software package (van Achterbergh *et al.*, 2000).

Reproducibility and accuracy of the analytical results were controlled by measuring the NIST SRM 614 glass (SIMS data by Horn *et al.*, 1997) and the international geostandard BE-N (Govindaraju, 1994) (Table A.2).

A blank glasses of Merck Spectromelt A 1000 were prepared and analysed for trace elements (Table A.2). The unknowns were corrected accordingly, although the contamination is negligible due to high trace element abundances of the lamprophyre samples.

A.5. Thermal ionization mass spectrometry – TIMS

Strontium, Nd and Pb isotope analyses were performed at the Deutsches GeoForschungsZentrum (GFZ), Potsdam, using splits of the powders used for whole rock elemental analyses. The ion exchange chromatography and isotopic measurements were performed at GFZ Potsdam in cooperation with Rolf L. Romer. The samples were digested in concentrated HF in Savillex beakers on a hotplate for 4 days at 160°C. Samples were then dried, taken up in 2 N HNO_3 to convert fluorides to nitrates, slowly dried again at 80 or 90°C, and eventually redissolved in 6 N HCl. The clear solutions were then split in two aliquots, one half being used for the separation of Sr and Nd and the other one for Pb separation. Strontium, Nd and Pb were separated using standard ion exchange procedures.

Lead Pb was separated using anion exchange resin Bio Rad AG 50W-X8 (100-200 mesh) in teflon columns (column volume CV = 0.5 ml) by HCl-HBr ion exchange chemistry. The resin was cleaned with 8 CV 6N HCl and conditioned with 5 CV 2N HCl. Samples were loaded in 1 CV 2N HCl, rinsed with 1 CV 2N HCl, 6 CV 0.8N HBr, and 2 CV 2N HCl. Pb was eluted in 6 CV 6N HCl and purified by a second pass over the column. Pb was loaded together with H_3PO_4 and silica-gel on single Re-filaments (Gerstenberger & Haase, 1997).

The Pb isotopic composition was measured at 1200–1250°C on a Triton thermal ionization mass spectrometer operated in static multi-collection. Instrumental fractionation was corrected by 0.1 % per a.m.u. as determined from the long-term laboratory reproducibility of Pb reference material NBS SRM 981. The accuracy and precision of the reported Pb isotope ratios is better than 0.1 % at the 2 σ level of uncertainty. Total procedural blanks for whole-rock samples are better than 15–30 pg Pb.

Strontium Sr was separated using cation exchange techniques (Bio Rad AG50 W-X8, 100-200 mesh, 3.8 ml resin volume) in 2.5N HCl medium. Its isotopic composition was determined on a Triton thermal ionization mass spectrometer operated in dynamic multi-collection mode using Ta single filaments. The $^{87}Sr/^{86}Sr$ data are normalised with $^{86}Sr/^{88}Sr = 0.1194$. During the measurement period, NBS SRM 987 Sr reference material gave average $^{87}Sr/^{86}Sr$ value of 0.710249 ± 0.000012 (2σ reproducibility for n = 20 measurements). Analytical uncertainties of the individual measurements are reported as $2\sigma_m$. Total procedural blanks are less than 50 pg Sr.

Neodymium Rare earth elements (REE) were cleaned in a first step using the same column and procedure as for Sr and collected after Sr. To avoid interferences of BaO on mass ^{146}Nd, Ba was removed before elution of the other REE fraction using an additional washing step with 2.5 N HNO_3. Nd was separated from other REEs using standard cation exchange techniques (HDEHP-coated teflon, 2ml resin volume) in 0.18N HCl medium. It was loaded on Re double filaments and its isotopic composition was measured on a Triton thermal ionization mass spectrometer operated in dynamic multi-collection mode. The $^{143}Nd/^{144}Nd$ data are normalised with $^{146}Nd/^{144}Nd = 0.7219$. Repeated measurement of La Jolla and JNDi-1 Nd standards during the measurement period gave $^{143}Nd/^{144}Nd = 0.511850 \pm 0.000007$ (2σ reproducibility for n = 11 independent analyses) and $^{143}Nd/^{144}Nd = 0.512095 \pm 0.000018$ (2σ; n=18), respectively. Analytical uncertainties of the individual measurements are reported as $2\sigma_m$. Total procedural blanks are less than 30 pg Nd.

A.6. Secondary ion mass spectrometry – SIMS

U-Pb isotope analyses of zircon were performed using the Heidelberg CAMECA ims 1280-HR ion microprobe. The ion probe was operated with a $\sim 8-14$ nA O^- primary beam producing an elliptical spot of about $\sim$ 20µm in size (long axis). Presputtering time was set to 30 s. Oxygen flooding of the sample chamber was used to enhance secondary Pb yields. Positive secondary ions were extracted at 10 kV. The mass spectrometer's energy window was set to 50eV without offset at a mass resolving power m/Δm of $\sim$ 7000 to suppress interfering molecules.

16 analytical cycles were acquired with the magnet cycling from the masses of Zr_2O^+ to $UO_2{}^+$. The sequence included $^{94}Zr_2\ ^{16}O^+$, $^{204}Pb^+$, $^{206}Pb^+$, $^{207}Pb^+$, $^{208}Pb^+$, $^{232}Th^+$, $^{238}U^+$, $^{232}Th^{16}O^+$, $^{238}U^{16}O^+$ and $^{238}U^{16}O_2{}^+$. The $^{94}Zr_2{}^{16}O^+$ signal was used as the reference peak for centering secondary ion beam. A single electron multiplier (EM) was used as the detection device.

For calibration of U/Pb ratios, zircon standards 91500 and AS3 were used, which have $^{207}Pb/^{206}Pb$ ages of 1065.4 ± 0.3 Ma and 1099.1 ± 0.2 Ma, respectively (Wiedenbeck *et al.*, 1995; Schmitz *et al.*, 2003). The measured ratios of $^{206}Pb^+/^{238}U^+$ are plotted against $^{254}UO^+/^{238}U^+$ and a linear regression was applied. Relative ion yields (RIYs) are derived by dividing the measured $^{206}Pb^+/^{238}U^+$ of the standard at a reference

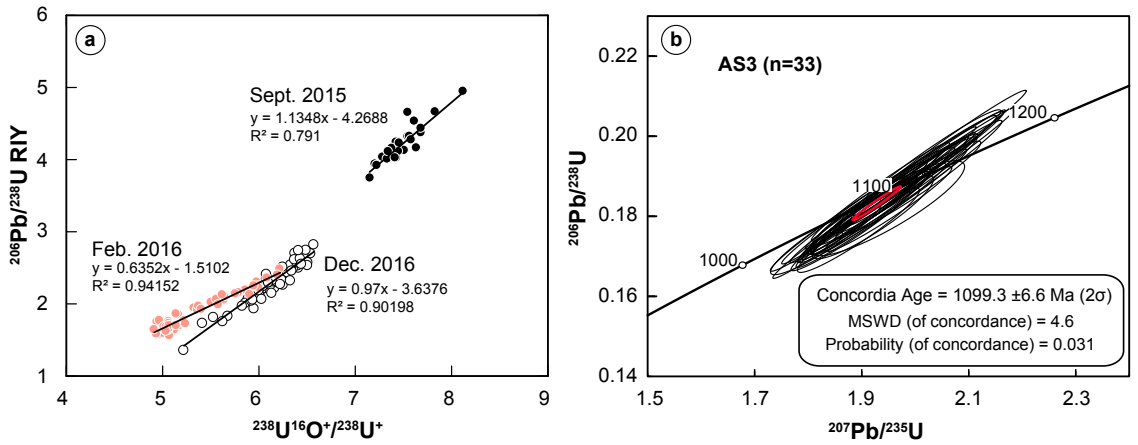

Fig. A.1. (a) The measurement of standard zircons allows for the calibrating of the U-Pb relative sensitivity as a function of $^{238}U^{16}O^{+}/^{238}U^{+}$ measured on the unknowns under the same conditions. The zircon standards AS3 and 91500 are used for construction of a calibration curve of $^{238}U^{16}O^{+}/^{238}U^{+}$ RIY vs $^{206}Pb^{+}/^{238}U^{+}$.The $^{206}Pb^{+}/^{238}U^{+}$ RIYs are calculated as $(^{206}Pb^{+}/^{238}U^{+})_{measured}/\ (^{206}Pb^{+}/^{238}U^{+})_{true}$ and shows that interelement fractionation between U and Pb during the measurements varied between ~ 1 and ~ 6 and are linearly correlated. (b) Concordia diagrams with the results of analyses on AS3 reference zircons (February 2016 session; no common-Pb correction applied).

$^{254}UO^{+}/^{238}U^{+}$ value by its known $^{206}Pb^{+}/^{238}U^{+}$ ratio. The RIY allows for calibrating the U/Pb ratio as a function of $^{238}U^{16}O^{+}/^{238}U^{+}$ measured on the unknowns under identical conditions (Fig. A.1). The precision of the method is limited by the reproducibility of this calibration curve.

Isotope ratios are corrected for common lead using the ^{207}Pb-based correction (Williams, 1998) with the Stacey & Kramers (1975) model composition for modern Pb. Data reduction including common Pb correction was done using the ZIPS v. 3.1 software (courtesy of Chris Coath, University of Bristol).Visualisation of U–Pb concordia and zircon ages is done using Isoplot 4.15 (Ludwig, 2012).

Though U, Th and Pb concentrations are not required for zircon U–Pb dating, they provide useful additional information for characterisation. In general, the U concentrations were calculated based on a ratio of $UO^{+}{}_{x(x=1,2)}$ to the intensity of matrix ions of zircon, such as $^{94}Zr_2O^{+}$. The concentration of U was estimated by UO^{+} ion yield based on the compositionally homogeneous 91500 standard with 81.2 µg/g U (Wiedenbeck *et al.*, 1995).

Table A.1. Analytical parameters and setups used during electron probe microanalysis

Atomic number	Element	Spectral line	Crystal	Analysed minerals	Standard	Concentration in standard (wt %)	Counting time (s)	Detection limit* at 15kV / 20 nA
9	F	Kα	PC0	Amp, Bt/Phl	Topaz	20.65	40	0.05 % F
11	Na	Kα	TAP	all	Albite	8.71	10	0.04 % Na_2O
12	Mg	Kα	TAP	Cpx, Amp, Bt/Phl	MgO	60.31	20	0.07 % MgO
13	Al	Kα	TAP	Fsp	Anorthite	19.07	20	0.04 % Al_2O_3
				Cpx, Amp, Bt/Phl	Al_2O_3	52.93	30	0.04 % Al_2O_3
14	Si	Kα	TAP	all	Wollastonite	24.08	20	0.03 % SiO_2
17	Cl	Kα	PET	Amp, Bt	Scapolite	1.43	30	0.01 % Cl
19	K	Kα	PET	all	Orthoclase	12.18	10	0.03 % K_2O
20	Ca	Kα	PET	Fsp	Anorthite	13.64	10	0.03 % CaO
				Cpx, Amp, Bt/Phl	Wollastonite	34.12	20	0.04 % CaO
22	Ti	Kα	PET	Cpx, Amp, Bt/Phl	TiO_2	59.95	20	0.06 % TiO_2
24	Cr	Kα	PET	Cpx, Amp, Bt/Phl	Cr_2O_3	68.42	20	0.07 % Cr_2O_3
25	Mn	Kα	LiF	Cpx, Amp, Bt/Phl	Rhonodite	33.68	20	0.08 % MnO
26	Fe	Kα	LiF	all	Fe_2O_3	69.94	20	0.11 % FeO
38	Sr	Lα	PET	Fsp, Amp, Bt/Phl	Celestine	47.70	20	0.14 % SrO
56	Ba	Lα	PET	Fsp, Amp, Bt/Phl	Baryte	58.84	20	0.09 % BaO

* 3$\times$RSD (relative standard deviation) of background.

Table A.2. LA-ICP-MS analyses of standards and materials (concentrations in $\mu g/g$)

	BE-N					NIST 614			
	measured (n=14) mean	$\pm 2\sigma$	rel. Stdev.	GeoReM[a,c] compiled	% diff.	measured (n=4) mean	$\pm 2\sigma$	SIMS[b] values**	% diff.
Sc	25	1	5	22	12	0.62	0.84		
V	237	14	6	235	1	1.02	0.17	0.9	13
Cr	369	25	7	360	2	1.58	0.84	0.99	60
Co	60	3	5	60	-1	0.58	0.78		
Ni	243	16	7	267	-9	1.32	1.77		
Rb	46	2	4	47	-3	0.94	0.10	0.88	7
Cs	0.7	0.1	9	0.8	-9	0.74	0.12	0.76	-3
Sr	1386	121	9	1370	1	43.97	1.27	44	0
Ba	1089	62	6	1025	6	3.30	0.47	3.02	9
Y	29	2	6	30	-4	0.80	0.03	0.78	2
Zr	259	17	7	260	0	0.84	0.05	0.83	1
Nb	109	4	4	105	4	0.82	0.06	0.79	4
La	86	7	8	82	4	0.71	0.06	0.68	5
Ce	153	9	6	152	1	0.80	0.06	0.76	5
Pr	17	1	6	17.5	0	0.76	0.05	0.74	3
Nd	69	4	6	67	2	0.74	0.02	0.73	2
Sm	12.6	1.0	8	12.2	3	0.77	0.03	0.79	-3
Eu	3.8	0.2	6	3.6	5	0.75	0.03	0.75	0
Gd	10.1	0.8	8	9.7	4	0.76	0.03	0.74	3
Tb	1.3	0.1	7	1.3	-3	0.72	0.06	0.69	4
Dy	6.6	0.4	7	6.4	3	0.76	0.05	0.74	3
Ho	1.1	0.1	9	1.1	3	0.75	0.03	0.73	3
Er	2.6	0.2	8	2.5	5	0.72	0.03	0.73	-1
Tm	0.34	0.02	7	0.34	-1	0.73	0.02	0.72	1
Yb	2.0	0.1	7	1.8	9	0.79	0.03	0.81	-2
Lu	0.25	0.02	9	0.24	6	0.73	0.04	0.7	4
Hf	5.6	0.5	9	5.6	0	0.68	0.03	0.66	3
Ta	6.0	0.4	6	5.7	5	0.83	0.05	0.79	4
Pb	4	1	15	4	5	2.93	0.38	2.8	5
Th	11	1	7	10.4	4	0.74	0.04	0.73	1
U	2.3	0.2	6	2.4	-2	0.83	0.07	0.78	6
Be	2.1	0.2	12	1.9	11	0.78	0.04	0.76	2

[a] values from Govindaraju (1994), [b]SIMS data by Horn *et al.* (1997)
[c]GeoReM v. 18 values from http://www.georem.mpch-mainz.gwdg.de/

Table A.2. *(continued)* LA-ICP-MS analyses of standards and materials (concentrations in µg/g)

	BCR-2			BHVO-2			Lithium borate blank glass
	meas.	GeoReM[c] preferred	% diff.	meas.	GeoReM[c] preferred	% diff.	Merck Millipore Spectromelt® A 1000
Sc	36	33	8	36	32	14	0.11
V	437	416	5	335	317	6	10.2
Cr	19	18	4	302	280	8	2.09
Co	34	37	-7	43	45	-5	0.18
Ni	14	18	-22	105	119	-12	1.84
Rb	51	47	9	10	9.11	5	0.05
Cs	1.3	1.1	14	0.1	0.1	11	0.10
Sr	342	340	1	458	396	16	1.07
Ba	678	677	0	141	131	7	0.43
Y	33	37	-12	28	26	8	0.05
Zr	168	184	-9	176	172	2	0.04
Nb	13	13	0	20	18.1	8	0.07
La	25	25	-2	17	15.2	9	0.06
Ce	50	53	-5	38	37.5	2	0.08
Pr	6	7	-7	5.5	5.35	3	0.03
Nd	28	29	-2	25.6	24.5	5	0.04
Sm	6.5	6.6	-1	6.6	6.07	9	0.04
Eu	2.1	2.0	5	2.4	2.07	14	0.02
Gd	6.4	6.8	-6	6.4	6.24	2	0.10
Tb	1.0	1.1	-8	0.9	0.92	2	0.03
Dy	6.6	6.4	3	5.5	5.31	3	0.06
Ho	1.3	1.3	-1	1.1	0.98	11	0.01
Er	3.5	3.7	-4	2.6	2.54	2	0.00
Tm	0.52	0.54	-4	0.35	0.33	5	0.09
Yb	3.5	3.4	3	2.1	2.0	5	0.01
Lu	0.52	0.50	4	0.29	0.274	7	0.00
Hf	4.5	4.9	-7	4.3	4.36	-1	0.00
Ta	0.8	0.7	14	1.3	1.14	11	0.02
Pb	10	11	-6	1.9	1.6	19	0.36
Th	5	6	-4	1.3	1.22	3	0.02
U	1.6	1.7	-6	0.36	0.403	-11	0.03
Be	3.8			1.1	1.0	10	0.15

[a] values from Govindaraju (1994), [b] SIMS data by Horn *et al.* (1997)
[c] GeoReM v. 18 values from http://www.georem.mpch-mainz.gwdg.de/

B. Sample locations

The sample locations for Kos lamprophyres are given on Fig. 2.1c.
The sample locations for Variscan lamprophyres are given in a separate table (Table B.1).

Table B.1. Sample localities for Variscan lamprophyres

Sample	Group	Region	Type	Locality	GPS coordinats*	
TA01	Group I	Taunus	K	Langenschwalbach	50.1608	8.0758
OD153B	Group I	Odenwald-N	PM	Heppenheim-Erbach	49.6347	8.6708
OD154	Group I	Odenwald-N	PM	Hochstätten, Salzwiese	49.7245	8.6631
OD154B	Group I	Odenwald-N	PM	Hochstätten, Salzwiese	49.7245	8.6631
OD169R	Group I	Odenwald-N	PM	Zwingenberg, Weidental	49.7207	8.6197
OD175	Group I	Odenwald-N	PM	Hemsbach, Kreuzberg	49.5952	8.6606
OD178	Group I	Odenwald-N	PM	Laudenbach, Sonnberg	49.6068	8.6600
OD018	Group I	Odenwald-N	K	Kirschhausen	49.6425	8.7006
OD041	Group I	Odenwald-N	K	Igelsbach	49.6527	8.7254
OD043	Group I	Odenwald-N	K	Leutershausen, S Ruine Hirschburg	49.4880	8.6769
OD113	Group I	Odenwald-N	K	Schriesheim, Branich-Tunnel	49.4792	8.6758
OD114	Group I	Odenwald-N	K	Unter-Ostern, Dachsberg	49.6890	8.8464
OD129	Group I	Odenwald-N	K	Juhöhe, Mörlenbach	49.6186	8.6929
OD149	Group I	Odenwald-N	K	Brensbach	49.7799	8.8987
OD151C	Group I	Odenwald-N	K	Heppenheim-Erbach	49.6346	8.6708
OD156B	Group I	Odenwald-N	K	Heppenheim-Erbach	49.6323	8.6744
OD167	Group I	Odenwald-N	M	Heppenheim-Erbach	49.6321	8.6747
OD011	Group I	Odenwald-N	S	E Hilsenhain	49.5117	8.7797
OD029	Group I	Odenwald-N	S	Sonderbach	49.6378	8.6865
OD038	Group I	Odenwald-N	S	Mittershausen, N Igelsbach	49.6600	8.7197
OD040	Group I	Odenwald-N	S	W Mittershausen	49.6551	8.7100
OD060	Group I	Odenwald-N	S	Zwingenberg	49.7240	8.6214
OD064	Group I	Odenwald-N	S	Hemsbach (Bennberg/Espersbach)	49.5967	8.6594
OD065	Group I	Odenwald-N	S	Kirschhausen	49.6451	8.6772
OD080	Group I	Odenwald-N	S	Heppenheim, Steinmauer	49.6277	8.6709
OD147	Group I	Odenwald-N	S	Laudenbach	49.6046	8.6557
OD150	Group I	Odenwald-N	S	Zwingenberg	49.7930	8.6690
OD159	Group I	Odenwald-N	S	SW Mittershausen	49.6502	8.7098
OD168	Group I	Odenwald-N	S	Heppenheim-Erbach	49.6342	8.6692
OD170	Group I	Odenwald-N	S	Alsbach, Katharinen-Berg	49.7413	8.6314
OD025	Group I	Odenwald-N	S–K	Sonderbach	49.6302	8.6920
OD027	Group I	Odenwald-N	S–K	Sonderbach	49.6302	8.6920
SP12	Group I	Spessart	PM	Aschaffenburg, Gailbach (cutting aschaffite)	49.9490	9.2043
SP14	Group I	Spessart	K	Stengerts bei Aschaffenburg	49.9470	9.1896
SP15	Group I	Spessart	S	Stengerts bei Aschaffenburg	49.9459	9.1852
SP19	Group I	Spessart	S	NW Soden	49.9293	9.1947
VO03	Group I	Vosges-N	PM	Vacquenoux (Wackenbach), Schirmeck	48.4926	7.1848
VO86	Group I	Vosges-N	PM	Vacquenoux (Wackenbach), Schirmeck	48.4926	7.1848
VO11	Group I	Vosges-N	K	Wisembach	48.2615	7.1078
VO23	Group I	Vosges-N	K	Breitenbach	48.3711	7.2958
VO30	Group I	Vosges-N	K	S Russ	48.4752	7.2711
VO33B	Group I	Vosges-N	K	Les Quelles	48.4504	7.1673
VO34	Group I	Vosges-N	K	Haut Fourneau	48.4726	7.1474
VO35	Group I	Vosges-N	K	Haut Fourneau	48.4734	7.1517
VO88	Group I	Vosges-N	K	Route Forestière du Heymorrupt	48.4709	7.1687
VO95A	Group I	Vosges-N	K	Cascade de la Crache, S Raon-sur-Plaine	48.4953	7.1080
VO96B	Group I	Vosges-N	K	Maison Forestière Hungerplatz	48.4041	7.3970
VO12	Group I	Vosges-N	M	Bipierre	48.4772	7.1375
VO16	Group I	Vosges-N	M	Barr, Spesbourg	48.4015	7.4126
VO21	Group I	Vosges-N	M	Le Hohwald, S Welschenbruch	48.4082	7.3516
VO22	Group I	Vosges-N	M	N Breitenbach	48.3821	7.2933
VO24	Group I	Vosges-N	M	Ranrupt	48.3820	7.1910
VO27	Group I	Vosges-N	M	Russ	48.4869	7.2720
VO36	Group I	Vosges-N	M	Les Minières, Tête Mathis	48.4820	7.1362

K, kersantite; M, minette; PM, peralkaline minette; S, spessartite; S–K, spessartite to kersantite (gradational type)
*GPS coordinates are given in decimal degrees

Table B.1. *(continued)* Sample localities for Variscan lamprophyres

Sample	Group	Region	Type	Locality	GPS coordinats*	
VO37	Group I	Vosges-N	M	Vacquenoux (Wackenbach), Schirmeck	48.4921	7.1834
VO40	Group I	Vosges-N	M	Vacquenoux (Wackenbach), Schirmeck	48.4925	7.1846
VO41A	Group I	Vosges-N	M	Vacquenoux (Wackenbach), Schirmeck	48.4928	7.1852
VO48	Group I	Vosges-N	M	Le Ménil	48.3510	6.8490
VO90A	Group I	Vosges-N	M	Schrimeck	48.4836	7.2023
VO91	Group I	Vosges-N	M	Schrimeck	48.4840	7.2014
VO33A	Group I	Vosges-N	S	Les Quelles	48.4504	7.1673
VO89	Group I	Vosges-N	S	S Russ	48.4859	7.2672
VO15	Group I	Vosges-N	S–K	Andlautal, Le Hohwald	48.3997	7.3388
OD005B	Group II	Odenwald-S	K	Gorxheim, Haubenböhl	49.5449	8.7102
OD006C	Group II	Odenwald-S	K	Mackenheim	49.5666	8.7814
OD152	Group II	Odenwald-S	K	Heppenheim-Erbach	49.6346	8.6708
OD007	Group II	Odenwald-S	M	Birkenau	49.5614	8.6953
OD019	Group II	Odenwald-S	M	Kirchhausen	49.6423	8.7004
OD058B	Group II	Odenwald-S	M	Birkenau, Kallstätter Tal	49.5524	8.7179
OD079B	Group II	Odenwald-S	M	Rohrbacher Höhe	49.5628	8.7555
OD124	Group II	Odenwald-S	M	Hammelbach	49.6537	8.8297
OD145	Group II	Odenwald-S	M	Weinheim	49.5555	8.6868
OD157A	Group II	Odenwald-S	M	Nieder-Liebersbach	49.5829	8.7114
OD157B	Group II	Odenwald-S	M	Nieder-Liebersbach	49.5829	8.7114
OD163	Group II	Odenwald-S	M	Kreidach	49.5629	8.7969
OD164	Group II	Odenwald-S	M	Hemsbach, Kreuzberg	49.5954	8.6606
PF01	Group II	Pfalz	M	Weiler near Weißenburg	49.0435	7.9019
PF02	Group II	Pfalz	M	Weiler near Weißenburg	49.0435	7.9019
PF03	Group II	Pfalz	M	Weiler near Weißenburg	49.0433	7.9020
PF05	Group II	Pfalz	M	Weiler near Weißenburg	49.0390	7.9072
PF04	Group II	Pfalz	S–K	Weiler near Weißenburg	49.0410	7.9048
VO07	Group II	Vosges-C	K	Sainte-Marie-aux-Mines, Col de St. Marie	48.2460	7.1339
VO08	Group II	Vosges-C	K	Plancher les mines	47.7997	6.7922
VO10	Group II	Vosges-C	K	Laveline	48.2461	7.0611
VO13	Group II	Vosges-C	K	Fouday	48.4277	7.1878
VO14	Group II	Vosges-C	K	Sainte-Marie-aux-Mines - Haut de Faite	48.2454	7.1446
VO19	Group II	Vosges-C	K	St. Die	48.2608	7.0387
VO52	Group II	Vosges-C	K	N Natzweiler	48.4470	7.2631
VO78A	Group II	Vosges-C	K	Val d'Argent	48.2246	7.1382
VO76A	Group II	Vosges-C	M	Sainte-Marie-aux-Mines	48.2469	7.1534
VO76B	Group II	Vosges-C	M	Sainte-Marie-aux-Mines	48.2469	7.1534
VO09	Group II	Vosges-C	S	Le Hohwlad, Sperberbächel	48.4036	7.3294
VO77	Group II	Vosges-C	S–K	Val d'Argent	48.2225	7.1358
VO79	Group II	Vosges-C	S–K	Val d'Argent, Saint-Pierre sur l'Hâte	48.2213	7.1642
VO66	Group II	Vosges-S	K	Larmet	47.7621	6.7036
VO67	Group II	Vosges-S	K	La Chevestraye	47.7588	6.7226
VO73	Group II	Vosges-S	K	Miellin, La Doue de l'Eau	47.8125	6.7481
VO05	Group II	Vosges-S	M	Thalhorn, St. Amarintal	47.9024	6.9672
VO06	Group II	Vosges-S	M	Vallée de Saint-Amarin	47.8716	7.0370
VO18	Group II	Vosges-S	M	Cleurie	48.0547	6.6718
VO56	Group II	Vosges-S	M	Sickert	47.7937	6.9764
VO57	Group II	Vosges-S	M	Kruth	47.9248	6.9697
VO59	Group II	Vosges-S	M	Col de Croix, Le Thillot	47.8561	6.7401
VO60	Group II	Vosges-S	M	Le Crossenière, Beulotte-Saint-Laurent	47.8710	6.6695
VO64B	Group II	Vosges-S	M	Saint Bresson, La Goutte	47.8723	6.5416
VO69	Group II	Vosges-S	M	Miellin, La Doue de l'Eau	47.8122	6.7470
VO70	Group II	Vosges-S	M	Miellin, La Doue de l'Eau	47.8122	6.7473
VO72	Group II	Vosges-S	M	Miellin, La Doue de l'Eau	47.8125	6.7477
VO82	Group II	Vosges-S	M	Rovillers	47.8742	6.5289

K, kersantite; M, minette; PM, peralkaline minette; S, spessartite; S–K, spessartite to kersantite (gradational type)
*GPS coordinates are given in decimal degrees

Table B.1. *(continued)* Sample localities for Variscan lamprophyres

Sample	Group	Region	Type	Locality	GPS coordinats*	
VO83	Group II	Vosges-S	M	Ballon d'Alsace, S flank	47.8015	6.8335
VO84	Group II	Vosges-S	M	Miellin, La Doue de l'Eau	47.8123	6.7468
VO97	Group II	Vosges-S	M	Col de la Grosse Pierre, N La Bresse	48.4041	7.3970
SCH05	Group II	Schwarzwald	K	Wehratal	47.6683	7.9338
SCH06	Group II	Schwarzwald	K	Albtal, Niedermühle	47.6814	8.1233
SCH13	Group II	Schwarzwald	K	Schlageten, St. Blasien, Albtal	47.7078	8.1217
SCH20	Group II	Schwarzwald	K	Häusern	47.7481	8.1667
SCH21	Group II	Schwarzwald	K	Schlüchttal	47.6828	8.2577
SCH23	Group II	Schwarzwald	K	Schwarzatal	47.7115	8.2164
SCH24	Group II	Schwarzwald	K	Schlüchttal	47.6880	8.2769
SCH25	Group II	Schwarzwald	K	N Untermettingen, Steinatal	47.7116	8.3488
SCH26	Group II	Schwarzwald	K	N Untermettingen, Steinatal	47.7208	8.3484
SCH27	Group II	Schwarzwald	K	N Untermettingen, Steinatal	47.7206	8.3483
SCH28	Group II	Schwarzwald	K	N Untermettingen, Steinatal	47.7206	8.3483
SCH30	Group II	Schwarzwald	K	Häg-Ehrsberg	47.7333	7.9246
SCH31	Group II	Schwarzwald	K	Wiesetal, N Mambach	47.7368	7.8838
SCH32A	Group II	Schwarzwald	K	Unterkastel (Fröhnd), Wiesetal	47.7610	7.8850
SCH32B	Group II	Schwarzwald	K	Unterkastel (Fröhnd), Wiesetal	47.7610	7.8850
SCH33	Group II	Schwarzwald	K	Kleines Wiesetal, Ober-Bürchau	47.7759	7.8154
SCH34	Group II	Schwarzwald	K	Kleines Wiesetal	47.7509	7.8272
SCH35	Group II	Schwarzwald	K	Zell im Wiesenthal	47.7007	7.8542
SCH36	Group II	Schwarzwald	K	Mambach, Wiesental	47.7285	7.8812
SCH37	Group II	Schwarzwald	K	Mambach, Wiesental	47.7285	7.8812
SCH38	Group II	Schwarzwald	K	Murgtal	47.6065	7.9965
SCH39	Group II	Schwarzwald	K	Murgtal	47.6079	7.9959
SCH09	Group II	Schwarzwald	K–M	Gaggenau	48.7982	8.3112
SCH07	Group II	Schwarzwald	M	Görwihl, Tiefenstein	47.6163	8.0898
SCH12	Group II	Schwarzwald	M	Zipfelhof, Feldberg-Bärental	47.8732	8.0700
SCH14	Group II	Schwarzwald	M	Albtal	47.6620	8.1099
SCH15	Group II	Schwarzwald	M	Albtal	47.6306	8.0955
SCH17	Group II	Schwarzwald	M	Albtal	47.6171	8.0883
SCH18	Group II	Schwarzwald	M	Albtal	47.6171	8.0883
SCH19	Group II	Schwarzwald	M	Albtal	47.6171	8.0883
SCH29	Group II	Schwarzwald	M	Steinatal	47.7490	8.3450

K, kersantite; M, minette; PM, peralkaline minette; S, spessartite; S–K, spessartite to kersantite (gradational type)
*GPS coordinates are given in decimal degrees

C. Whole-rock geochemistry

Major and trace element whole rock analyses of the 189 samples are presented in three tables. Analyses of major elements (SiO_2 to P_2O_5) are given in wt % and were performed by XRF. Trace element abundances (Sc–U) are given in $\mu g/g$ and were analysed by ICP-MS.

Detailed chondrite-normalised rare earth element (REE) diagrams and multi-element variation diagrams for Variscan lamprophyres (additional to Fig. 3.6) are presented in two supplementary figures. Primitive mantle and chondrite concentration normalisation values are from Sun & McDonough (1989) and McDonough & Sun (1995), respectively.

Table C.1. Whole-rock major (wt %) and trace element (µg/g) analyses of lamprophyre dyke rocks from Kos, Greece

Rock type	Mica-Lamprophyre									
Group	low Nb	medium Nb								
Sample	KL54	KL66	KL71	KL72	KL37	KL40	KL42	KL45	KL58	KL22
SiO_2	48.3	44.7	47.0	45.5	48.5	48.3	46.1	49.0	43.7	47.0
TiO_2	1.00	1.05	0.95	1.14	0.87	1.00	1.03	0.84	1.47	1.13
Al_2O_3	14.3	14.6	15.7	15.8	15.4	16.6	16.9	14.8	15.0	14.7
Fe_2O_3	7.73	8.11	7.56	7.93	7.03	7.42	8.17	6.75	9.35	7.89
MnO	0.14	0.14	0.13	0.14	0.14	0.15	0.15	0.12	0.18	0.16
MgO	7.77	9.24	7.73	7.67	5.70	4.49	4.89	5.75	6.44	6.70
CaO	9.68	10.4	9.41	9.80	10.6	9.02	9.89	8.02	9.76	9.74
Na_2O	2.35	2.75	2.20	3.09	2.62	2.34	3.02	3.02	2.53	2.48
K_2O	3.79	2.71	4.22	2.85	3.80	5.19	3.56	5.19	4.29	4.49
P_2O_5	0.73	1.18	0.99	1.29	1.21	1.09	1.22	0.98	1.27	1.05
BaO	0.26	0.20	0.33	0.21	0.19	0.28	0.24	0.42	0.24	0.22
SrO	0.17	0.17	0.26	0.19	0.26	0.26	0.30	0.26	0.14	0.17
LOI	2.46	3.94	2.04	3.83	2.83	2.96	4.07	4.43	5.00	3.59
Sum	98.6	99.2	98.5	99.5	99.1	99.0	99.5	99.5	99.4	99.2
Sc	35	41	37	35	36	24	25	31	33	39
V	235	231	226	242	231	219	260	209	277	261
Cr	383	287	255	208	159	50	32	147	55	178
Co	29	34	29	31	25	27	24	27	31	30
Ni	74	111	81	76	38	22	19	39	31	43
Rb	124	72	93	65	107	134	86	110	149	161
Cs	3.1	3.0	2.2	1.6	2.2	2.2	1.8	1.7	4.8	3.2
Sr	1430	1410	2230	1640	2180	2180	2560	2200	1190	1420
Ba	2360	1780	2930	1900	1650	2530	2100	3790	2170	1950
Y	29	30	30	32	35	34	36	33	26	31
Zr	260	299	308	322	391	387	393	367	270	361
Nb	18	35	34	39	42	71	39	38	63	53
La	71	69	77	74	101	145	111	176	80	85
Ce	156	153	161	163	206	282	241	347	173	181
Pr	19	18	20	20	24	31	29	39	20	21
Nd	76	75	79	78	94	114	113	150	75	82
Sm	13.4	13.0	13.4	13.6	16.3	17.0	18.9	23.3	11.8	13.8
Eu	3.4	3.4	3.6	3.7	4.3	4.4	5.2	5.8	3.3	3.5
Gd	9.2	9.1	9.1	9.7	11.4	11.2	12.3	14.2	8.1	9.6
Tb	1.13	1.10	1.09	1.18	1.35	1.28	1.40	1.51	0.94	1.16
Dy	6.1	6.0	6.0	6.6	7.3	7.1	7.6	7.6	5.4	6.4
Ho	1.08	1.08	1.07	1.16	1.30	1.24	1.28	1.23	0.95	1.16
Er	2.8	2.8	2.9	3.0	3.4	3.2	3.4	3.1	2.5	2.9
Tm	0.37	0.37	0.39	0.41	0.45	0.45	0.45	0.38	0.36	0.38
Yb	2.5	2.7	2.7	2.8	3.0	3.0	3.0	2.7	2.3	2.5
Lu	0.36	0.38	0.42	0.41	0.45	0.42	0.45	0.38	0.32	0.38
Hf	6.6	7.5	7.4	7.9	9.8	9.1	9.1	9.1	6.6	8.9
Ta	0.9	1.6	1.6	1.8	2.0	3.0	1.7	1.8	2.5	2.2
Pb	17	5	9	9	5	5	7	15	13	49
Th	17	13	18	14	30	27	18	45	12	16
U	3.5	2.9	3.7	3.0	7.5	6.3	4.5	9.7	2.9	4.3

Table C.1. *(continued)* Whole-rock major (wt %) and trace element (µg/g) analyses of lamprophyre dyke rocks from Kos, Greece

Rock type	Mica-Lamprophyre									
Group	medium Nb									
Sample	KL27	KL28	KL39	KL59	KL62	KL17	KL18	KL19	KL38	KL67
SiO_2	49.8	48.5	52.0	49.6	50.7	49.8	47.7	49.0	47.4	49.0
TiO_2	1.00	1.16	0.94	1.03	1.17	1.06	1.06	0.85	1.14	0.97
Al_2O_3	15.6	14.7	16.0	15.1	15.6	15.8	15.5	16.3	15.7	17.2
Fe_2O_3	6.52	7.98	6.24	7.06	7.37	7.80	7.47	7.23	7.89	7.35
MnO	0.11	0.15	0.12	0.14	0.14	0.14	0.15	0.14	0.15	0.10
MgO	5.41	6.95	4.97	6.33	5.51	5.09	5.12	4.92	5.30	4.49
CaO	7.30	9.65	7.25	8.33	7.83	8.13	8.61	8.49	8.85	7.35
Na_2O	2.34	1.86	2.94	3.11	2.71	2.80	3.15	2.25	2.18	3.00
K_2O	6.38	5.46	5.47	4.00	4.51	5.08	4.76	5.87	5.42	5.38
P_2O_5	0.85	1.02	0.79	0.96	1.06	1.16	1.05	0.90	1.09	1.02
BaO	0.24	0.25	0.19	0.20	0.24	0.25	0.24	0.28	0.22	0.38
SrO	0.14	0.21	0.13	0.11	0.17	0.21	0.20	0.28	0.23	0.27
LOI	3.73	1.01	2.74	3.25	1.66	0.95	4.70	2.09	3.42	2.40
Sum	99.4	98.8	99.8	99.3	98.7	98.3	99.6	98.6	99.1	98.9
Sc	34	43	31	37	32	27	30	29	30	27
V	213	270	194	205	227	227	225	239	251	241
Cr	164	164	147	193	113	71	94	149	66	44
Co	22	29	19	23	21	25	23	24	26	21
Ni	36	44	33	52	23	28	29	32	30	21
Rb	236	221	144	110	120	179	148	125	187	164
Cs	5.1	5.6	1.5	3.1	3.1	3.5	4.8	15.1	5.5	10.2
Sr	1170	1750	1100	929	1400	1760	1730	2370	1940	2310
Ba	2110	2200	1670	1810	2180	2210	2160	2490	2000	3360
Y	30	31	28	29	34	31	31	37	30	34
Zr	412	380	405	391	430	324	377	393	384	463
Nb	42	51	42	40	43	53	63	29	56	52
La	76	83	77	74	83	94	101	83	86	107
Ce	154	182	153	153	178	188	208	173	185	218
Pr	18	21	18	18	21	21	23	20	21	26
Nd	70	84	69	72	85	84	87	82	83	100
Sm	11.8	14.8	11.5	12.4	15.3	13.8	14.1	14.9	13.8	16.4
Eu	2.9	3.7	2.8	3.2	3.7	3.5	3.8	4.3	3.5	4.3
Gd	8.3	10.4	8.0	8.5	10.5	9.9	10.1	11.9	9.6	10.9
Tb	1.04	1.24	1.01	1.05	1.24	1.19	1.22	1.38	1.30	1.30
Dy	6.0	6.5	5.5	5.7	7.0	6.6	6.7	7.8	6.4	6.9
Ho	1.09	1.17	1.04	1.04	1.20	1.12	1.19	1.30	1.16	1.24
Er	2.9	2.9	2.7	2.9	3.3	2.9	2.9	3.3	3.0	3.2
Tm	0.41	0.40	0.42	0.42	0.47	0.39	0.41	0.45	0.38	0.47
Yb	2.8	2.6	2.8	2.8	3.1	2.5	2.5	2.6	2.3	3.1
Lu	0.43	0.39	0.42	0.40	0.44	0.35	0.39	0.39	0.36	0.45
Hf	10.3	9.7	9.9	9.4	10.1	8.2	8.7	8.6	9.6	10.7
Ta	2.2	2.2	2.3	2.0	2.1	2.3	3.0	1.3	2.4	2.1
Pb	35	22	47	9	14	12	67	16	26	6
Th	25	16	27	20	23	22	19	18	19	21
U	5.9	4.8	6.0	4.8	4.8	5.0	4.7	3.7	5.1	4.7

Table C.1. *(continued)* Whole-rock major (wt %) and trace element (µg/g) analyses of lamprophyre dyke rocks from Kos, Greece

Rock type	Mica-Lamprophyre				Amphibole-Lamprophyre					
Group	medium Nb				low Nb					
Sample	KL80	KL16	KL50	KL63	KL04	KL07	KL09	KL36	KL51	KL78/1
SiO_2	48.2	51.5	51.8	54.2	51.4	51.5	53.1	52.3	52.6	53.5
TiO_2	0.89	0.59	0.71	0.67	0.85	0.84	0.80	0.96	0.92	0.89
Al_2O_3	17.2	17.5	17.2	17.3	14.0	13.2	14.2	14.8	14.7	14.2
Fe_2O_3	6.96	5.27	6.25	5.93	7.89	8.08	7.44	6.66	6.46	6.68
MnO	0.13	0.12	0.12	0.12	0.15	0.14	0.13	0.12	0.11	0.12
MgO	4.43	2.81	3.53	3.18	7.93	8.74	7.30	6.18	6.18	7.19
CaO	7.97	6.03	7.24	5.67	9.69	11.0	9.45	8.64	8.56	8.80
Na_2O	2.96	3.01	3.29	3.60	2.37	2.28	2.47	2.82	2.92	2.85
K_2O	4.38	7.21	4.77	5.80	1.82	1.23	2.48	2.85	2.92	3.10
P_2O_5	1.06	0.54	0.78	0.70	0.41	0.40	0.45	0.46	0.43	0.41
BaO	0.31	0.49	0.39	0.38	0.16	0.13	0.20	0.16	0.16	0.15
SrO	0.23	0.42	0.39	0.32	0.16	0.16	0.20	0.15	0.14	0.12
LOI	5.28	3.70	1.92	1.25	2.63	2.02	0.96	3.83	3.74	0.90
Sum	100.1	99.2	98.4	99.1	99.5	99.6	99.2	99.9	99.8	98.9
Sc	24	15	21	19	35	41	33	31	31	33
V	229	174	203	185	207	230	206	200	191	179
Cr	57	42	28	26	200	234	205	178	200	247
Co	20	16	16	15	32	35	28	26	25	24
Ni	19	16	14	16	46	56	45	46	50	53
Rb	92	134	82	96	41	33	65	81	113	66
Cs	4.2	4.4	1.2	1.7	1.0	1.9	1.7	10.7	6.7	1.3
Sr	1970	3560	3270	2710	1370	1360	1660	1290	1230	992
Ba	2750	4390	3510	3350	1430	1190	1810	1430	1390	1330
Y	29	37	35	36	24	24	25	29	28	23
Zr	395	422	433	457	158	154	185	241	235	189
Nb	45	43	43	51	15	15	21	23	23	17
La	101	222	160	154	59	61	84	66	68	53
Ce	207	410	309	299	120	126	165	134	137	105
Pr	24	47	35	34	14	15	19	15	16	12
Nd	94	175	131	127	55	60	72	60	60	47
Sm	15.4	26.0	20.7	20.4	9.5	10.5	11.5	10.6	10.7	8.7
Eu	4.3	6.8	5.6	5.1	2.4	2.6	2.8	2.7	2.6	2.2
Gd	10.3	15.2	13.0	13.4	6.7	7.4	7.7	8.3	7.9	6.7
Tb	1.18	1.57	1.46	1.52	0.80	0.88	0.93	1.05	0.99	0.86
Dy	6.1	7.7	7.4	7.9	4.5	4.9	5.1	6.0	5.5	4.8
Ho	1.06	1.24	1.26	1.26	0.81	0.91	0.93	1.07	0.96	0.87
Er	2.9	3.0	3.1	3.4	2.1	2.5	2.4	2.8	2.6	2.4
Tm	0.37	0.43	0.42	0.45	0.31	0.33	0.34	0.38	0.37	0.33
Yb	2.6	2.8	2.9	2.8	2.0	2.2	2.2	2.6	2.4	2.1
Lu	0.39	0.39	0.40	0.41	0.29	0.31	0.33	0.41	0.37	0.33
Hf	9.2	8.4	9.6	10.2	4.3	4.3	4.7	6.3	6.1	5.3
Ta	1.8	2.0	2.1	2.5	0.8	0.8	1.1	1.3	1.4	1.1
Pb	19	91	14	51	18	18	34	19	17	23
Th	22	45	35	37	19	20	25	27	28	22
U	4.9	8.5	7.2	6.9	5.5	5.6	6.4	7.1	6.7	5.9

Table C.1. *(continued)* Whole-rock major (wt %) and trace element (µg/g) analyses of lamprophyre dyke rocks from Kos, Greece

Rock type	Amphibole-Lamprophyre									
Group	low Nb		medium Nb						high Nb	
Sample	KL92	KL96	KL02	KL06	KL10	KL52	KL64	KL73	KL12	KL14
SiO_2	53.0	51.1	53.2	54.5	49.4	48.3	57.1	53.4	45.5	43.5
TiO_2	0.86	0.89	0.70	0.69	0.84	0.85	0.72	0.82	1.31	1.00
Al_2O_3	15.2	13.4	14.7	15.1	15.2	13.2	16.4	16.0	14.1	16.4
Fe_2O_3	7.04	8.68	7.14	6.86	8.56	7.69	5.80	6.36	8.51	8.12
MnO	0.13	0.17	0.11	0.12	0.16	0.16	0.11	0.09	0.14	0.15
MgO	6.94	8.66	5.69	5.10	6.42	7.98	3.12	3.65	7.06	5.62
CaO	9.07	9.87	7.55	7.23	8.15	11.7	5.82	6.71	11.5	9.98
Na_2O	2.98	2.30	2.90	2.73	2.75	2.50	3.49	3.62	2.43	2.95
K_2O	2.39	1.91	3.25	3.28	3.38	2.37	4.23	4.57	3.55	3.37
P_2O_5	0.36	0.39	0.71	0.69	0.88	0.75	0.67	0.77	1.72	1.52
BaO	0.14	0.14	0.37	0.45	0.55	0.31	0.32	0.33	0.41	0.43
SrO	0.12	0.14	0.36	0.42	0.47	0.28	0.27	0.21	0.28	0.35
LOI	1.20	2.11	2.02	2.21	2.02	2.75	1.01	2.84	2.57	6.25
Sum	99.5	99.8	98.6	99.3	98.7	98.8	99.1	99.4	99.0	99.6
Sc	31	45	26	25	28	42	16	17	35	25
V	188	225	180	185	240	237	171	184	293	274
Cr	316	199	138	120	36	245	19	16	59	28
Co	24	33	22	22	33	27	17	19	29	26
Ni	27	52	26	27	33	52	12	14	29	24
Rb	60	52	64	77	73	33	126	120	139	95
Cs	1.6	1.1	3.7	2.6	2.0	1.0	5.0	2.1	3.8	2.7
Sr	1060	1160	3010	3550	3960	2350	2290	1800	2380	2950
Ba	1290	1250	3310	3990	4950	2810	2870	2980	3640	3800
Y	26	23	27	31	31	29	32	31	36	34
Zr	199	142	195	239	202	188	320	280	280	259
Nb	20	14	33	38	34	27	64	59	144	111
La	60	57	182	207	250	160	167	157	209	159
Ce	120	121	345	396	450	337	325	313	406	333
Pr	13	14	40	45	58	39	36	35	43	37
Nd	50	56	151	171	217	153	133	131	153	137
Sm	8.6	10.1	20.9	23.6	29.2	23.3	19.4	19.4	21.6	19.9
Eu	2.2	2.3	4.9	5.3	7.1	5.8	4.5	4.5	5.5	5.2
Gd	6.5	7.0	11.5	12.7	15.0	13.9	11.9	11.6	13.6	12.0
Tb	0.81	0.85	1.16	1.23	1.52	1.41	1.25	1.29	1.45	1.34
Dy	4.9	4.8	5.7	6.3	6.9	6.9	6.6	6.5	7.5	6.9
Ho	0.94	0.85	0.96	1.01	1.10	1.05	1.07	1.09	1.21	1.22
Er	2.5	2.3	2.4	2.7	2.8	2.7	2.7	2.8	3.0	3.0
Tm	0.38	0.31	0.34	0.36	0.35	0.35	0.39	0.39	0.40	0.44
Yb	2.6	2.1	2.3	2.4	2.4	2.2	2.6	2.5	2.6	2.8
Lu	0.40	0.29	0.31	0.37	0.34	0.30	0.39	0.37	0.36	0.42
Hf	5.4	4.1	4.8	5.6	4.8	4.5	7.2	6.3	6.0	5.8
Ta	1.3	0.7	1.4	1.6	1.3	1.3	3.5	3.1	4.7	3.9
Pb	44	28	23	29	38	23	19	21	12	20
Th	28	18	41	47	46	30	51	44	29	26
U	6.9	5.3	7.8	8.5	7.9	5.6	11.4	9.8	6.1	5.9

Table C.1. *(continued)* Whole-rock major (wt %) and trace element (μg/g) analyses of lamprophyre dyke rocks from Kos, Greece

Rock type	Amphibole-Lamprophyre			Micro-monzonite dyke
Group	high Nb			
Sample	KL41	KL46	KL95	KL23
SiO_2	41.8	43.3	42.7	52.9
TiO_2	1.17	1.18	1.20	0.98
Al_2O_3	16.2	17.1	15.8	19.3
Fe_2O_3	8.67	8.81	9.23	6.71
MnO	0.10	0.14	0.15	0.12
MgO	5.71	5.79	6.85	2.37
CaO	11.3	9.75	11.3	5.80
Na_2O	2.89	3.34	2.75	3.80
K_2O	2.70	2.35	3.03	4.93
P_2O_5	1.25	1.29	1.78	0.58
BaO	0.38	0.42	0.33	0.21
SrO	0.28	0.29	0.28	0.16
LOI	7.22	6.82	4.20	0.90
Sum	99.7	100.6	99.6	98.8
Sc	28	26	32	15
V	295	284	296	167
Cr	19	16	36	4
Co	25	29	29	15
Ni	20	19	31	4
Rb	66	62	65	169
Cs	5.0	2.1	2.4	9.9
Sr	2400	2440	2390	1370
Ba	3420	3790	2910	1900
Y	33	33	30	33
Zr	220	227	207	499
Nb	80	78	88	43
La	197	198	132	102
Ce	400	397	286	209
Pr	43	43	33	23
Nd	160	158	121	87
Sm	22.2	22.7	18.3	13.8
Eu	5.9	5.8	4.7	3.2
Gd	13.2	13.6	11.6	9.6
Tb	1.43	1.43	1.29	1.21
Dy	7.1	7.4	6.7	6.6
Ho	1.20	1.16	1.17	1.17
Er	3.0	3.2	2.8	3.2
Tm	0.42	0.42	0.37	0.44
Yb	2.6	2.6	2.4	3.1
Lu	0.37	0.35	0.35	0.45
Hf	4.8	5.1	5.1	11.8
Ta	2.7	3.0	3.1	2.5
Pb	16	14	16	42
Th	34	37	19	53
U	7.1	7.5	4.2	11.7

Table C.2. Representative major (wt %) and trace element (μg/g) analyses of Variscan Group I lamprophyres

Region	Taunus	Odenwald-N								
Rock type	Kersantite	Peralkaline minette						Kersantite		
Sample	TA 01	OD 153B	OD 154	OD 154B	OD 169R	OD 175	OD 178	OD 18	OD 41	OD 43
SiO_2	49.6	54.2	55.9	55.2	55.9	57.0	55.9	55.6	55.4	45.9
TiO_2	1.16	2.04	2.06	2.01	2.30	2.08	2.17	0.97	0.97	1.18
Al_2O_3	14.0	12.2	12.1	12.0	11.2	11.4	11.5	12.8	13.6	11.1
Fe_2O_3	8.04	5.39	5.09	5.01	4.60	4.81	4.60	6.32	7.24	9.71
MnO	0.13	0.08	0.09	0.11	0.07	0.08	0.08	0.09	0.12	0.15
MgO	10.4	5.18	4.18	4.32	5.49	4.84	3.82	6.78	6.92	12.3
CaO	6.63	5.27	5.98	6.36	6.35	4.53	6.17	5.86	4.56	8.01
Na_2O	2.17	0.92	0.28	0.38	0.31	1.11	0.20	2.59	2.93	2.57
K_2O	2.66	10.1	9.30	9.31	8.80	10.0	10.5	4.81	4.49	3.33
P_2O_5	0.47	1.72	1.28	1.26	1.56	1.45	1.50	0.46	0.32	0.46
BaO	0.37	0.44	0.23	0.26	0.13	0.44	0.30	0.28	0.30	0.29
SrO	0.13	0.12	0.04	0.05	0.07	0.10	0.06	0.16	0.09	0.16
ZrO_2	0.03	0.20	0.20	0.26	0.29	0.31	0.31	0.05	0.06	0.02
$\sum REE_2O_3$	0.04	0.12	0.07	0.08	0.09	0.09	0.09	0.07	0.06	0.05
LOI	3.32	1.91	3.15	3.21	2.98	1.77	2.56	2.22	2.15	4.21
Sum	99.1	99.9	99.9	99.9	100.1	100.0	99.7	99.1	99.2	99.5
Sc	29	23	23	24	21	22	21	21	22	29
V	192	161	146	153	121	129	148	172	137	202
Cr	543	173	239	241	223	196	335	358	285	885
Co	39	20	20	23	20	20	15	29	30	47
Ni	231	95	121	137	134	136	185	214	178	273
Ga	15	21	18	20	19	22	23	21	18	15
Rb	95	245	369	430	292	408	411	133	112	182
Sr	1120	1060	337	403	576	805	511	1360	741	1330
Y	25	30	29	34	24	30	29	29	26	25
Zr	225	1506	1497	1913	2139	2302	2328	399	440	164
Nb	11	71	59	70	62	76	80	15	32	21
Cs	3.9	2.0	3.4	3.8	2.3	2.0	6.2	3.2	2.5	7.5
Ba	3300	3930	2090	2360	1120	3890	2690	2520	2700	2590
La	77	219	115	138	173	182	171	119	111	77
Ce	164	425	239	277	317	355	354	242	217	178
Pr	20	55	30	35	38	42	43	30	25	23
Nd	75	214	121	143	144	160	164	116	92	93
Sm	12	30	20	24	24	24	25	18	13	13
Eu	2.7	6.5	4.2	5.1	4.3	5.0	5.1	4.1	3.0	3.0
Gd	7.6	16	12	14	12	15	14	11	8.3	7.7
Tb	0.90	1.5	1.3	1.5	1.3	1.5	1.6	1.2	1.01	0.92
Dy	5.0	7.4	6.7	7.6	6.0	7.3	7.7	6.0	5.5	5.2
Ho	0.86	1.2	1.1	1.3	0.91	1.2	1.2	1.0	0.94	0.90
Er	2.3	2.7	2.8	3.3	2.3	2.9	3.1	2.7	2.5	2.5
Tm	0.33	0.34	0.39	0.45	0.3	0.4	0.4	0.36	0.35	0.32
Yb	2.2	2.3	2.4	2.9	1.7	2.4	2.4	2.3	2.2	2.1
Lu	0.32	0.35	0.33	0.41	0.24	0.33	0.33	0.32	0.36	0.34
Hf	5.7	41	42	55	55	69	67	10	16	4.2
Ta	0.7	3.6	3.1	4.0	3.4	3.9	4.2	0.9	2.4	1.0
Pb	18	24	89	87	7	91	35	37	70	18
Th	16	63	42	56	67	85	69	34	41	14
U	2.8	9.4	8.2	11.3	11	13	13	6.2	5.9	2.7

Table C.2. *(continued)* Representative major (wt %) and trace element (μg/g) analyses of Variscan Group I lamprophyres

Region	Odenwald-N									
Rock type	Kersantite						Minette	Spessartite		
Sample	OD 113	OD 114	OD 129	OD 149	OD 151C	OD 156B	OD 167	OD 11	OD 29	OD 38
SiO_2	44.9	52.1	53.2	55.2	53.9	55.6	55.7	51.3	51.3	54.8
TiO_2	1.26	1.31	1.09	1.28	0.96	1.05	0.93	1.08	1.03	0.89
Al_2O_3	10.7	14.0	14.2	14.2	14.1	14.7	13.7	14.5	13.6	13.4
Fe_2O_3	9.95	8.53	7.06	6.32	6.54	7.15	6.28	9.40	8.67	7.45
MnO	0.17	0.14	0.12	0.11	0.10	0.10	0.10	0.15	0.13	0.12
MgO	14.0	7.18	7.98	7.31	6.84	6.48	7.45	7.22	7.88	7.13
CaO	6.51	6.56	5.83	4.29	4.94	5.90	5.46	6.44	6.81	6.26
Na_2O	2.43	2.58	3.24	3.01	3.20	3.31	2.61	2.21	3.01	3.64
K_2O	3.37	4.48	4.31	5.26	4.62	3.87	5.23	2.71	2.74	2.81
P_2O_5	0.49	0.79	0.60	0.65	0.58	0.34	0.47	0.24	0.31	0.38
BaO	0.40	0.35	0.35	0.33	0.30	0.21	0.27	0.10	0.20	0.09
SrO	0.13	0.14	0.14	0.12	0.11	0.11	0.16	0.08	0.09	0.08
ZrO_2	0.02	0.05	0.05	0.08	0.06	0.05	0.06	0.03	0.03	0.03
$\sum REE_2O_3$	0.05	0.08	0.08	0.07	0.06	0.04	0.05	0.03	0.04	0.05
LOI	5.66	1.40	1.65	1.42	3.42	1.02	1.23	3.93	3.91	2.40
Sum	100.0	99.6	99.9	99.7	99.7	99.9	99.7	99.4	99.7	99.6
Sc	31	22	24	21	22	20	20	25	24	22
V	224	169	166	144	138	149	155	180	172	161
Cr	925	248	310	340	262	280	399	250	392	310
Co	53	24	30	27	26	28	29	38	38	32
Ni	311	146	188	202	162	150	226	150	206	180
Ga	15	20	19	22	18	19	19	18	17	17
Rb	181	129	136	161	107	108	163	81	82	71
Sr	1140	1210	1160	1040	927	967	1380	682	725	692
Y	25	32	30	28	26	20	21	25	23	27
Zr	167	364	396	610	440	341	404	202	188	225
Nb	21	20	32	28	24	19	25	15	19	17
Cs	10.7	6.5	4.0	3.9	3.6	2.7	5.8	6.0	1.3	0.6
Ba	3530	3110	3110	2940	2680	1830	2430	933	1760	791
La	83	141	158	133	117	67	100	60	72	89
Ce	192	283	322	266	224	130	196	129	149	177
Pr	24	34	38	32	27	16	23	15	17	21
Nd	97	133	143	122	101	59	84	57	64	81
Sm	13	21	19	18	15	9.1	12	8.9	10	13
Eu	3.0	5.2	4.5	4.1	3.4	2.2	2.7	2.4	2.3	2.9
Gd	8.1	13	12	11	9.0	6.5	7.3	6.5	6.4	8.2
Tb	0.93	1.4	1.3	1.2	1.00	0.76	0.85	0.84	0.79	0.98
Dy	5.1	7.4	6.5	5.9	5.4	4.2	4.5	4.8	4.4	5.3
Ho	0.91	1.2	1.1	1.0	0.92	0.76	0.76	0.93	0.83	0.93
Er	2.5	2.9	2.8	2.6	2.4	1.9	2.0	2.4	2.3	2.5
Tm	0.33	0.36	0.37	0.37	0.31	0.28	0.28	0.34	0.3	0.35
Yb	2.2	2.4	2.4	2.2	2.1	1.7	1.8	2.3	2.0	2.4
Lu	0.34	0.31	0.33	0.31	0.30	0.23	0.27	0.34	0.28	0.34
Hf	4.0	9.8	11	17	12	9.1	11	5.9	5.2	6.1
Ta	1.0	1.2	1.8	1.8	1.6	1.2	1.5	0.8	1.1	1.1
Pb	6	16	28	22	29	23	35	15	35	18
Th	15	36	30	30	39	22	43	18	18	29
U	2.8	5.7	4.5	4.5	5.6	3.0	6.7	3.0	3.3	5.3

Table C.2. *(continued)* Representative major (wt %) and trace element (μg/g) analyses of Variscan Group I lamprophyres

Region	Odenwald-N									
Rock type	Spessartite									
Sample	OD 40	OD 60	OD 64	OD 65	OD 80	OD 147	OD 150	OD 159	OD 168	OD 170
SiO_2	50.2	52.4	51.5	53.6	50.4	54.3	59.4	50.4	56.3	55.3
TiO_2	1.30	1.55	1.14	1.01	1.59	1.01	0.76	1.34	0.93	1.53
Al_2O_3	14.0	13.3	14.7	13.9	13.7	13.5	17.2	13.9	14.4	13.4
Fe_2O_3	10.5	8.10	10.2	8.10	9.49	8.07	6.31	10.6	7.52	7.96
MnO	0.16	0.12	0.13	0.12	0.15	0.15	0.12	0.17	0.11	0.11
MgO	8.57	7.02	7.49	7.21	8.88	8.33	3.83	8.40	5.87	6.17
CaO	6.37	6.91	6.89	5.66	7.52	5.31	5.97	6.86	4.90	6.20
Na_2O	2.65	2.24	3.14	3.32	3.63	3.28	3.76	2.96	3.62	3.89
K_2O	2.85	4.53	1.03	2.85	2.45	3.10	1.39	2.62	3.82	3.40
P_2O_5	0.31	0.37	0.21	0.47	0.30	0.44	0.23	0.32	0.29	0.36
BaO	0.12	0.17	0.08	0.16	0.21	0.20	0.09	0.12	0.17	0.13
SrO	0.07	0.11	0.07	0.08	0.10	0.10	0.07	0.07	0.13	0.09
ZrO_2	0.03	0.03	0.02	0.04	0.02	0.04	0.02	0.03	0.04	0.03
$\sum REE_2O_3$	0.03	0.03	0.02	0.04	0.04	0.07	0.02	0.03	0.03	0.03
LOI	2.84	3.57	3.29	3.76	1.39	2.05	1.39	2.12	1.32	1.94
Sum	100.0	100.4	99.9	100.3	99.9	99.9	100.5	100.0	99.5	100.4
Sc	23	18	23	20	34	22	17	23	19	18
V	184	151	190	150	224	171	133	180	139	160
Cr	320	265	254	298	371	340	113	313	241	236
Co	46	32	41	33	40	33	17	42	28	30
Ni	212	168	148	193	207	221	32	200	160	156
Ga	18	20	19	18	17	19	19	19	18	18
Rb	111	125	49	86	58	67	37	108	85	91
Sr	554	923	627	684	840	850	616	617	1080	720
Y	20	21	20	22	25	32	15	23	22	20
Zr	188	203	152	266	176	281	163	194	285	188
Nb	13	17	8	14	20	17	9	13	15	17
Cs	2.0	5.0	5.3	2.2	0.6	2.7	1.5	2.3	1.1	0.6
Ba	1080	1490	728	1420	1890	1790	805	1030	1560	1170
La	46	51	37	84	72	135	31	49	67	48
Ce	95	100	77	168	149	263	64	103	127	97
Pr	11	13	8.8	20	18	31	7.4	12	15	12
Nd	44	52	35	74	72	120	29	48	56	52
Sm	7.6	10	6.1	11	11	19	5.4	8.4	8.9	10
Eu	2.0	2.8	1.7	2.6	2.7	4.1	1.4	2.1	2.1	2.7
Gd	5.7	7.7	4.8	7.3	7.6	11	3.8	6.0	6.1	7.5
Tb	0.74	0.85	0.67	0.87	0.95	1.2	0.49	0.78	0.75	0.82
Dy	4.3	4.4	3.9	4.5	5.3	6.7	2.9	4.5	4.2	4.6
Ho	0.77	0.72	0.70	0.80	0.92	1.1	0.56	0.81	0.76	0.82
Er	2.0	1.9	2.0	2.1	2.6	3.0	1.5	2.2	2.1	1.9
Tm	0.28	0.25	0.28	0.27	0.35	0.41	0.22	0.3	0.28	0.25
Yb	1.9	1.5	1.8	1.8	2.1	2.7	1.5	2.0	1.9	1.4
Lu	0.27	0.20	0.26	0.27	0.31	0.39	0.24	0.28	0.28	0.19
Hf	5.3	5.5	4.0	6.9	5.3	7.5	4.4	5.5	7.6	5.4
Ta	0.7	1.0	0.5	0.9	1.2	1.1	0.7	0.8	0.9	1.0
Pb	28	53	19	152	12	28	69	29	21	4
Th	14	16	11	27	16	41	7.6	15	25	16
U	2.3	4.3	2.0	4.5	2.7	7.7	2.1	2.5	3.8	3.4

Table C.2. *(continued)* Representative major (wt %) and trace element (μg/g) analyses of Variscan Group I lamprophyres

Region	Odenwald-N		Spessart				Vosges-N	
Rock type	Spess.-Kers.		Peralk. minette	Kers.	Spessartite		Peralk. minette	
Sample	OD 25	OD 27	SP 12	SP 14	SP 15	SP 19	VO 03	VO 86
SiO_2	53.3	53.5	55.9	55.3	57.1	56.5	48.7	48.1
TiO_2	0.83	0.88	2.28	1.05	0.82	0.97	1.76	1.73
Al_2O_3	12.5	12.8	11.3	13.9	15.3	14.5	11.0	10.8
Fe_2O_3	7.43	7.90	4.98	6.77	7.90	7.31	7.35	7.15
MnO	0.12	0.11	0.08	0.10	0.12	0.10	0.10	0.10
MgO	9.32	9.96	5.53	6.73	5.70	6.49	7.05	6.97
CaO	6.44	5.11	4.64	5.68	5.75	5.02	6.93	7.86
Na_2O	3.03	3.58	1.15	3.39	3.32	3.57	2.30	1.57
K_2O	2.96	2.16	9.72	4.72	2.90	3.62	6.99	7.10
P_2O_5	0.46	0.46	1.56	0.78	0.14	0.39	2.05	2.14
BaO	0.21	0.17	0.51	0.32	0.12	0.21	0.95	1.19
SrO	0.13	0.09	0.08	0.14	0.07	0.11	0.28	0.29
ZrO_2	0.03	0.03	0.28	0.06	0.02	0.03	0.13	0.14
$\sum REE_2O_3$	0.06	0.06	0.09	0.08	0.02	0.05	0.15	0.16
LOI	2.40	2.55	1.59	1.10	0.70	1.03	4.27	4.17
Sum	99.3	99.4	99.7	100.1	100.0	99.9	100.0	99.4
Sc	21	22	21	21	23	20	19	21
V	164	172	125	142	140	142	157	171
Cr	452	492	236	263	163	222	218	238
Co	37	38	21	28	29	27	27	32
Ni	333	324	150	161	98	140	137	156
Ga	18	18	20	18	17	18	19	21
Rb	77	66	366	125	93	99	159	196
Sr	1090	721	709	1200	574	942	2370	2430
Y	27	28	27	28	19	24	34	37
Zr	230	226	2070	472	175	247	933	1040
Nb	17	17	68	22	16	15	38	52
Cs	1.4	3.3	3.1	3.1	5.0	4.6	6.4	7.2
Ba	1850	1530	4560	2860	1110	1900	8450	10600
La	116	113	172	143	32	99	290	305
Ce	234	233	323	278	63	191	561	644
Pr	28	28	37	35	7.3	23	70	74
Nd	106	107	142	141	28	89	272	287
Sm	16	17	21	22	4.9	14	39	40
Eu	3.8	3.8	4.4	5.2	1.4	3.1	7.8	8.2
Gd	10	10	13	14	4.5	8.8	20	20
Tb	1.1	1.1	1.2	1.4	0.63	0.99	1.9	2.0
Dy	5.5	5.7	6.0	6.6	3.8	5.1	8.3	8.7
Ho	0.98	1.0	0.98	1.1	0.78	0.86	1.2	1.3
Er	2.5	2.6	2.5	2.6	2.1	2.2	2.9	3.0
Tm	0.34	0.37	0.33	0.36	0.31	0.29	0.35	0.38
Yb	2.3	2.4	2.2	2.2	2.0	2.0	2.2	2.4
Lu	0.31	0.35	0.31	0.30	0.28	0.26	0.32	0.34
Hf	6.1	5.9	57	12	6.3	6.6	23	27
Ta	1.0	1.0	3.4	1.5	1.1	1.0	2.4	2.9
Pb	19	42	151	19	15	26	46	34
Th	35	35	63	36	18	33	42	65
U	6.7	6.7	10.2	5.7	3.4	4.8	4.9	5.9

Table C.2. *(continued)* Representative major (wt %) and trace element (μg/g) analyses of Variscan Group I lamprophyres

Region	Vosges-N										
Rock type	Kersantite									Minette	
Sample	VO 11	VO 23	VO 30	VO 33B	VO 34	VO 35	VO 88	VO 95A	VO 96B	VO 12	VO 16
SiO_2	46.4	48.6	49.6	47.3	43.8	51.7	46.4	47.3	46.7	50.5	48.2
TiO_2	1.51	1.49	1.32	1.64	1.66	1.34	1.57	1.51	1.71	1.56	1.50
Al_2O_3	13.8	13.9	12.8	13.0	14.0	14.4	12.0	14.1	12.4	13.4	13.1
Fe_2O_3	7.90	8.15	6.76	8.19	9.11	7.66	8.15	8.57	7.58	6.84	6.61
MnO	0.27	0.12	0.13	0.14	0.21	0.12	0.13	0.18	0.15	0.10	0.09
MgO	8.00	7.62	7.76	9.76	8.77	8.52	10.2	9.89	6.14	7.23	5.09
CaO	7.82	7.45	7.69	5.81	6.04	5.58	8.99	4.83	8.55	5.38	8.94
Na_2O	2.58	3.87	3.34	2.20	2.85	2.65	2.31	2.25	2.22	2.58	2.53
K_2O	3.56	1.54	4.90	5.10	5.07	4.50	3.40	4.76	4.91	6.93	5.44
P_2O_5	1.06	0.83	1.64	1.10	1.54	0.50	1.58	1.09	1.99	1.48	1.35
BaO	0.27	0.28	0.64	0.39	0.46	0.24	0.45	0.39	0.64	0.48	0.44
SrO	0.10	0.20	0.28	0.11	0.15	0.14	0.27	0.12	0.16	0.19	0.17
ZrO_2	0.05	0.05	0.09	0.07	0.06	0.06	0.05	0.05	0.07	0.10	0.07
$\sum REE_2O_3$	0.06	0.06	0.14	0.06	0.09	0.04	0.08	0.07	0.08	0.08	0.08
LOI	7.50	6.82	3.15	5.48	7.46	2.89	4.57	4.73	6.20	2.79	6.86
Sum	100.8	100.9	100.2	100.4	101.2	100.3	100.2	99.8	99.6	99.6	100.4
Sc	23	24	20	25	25	24	27	24	21	18	20
V	178	177	152	171	197	181	185	175	161	138	159
Cr	377	316	226	426	277	356	1136	384	247	283	270
Co	36	31	28	35	34	34	38	35	29	24	26
Ni	196	153	151	217	148	203	242	179	135	153	132
Ga	17	17	21	15	19	20	16	17	16	17	18
Rb	83	42	121	108	82	107	82	104	128	186	163
Sr	847	1680	2380	903	1240	1210	2270	984	1330	1640	1420
Y	25	26	36	26	35	23	29	29	27	27	23
Zr	372	387	626	515	447	412	395	385	501	769	493
Nb	30	33	43	31	34	36	36	31	41	37	26
Cs	16.9	3.5	3.9	3.6	9.8	6.6	4.9	20.7	2.7	4.2	4.1
Ba	2400	2480	5740	3510	4130	2140	4010	3450	5740	4290	3900
La	117	117	269	115	170	80	154	124	153	144	158
Ce	250	240	530	241	357	162	321	265	308	304	319
Pr	29	28	68	29	43	19	39	31	36	37	40
Nd	112	106	270	115	166	72	150	121	140	144	154
Sm	16	16	39	18	24	11	22	18	20	21	22
Eu	3.8	3.5	8.4	4.0	5.5	2.7	4.8	4.3	4.3	5.0	4.7
Gd	10	9.4	21	11	14	7.3	12	11	11	12	11
Tb	1.1	1.1	2.0	1.1	1.5	0.88	1.2	1.2	1.2	1.3	1.1
Dy	5.7	5.8	8.9	6.0	7.7	4.7	6.3	6.2	5.7	6.0	5.5
Ho	0.94	0.99	1.4	1.0	1.26	0.82	1.03	1.10	0.95	0.96	0.84
Er	2.4	2.5	3.0	2.6	3.1	2.2	2.6	2.6	2.3	2.4	2.0
Tm	0.33	0.33	0.39	0.34	0.42	0.29	0.33	0.35	0.33	0.3	0.27
Yb	2.1	2.2	2.4	2.2	2.6	2.0	2.1	2.2	2.1	1.8	1.7
Lu	0.29	0.32	0.34	0.32	0.38	0.27	0.33	0.33	0.27	0.27	0.23
Hf	8.9	9.7	15	13	10	10	9.7	8.4	12	19	13
Ta	1.7	2.0	2.5	1.9	2.0	2.0	2.1	1.9	2.2	2.1	1.6
Pb	24	37	14	28	22	18	21	33	561	46	36
Th	20	24	56	24	31	17	28	26	34	37	30
U	3.2	4.0	7.9	3.4	4.2	3.6	2.9	3.6	5.4	5.8	4.5

Table C.2. *(continued)* Representative major (wt %) and trace element (μg/g) analyses of Variscan Group I lamprophyres

Region	Vosges-N										
Rock type	Minette										
Sample	VO 21	VO 22	VO 24	VO 27	VO 36	VO 37	VO 40	VO 41A	VO 48	VO 90A	VO 91
SiO_2	48.0	50.1	47.3	46.1	49.3	52.5	45.2	48.4	56.7	45.4	45.9
TiO_2	1.34	1.14	2.70	1.57	1.79	1.93	1.45	1.60	1.36	1.55	1.19
Al_2O_3	13.9	12.5	12.4	12.1	12.8	13.4	11.6	11.4	13.8	11.2	11.8
Fe_2O_3	7.36	6.00	11.9	7.62	7.83	6.55	7.96	7.24	5.58	6.69	6.77
MnO	0.18	0.12	0.14	0.15	0.12	0.07	0.10	0.10	0.11	0.31	0.15
MgO	7.69	6.59	6.35	7.99	8.94	6.63	10.3	7.37	5.80	8.26	7.71
CaO	7.05	5.87	6.38	8.25	6.37	4.50	7.76	8.18	3.99	8.56	7.62
Na_2O	2.06	2.32	1.77	2.39	2.74	1.33	1.79	2.43	2.49	2.61	1.86
K_2O	5.15	5.18	5.55	5.09	5.84	7.75	5.14	5.16	6.88	5.06	6.03
P_2O_5	1.21	1.11	1.43	1.61	1.35	1.11	1.72	1.83	1.16	1.77	2.29
BaO	0.50	0.44	0.18	0.69	0.59	0.29	0.77	0.67	0.46	0.70	1.21
SrO	0.20	0.00	0.19	0.24	0.13	0.11	0.12	0.21	0.21	0.24	0.25
ZrO_2	0.08	0.07	0.04	0.08	0.08	0.14	0.08	0.09	0.09	0.10	0.20
$\sum REE_2O_3$	0.09	0.08	0.05	0.13	0.09	0.07	0.13	0.13	0.12	0.16	0.18
LOI	5.88	7.51	3.91	6.27	1.78	4.18	6.19	5.94	1.39	7.54	7.45
Sum	100.6	99.0	100.3	100.3	99.8	100.6	100.3	100.7	100.1	100.1	100.6
Sc	25	21	18	22	24	17	25	22	18	22	24
V	164	148	235	164	175	126	163	173	137	167	156
Cr	355	283	190	394	406	188	517	286	245	315	314
Co	30	24	36	30	33	23	36	32	20	29	33
Ni	166	139	106	224	207	130	245	175	124	180	193
Ga	18	19	23	20	19	20	16	19	23	20	19
Rb	141	132	90	115	126	153	111	130	166	134	163
Sr	1670	0	1570	2030	1100	913	984	1750	1770	2010	2090
Y	31	29	18	36	33	27	37	30	29	38	33
Zr	602	478	313	595	609	1050	571	627	685	746	1475
Nb	39	41	43	40	40	112	40	32	44	39	123
Cs	12.7	7.6	3.2	4.7	4.7	1.6	10.5	7.1	4.3	5.6	8.2
Ba	4480	3900	1580	6200	5270	2560	6870	5990	4100	6270	10800
La	173	159	92	243	154	127	245	243	213	295	379
Ce	347	315	205	478	326	251	484	474	459	609	683
Pr	42	38	23	59	40	29	61	60	51	75	77
Nd	157	146	81	232	162	109	243	233	197	293	281
Sm	22	21	11	34	25	16	37	33	28	41	34
Eu	5.0	4.5	2.4	7.4	5.8	3.5	7.9	6.9	5.8	8.5	7.0
Gd	12	12	6.6	19	15	10	21	17	15	22	18
Tb	1.3	1.3	0.74	1.9	1.6	1.1	2.0	1.6	1.5	2.0	1.7
Dy	7.0	6.3	4.2	8.9	7.5	6.1	9.1	7.3	7.2	9.5	8.4
Ho	1.2	1.0	0.77	1.3	1.2	0.99	1.4	1.1	1.1	1.4	1.3
Er	2.9	2.5	2.0	3.0	3.0	2.4	3.1	2.6	2.6	3.2	3.0
Tm	0.38	0.34	0.23	0.37	0.38	0.31	0.4	0.33	0.32	0.43	0.4
Yb	2.6	2.3	1.7	2.2	2.3	1.8	2.3	2.0	2.0	2.7	2.4
Lu	0.36	0.29	0.23	0.28	0.34	0.27	0.35	0.28	0.28	0.37	0.36
Hf	15	12	8.4	13	15	25	14	16	17	20	32
Ta	2.4	2.6	2.5	2.2	2.4	7.4	2.2	1.8	2.9	2.3	4.7
Pb	42	143	38	42	23	24	24	28	18	71	64
Th	42	40	13	41	31	29	48	42	69	57	83
U	5.0	7.4	4.5	4.9	4.0	5.4	5.1	4.3	7.7	7.3	10

Table C.2. *(continued)* Representative major (wt %) and trace element (μg/g) analyses of Variscan Group I lamprophyres

Region	Vosges-N		
Rock type	Spessartite		Spessartite-Kersantite
Sample	VO 33A	VO 89	VO 15
SiO_2	50.8	51.6	55.2
TiO_2	1.28	1.39	1.22
Al_2O_3	13.8	14.6	15.5
Fe_2O_3	7.70	7.89	6.60
MnO	0.13	0.17	0.10
MgO	7.46	7.79	6.68
CaO	7.66	6.47	3.68
Na_2O	4.00	3.65	3.30
K_2O	1.79	3.28	4.34
P_2O_5	0.84	1.13	0.57
BaO	0.13	0.28	0.18
SrO	0.17	0.20	0.08
ZrO_2	0.04	0.05	0.05
$\sum REE_2O_3$	0.07	0.07	0.05
LOI	4.96	1.45	3.20
Sum	100.8	100.0	100.8
Sc	21	22	17
V	160	180	147
Cr	213	265	226
Co	27	30	24
Ni	143	138	124
Ga	17	18	19
Rb	26	76	121
Sr	1470	1730	642
Y	26	30	20
Zr	322	339	347
Nb	27	41	20
Cs	0.7	3.0	10.7
Ba	1150	2480	1630
La	139	155	88
Ce	263	282	179
Pr	31	32	21
Nd	120	118	75
Sm	17	17	11
Eu	3.9	3.9	2.6
Gd	10	11	6.7
Tb	1.1	1.3	0.75
Dy	5.5	6.8	4.1
Ho	0.97	1.2	0.74
Er	2.4	3.0	1.9
Tm	0.32	0.41	0.26
Yb	2.1	2.5	1.7
Lu	0.31	0.36	0.25
Hf	7.5	8.2	8.5
Ta	1.5	2.3	1.3
Pb	21	65	27
Th	33.1	50.8	21.5
U	5.8	9.3	3.8

Table C.3. Representative major (wt %) and trace element (μg/g) analyses of Variscan Group II lamprophyres

Region	Odenwald-S									
Rock type	Kersantite			Minette						
Sample	VO 05B	VO 06C	VO 152	VO 07	VO 19	VO 58B	VO 79B	VO 124	VO 145	VO 157A
SiO_2	52.8	47.2	53.8	53.7	50.4	47.5	50.2	53.2	48.5	54.7
TiO_2	0.99	1.16	0.98	1.32	1.12	1.12	1.22	1.04	1.13	1.39
Al_2O_3	13.3	12.8	13.3	12.5	14.1	12.0	11.8	14.0	12.4	13.1
Fe_2O_3	8.59	8.53	7.87	8.03	8.04	8.13	8.21	8.57	8.46	7.80
MnO	0.14	0.14	0.12	0.12	0.13	0.13	0.15	0.17	0.13	0.11
MgO	5.91	8.80	8.10	6.90	5.90	7.52	7.57	6.51	7.45	5.59
CaO	6.94	8.79	5.86	5.71	7.20	7.67	6.29	5.90	7.56	5.28
Na_2O	2.84	2.99	2.55	1.84	2.17	2.11	1.80	2.61	1.88	1.79
K_2O	4.54	3.71	4.63	6.28	6.03	4.90	5.01	5.15	5.55	7.70
P_2O_5	0.68	0.98	0.57	0.82	0.85	1.05	0.77	0.79	1.06	0.87
BaO	0.14	0.36	0.25	0.14	0.41	0.91	0.31	0.20	0.58	0.17
SrO	0.07	0.13	0.09	0.06	0.09	0.10	0.07	0.06	0.08	0.08
ZrO_2	0.03	0.04	0.04	0.06	0.04	0.05	0.05	0.04	0.04	0.07
$\sum REE_2O_3$	0.02	0.04	0.02	0.04	0.03	0.03	0.04	0.03	0.03	0.04
LOI	2.58	4.21	1.55	1.53	3.18	6.61	6.37	1.48	5.47	1.28
Sum	99.6	99.8	99.7	99.1	99.7	99.8	99.8	99.7	100.3	100.0
Sc	31	37	28	29	34	34	31	36	32	30
V	203	225	187	201	221	213	206	214	208	206
Cr	191	510	550	345	217	363	590	328	342	226
Co	29	38	34	32	29	35	35	30	35	26
Ni	39	119	137	62	38	95	127	74	98	36
Ga	15	14	17	18	16	14	16	15	15	18
Rb	239	126	167	335	276	299	199	257	311	362
Sr	547	1110	726	519	772	836	601	500	680	649
Y	31	38	26	30	35	32	30	37	30	34
Zr	206	324	273	442	321	337	376	269	323	516
Nb	20	17	15	25	19	18	25	17	18	28
Cs	3.7	6.8	4.5	5.6	3.4	17.7	6.1	6.5	14.2	5.7
Ba	1210	3240	2190	1250	3670	8090	2730	1790	5140	1510
La	36	55	37	48	46	42	54	41	40	54
Ce	79	119	79	120	100	103	123	87	102	130
Pr	10	16	10	16	13	15	16	12	15	18
Nd	43	74	42	73	52	70	70	55	70	82
Sm	8.3	16	8.4	14	11	15	13	12	15	15
Eu	1.9	3.9	1.9	2.7	2.7	3.2	2.8	2.4	3.2	3.0
Gd	6.6	13	6.7	8.5	8.7	11	9.2	8.8	10	10
Tb	0.94	1.5	0.87	1.1	1.2	1.2	1.2	1.2	1.2	1.3
Dy	5.7	8.6	5.1	6.1	6.9	6.7	6.5	7.1	6.6	7.1
Ho	1.1	1.4	0.94	1.2	1.3	1.2	1.2	1.3	1.2	1.3
Er	3.3	3.6	2.6	3.1	3.2	3.0	3.2	3.7	3.0	3.5
Tm	0.47	0.5	0.38	0.42	0.45	0.4	0.44	0.54	0.38	0.47
Yb	3.3	3.2	2.4	3.0	3.0	2.7	2.8	3.5	2.7	3.3
Lu	0.48	0.44	0.35	0.42	0.44	0.39	0.41	0.49	0.38	0.50
Hf	5.9	8.9	7.3	12	8.0	8.8	10	7.5	9.1	14
Ta	1.2	1.0	1.0	1.5	1.1	1.0	1.6	1.1	1.0	1.9
Pb	18	52	30	13	27	31	26	17	38	24
Th	13	29	18	33	18	38	25	24	37	37
U	3.2	4.6	4.2	7.3	3.8	6.1	4.7	5.6	6.1	7.3

Table C.3. *(continued)* Representative major (wt %) and trace element (μg/g) analyses of Variscan Group II lamprophyres

Region	Odenwald-S			Pfalz					Vosges-C	
Rock type	Minette			Minette				Spess.-Kers.	Kersantite	
Sample	VO 157B	VO 163	VO 164	VO 01	VO 02	VO 03	VO 05	VO 04	VO 07	VO 08
SiO_2	55.6	51.0	54.0	52.8	53.3	52.2	52.9	46.1	53.8	53.1
TiO_2	1.35	1.14	1.21	1.30	1.32	1.17	1.17	1.52	1.24	1.22
Al_2O_3	13.0	11.2	13.4	14.8	14.9	14.5	14.1	11.6	15.2	14.6
Fe_2O_3	7.71	7.24	8.29	8.25	8.42	8.31	8.00	10.4	7.26	7.60
MnO	0.11	0.14	0.14	0.12	0.11	0.13	0.12	0.17	0.11	0.11
MgO	5.64	11.5	6.81	5.80	5.83	6.08	6.88	10.8	6.87	9.56
CaO	5.30	4.11	6.25	5.90	5.76	3.96	5.66	8.05	5.10	4.44
Na_2O	2.54	1.10	2.31	2.41	2.69	2.19	2.67	2.27	2.57	1.79
K_2O	6.14	6.54	5.35	5.67	5.34	6.12	5.14	3.47	4.13	4.49
P_2O_5	0.82	1.02	0.76	0.79	0.78	0.83	0.72	0.96	0.46	0.46
BaO	0.17	0.55	0.21	0.24	0.24	0.26	0.28	0.30	0.24	0.23
SrO	0.07	0.08	0.07	0.09	0.09	0.07	0.10	0.10	0.08	0.06
ZrO_2	0.07	0.05	0.06	0.05	0.05	0.04	0.05	0.04	0.04	0.04
$\sum REE_2O_3$	0.04	0.05	0.03	0.03	0.03	0.02	0.04	0.04	0.04	0.04
LOI	1.13	4.18	1.76	2.36	1.22	4.67	2.75	4.14	3.14	2.62
Sum	99.7	99.9	100.6	100.6	100.1	100.6	100.6	100.0	100.3	100.4
Sc	30	23	33	31	29	34	28	33	26	26
V	203	182	215	212	207	214	197	247	148	149
Cr	230	482	314	204	216	318	314	586	335	471
Co	25	37	31	29	26	31	29	46	26	32
Ni	37	334	55	43	49	72	79	269	84	145
Ga	17	16	16	17	18	16	17	19	17	17
Rb	335	224	245	265	258	288	197	154	204	260
Sr	557	667	613	719	733	557	874	808	674	504
Y	35	43	33	34	34	33	35	29	29	26
Zr	532	352	429	394	400	290	382	322	300	317
Nb	28	19	23	26	27	21	22	32	14	14
Cs	4.8	11	3.8	20	17	21	3.5	21	39	43
Ba	1490	4950	1840	2120	2150	2300	2460	2710	2100	2090
La	57	81	43	53	54	34	59	65	75	74
Ce	132	159	102	114	117	79	121	140	157	156
Pr	18	20	14	15	16	11	16	17	19	19
Nd	81	80	62	66	65	47	65	69	77	73
Sm	15	17	13	13	13	11	12	12	12	12
Eu	3.0	4.1	2.8	2.9	2.8	2.4	2.9	3.0	3.0	2.7
Gd	10	14	8.6	9.4	9.4	8.5	9.3	9.0	8.5	7.9
Tb	1.2	1.7	1.1	1.2	1.2	1.1	1.2	1.1	1.03	0.96
Dy	6.8	8.8	6.4	7.0	6.9	6.5	6.9	6.2	5.8	5.4
Ho	1.3	1.4	1.2	1.3	1.2	1.2	1.2	1.1	1.1	1.0
Er	3.5	3.6	3.1	3.4	3.2	3.2	3.2	2.8	2.8	2.6
Tm	0.5	0.47	0.46	0.5	0.48	0.48	0.48	0.37	0.39	0.37
Yb	3.4	2.9	3.4	3.2	3.2	2.8	3.2	2.4	2.5	2.4
Lu	0.48	0.43	0.49	0.47	0.44	0.43	0.43	0.33	0.38	0.36
Hf	15	8.8	12	10.8	10.2	7.5	9.4	8.4	7.6	8.3
Ta	1.9	1.2	1.5	1.7	1.7	1.3	1.4	1.8	0.8	0.9
Pb	17	12	26	21	21	19	21	26	14	10
Th	41	21	27	29	29	20	23	19	19	19
U	8.1	4.7	4.5	4.8	5.8	3.6	4.3	2.9	3.3	4.7

Table C.3. *(continued)* Representative major (wt %) and trace element (μg/g) analyses of Variscan Group II lamprophyres

Region	Vosges-C										
Rock type	Kersantite						Minette		Spessartite-Kersantite		
Sample	VO 10	VO 13	VO 14	VO 19	VO 52	VO 78A	VO 76A	VO 76B	VO 09	VO 77	VO 79
SiO_2	51.9	54.2	54.0	52.7	52.3	54.0	51.5	51.8	59.4	53.4	56.7
TiO_2	1.13	1.42	1.35	1.29	1.31	1.29	1.54	1.40	0.77	1.27	0.85
Al_2O_3	16.3	15.8	15.1	14.8	14.8	15.3	15.0	14.8	15.3	15.0	15.0
Fe_2O_3	7.70	8.35	7.55	7.86	9.45	7.64	8.85	8.26	5.56	8.08	6.69
MnO	0.12	0.13	0.11	0.11	0.12	0.11	0.08	0.09	0.11	0.13	0.12
MgO	7.07	6.39	7.73	8.53	6.97	6.78	10.4	9.48	5.49	8.02	6.94
CaO	5.61	4.99	4.90	5.23	3.97	5.47	1.80	2.60	4.91	5.62	4.69
Na_2O	2.41	2.61	2.77	2.12	3.71	2.46	0.94	1.23	3.15	2.44	2.85
K_2O	2.41	3.59	3.93	4.12	4.47	4.36	5.29	5.39	3.38	3.37	3.81
P_2O_5	0.23	0.39	0.47	0.49	1.02	0.50	0.61	0.56	0.27	0.49	0.32
BaO	0.12	0.11	0.24	0.24	0.29	0.25	0.26	0.24	0.06	0.22	0.17
SrO	0.04	0.05	0.08	0.06	0.10	0.11	0.02	0.04	0.05	0.09	0.08
ZrO_2	0.03	0.04	0.04	0.04	0.05	0.04	0.04	0.04	0.02	0.04	0.03
$\sum REE_2O_3$	0.02	0.03	0.04	0.04	0.06	0.04	0.04	0.04	0.02	0.04	0.04
LOI	5.12	1.44	1.76	2.62	1.46	1.44	4.33	4.51	2.17	1.76	1.25
Sum	100.1	99.6	100.0	100.3	100.0	99.8	100.7	100.5	100.6	100.0	99.5
Sc	25	25	24	27	21	27	29	26	20	28	25
V	151	142	158	154	179	157	174	156	122	149	140
Cr	298	227	313	390	224	293	325	317	231	340	375
Co	47	27	27	30	18	26	31	28	20	28	26
Ni	248	60	93	109	101	71	86	85	92	79	115
Ga	17	17	17	16	22	17	17	16	15	17	17
Rb	87	156	168	215	328	204	321	305	123	164	189
Sr	363	386	684	519	878	901	193	301	388	750	687
Y	23	30	27	25	30	31	28	27	20	30	27
Zr	210	295	309	287	331	327	293	280	169	286	243
Nb	9	17	13	12	38	15	14	13	19	14	12
Cs	16	36	33	39	19	27	56	43	3.8	34	30
Ba	1100	955	2130	2130	2550	2250	2320	2120	506	1990	1470
La	32	41	72	69	124	77	70	69	36	81	72
Ce	68	91	151	146	233	155	146	147	73	161	136
Pr	8.1	11	19	18	27	19	18	18	8.7	19	16
Nd	32	45	74	70	100	76	74	74	34	78	64
Sm	6.0	8.8	12	12	15	13	12	12	6.5	13	11
Eu	1.5	1.9	2.9	2.8	3.3	3.0	2.7	2.8	1.5	3.1	2.5
Gd	4.8	7.0	8.2	7.7	10	8.9	8.6	8.5	5.2	8.8	7.5
Tb	0.72	0.95	0.98	0.95	1.2	1.1	0.96	1.00	0.68	1.04	0.90
Dy	4.5	5.9	5.6	5.4	6.4	6.2	5.7	5.6	4.0	6.0	5.4
Ho	0.86	1.1	1.0	0.98	1.1	1.1	0.99	1.1	0.72	1.1	0.94
Er	2.5	3.0	2.7	2.7	2.7	3.0	2.8	2.8	1.9	3.1	2.6
Tm	0.37	0.44	0.38	0.36	0.38	0.43	0.38	0.39	0.28	0.43	0.37
Yb	2.4	2.9	2.4	2.5	2.2	2.8	2.5	2.7	1.8	2.9	2.5
Lu	0.35	0.41	0.36	0.34	0.33	0.42	0.34	0.39	0.25	0.38	0.36
Hf	5.5	7.7	8.0	7.7	7.7	8.5	7.2	7.9	4.5	7.4	6.1
Ta	0.6	1.2	0.8	0.8	2.1	1.0	0.9	0.9	1.8	0.9	0.9
Pb	48	17	20	15	9	21	9	12	16	29	27
Th	11	16	19	18	40	20	17	17	14	18	18
U	2.2	2.9	3.5	4.4	6.6	3.5	3.0	3.1	4.2	3.1	4.0

Table C.3. *(continued)* Representative major (wt %) and trace element (μg/g) analyses of Variscan Group II lamprophyres

Region	Vosges-S										
Rock type	Kersantite			Minette							
Sample	VO 66	VO 67	VO 73	VO 05	VO 06	VO 18	VO 56	VO 57	VO 59	VO 60	VO 64B
SiO_2	50.4	49.6	56.0	56.9	48.9	56.2	54.3	58.9	59.1	59.7	63.7
TiO_2	0.93	0.89	1.62	1.01	1.07	0.90	0.95	0.99	1.06	0.86	0.81
Al_2O_3	14.2	13.3	12.4	12.4	12.5	12.4	11.3	12.6	12.7	13.0	12.4
Fe_2O_3	8.33	8.11	6.21	6.13	7.78	5.96	6.36	4.54	4.84	5.25	4.13
MnO	0.13	0.14	0.09	0.10	0.13	0.09	0.10	0.10	0.08	0.08	0.06
MgO	7.15	7.80	6.01	8.58	6.72	8.76	7.35	4.62	6.60	6.06	4.99
CaO	6.43	6.63	4.97	4.60	7.43	4.10	5.69	5.14	3.36	3.65	2.55
Na_2O	2.46	2.25	3.36	2.02	1.95	2.09	0.97	1.92	1.66	2.07	1.82
K_2O	4.73	4.15	4.83	6.34	5.66	5.41	4.95	6.58	6.78	6.40	7.53
P_2O_5	0.85	0.80	1.50	0.97	0.99	0.80	1.22	1.06	1.10	1.17	1.02
BaO	0.24	0.21	0.35	0.28	0.95	0.28	0.22	0.36	0.27	0.24	0.25
SrO	0.09	0.07	0.05	0.05	0.12	0.06	0.08	0.07	0.05	0.06	0.05
ZrO_2	0.03	0.03	0.07	0.05	0.05	0.05	0.05	0.08	0.08	0.05	0.06
$\sum REE_2O_3$	0.03	0.02	0.04	0.03	0.04	0.03	0.03	0.04	0.04	0.03	0.04
LOI	4.63	6.21	3.06	0.63	6.56	2.10	6.93	3.96	2.76	1.65	0.61
Sum	100.6	100.2	100.5	100.1	100.9	99.2	100.5	100.9	100.5	100.3	100.1
Sc	40	37	24	24	33	27	24	22	21	24	18
V	229	213	143	138	205	147	146	118	119	131	99
Cr	331	347	195	548	302	575	443	315	335	280	341
Co	32	27	20	26	31	25	25	20	21	19	19
Ni	90	98	107	188	71	88	94	88	86	61	98
Ga	16	14	18	16	14	15	16	19	20	17	18
Rb	230	201	257	335	318	267	213	299	302	318	407
Sr	748	583	440	456	998	502	696	624	459	485	430
Y	35	30	31	24	35	32	30	31	34	28	32
Zr	237	198	488	393	383	350	364	560	608	336	465
Nb	17	14	39	35	20	24	31	42	42	26	35
Cs	12	10	9.3	39	18	20	18	15	13	44	34
Ba	2120	1860	3140	2460	8460	2480	1940	3220	2380	2170	2230
La	37	33	54	35	46	41	37	54	52	35	42
Ce	78	72	134	87	109	91	88	126	129	88	106
Pr	11	10	20	13	16	13	14	18	20	14	17
Nd	48	44	95	63	76	61	71	89	102	73	87
Sm	10	10	21	15	16	14	18	20	26	19	23
Eu	2.2	2.0	3.6	2.5	3.4	2.4	2.9	3.6	4.0	3.0	3.5
Gd	8.1	7.5	12	8.8	12	10	11	12	15	11	12
Tb	1.1	0.97	1.3	0.98	1.4	1.1	1.1	1.3	1.5	1.1	1.3
Dy	6.5	5.8	6.7	5.1	7.5	6.6	6.0	6.8	7.6	5.8	6.5
Ho	1.2	1.1	1.1	0.85	1.3	1.1	1.1	1.1	1.3	0.98	1.1
Er	3.4	3.0	2.8	2.2	3.5	3.0	2.7	2.9	3.1	2.5	2.9
Tm	0.52	0.42	0.39	0.32	0.45	0.45	0.36	0.37	0.41	0.36	0.43
Yb	3.5	2.9	2.4	2.0	3.1	2.9	2.6	2.5	2.6	2.4	3.0
Lu	0.47	0.42	0.37	0.30	0.44	0.42	0.35	0.35	0.41	0.35	0.43
Hf	6.4	5.6	14	12	10	10	9.7	16	18	9.0	13.0
Ta	1.2	1.0	2.5	2.9	1.2	1.8	2.2	3.1	3.0	1.8	2.5
Pb	22	14	35	18	29	28	26	37	17	23	387
Th	26	22	60	68	43	46	55	83	95	59	82
U	11	9.3	17	22	6.7	13	18	25	29	17	27

Table C.3. *(continued)* Representative major (wt %) and trace element (μg/g) analyses of Variscan Group II lamprophyres

Region	Vosges-S							Schwarzwald			
Rock type	Minette							Kersantite			
Sample	VO 69	VO 70	VO 72	VO 82	VO 83	VO 84	VO 97	SCH 05	SCH 06	SCH 13	SCH 20
SiO_2	56.2	60.1	60.4	57.9	60.5	55.0	62.0	59.7	52.9	54.5	55.7
TiO_2	1.52	1.04	1.04	1.22	1.25	1.71	0.88	0.77	0.96	1.15	1.29
Al_2O_3	12.1	13.0	13.0	14.5	12.7	11.7	13.1	14.5	13.5	14.5	15.9
Fe_2O_3	5.99	4.65	4.67	6.10	3.87	6.09	4.43	5.64	7.00	7.20	7.36
MnO	0.10	0.08	0.07	0.09	0.12	0.09	0.06	0.09	0.11	0.12	0.11
MgO	5.15	5.04	5.52	4.77	5.71	6.02	5.02	5.12	8.52	7.50	7.43
CaO	4.93	3.43	3.31	4.04	3.41	5.62	2.38	4.37	5.59	4.31	5.39
Na_2O	0.98	1.85	2.38	2.64	1.49	0.94	2.18	2.56	1.70	2.40	2.48
K_2O	8.08	6.87	6.44	6.83	7.90	7.87	7.05	4.61	4.26	4.01	1.97
P_2O_5	1.46	0.84	0.84	0.89	1.02	1.74	0.56	0.59	0.70	0.70	0.46
BaO	0.44	0.25	0.22	0.26	0.31	0.49	0.23	0.19	0.21	0.24	0.07
SrO	0.08	0.06	0.04	0.18	0.03	0.09	0.06	0.05	0.05	0.05	0.06
ZrO_2	0.07	0.07	0.06	0.05	0.09	0.07	0.08	0.03	0.05	0.04	0.04
$\sum REE_2O_3$	0.05	0.04	0.03	0.05	0.06	0.05	0.05	0.02	0.02	0.03	0.03
LOI	3.59	2.94	2.17	1.31	1.83	2.17	1.95	1.20	4.87	3.68	1.74
Sum	100.7	100.3	100.2	100.8	100.3	99.6	100.1	99.4	100.4	100.4	100.0
Sc	26	20	19	25	20	25	19	24	29	26	22
V	161	114	112	168	117	152	101	133	160	154	139
Cr	210	212	229	143	247	203	321	428	600	453	307
Co	21	16	17	20	21	20	18	22	31	25	27
Ni	105	48	52	45	111	84	75	82	183	89	105
Ga	18	18	18	18	21	17	21	17	16	15	17
Rb	428	380	329	360	426	417	425	216	174	135	138
Sr	709	510	362	1510	265	771	506	455	435	415	483
Y	34	31	31	30	32	32	33	24	34	31	30
Zr	530	492	438	383	649	533	580	232	350	308	283
Nb	42	33	31	29	39	44	38	16	26	25	22
Cs	19	20	18	56	20	17	39	15	9.2	23	39
Ba	3950	2270	1950	2340	2750	4330	2070	1720	1910	2100	660
La	58	48	43	74	75	64	71	36	35	41	44
Ce	146	111	99	163	179	154	154	76	74	83	93
Pr	22	17	16	23	28	24	21	10	10	10	12
Nd	106	86	82	104	134	111	97	42	45	43	47
Sm	23	21	20	20	30	24	20	8.9	10	9.2	8.9
Eu	3.8	3.4	3.3	3.5	4.1	4.0	3.2	1.7	2.1	1.8	2.1
Gd	14	12	12	11	15	13	12	6.6	8.1	7.6	7.4
Tb	1.5	1.3	1.2	1.2	1.5	1.4	1.2	0.81	1.1	1.0	1.1
Dy	7.3	6.3	6.1	6.2	7.3	7.0	6.9	4.8	6.7	6.0	6.2
Ho	1.2	0.98	1.1	1.1	1.2	1.2	1.3	0.93	1.3	1.1	1.1
Er	3.2	2.6	2.7	2.8	2.9	2.9	3.5	2.5	3.4	2.9	3.0
Tm	0.46	0.36	0.35	0.42	0.4	0.4	0.44	0.37	0.49	0.44	0.41
Yb	2.8	2.4	2.3	2.5	2.4	2.6	3.0	2.6	3.1	2.9	2.6
Lu	0.40	0.34	0.30	0.39	0.32	0.38	0.45	0.34	0.44	0.39	0.41
Hf	14.8	13.8	12.4	10.9	18.9	15.2	16.8	7.0	9.8	8.1	7.6
Ta	2.7	2.3	2.2	2.1	2.8	2.8	3.2	1.2	1.9	1.8	1.8
Pb	41	26	22	14	108	258	38	23	29	35	17
Th	66	72	64	49	95	66	72	30	36	29	17
U	23	21	20	13	25	19	19	10	10	7.1	4.3

Table C.3. *(continued)* Representative major (wt %) and trace element (μg/g) analyses of Variscan Group II lamprophyres

Region	Schwarzwald										
Rock type	Kersantite										
Sample	SCH 21	SCH 23	SCH 24	SCH 25	SCH 26	SCH 27	SCH 28	SCH 30	SCH 31	SCH 32A	SCH 32B
SiO_2	58.0	56.6	53.8	62.1	57.7	57.8	63.3	59.5	60.9	64.2	63.3
TiO_2	0.85	0.85	1.00	0.99	1.04	1.06	0.72	0.85	0.96	0.75	0.83
Al_2O_3	13.6	13.7	13.7	15.3	14.0	14.1	14.8	15.1	14.5	14.1	16.4
Fe_2O_3	6.55	6.66	7.75	5.38	6.28	6.44	4.83	5.47	5.66	4.19	4.79
MnO	0.10	0.10	0.11	0.09	0.10	0.10	0.06	0.08	0.10	0.07	0.07
MgO	8.21	8.61	10.1	3.38	6.68	6.97	4.17	5.18	6.20	4.61	2.71
CaO	3.10	3.41	5.08	3.32	4.37	3.87	2.85	3.35	3.46	2.92	3.60
Na_2O	2.22	1.56	2.23	3.16	2.42	2.50	3.02	2.68	3.04	2.76	3.50
K_2O	4.50	4.29	3.32	5.03	4.81	4.87	4.52	4.43	3.41	5.22	3.72
P_2O_5	0.80	0.73	0.66	0.78	0.88	0.91	0.65	0.30	0.39	0.53	0.28
BaO	0.25	0.23	0.36	0.24	0.27	0.28	0.20	0.14	0.23	0.32	0.14
SrO	0.05	0.04	0.06	0.06	0.06	0.06	0.05	0.06	0.06	0.10	0.06
ZrO_2	0.04	0.04	0.04	0.04	0.06	0.06	0.04	0.03	0.04	0.05	0.03
$\sum REE_2O_3$	0.03	0.03	0.02	0.03	0.05	0.05	0.03	0.02	0.03	0.03	0.02
LOI	1.58	3.72	1.78	0.82	1.21	1.31	1.27	2.16	1.62	0.73	0.99
Sum	99.9	100.5	100.0	100.8	99.9	100.4	100.5	99.3	100.6	100.5	100.4
Sc	23	24	29	19	24	25	16	20	18	14	16
V	134	144	164	118	137	145	100	122	123	93	111
Cr	441	491	577	216	450	447	201	264	267	230	59
Co	24	27	33	15	24	23	12	19	19	16	11
Ni	100	117	203	70	60	58	30	80	84	131	25
Ga	17	17	16	20	18	18	17	17	18	20	19
Rb	210	194	139	221	228	261	199	172	129	167	145
Sr	410	340	520	526	480	482	398	468	526	844	540
Y	37	36	37	34	37	39	30	22	24	22	22
Zr	279	286	268	307	421	436	266	238	262	358	248
Nb	20	19	18	21	32	33	22	16	19	22	14
Cs	33	11	31	21	16	19	19	28	16	8.9	11
Ba	2260	2020	3210	2160	2440	2460	1780	1260	2080	2890	1260
La	39	42	36	42	66	69	43	37	46	59	43
Ce	85	87	78	91	150	153	91	74	92	120	86
Pr	11	12	11	13	22	22	12	8.8	12	15	10
Nd	51	52	46	59	99	97	53	36	48	61	41
Sm	12	11	10	13	20	20	11	7.6	9.3	11	7.6
Eu	2.0	2.1	2.1	2.6	3.4	3.4	2.1	1.6	1.9	2.3	1.6
Gd	9.2	9.0	8.3	9.4	11	13	7.4	5.6	6.5	8.0	5.7
Tb	1.3	1.2	1.2	1.2	1.4	1.5	1.0	0.76	0.91	0.90	0.80
Dy	7.4	7.4	7.3	7.3	8.0	8.6	5.9	4.4	4.7	4.6	4.3
Ho	1.4	1.4	1.4	1.3	1.5	1.6	1.1	0.85	0.88	0.85	0.79
Er	3.7	3.8	3.8	3.4	3.7	4.0	3.0	2.1	2.3	2.1	2.0
Tm	0.53	0.54	0.51	0.47	0.54	0.54	0.45	0.29	0.35	0.28	0.29
Yb	3.4	3.8	3.5	3.0	3.4	3.7	2.8	1.8	2.2	1.8	2.0
Lu	0.50	0.51	0.50	0.43	0.53	0.52	0.43	0.25	0.30	0.26	0.29
Hf	7.9	8.5	7.4	9.0	13	13	8.2	6.7	7.4	9.9	6.7
Ta	1.5	1.4	1.3	1.7	2.3	2.4	1.9	1.5	1.5	2.4	1.3
Pb	325	12	22	13	14	11	13	99	52	123	58
Th	44	39	23	35	66	66	39	19	22	35	18
U	11	9.4	5.9	11	15	15	10	6.0	5.7	7.8	5.4

Table C.3. *(continued)* Representative major (wt %) and trace element (μg/g) analyses of Variscan Group II lamprophyres

Region	Schwarzwald							
Rock type	Kersantite							Kers.-Minette
Sample	SCH 33	SCH 34	SCH 35	SCH 36	SCH 37	SCH 38	SCH 39	SCH 09
SiO_2	63.3	55.7	55.6	60.0	58.5	52.4	53.6	58.7
TiO_2	0.76	0.81	1.02	0.77	0.77	0.91	0.97	1.27
Al_2O_3	15.1	12.8	14.5	14.0	13.4	13.1	14.5	14.4
Fe_2O_3	4.50	5.74	7.07	5.33	5.87	7.45	7.66	6.74
MnO	0.06	0.10	0.11	0.09	0.09	0.12	0.11	0.06
MgO	4.39	8.22	7.85	6.26	8.45	9.73	8.96	5.88
CaO	2.48	4.22	5.98	4.16	3.80	5.70	5.33	1.93
Na_2O	3.18	1.91	2.84	2.48	2.46	1.82	2.16	2.95
K_2O	4.33	3.92	3.47	3.84	3.79	3.96	3.63	5.20
P_2O_5	0.44	0.71	0.42	0.47	0.52	0.73	0.55	0.96
BaO	0.22	0.17	0.23	0.26	0.31	0.27	0.17	0.29
SrO	0.08	0.04	0.07	0.07	0.08	0.06	0.05	0.11
ZrO_2	0.04	0.04	0.04	0.03	0.03	0.04	0.03	0.07
$\sum REE_2O_3$	0.03	0.03	0.03	0.02	0.02	0.04	0.02	0.04
LOI	1.81	4.82	1.17	2.18	1.96	3.16	2.21	1.11
Sum	100.7	99.3	100.3	99.9	100.0	99.5	99.9	99.8
Sc	15	20	28	18	20	31	29	23
V	100	121	166	123	124	172	174	170
Cr	195	545	462	310	443	762	657	215
Co	15	28	28	21	24	33	32	27
Ni	93	243	129	147	185	209	160	120
Ga	20	17	16	17	16	15	16	20
Rb	183	123	159	150	125	175	180	177
Sr	651	361	595	575	661	515	428	914
Y	21	24	27	24	24	31	26	30
Zr	271	278	290	236	220	329	234	545
Nb	20	19	18	16	16	24	18	25
Cs	14	13	15	22	16	18	29	60
Ba	1920	1520	2090	2350	2740	2390	1540	2560
La	45	38	46	38	36	62	33	67
Ce	88	83	92	77	74	135	74	139
Pr	11	12	12	10	9.1	17	10	17
Nd	43	52	49	41	36	71	42	72
Sm	8.1	11	9.0	7.8	7.4	13	9.3	13
Eu	1.8	1.9	1.9	1.7	1.7	2.5	1.8	2.8
Gd	5.7	6.8	6.9	6.0	6.0	9.2	6.4	9.2
Tb	0.74	0.83	0.81	0.78	0.75	1.1	0.90	1.1
Dy	4.2	4.8	5.1	4.7	4.7	6.4	5.4	6.0
Ho	0.73	0.90	0.93	0.87	0.83	1.2	0.98	1.1
Er	2.0	2.3	2.5	2.4	2.3	3.2	2.7	2.9
Tm	0.28	0.32	0.34	0.34	0.32	0.45	0.37	0.38
Yb	1.8	2.1	2.3	2.2	2.2	3.0	2.5	2.6
Lu	0.27	0.31	0.35	0.34	0.35	0.42	0.37	0.36
Hf	7.7	8.0	7.8	6.7	6.4	9.9	6.5	15
Ta	2.2	1.4	1.4	1.3	1.4	1.5	1.4	1.6
Pb	58	50	27	44	35	18	20	10
Th	29	43	21	26	20	43	27	27
U	9.4	13	4.7	8	7.7	9.3	6.8	6.0

Table C.3. *(continued)* Representative major (wt %) and trace element (μg/g) analyses of Variscan Group II lamprophyres

Region	Schwarzwald							
Rock type	Minette							
Sample	SCH 07	SCH 12	SCH 14	SCH 15	SCH 17	SCH 18	SCH 19	SCH 29
SiO_2	55.1	60.0	54.2	51.2	57.5	54.6	52.3	62.2
TiO_2	1.32	1.19	0.98	1.03	0.95	1.26	1.23	0.85
Al_2O_3	14.2	12.1	12.0	14.2	12.8	13.1	12.8	13.2
Fe_2O_3	6.11	5.26	6.47	6.66	5.82	7.31	6.39	4.84
MnO	0.17	0.09	0.10	0.11	0.10	0.11	0.13	0.09
MgO	5.40	5.74	9.35	7.29	5.37	8.28	7.22	5.53
CaO	5.27	3.93	4.91	6.04	4.81	4.17	5.88	3.03
Na_2O	1.66	1.51	0.87	1.28	1.63	1.78	1.73	2.29
K_2O	5.81	7.38	5.23	5.40	6.33	5.43	5.14	5.60
P_2O_5	0.74	1.55	0.94	0.44	1.10	0.79	0.80	0.59
BaO	0.25	0.34	0.32	0.18	0.27	0.27	0.27	0.20
SrO	0.06	0.08	0.06	0.02	0.06	0.06	0.06	0.05
ZrO_2	0.08	0.08	0.06	0.05	0.05	0.08	0.08	0.04
$\sum REE_2O_3$	0.04	0.05	0.02	0.04	0.04	0.03	0.03	0.03
LOI	4.34	1.21	4.17	6.82	3.17	2.61	5.28	1.68
Sum	100.5	100.5	99.7	100.7	100.0	99.8	99.3	100.2
Sc	32	22	26	31	23	30	29	16
V	189	130	145	170	136	177	177	102
Cr	413	235	797	557	152	570	617	427
Co	25	20	30	30	22	30	30	21
Ni	50	125	111	162	66	97	105	93
Ga	19	18	15	15.7	19	16.4	16.3	16
Rb	238	219	206	227	286	194	189	229
Sr	492	660	542	201	476	519	505	442
Y	36	35	37	32	28	32	35	26
Zr	590	600	419	367	377	580	576	306
Nb	29	33	34	20	27	27	26	27
Cs	39	5.3	12	25	16	17	12	24
Ba	2220	3050	1840	1580	1410	2380	2440	1750
La	55	59	37	63	49	42	43	52
Ce	122	153	77	131	114	93.4	92.3	116
Pr	16	26	10	17	18	12	12	15
Nd	69	133	45	69	88	52	52	66
Sm	13	28	11	12	20	11	10	12
Eu	2.5	4.5	2.1	2.5	3.5	2.2	2.2	2.1
Gd	9.5	15	8.8	8.1	11	8.5	8.5	8.2
Tb	1.2	1.5	1.2	1.0	1.2	1.1	1.1	1.0
Dy	7.4	7.6	7.2	6.4	6.1	6.6	6.9	5.4
Ho	1.3	1.2	1.4	1.1	1.0	1.2	1.2	0.90
Er	3.5	3.1	3.4	3.1	2.7	3.1	3.3	2.4
Tm	0.51	0.43	0.46	0.5	0.4	0.5	0.5	0.4
Yb	3.4	2.8	3.1	3.1	2.3	2.9	3.0	2.1
Lu	0.48	0.41	0.45	0.40	0.30	0.40	0.40	0.30
Hf	16	16	11	10	11	17	16	9.4
Ta	2.0	1.9	2.6	1.5	1.9	1.9	2.0	2.4
Pb	34	10	42	17	19	25	20	15
Th	34	115	35	31	69	28	27	43
U	7.0	20	11	6.4	18	7.3	6.3	6.6

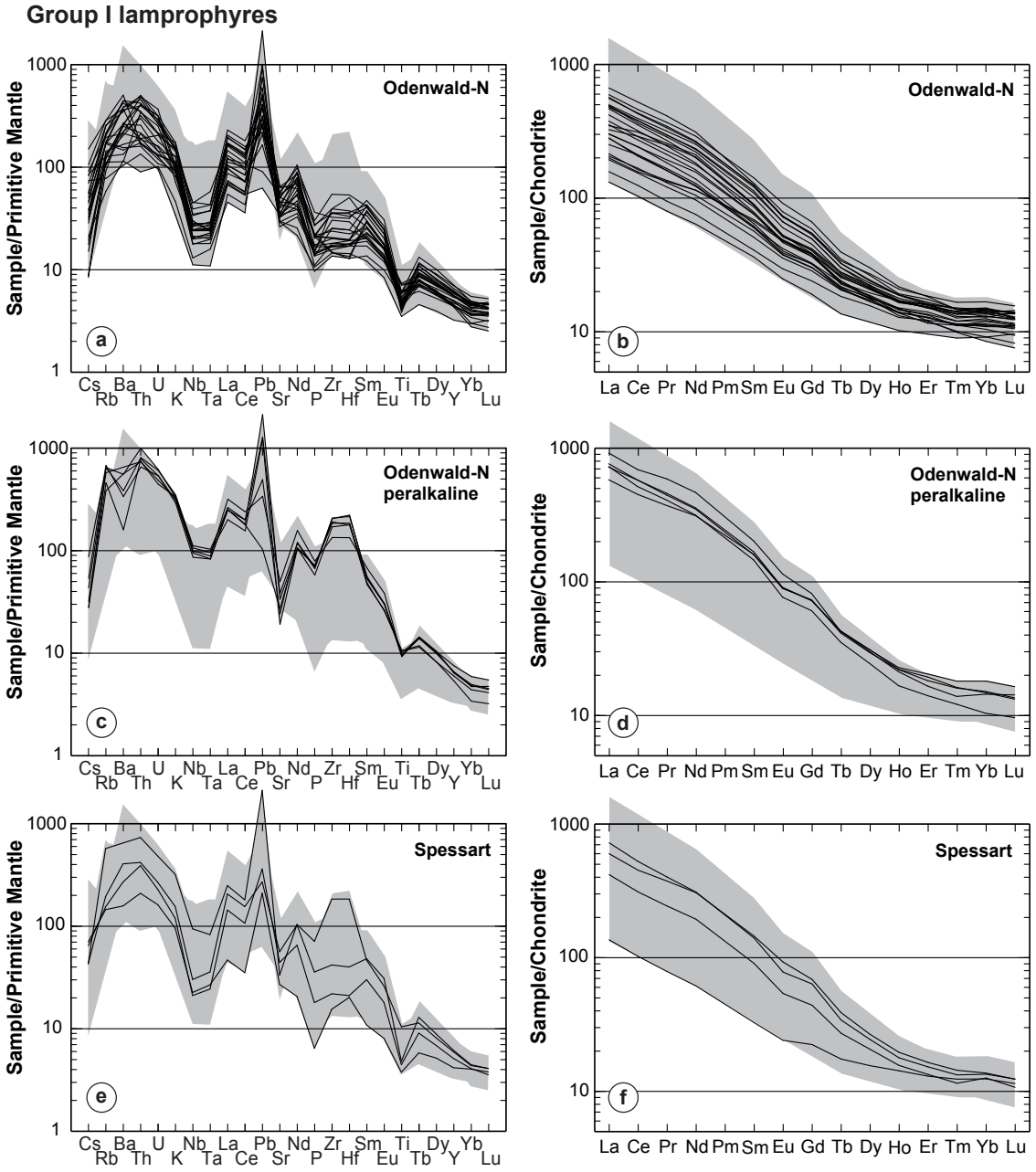

Fig. C.1. *(continued on next page)*

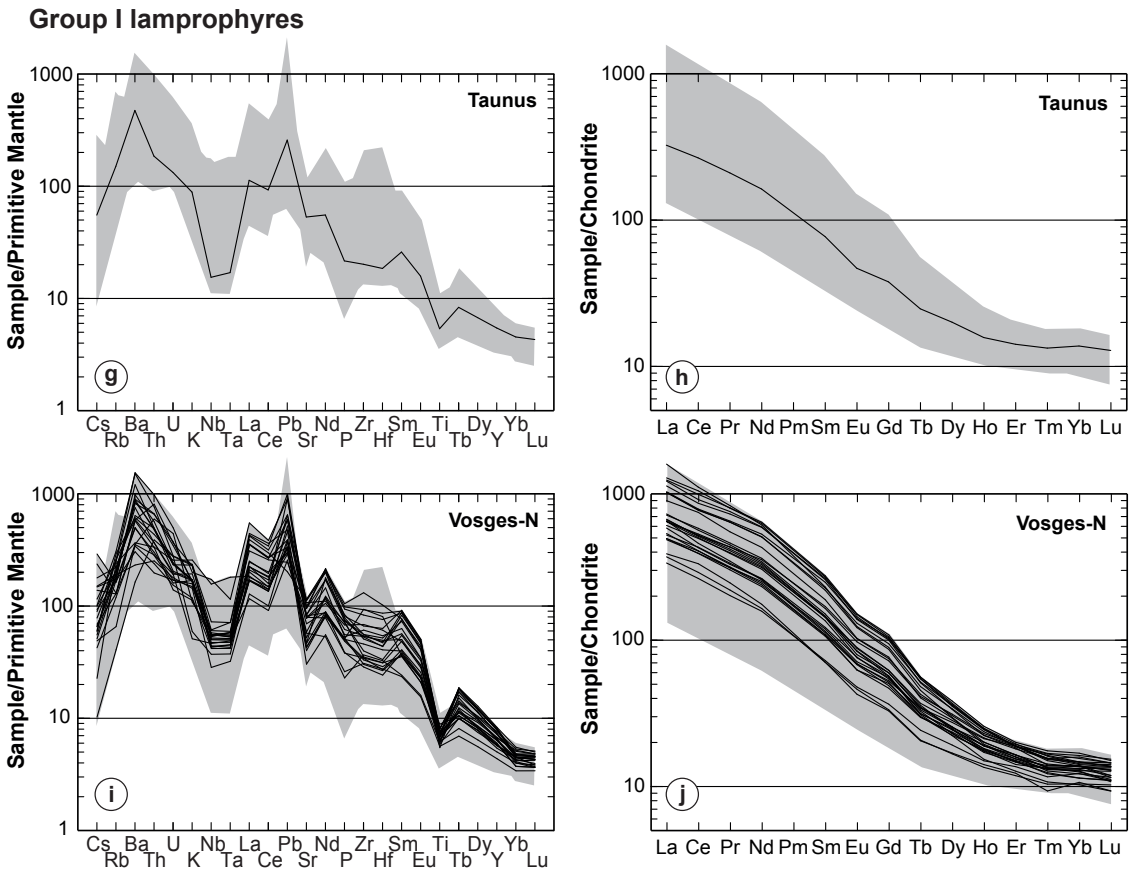

Fig. C.1. Primitive mantle-normalised element concentration diagrams (a, c, e, g, i) (normalisation values from Sun & McDonough, 1989) and chondrite-normalised rare earth element (REE) diagrams (b, d, f, h, j) for Variscan Group I lamprophyres. Chondrite concentration values from McDonough & Sun (1995). Shaded areas correspond to total variation of Variscan Group I lamprophyres.

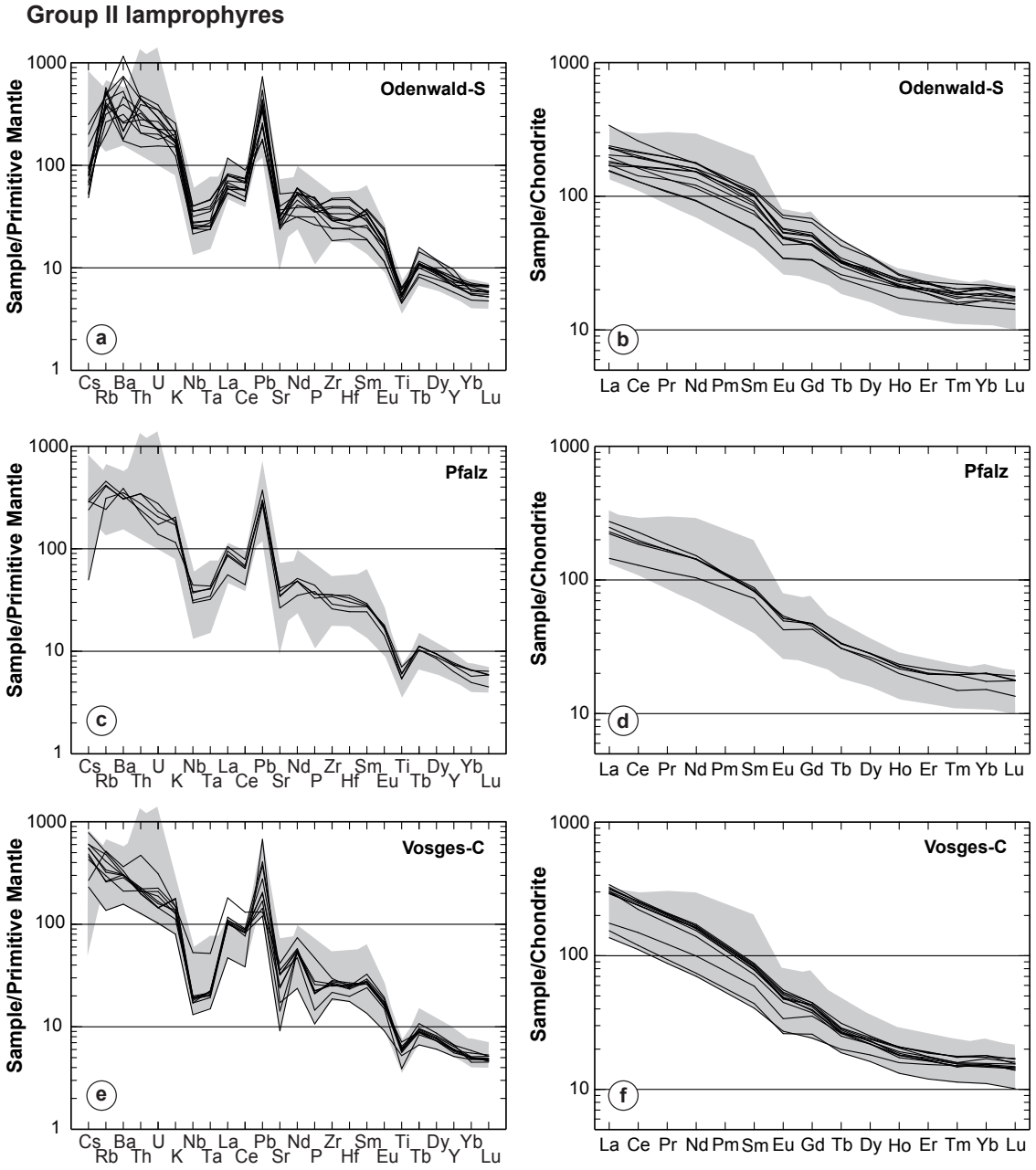

Fig. C.2. *(continued on next page)*

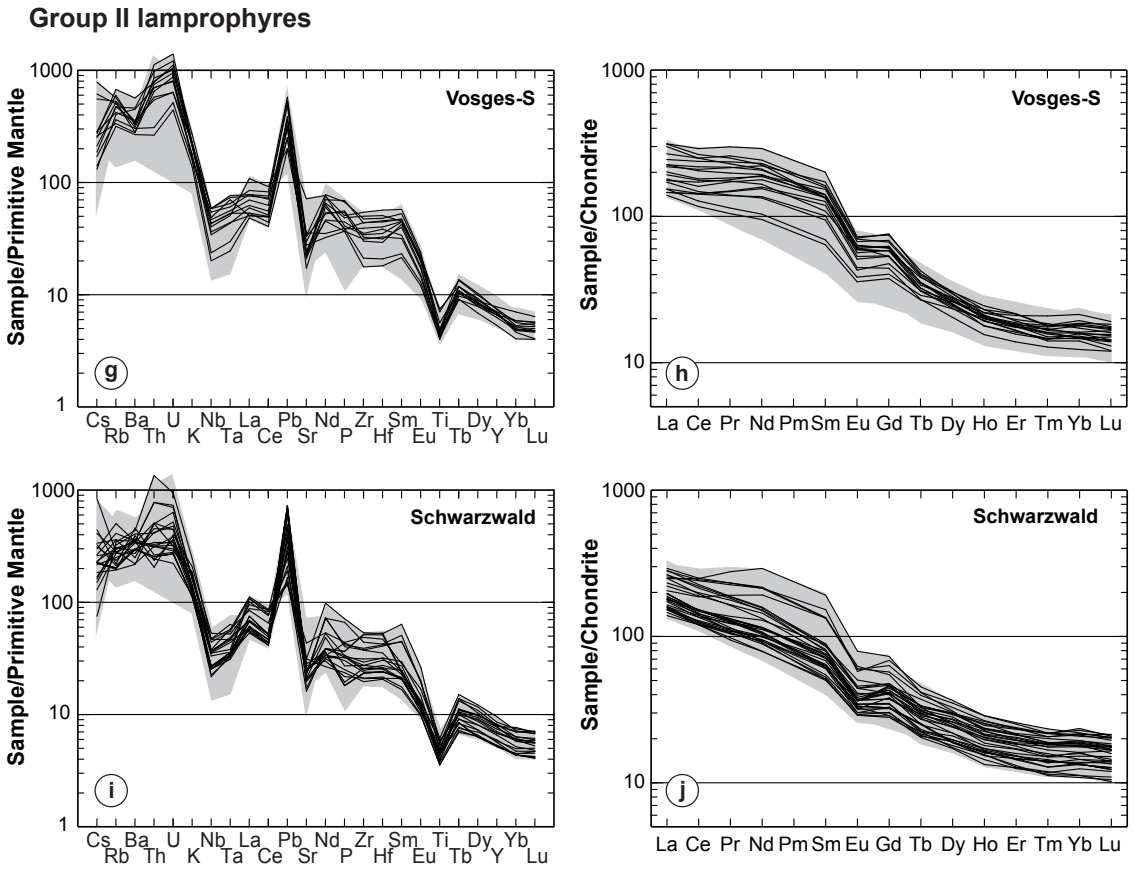

Fig. C.2. Primitive mantle-normalised element concentration diagrams (a, c, e, g, i) (normalisation values from Sun & McDonough, 1989) and chondrite-normalised rare earth element (REE) diagrams (b, d, f, h, j) for Variscan Group II lamprophyres. Chondrite concentration values from McDonough & Sun (1995). Shaded areas correspond to total variation of Variscan Group II lamprophyres.

D. Representative analyses from EPMA

Representative mineral analyses of **Variscan lamprophyres** are reported in four tables:

Table D.1: Representative analyses of clinopyroxene
Table D.2: Representative analyses of phlogopite and biotite in peralkaline minettes
Table D.3: Representative analyses of amphibole
Table D.4: Representative analyses of K-feldspar in peralkaline minettes

Representative mineral analyses of **HP xenolith samples** are reported in seven tables:

Table D.5: Representative analyses of clinopyroxene in the felsic granulite
Table D.6: Representative analyses of clinopyroxene in the eclogite
Table D.7: Representative analyses of garnet
Table D.8: Representative analyses of mica
Table D.9: Representative analyses of feldspar
Table D.10: Representative analyses of amphibole and clinozoisite
Table D.11: Representative analyses of sapphirine and spinel

Table D.1. Representative analyses of clinopyroxene in Variscan lamprophyres

	Peralkaline minette									
	Phenocrysts				Groundmass/rim (zirconian) aegirine–aegirine augite					
Sample	OD 153	OD 153	OD 154	OD 154	OD 153	OD 153	OD 153	OD 154	OD 154	OD 154
Analysis	35	68	28	60	49	16	71	14	16	38
SiO_2	54.88	54.38	54.32	55.16	51.59	53.81	53.09	52.40	52.61	52.22
TiO_2	0.44	0.58	0.52	0.26	0.85	0.06	0.06	0.86	3.90	0.94
ZrO_2	0.00	0.00	0.04	0.00	0.44	0.00	0.02	4.25	0.71	2.87
Al_2O_3	0.43	0.62	0.53	0.91	0.43	0.33	0.33	0.16	0.47	0.26
Cr_2O_3	0.02	0.02	0.05	0.27	0.05	0.09	0.03	0.00	0.01	0.00
Fe_2O_3	0.16	1.10	1.22	0.95	13.40	7.86	13.45	19.79	21.25	20.70
FeO	3.63	2.83	4.45	3.38	10.08	7.26	7.31	7.09	5.95	6.41
MnO	0.15	0.16	0.26	0.11	0.64	0.35	0.38	0.50	0.29	0.54
MgO	16.93	17.03	16.79	17.90	4.09	9.49	6.56	1.38	1.10	1.83
CaO	24.28	24.16	23.11	22.04	12.30	18.03	13.24	2.84	1.25	5.28
Na_2O	0.20	0.27	0.26	0.55	6.24	3.61	5.87	11.26	12.30	10.35
Total	101.11	101.14	101.53	101.53	100.10	100.90	100.33	100.54	99.83	101.41
Formulae were calculated based on 6 oxygens and 4 cations										
Si	1.984	1.965	1.966	1.976	1.995	2.010	2.014	2.025	2.014	1.999
Ti	0.012	0.016	0.014	0.007	0.025	0.002	0.002	0.025	0.112	0.027
Zr	0.000	0.000	0.001	0.000	0.008	0.000	0.000	0.080	0.013	0.054
Al	0.018	0.026	0.023	0.039	0.019	0.015	0.015	0.007	0.021	0.012
Cr	0.000	0.000	0.001	0.008	0.001	0.003	0.001	0.000	0.000	0.000
Fe^{3+}	0.004	0.030	0.033	0.026	0.390	0.221	0.384	0.575	0.612	0.596
Fe^{2+}	0.110	0.086	0.135	0.101	0.326	0.227	0.232	0.229	0.190	0.205
Mn	0.005	0.005	0.008	0.003	0.021	0.011	0.012	0.016	0.009	0.017
Mg	0.912	0.918	0.906	0.956	0.236	0.529	0.371	0.079	0.063	0.104
Ca	0.940	0.936	0.896	0.846	0.510	0.722	0.538	0.118	0.051	0.217
Na	0.014	0.019	0.018	0.038	0.468	0.262	0.432	0.844	0.913	0.768
Total	4.000	4.000	4.000	4.000	4.000	4.000	4.000	4.000	4.000	4.000
Mg#	89.3	91.5	87.1	90.4	42.0	70.0	61.5	25.7	24.8	33.7

Table D.1. *(continued)* Representative analyses of clinopyroxene in Variscan lamprophyres

	Spessartite						Kersantite	
	Phenocrysts						Phenocrysts	
Sample	OD	OD	OD	OD	OD	OD	OD	OD
	11	11	11	11	40	40	43	43
Analysis	2	25	4	7	2	3	1	5
SiO_2	52.28	49.98	47.60	47.86	50.96	51.10	52.01	49.04
TiO_2	0.51	0.96	1.82	1.73	0.56	0.51	0.45	1.00
ZrO_2	n.d.	n.d.	n.d.	n.d.	n.d.	n.d.	n.d.	n.d.
Al_2O_3	2.67	4.55	6.18	6.21	4.27	3.08	3.49	4.15
Cr_2O_3	0.42	0.37	0.00	0.02	0.78	0.43	0.86	0.01
Fe_2O_3	2.00	3.68	4.41	3.90	2.70	2.81	2.15	4.67
FeO	5.03	4.29	5.49	6.20	4.57	4.66	2.80	6.13
MnO	0.20	0.16	0.24	0.22	0.15	0.20	0.16	0.33
MgO	16.53	14.78	13.11	12.99	16.60	16.66	16.13	11.62
CaO	21.08	22.03	21.71	21.43	19.33	19.70	21.94	23.50
Na_2O	0.27	0.35	0.36	0.38	0.51	0.38	0.59	0.49
Total	100.99	101.15	100.90	100.93	100.43	99.54	100.59	100.93
Formulae were calculated based on 6 oxygens and 4 cations								
Si	1.905	1.831	1.766	1.775	1.862	1.887	1.892	1.832
Ti	0.014	0.027	0.051	0.048	0.015	0.014	0.012	0.028
Zr	n.d.	n.d.	n.d.	n.d.	n.d.	n.d.	n.d.	n.d.
Al	0.115	0.196	0.270	0.271	0.184	0.134	0.150	0.183
Cr	0.012	0.011	0.000	0.001	0.023	0.012	0.025	0.000
Fe^{3+}	0.055	0.101	0.123	0.109	0.074	0.078	0.059	0.131
Fe^{2+}	0.153	0.131	0.170	0.192	0.140	0.144	0.085	0.191
Mn	0.006	0.005	0.007	0.007	0.005	0.006	0.005	0.011
Mg	0.898	0.807	0.725	0.718	0.904	0.917	0.875	0.647
Ca	0.823	0.865	0.863	0.851	0.757	0.779	0.855	0.941
Na	0.019	0.025	0.026	0.027	0.036	0.027	0.042	0.035
Total	4.000	4.000	4.000	4.000	4.000	4.000	4.000	4.000
Mg#	85.4	86.0	81.0	78.9	86.6	86.4	91.1	77.2

Table D.2. Representative analyses of phlogopite and biotite in peralkaline minettes

	Phenocrysts							
Sample	OD 153	OD 154	OD 155	OD 169	OD 175	SP 12	VO 03	VO 84
Analysis	1	49	2	5	87	4	2	28
SiO_2	40.82	41.50	41.43	41.47	41.29	41.11	40.42	40.04
TiO_2	3.83	3.48	3.59	3.63	3.71	3.80	4.72	2.58
Al_2O_3	12.80	12.38	12.39	12.24	12.02	12.48	12.58	12.58
Cr_2O_3	0.24	1.09	1.17	0.11	0.55	1.12	0.95	0.55
Fe_2O_3	0.95	0.50	0.64	1.23	1.12	1.02	1.21	0.95
FeO	3.25	5.69	2.71	3.11	2.96	2.82	5.00	3.58
MnO	0.04	0.08	0.01	0.05	0.00	0.04	0.02	0.03
MgO	23.32	21.33	22.96	23.67	23.14	22.85	20.73	23.60
BaO	0.43	0.24	0.27	0.30	0.25	0.22	0.52	0.48
Na_2O	0.07	0.12	0.08	0.13	0.04	0.05	0.11	0.22
K_2O	10.29	10.15	10.10	10.04	10.03	10.25	9.95	9.94
H_2O	4.24	4.23	4.24	4.26	4.22	4.24	4.21	4.17
Total	100.28	100.28	100.28	100.28	100.28	100.28	100.28	100.28
Formulae were calculated on the basis of 10 oxygens and 2 OH								
Fe oxidation was adjusted to Σ(Tet) = 4.000 cations								
Si	2.884	2.940	2.933	2.919	2.933	2.906	2.879	2.881
Al	1.066	1.034	1.033	1.016	1.007	1.040	1.056	1.067
Fe^{3+}	0.050	0.027	0.034	0.065	0.060	0.054	0.065	0.052
Σ(Tet)	4.000	4.000	4.000	4.000	4.000	4.000	4.000	4.000
Al	0.000	0.000	0.000	0.000	0.000	0.000	0.000	0.000
Ti	0.204	0.185	0.191	0.192	0.198	0.202	0.253	0.139
Cr	0.013	0.061	0.065	0.006	0.031	0.063	0.053	0.031
Fe^{2+}	0.192	0.337	0.160	0.183	0.176	0.167	0.298	0.215
Mn	0.002	0.005	0.001	0.003	0.000	0.002	0.001	0.002
Mg	2.456	2.253	2.422	2.484	2.451	2.408	2.202	2.532
Σ(Oct)	2.867	2.841	2.840	2.868	2.855	2.842	2.807	2.919
Ba	0.012	0.007	0.007	0.008	0.007	0.006	0.015	0.013
Na	0.009	0.016	0.010	0.018	0.006	0.007	0.015	0.030
K	0.927	0.917	0.912	0.901	0.909	0.924	0.904	0.912
Σ(X)	0.948	0.940	0.931	0.937	0.922	0.937	0.933	0.956
Mg#	92.7	87.0	93.8	93.1	93.3	93.5	88.1	92.2
XFe^{3+}	0.21	0.07	0.18	0.26	0.25	0.24	0.18	0.19

Table D.2. *(continued)* Representative analyses of phlogopite and biotite in peralkaline minettes

	Groundmass biotite / phenocryst rims						
Sample	OD 153	OD 154	OD 169	OD 175	SP 12	VO 03	VO 84
Analysis	28	50	8	89	26	13	8
SiO_2	37.01	38.52	39.16	39.23	38.97	37.47	36.03
TiO_2	5.21	5.11	5.37	4.76	5.02	4.62	7.34
Al_2O_3	11.68	12.15	11.77	11.30	10.87	12.23	11.75
Cr_2O_3	0.00	0.00	0.00	0.00	0.00	0.00	0.00
Fe_2O_3	2.26	1.82	2.77	2.20	2.65	1.94	2.73
FeO	17.84	11.82	8.06	11.61	14.74	14.85	18.45
MnO	0.35	0.23	0.17	0.25	0.22	0.14	0.17
MgO	11.86	16.28	18.60	16.49	14.29	14.69	9.24
BaO	1.17	0.69	0.70	0.52	0.67	1.44	2.17
Na_2O	0.02	0.31	0.22	0.04	0.04	0.19	0.18
K_2O	9.21	9.21	9.52	9.72	9.41	9.02	8.55
H_2O	3.93	4.06	4.13	4.06	4.03	4.00	3.89
Total	100.54	100.20	100.47	100.18	100.91	100.59	100.50
Formulae were calculated on the basis of 10 oxygens and 2 OH							
Fe oxidation was adjusted to Σ(Tet) = 4.000 cations							
Si	2.821	2.842	2.841	2.895	2.899	2.810	2.775
Al	1.049	1.057	1.007	0.982	0.953	1.081	1.066
Fe^{3+}	0.130	0.101	0.151	0.122	0.148	0.109	0.158
Σ(Tet)	4.000	4.000	4.000	4.000	4.000	4.000	4.000
Al	0.000	0.000	0.000	0.000	0.000	0.000	0.000
Ti	0.299	0.283	0.293	0.264	0.281	0.261	0.425
Cr	0.000	0.000	0.000	0.000	0.000	0.000	0.000
Fe^{2+}	1.137	0.729	0.489	0.716	0.917	0.931	1.189
Mn	0.023	0.014	0.010	0.015	0.014	0.009	0.011
Mg	1.347	1.791	2.012	1.814	1.585	1.642	1.061
Σ(Oct)	2.805	2.817	2.805	2.810	2.797	2.842	2.686
Ba	0.035	0.020	0.020	0.015	0.020	0.042	0.066
Na	0.004	0.044	0.031	0.006	0.006	0.027	0.026
K	0.895	0.866	0.881	0.915	0.893	0.863	0.840
Σ(X)	0.936	0.934	0.938	0.939	0.923	0.938	0.935
Mg#	54.2	71.1	80.4	71.7	63.3	63.8	47.2
$Fe^{3+}/\Sigma Fe$	0.10	0.12	0.24	0.15	0.14	0.10	0.12

Table D.3. Representative analyses of amphibole in lamprophyres

	Peralkaline minette									
Sample	OD153					OD175				
Analysis	51	47	19	41	40	37	62	38	42	53
Position	core	core	rim-1	rim-1	rim-2	core	core	rim	rim	rim
Mineral	Arf	Arf	Mrbk	Wnc	Act	Arf	Arf	K-Rct	Marf	Mrbk
SiO_2	52.35	52.34	55.02	53.47	55.06	53.03	51.23	54.12	54.10	56.71
TiO_2	2.72	2.99	2.28	0.86	0.08	2.72	3.69	1.07	1.14	1.45
ZrO_2	0.02	1.88	0.13	2.18	0.00	4.08	1.43	0.34	1.19	1.34
Al_2O_3	0.49	0.46	0.92	0.48	0.91	0.37	0.51	0.55	0.46	0.35
Cr_2O_3	0.01	0.03	0.04	0.00	0.00	0.04	0.01	0.00	0.02	0.04
Fe_2O_3	4.85	0.27	12.46	5.95	3.21	0.00	1.77	2.87	7.22	8.24
FeO	16.57	20.05	7.55	13.91	11.43	17.58	22.27	11.12	10.23	2.39
MnO	0.99	0.92	0.14	0.66	0.41	0.66	0.82	0.45	0.44	0.38
MgO	8.78	8.03	11.23	10.19	15.18	8.83	5.39	14.76	12.73	16.90
CaO	0.74	0.77	1.21	4.67	10.84	0.44	0.56	5.62	2.37	2.01
Na_2O	8.03	8.12	6.11	3.89	1.49	7.24	7.10	4.97	6.65	6.56
K_2O	2.15	2.21	0.52	1.42	0.29	2.45	2.30	2.47	2.00	1.50
H_2O	1.99	1.98	2.09	2.02	2.10	1.99	1.94	2.07	2.06	2.14
Total	99.68	100.05	99.69	99.71	101.00	99.41	99.00	100.41	100.61	100.00
Formulae were calculated on the basis of 22 oxygens and 2 OH										
Fe^{3+} calculated by normalisation of the sum of cations (except Ca, Na and K) to 13										
Si	7.875	7.931	7.906	7.935	7.853	8.009	7.929	7.854	7.864	7.961
Al	0.087	0.082	0.156	0.084	0.153	0.066	0.092	0.095	0.078	0.057
Fe^{3+}	0.549	0.031	1.347	0.665	0.344	0.000	0.206	0.313	0.789	0.871
Ti	0.308	0.341	0.246	0.096	0.009	0.308	0.429	0.117	0.124	0.153
Zr	0.002	0.139	0.009	0.158	0.000	0.300	0.108	0.024	0.085	0.092
Cr	0.001	0.003	0.004	0.000	0.000	0.004	0.001	0.000	0.002	0.004
Fe^{2+}	2.085	2.541	0.907	1.727	1.363	2.220	2.882	1.350	1.244	0.281
Mn	0.126	0.118	0.017	0.083	0.050	0.084	0.108	0.055	0.055	0.046
Mg	1.968	1.815	2.406	2.253	3.228	1.988	1.244	3.192	2.759	3.537
Ca	0.120	0.125	0.186	0.742	1.657	0.072	0.092	0.873	0.369	0.303
Na	2.343	2.387	1.703	1.120	0.411	2.119	2.129	1.399	1.874	1.784
K	0.412	0.427	0.095	0.270	0.053	0.473	0.454	0.457	0.371	0.269
Total	15.874	15.939	14.983	15.132	15.121	15.643	15.676	15.729	15.614	15.356

Mineral abbreviations are: Arf = arfvedsonite; Mrbk = magnesio-riebeckite; Wnc = winchite; Act = actinolite; K-Rct = K-richterite; Mhs = magnesio-hastingsite; Hst = hastingsite. n. d. = not determined.

Table D.3. *(continued)* Representative analyses of amphibole in lamprophyres

	Peralkaline minette							Spessartite	
Sample	SP12			OD169		VO03		OD11	OD43
Analysis	36	17	35	13	12	45	38	12	8
Position	core	rim-1	rim-2	core	core	core	core	core	core
Mineral	Arf	Wnc	Mrbk	Arf	Arf	Mrbk	Mrbk	Mhs	Hst
SiO_2	52.15	55.16	55.12	52.73	52.93	56.16	56.52	40.94	37.43
TiO_2	3.18	0.44	0.23	2.45	4.13	0.48	0.15	4.15	1.64
ZrO_2	1.57	0.35	0.12	4.96	0.51	0.03	0.06	n.d.	0.19
Al_2O_3	0.34	0.36	0.62	0.19	0.12	0.40	0.38	12.55	13.10
Cr_2O_3	0.00	0.00	0.01	0.00	0.01	0.06	0.13	0.02	0.03
Fe_2O_3	1.21	3.72	9.95	2.09	2.57	16.26	16.87	4.37	4.44
FeO	18.70	10.19	9.68	16.90	16.99	4.07	4.28	7.43	19.04
MnO	0.80	0.97	0.14	1.07	0.61	0.14	0.12	0.13	0.93
MgO	8.60	14.84	11.98	6.85	7.56	12.67	12.02	13.93	5.65
CaO	1.03	6.68	3.22	0.65	0.71	1.34	0.88	11.83	11.06
Na_2O	7.18	4.11	6.06	7.73	8.02	6.25	6.84	2.20	2.29
K_2O	3.04	1.69	0.27	2.63	3.10	0.22	0.18	1.15	2.18
H_2O	1.98	2.08	2.07	1.98	1.98	2.12	2.12	2.06	1.91
Total	99.77	100.58	99.47	100.23	99.25	100.21	100.56	100.75	99.87
Formulae were calculated on the basis of 22 oxygens and 2 OH									
Fe^{3+} calculated by normalisation of the sum of cations (except Ca, Na and K) to 13									
Si	7.906	7.939	7.993	7.990	7.998	7.961	8.000	5.964	5.885
Al	0.060	0.060	0.106	0.033	0.020	0.067	0.063	2.154	2.427
Fe^{3+}	0.138	0.403	1.086	0.238	0.293	1.735	1.797	0.479	0.525
Ti	0.363	0.047	0.025	0.279	0.470	0.051	0.016	0.454	0.194
Zr	0.116	0.024	0.009	0.367	0.038	0.002	0.004	n.d.	0.014
Cr	0.000	0.000	0.001	0.000	0.001	0.007	0.015	0.003	0.004
Fe^{2+}	2.370	1.226	1.173	2.142	2.147	0.482	0.507	0.906	2.503
Mn	0.103	0.118	0.017	0.137	0.078	0.017	0.014	0.016	0.124
Mg	1.944	3.183	2.590	1.548	1.704	2.677	2.537	3.024	1.324
Ca	0.167	1.029	0.500	0.106	0.115	0.203	0.134	1.846	1.862
Na	2.110	1.148	1.704	2.271	2.349	1.717	1.877	0.622	0.697
K	0.588	0.310	0.051	0.507	0.598	0.040	0.033	0.213	0.437
Total	15.865	15.487	15.254	15.618	15.811	14.960	14.997	15.681	15.996

Mineral abbreviations are: Arf = arfvedsonite; Mrbk = magnesio-riebeckite; Wnc = winchite; Act = actinolite; K-Rct = K-richterite; Mhs = magnesio-hastingsite; Hst = hastingsite. n. d. = not determined.

Table D.4. Representative analyses of K-feldspar in peralkaline minettes

Region	Odenwald (Group I)							
Sample	OD153			OD175			OD178	
Analysis	10	12	87	33	67	69	9	3
SiO_2	63.24	64.03	65.05	65.34	64.90	64.82	65.09	65.63
Al_2O_3	18.38	18.31	17.75	16.81	17.85	15.12	17.30	18.83
Fe_2O_3	1.27	1.24	1.68	2.65	1.49	4.88	2.07	0.11
CaO	0.02	0.00	0.00	0.00	0.00	0.04	0.00	0.00
SrO	0.19	0.05	0.12	0.00	0.03	0.00	0.06	0.00
BaO	2.13	0.96	0.32	0.07	0.57	0.17	0.42	0.00
Na_2O	0.59	0.64	0.89	0.48	0.64	0.61	0.54	0.49
K_2O	14.89	15.16	15.06	15.61	15.37	15.25	15.34	15.75
Total	100.70	100.40	100.85	100.96	100.84	100.90	100.83	100.81
Formulae were calculated on the basis of 8 oxygens								
Si	2.951	2.969	2.990	3.007	2.989	3.010	2.999	2.997
Al	1.011	1.001	0.962	0.911	0.969	0.827	0.940	1.014
Fe^{3+}	0.045	0.043	0.058	0.092	0.052	0.171	0.072	0.004
Ca	0.001	0.000	0.000	0.000	0.000	0.002	0.000	0.000
Sr	0.005	0.001	0.003	0.000	0.001	0.000	0.002	0.000
Ba	0.039	0.017	0.006	0.001	0.010	0.003	0.007	0.000
Na	0.053	0.058	0.079	0.043	0.058	0.055	0.048	0.043
K	0.886	0.897	0.883	0.916	0.903	0.903	0.902	0.917
Total	4.991	4.987	4.981	4.971	4.981	4.971	4.970	4.975
Or (mol %)	86.3	88.3	85.7	86.6	88.3	77.7	87.3	95.1
Fe-Or	3.8	3.8	5.2	8.7	4.7	16.0	6.7	0.4
Ab	5.4	5.9	8.2	4.5	5.9	5.7	5.0	4.5
An	0.1	0.0	0.0	0.0	0.0	0.2	0.0	0.0
Slw	0.5	0.1	0.3	0.0	0.1	0.0	0.2	0.0
Cls	4.0	1.8	0.6	0.1	1.0	0.3	0.8	0.0

Mineral abbreviations are: Fe-Or = 'Fe-orthoclase'; Or = orthoclase; Ab = albite; An = anorthite; Slw = slawsonite; Cls = celsian.

Table D.4. *(continued)* Representative analyses of K-feldspar in peralkaline minettes

Region	Spessart (Group I)			Vosges-N (Group I)			Vosges-S (Group II)		
Sample	SP12			VO03			VO84		
Analysis	10	11	31	34	51	52	12	20	22
SiO_2	64.95	65.66	64.82	62.16	63.05	65.34	64.16	65.02	64.94
Al_2O_3	15.11	18.80	17.59	18.61	18.41	18.55	18.34	17.70	17.57
Fe_2O_3	5.06	0.12	1.68	1.46	1.23	0.44	1.03	1.67	1.38
CaO	0.00	0.00	0.00	0.00	0.03	0.00	0.04	0.03	0.12
SrO	0.00	0.00	0.02	0.35	0.38	0.05	0.25	0.11	0.10
BaO	0.12	0.05	0.53	3.35	2.05	0.16	1.59	0.98	0.49
Na_2O	0.83	0.56	0.48	0.96	0.64	0.49	2.83	1.63	0.83
K_2O	15.15	15.87	15.72	13.71	14.55	16.04	11.77	13.65	15.00
Total	101.21	101.06	100.84	100.59	100.34	101.07	100.01	100.78	100.42
Formulae were calculated on the basis of 8 oxygens									
Si	3.006	2.995	2.991	2.924	2.950	2.991	2.967	2.990	2.999
Al	0.824	1.011	0.957	1.032	1.015	1.001	1.000	0.959	0.956
Fe^{3+}	0.176	0.004	0.058	0.052	0.043	0.015	0.036	0.058	0.048
Ca	0.000	0.000	0.000	0.000	0.002	0.000	0.002	0.002	0.006
Sr	0.000	0.000	0.001	0.009	0.010	0.001	0.007	0.003	0.003
Ba	0.002	0.001	0.010	0.062	0.038	0.003	0.029	0.018	0.009
Na	0.074	0.049	0.043	0.088	0.058	0.044	0.254	0.145	0.074
K	0.895	0.923	0.925	0.823	0.868	0.937	0.694	0.801	0.883
Total	4.978	4.984	4.985	4.989	4.984	4.991	4.989	4.975	4.978
Or (mol %)	75.9	94.5	89.1	79.8	85.4	93.7	68.0	78.0	86.3
Fe-Or	16.2	0.4	5.4	4.0	3.6	1.4	2.4	4.7	4.3
Ab	7.6	5.0	4.4	8.9	5.9	4.4	25.7	15.0	7.6
An	0.0	0.0	0.0	0.0	0.2	0.0	0.2	0.2	0.6
Slw	0.0	0.0	0.1	1.0	1.1	0.1	0.7	0.3	0.3
Cls	0.2	0.1	1.0	6.3	3.9	0.3	2.9	1.8	0.9

Mineral abbreviations are: Fe-Or = 'Fe-orthoclase'; Or = orthoclase; Ab = albite; An = anorthite;
Slw = slawsonite; Cls = celsian.

Table D.5. Representative analyses of clinopyroxene in the felsic granulite

Rock type	Felsic granulite		
Stage	I	II	III
Analysis	E-036	E-004	E-006
SiO_2	55.32	53.12	51.06
TiO_2	0.42	0.45	0.59
Al_2O_3	11.51	8.28	5.34
Cr_2O_3	0.03	0.06	0.11
Fe_2O_3	0.00	1.39	3.83
FeO	7.58	7.67	7.16
MnO	0.05	0.05	0.05
MgO	7.20	9.81	11.70
CaO	14.03	17.80	20.24
Na_2O	5.89	3.43	1.63
K_2O	0.01	0.01	0.00
Total	102.04	102.07	101.72
Formulae were calculated on the basis of 6 O			
Si	1.958	1.912	1.872
Ti	0.011	0.012	0.016
Al	0.480	0.351	0.231
Cr	0.001	0.002	0.003
Fe^{3+}	0.000	0.038	0.106
Fe^{2+}	0.224	0.231	0.219
Mn	0.001	0.001	0.002
Mg	0.380	0.526	0.640
Ca	0.532	0.686	0.795
Na	0.404	0.239	0.116
K	0.001	0.000	0.000
Total	3.993	4.000	4.000
Jd	38.2	17.7	–
Ca-Ts	4.2	8.8	12.8
$Fe^{3+}/\Sigma Fe$	0.0	0.1	0.3
Mg#	62.9	69.5	74.5

Fe^{3+} calculated by normalisation to 4 cations.
Jd = $(Na-Fe^{3+}-2Ti)\times 100$;
Mg#=$Mg/(Mg+Fe^{2+})\times 100$;
Ca-Ts = $Al^{IV} = (2-Si)\times 100$

Table D.6. Representative analyses of clinopyroxene in the eclogite

Rock type	Retrogressed eclogite							
Stage	I – Eclogite		II – HP granulite		III – Pyrometamorphism Cpx symplectite domains*			
					IIIa	IIIb	IIIc	IIId
Analysis	112-326	118	112-N019	112-109	134	112-407	111-106	151
SiO_2	54.82	54.87	53.94	53.60	51.73	50.50	51.74	34.34
TiO_2	0.17	0.14	0.16	0.25	0.28	0.19	0.02	0.27
Al_2O_3	11.44	11.48	9.76	8.74	5.47	7.48	3.92	24.52
Cr_2O_3	0.04	0.02	0.03	0.17	0.21	0.00	0.00	0.06
Fe_2O_3	1.30	1.62	1.25	1.27	4.06	3.70	0.69	10.45
FeO	3.62	3.22	4.48	4.73	2.73	8.47	18.34	3.07
MnO	0.05	0.00	0.05	0.04	0.07	0.35	0.47	0.20
MgO	8.80	8.75	9.33	9.97	12.67	13.00	22.49	3.76
CaO	14.08	13.71	16.23	16.83	20.32	14.76	1.78	23.82
Na_2O	6.10	6.33	4.89	4.36	2.30	2.08	0.15	0.10
K_2O	0.02	0.00	0.01	0.00	0.00	0.01	0.00	0.11
Total	100.42	100.13	100.12	99.97	99.84	100.53	99.60	100.68
Formulae were calculated on the basis of 6 oxygens; Fe^{3+} calculated by normalisation of the sum of cations to 4								
Si	1.948	1.952	1.942	1.940	1.897	1.856	1.910	1.301
Ti	0.004	0.004	0.004	0.007	0.008	0.005	0.000	0.008
Al	0.479	0.481	0.414	0.373	0.236	0.324	0.171	1.095
Cr	0.001	0.000	0.001	0.005	0.006	0.000	0.000	0.002
Fe^{3+}	0.035	0.043	0.034	0.035	0.112	0.102	0.019	0.298
Fe^{2+}	0.108	0.096	0.135	0.143	0.084	0.260	0.566	0.097
Mn	0.001	0.000	0.001	0.001	0.002	0.011	0.015	0.006
Mg	0.466	0.464	0.501	0.538	0.693	0.712	1.238	0.212
Ca	0.536	0.523	0.626	0.653	0.798	0.581	0.071	0.967
Na	0.420	0.437	0.341	0.306	0.164	0.148	0.011	0.007
K	0.001	0.000	0.000	0.000	0.000	0.001	0.000	0.005
Total	4.000	4.000	4.000	4.000	4.000	4.000	4.000	4.000
Jd	37.6	38.6	29.9	25.8	3.6	3.5	–	–
Ca-Ts	5.2	4.8	5.8	6.0	10.3	14.4	9.0	69.9
$Fe^{3+}/\Sigma Fe$	0.2	0.3	0.2	0.2	0.6	0.3	0.0	0.8
Mg#	81.2	82.9	78.8	79.0	89.2	73.2	68.6	68.6

*Cpx IIIa in symplectites replacing Cpx I; Cpx IIIb and Cpx IIIc in symplectites bewteen Grt and Cpx I; Cpx IIId in symplectites together with allanite replacing LREE-bearing epidote (see text).
Jd = $(Na-Fe^{3+}-2Ti)\times100$. Mg#=$Mg/(Mg+Fe^{2+})\times100$. Ca-Ts = $Al^{IV} = (2-Si)\times100$.

Table D.7. Representative analyses of garnet

Rock type	Felsic granulite			Retrogressed eclogite						
Stage	I	I/II	I/II	I		II		III		
Analysis	core E156	rim E384	rim E330	66	B-22	N014	204	IIIa 112-403	IIIb 109-161	IIIc 109-211
SiO_2	38.35	38.73	38.33	39.10	38.92	39.50	39.43	40.61	38.59	38.89
TiO_2	0.07	0.07	0.17	0.05	0.09	0.04	0.03	0.08	0.28	0.07
Al_2O_3	21.50	21.67	20.90	22.57	22.01	22.03	23.09	21.64	20.94	21.26
Cr_2O_3	0.00	0.01	0.02	0.00	0.08	0.02	0.01	0.06	0.11	0.01
Fe_2O_3	1.55	1.26	1.86	0.94	1.74	0.97	1.97	1.27	3.23	2.40
FeO	23.80	22.35	23.38	20.02	18.95	20.80	20.20	16.11	0.00	17.57
MnO	2.52	1.01	1.12	0.74	0.46	0.60	0.46	0.89	0.02	0.87
MgO	5.06	6.07	6.62	7.47	9.14	9.14	10.62	12.87	0.06	7.40
CaO	8.02	9.33	7.33	9.76	8.48	7.34	5.79	6.74	36.09	11.53
Na_2O	0.06	0.05	0.06	0.04	0.01	0.04	0.03	0.01	0.04	0.03
Total	100.92	100.55	99.78	100.69	99.87	100.49	101.62	100.28	99.34	100.02
Formulae were calculated on the basis of 12 oxygens; Fe^{3+} calculated by normalisation of the sum of cations to 8										
Si	2.973	2.980	2.982	2.965	2.958	2.990	2.933	3.013	2.946	2.972
Ti	0.004	0.004	0.010	0.003	0.005	0.002	0.001	0.004	0.016	0.004
Al	1.964	1.965	1.916	2.017	1.972	1.965	2.025	1.892	1.884	1.915
Cr	0.000	0.001	0.001	0.000	0.005	0.001	0.001	0.004	0.006	0.000
Fe^{3+}	0.090	0.073	0.109	0.053	0.100	0.055	0.110	0.071	0.186	0.138
Fe^{2+}	1.543	1.438	1.521	1.270	1.204	1.316	1.257	1.000	0.000	1.123
Mn	0.166	0.066	0.074	0.047	0.029	0.039	0.029	0.056	0.001	0.057
Mg	0.585	0.696	0.768	0.845	1.036	1.031	1.178	1.424	0.007	0.843
Ca	0.667	0.769	0.611	0.793	0.690	0.595	0.462	0.536	2.952	0.944
Na	0.008	0.008	0.009	0.006	0.002	0.006	0.005	0.001	0.005	0.005
Total	8.000	8.000	8.000	8.000	8.000	8.000	8.000	8.000	8.003	8.000
Prp	19.8	23.5	25.9	28.6	35.0	34.7	40.3	47.3	0.2	28.5
Alm	52.1	48.3	51.1	42.9	40.7	44.0	42.9	33.1	0.0	37.8
Sps	5.6	2.2	2.5	1.6	1.0	1.3	1.0	1.9	0.0	1.9
Grs	21.5	25.0	19.4	26.1	22.2	19.4	15.0	17.1	90.8	29.7
Adr	1.0	1.0	1.2	0.7	1.1	0.6	0.8	0.7	8.9	2.2
Mg#	27.5	32.7	33.6	40.0	46.2	44.0	48.5	58.8		43.0

Grt IIIa, newly grown early during stage III between grt I/II and cpx I/II; in contact to fsp, spl and cpx (cpx IIIb in Table D.6)
Grt IIIb, modified garnet in contact to destabilised inclusion of clinozoisite. Grt IIIc, grossular in pseudumorph after matrix Czo
Mg#=$Mg/(Mg+Fe^{2+})\times 100$. Prp, pyrope; Alm, almandine; Sps, spessartine; Grs, grossular; Adr, andradite

Table D.8. Representative analyses of micas

Rock type	Felsic granulite		Retrogressed eclogite		
Stage	I	II/III	I – Eclogite		
Mineral	Bt	Bt	Phe	Phe	Phe
Analysis	E/031	E/032	112/308	B/010	111/414
SiO_2	41.81	40.34	56.43	54.39	52.99
TiO_2	3.98	4.90	0.02	0.03	0.17
Al_2O_3	16.76	11.95	19.04	21.45	22.60
Cr_2O_3	0.05	0.21	0.03	0.01	0.00
FeO	11.62	15.38	5.05	3.48	4.97
MnO	0.07	0.20	0.04	0.06	0.03
MgO	12.80	14.29	6.27	5.80	5.21
CaO	0.00	0.00	0.15	0.26	0.24
BaO	0.33	0.29	0.00	0.04	0.00
Na_2O	0.21	0.18	0.04	0.04	0.00
K_2O	9.91	8.82	9.85	9.77	9.71
H_2O	4.22	4.08	4.54	4.50	4.49
Total	101.75	100.65	101.45	99.82	100.39
Formulae were calculated on the basis of 10 oxygens and 2 OH					
Si	2.971	2.964	3.725	3.627	3.542
Al	1.029	1.035	0.275	0.373	0.458
Σ(Tet)	4.000	4.000	4.000	4.000	4.000
AL	0.375	0.000	1.206	1.314	1.322
Ti	0.213	0.271	0.001	0.002	0.008
Cr	0.003	0.012	0.001	0.000	0.000
Fe^{2+}	0.691	0.945	0.279	0.194	0.278
Mn	0.004	0.012	0.002	0.003	0.001
Mg	1.356	1.566	0.617	0.577	0.519
Σ(Oct)	2.640	2.806	2.105	2.090	2.129
Ca	0.000	0.000	0.011	0.019	0.017
Ba	0.009	0.008	0.000	0.001	0.000
Na	0.029	0.026	0.005	0.005	0.000
K	0.899	0.827	0.829	0.831	0.828
Σ(X)	0.936	0.862	0.846	0.855	0.846
Mg#	66.2	62.4	68.9	74.8	65.1

Mg#=Mg/(Mg+Fe^{2+})×100. Bt = biotite; Phe = phengite.

Table D.9. Representative analyses of feldspar

Rock type	Felsic granulite		Retrogressed eclogite				
Stage	I		II		III		
Mineral	Kfs	Plg	Plg	Plg	Plg	Plg	Plg
Analysis	E/046	E/050	112/116	112b/209	111/150	046	109/57
SiO_2	68.75	67.77	64.38	65.29	53.68	59.44	61.87
Al_2O_3	19.22	21.49	22.65	22.48	29.40	25.48	23.78
Fe_2O_3	0.13	0.09	0.16	0.06	0.70	0.79	0.83
CaO	0.33	2.46	3.58	3.13	11.12	7.40	5.14
BaO	0.32	0.05	0.04	n.d.	0.05	0.07	0.02
SrO	0.13	0.13	0.15	n.d.	0.04	0.04	0.00
Na_2O	3.77	9.32	8.89	9.65	4.78	6.83	7.87
K_2O	11.01	1.61	0.53	0.32	0.32	0.84	1.15
Total	103.68	102.91	100.38	100.93	100.09	100.89	100.65
Formulae were calculated on the basis of 8 oxygens							
Si	3.007	2.908	2.832	2.850	2.427	2.643	2.741
Al	0.991	1.087	1.174	1.156	1.567	1.335	1.241
Fe^{3+}	0.004	0.003	0.005	0.002	0.024	0.026	0.028
Ca	0.016	0.113	0.169	0.146	0.539	0.353	0.244
Ba	0.006	0.001	0.001	n.d.	0.001	0.001	0.000
Sr	0.003	0.003	0.004	n.d.	0.001	0.001	0.000
Na	0.320	0.775	0.758	0.816	0.419	0.589	0.676
K	0.615	0.088	0.030	0.018	0.019	0.047	0.065
Total	4.962	4.978	4.973	4.988	4.996	4.995	4.995
Or	65	9	3.1	1.8	1.9	4.8	6.6
Ab	34	79	79	83	43	60	69
An	1.6	12	18	15	55	36	25

Or, orthoclase; Ab, albite; An, anorthite; Kfs, K-feldspar; Plg, plagioclase.

Table D.10. Representative analyses of clinozoisite and amphibole in the retrogressed eclogite

Mineral	Czo	Amphibole				
Stage	I	II		III		
Analysis	111/410	112/308	112/308	109/039	111/179	111/115
SiO_2	39.12	41.72	38.93	39.54	46.77	54.47
TiO_2	0.10	0.81	2.44	3.69	0.44	0.15
Al_2O_3	32.42	14.40	17.07	16.17	8.69	1.60
Cr_2O_3	0.05	0.07	0.00	0.08	0.07	0.00
Fe_2O_3	2.73	5.66	5.33	5.27	4.92	0.89
FeO	0.00	6.94	10.13	8.84	6.83	10.80
MnO	0.06	0.09	0.32	0.44	0.25	0.44
MgO	0.07	14.04	11.91	12.79	15.83	16.46
CaO	24.22	10.29	8.50	8.19	11.44	12.63
Na_2O	0.01	3.29	3.11	2.53	1.69	0.29
K_2O	0.00	0.51	0.52	0.67	0.64	0.09
H_2O	1.98	2.06	2.04	2.06	2.07	2.10
Total	100.76	99.86	100.29	100.27	99.65	99.91
Czo (Amp) formulae were calculated on the basis of 12 (22) oxygens and 1 (2) OH						
$Fe^{3+}/\Sigma Fe$ in amphibole calculated after Schumacher (1997); $Fe^{3+} = Fe_{tot}$ in Czo						
Si	2.964	6.076	5.716	5.765	6.764	7.791
Ti	0.006	0.088	0.269	0.405	0.048	0.016
Al	2.895	2.472	2.954	2.779	1.482	0.270
Cr	0.003	0.008	0.000	0.009	0.008	0.000
Fe^{3+}	0.156	0.620	0.589	0.578	0.535	0.096
Fe^{2+}	0.000	0.845	1.243	1.078	0.827	1.292
Mn	0.004	0.011	0.040	0.054	0.031	0.053
Mg	0.008	3.049	2.605	2.780	3.412	3.510
Ca	1.966	1.605	1.337	1.279	1.772	1.935
Na	0.001	0.929	0.885	0.714	0.474	0.082
K	0.000	0.095	0.097	0.125	0.119	0.016
Total	8.003	15.798	15.735	15.567	15.472	15.060
Mg#		78.3	67.7	72.1	80.5	73.1
X_{Czo}	0.85					

$X_{Czo}=(Al-2)/(Al+Fe^{3+}+Cr-2)$; $Mg\#=Mg/(Mg+Fe^{2+})\times 100$

Table D.11. Representative analyses of sapphirine and spinel

Rock type	Retrogressed eclogite				
Stage	III		III		
Mineral	sapphirine		spinel		
Position	core	rim			
Analysis	162/003	162/004	12/209	12/157	09-068
SiO_2	14.80	16.11	0.18	0.11	0.12
TiO_2	0.13	0.10	0.15	0.60	1.20
Al_2O_3	59.88	56.33	34.53	44.01	53.23
Cr_2O_3	0.00	0.00	0.00	0.27	0.84
Fe_2O_3	1.67	2.10	30.63	21.28	10.05
FeO	5.18	9.14	29.06	22.80	20.71
MnO	0.06	0.22	0.37	0.59	0.44
MgO	17.93	16.43	5.18	10.41	13.21
ZnO			0.02	0.03	0.00
CaO	0.33	0.34	0.10	0.06	0.08
Na_2O	0.09	0.05			
Total	100.06	100.82	100.22	100.17	99.92
Sapphirine (spinel) formulae were calculated on the basis of 20 (4) oxygens and 14 (3) cations					
Si	1.751	1.929	0.006	0.003	0.003
Ti	0.012	0.009	0.003	0.013	0.025
Al	8.347	7.949	1.265	1.499	1.719
Cr	0.000	0.000	0.000	0.006	0.018
Fe^{3+}	0.149	0.189	0.717	0.463	0.207
Fe^{2+}	0.512	0.915	0.755	0.551	0.475
Mn	0.006	0.022	0.010	0.014	0.010
Mg	3.162	2.931	0.240	0.448	0.540
Zn	n.d.	n.d.	0.001	0.001	0.000
Ca	0.041	0.044	0.003	0.002	0.002
Na	0.020	0.013	0.000	0.000	0.000
Total	14.000	14.000	3.000	3.000	3.000
Mg#	86.1	76.2	24.1	44.9	53.2
$Fe^{3+}/(Fe^{3+}+Al)$			0.36	0.24	0.11
$Fe^{3+}/\Sigma Fe$	0.22	0.17	0.49	0.46	0.30

$Mg\#=Mg/(Mg+Fe^{2+})\times 100$

E. SIMS data

Results of the SIMS U-Pb zircon dating of sample OD110 (felsic granulite) and OD109 (retrogressed eclogite) are given in Table E.1.

Table E.1. Results of U-Pb zircon dating

Spot	Th/U atomic	Pb_c %	$^{207}Pb^*/^{235}U$	$\pm1\sigma$	$^{206}Pb^*/^{238}U$	$\pm1\sigma$	$^{207}Pb/^{206}Pb$	$\pm1\sigma$
Felsic granulite (OD110)								
C-3-3-1	0.003	1.5	0.3783	0.0189	0.05332	0.00181	0.0630	0.0011
C-3-3-3	0.003	0.5	0.3832	0.0140	0.05275	0.00183	0.0562	0.0004
C-3-5-1	0.004	0.7	0.3882	0.0136	0.05348	0.00174	0.0584	0.0005
C-3-7-1	0.011	4.1	0.3816	0.0258	0.05339	0.00187	0.0840	0.0022
E-3-6-1	0.006	15.7	0.4096	0.0447	0.05324	0.00167	0.1816	0.0017
E-5-3-1	0.012	3.9	0.3831	0.0112	0.05298	0.00127	0.0840	0.0004
E-8-5-1	0.013	4.2	0.3740	0.0201	0.05295	0.00137	0.0851	0.0013
C-4-8-1	0.46	0.1	5.9640	0.1333	0.33400	0.00754	0.1301	0.0008
C-4-10-2	0.44	0.2	6.4360	0.1614	0.35870	0.00829	0.1314	0.0009
C-1-3-1	0.44	0.3	4.7110	0.1711	0.27120	0.00899	0.1279	0.0024
E-1-3-2	0.41	1.1	4.2430	0.1104	0.24690	0.00623	0.1323	0.0007
E-1-5-1	0.41	0.6	4.3990	0.1480	0.25750	0.00833	0.1283	0.0008
C-4-5-1	0.11	1.2	4.7920	0.1471	0.27840	0.00845	0.1337	0.0008
C-5-5-2	0.30	0.7	3.8480	0.1756	0.22250	0.00933	0.1284	0.0012
E-2-3-1	0.07	0.7	4.4990	0.1049	0.26290	0.00604	0.1290	0.0005
Retrogressed eclogite (OD109)								
109-1	0.010	0.4	0.3895	0.0177	0.05313	0.00102	0.0563	0.0012
109-2	0.009	0.4	0.3582	0.0252	0.05288	0.00137	0.0521	0.0020
109-3	0.197	0.9	0.3922	0.0231	0.05326	0.00105	0.0603	0.0013
109-6	0.010	1.7	0.3882	0.0220	0.05335	0.00130	0.0648	0.0021
109-7	0.013	2.6	0.3783	0.0329	0.05320	0.00214	0.0688	0.0037
109-8	0.011	0.4	0.3940	0.0287	0.05410	0.00162	0.0560	0.0025
109-9	0.288	2.3	0.5814	0.0752	0.07096	0.00196	0.0769	0.0024
109-10	0.106	1.0	0.5170	0.0201	0.06980	0.00141	0.0604	0.0009
109-11	0.020	2.3	0.5521	0.0250	0.07148	0.00156	0.0734	0.0016
109-12	1.176	2.6	0.5358	0.0351	0.07099	0.00167	0.0629	0.0022
109-14	0.017	0.3	0.5064	0.0117	0.06774	0.00130	0.0559	0.0005
109-15	0.732	6.7	0.4637	0.1085	0.06246	0.00174	0.1064	0.0077
109-16	0.500	0.8	0.4188	0.0557	0.06261	0.00202	0.0547	0.0039
109-17	0.187	0.0	0.4454	0.0196	0.06112	0.00154	0.0532	0.0020
109-18	0.045	0.4	0.4810	0.0163	0.06392	0.00128	0.0578	0.0009

Table E.1. *(continued)* Results of U-Pb zircon dating

Spot	$^{206}Pb/^{238}U$ Age (Ma)	$\pm1\sigma$	$^{207}Pb/^{206}Pb$ Age (Ma)	$\pm1\sigma$
C-3-3-1	334.9	11.1	261.4	78.6
C-3-3-3	331.4	11.2	315.2	25.2
C-3-5-1	335.9	10.6	313.4	28.7
C-3-7-1	335.3	11.4	278.5	129.8
E-3-6-1	334.4	10.2	444.5	217.3
E-5-3-1	332.8	7.8	305.1	36.9
E-8-5-1	332.6	8.4	251.0	102.3
C-4-8-1	1858.0	36	2092	11
C-4-10-2	1976.0	39	2100	13
C-1-3-1	1547.0	46	2043	36
E-1-3-2	1423.0	32	2023	11
E-1-5-1	1477.0	43	2013	14
C-4-5-1	1583.0	43	2026	14
C-5-5-2	1295.0	49	2035	24
E-2-3-1	1505.0	31	2016	8
109-1	333.7	6.3	335.7	91.8
109-2	332.2	8.4	153.9	141.6
109-3	334.5	6.4	346.2	122.3
109-6	335.1	8.0	318.9	112.3
109-7	334.1	13.1	266.5	202.6
109-8	339.6	9.9	321.5	159.5
109-9	442.0	11.8	582.6	259.1
109-10	435.0	8.5	359.0	71.3
109-11	445.0	9.4	453.3	85.9
109-12	442.1	10.0	401.6	120.0
109-14	422.5	7.9	380.2	28.6
109-15	390.6	10.6	364.8	496.8
109-16	391.5	12.3	124.7	296.7
109-17	382.4	9.3	322.2	84.3
109-18	399.4	7.7	394.9	60.9

Danksagung

An dieser Stelle möchte ich Prof. Rainer Altherr danken, der mir mit den Lamprophyren von Kos ein interessantes und ergiebiges Thema zur Verfügung gestellt hat. Ich danke ihm auch dafür, dass er mir alle Freiheiten für die Entwicklung eigener Ideen gelassen hat. In besonderer Erinnerung werden die zahlreichen gemeinsamen Gelände-Aufenthalte in Griechenland, Mazedonien und der Türkei bleiben.

Prof. Mario Trieloff danke ich für die Begutachtung dieser Arbeit und für den großen Rückhalt, den er mir während meiner Doktorandenzeit leistete.

Ich danke meiner Freundin Rebecca für die Unterstützung und Motivation während der gesamten Doktorarbeit. Ohne dich hätte die Geländearbeit weniger Spaß gemacht. Die sich über viele Tausende von Kilometern erstreckenden Proben-Kampagnen mit dem Auto wären alleine nicht möglich gewesen.

Schließlich möchte ich besonders meiner Familie, allen voran meiner Mutter, für die Unterstützung auf all meinen bisherigen Wegen und Umwegen danken.

Potsdam Ein herzlicher Dank gilt Rolf L. Romer, der große Geduld beim Entstehungsprozess meiner ersten Publikation hatte. Die dabei gesammelten Erfahrungen sind für mich sehr wertvoll. Ebenfalls möchte ich ihm für die Möglichkeit danken, Isotopenanalysen in seinen Laboren vornehmen zu können.
Auch möchte ich mich bei Bettina Hübner und Johannes Glodny für die Hilfe im clean lab und bei der Bedienung der Spektrometer bedanken.

Erlangen Mein Dank gilt Helene Brätz und Reiner Klemd für die Möglichkeit eine umfangreiche Anzahl an LA-ICP-MS-Analysen in Erlangen machen zu können.

Heidelberg Mein besonderer Dank gilt Thomas Ludwig, der immer zur Stelle war wenn es um Probleme mit Messgeräten ging oder nicht zu lösende Computerfragen auftauchten. Ebenfalls danke ich ihm für zahlreiche Ratschläge und Korrekturen zu Postern, Vorträgen oder Manuskripten.

Michael Hanel danke ich für die schöne gemeinsame Zeit unterwegs im Feld und auf Geländekursen im Schwarzwald und der Eifel. Von besonderem Wert war das regelmäßige gemeinsame Mikroskopieren und Diskutieren.

Ich danke Petra Fuchs für die Unterstützung in Verwaltungsangelegenheiten und für ein „offenes Ohr“ und lustige Gespräche während der Kaffeepausen.

Ein ganz besonderes Dankeschön geht an Ilona Fin und Oliver Wienand, deren exzellenten Dünnschliffen ich immer mit großer Vorfreude entgegenfiebere.

Ebenfalls möchte ich mich bei Hans-Peter Meyer für die Hilfe an der Mikrosonde und der RFA bedanken. Auch danke ich Johannes Grimm und Alexander Varychev für die Unterstützung an der Mikrosonde und dem Rasterelektronenmikroskop, sowie Ilse Glas für die Bestimmung zahlreicher Glühverluste.

Winfried Schwarz und Jens Hopp danke ich für die Möglichkeit einige meiner Lamprophyre im Edelgaslabor datieren zu dürfen. Winfried danke ich auch für die Betreuung an der SIMS und die generelle Unterstützung während der letzten Jahre.

Ich möchte mich bei Merislava Anguelova, Matthias Fladt, Christoph Deutschmann, Christoph Nitsche und Yuriy Gryaznov bedanken, mit denen ich eine tolle gemeinsame Zeit während Kursen und B.Sc.- sowie M.Sc.-Arbeiten hatte.

Ich danke Werner Fielitz für zahlreiche interessante Diskussionen.

Danken möchte ich auch allen Mitarbeitern des Instituts für Geowissenschaften, die mich im Laufe meines Studiums und der Doktorarbeit unterstützt haben.

Eidesstattliche Versicherung gemäß § 8 der Promotionsordnung der Naturwissenschaftlich-Mathematischen Gesamtfakultät der Universität Heidelberg

1. Bei der eingereichten Dissertation zu dem Thema

Geochemistry and petrology of lamprophyres from the Hellenides and the European Variscides

handelt es sich um meine eigenständig erbrachte Leistung.

2. Ich habe nur die angegebenen Quellen und Hilfsmittel benutzt und mich keiner unzulässigen Hilfe Dritter bedient. Insbesondere habe ich wörtlich oder sinngemäß aus anderen Werken übernommene Inhalte als solche kenntlich gemacht.

3. Die Arbeit oder Teile davon habe ich bislang nicht an einer Hochschule des In- oder Auslands als Bestandteil einer Prüfungs- oder Qualifikationsleistung vorgelegt.

4. Die Richtigkeit der vorstehenden Erklärungen bestätige ich.

5. Die Bedeutung der eidesstattlichen Versicherung und die strafrechtlichen Folgen einer unrichtigen oder unvollständigen eidesstattlichen Versicherung sind mir bekannt.

Ich versichere an Eides statt, dass ich nach bestem Wissen die reine Wahrheit erklärt und nichts verschwiegen habe.

Ort und Datum Unterschrift